Mathematical Approaches For The Clinical Translation Of Hyperpolarised ^{13}C Imaging In Oncology

Charlotte Jane Daniels
Corpus Christi College
University of Cambridge

This dissertation is submitted for the degree of
Doctor of Philosophy

September 2017

Declaration

I hereby declare that this dissertation is the result of my own work and includes nothing which is the outcome of work done in collaboration except as declared in the Preface and specified in the text. It is not substantially the same as any that I have submitted, or is being concurrently submitted, for a degree, diploma or other qualification at the University of Cambridge or any other University or similar institution. I further state that no substantial part of my dissertation has already been submitted, or, is being concurrently submitted for any such degree, diploma or other qualification at the University of Cambridge or any other University or similar institution except as declared in the Preface and specified in the text. It does not exceed the word limit of 60,000 words as prescribed by the degree committee for the University of Cambridge School of Clinical Medicine.

Charlotte J. Daniels, September 2017

Acknowledgements

I would first like to thank my supervisor at the University of Cambridge, Dr Ferdia Gallagher, for constant help and support over the last four years. Thank you for your many intellectual contributions to this work, for always being ready with a motivational talk and for the significant editing job to this manuscript. Most of all, thank you for trusting me enough to let me pursue my ideas, even when they seemed slightly eccentric, and for continuing to guide me throughout. I would also like to thank Dr Mary McLean for running the MRSI sequences for both the *in vitro* experiments and the clinical imaging, for teaching me so much about the MR system and for always being ready and willing to offer help and advice. Thank you Surrin Deen, James Brenton and to Roie Manavaki for sourcing the PET and histology data for the ovarian cancer project. Additional thanks to Martin Graves, Rose Eichenberger, Marie-Christine Laurent, Sarah Hilborne, James Grist, Andrew Priest, Nick McGlashan and Andrew Gill for both academic and administrative support and to all the staff, students and researchers of the Radiology and MRIS departments at Addenbrooke's hospital.

This doctorate is jointly supervised between the University of Cambridge and Moffitt Cancer Centre in Tampa, Florida USA. I would therefore also like to thank my second supervisor Dr Alexander Anderson, for agreeing to take me on as a student and for the huge amount of help and support provided. Special thanks also go to Mark Robertson-Tessi for advising on immune system dynamics, to Jan Poleszczuk for Matlab code optimisation and to Jill Gallaher for inspiration and Java code. Thanks to Dan Nichol for inadvertently catalysing this collaboration in the first place and to everyone in the IMO department at Moffitt Cancer Centre. I feel very grateful to have been a part of such a unique and brilliant research department and I wish everybody there the very best for the future.

I would like to further acknowledge Dr Rolf Schulte from GE Healthcare, Munich; thank you for providing a small but very well used animal data set and for the set-up of, and subsequent guidance with, the ^{13}C MNS sequences. Thank you to Dr Markus

Schwaiger for the original acquisition of the animal data and for being so kind as to share it with me, as well as to Dr Fraser Robb of Rapid Biomedical for providing the ^{13}C MR coils and for generally being so kind and supportive over that last four years. Finally, thank you to Phillip Murphy from GSK for providing both intellectual and financial support without which this work would not have been possible.

This scholarship is jointly funded by Glaxo Smith Kline and the Cambridge Biomedical Research Council.

Somebody one told me that "nobody ever finishes their thesis, but one day you will know it is time to abandon it". I have thought about this a lot. There were certainly many moments, many days over the last four years during which the temptation to walk away was quite compelling, at times unbearably so; yet ultimately there was always a reason to stay. There are many people who have been a positive part of this time and amongst them are small number to whom I truly owe the timely, rather than untimely, abandonment of the work contained within these pages.

To my strange and subcultural Cambridge family Dave and Luke, and to honorary member O'Keeffe, for always being whatever it is that you are and for making our home into something uniquely unimaginable and perfectly ours. For dominant evenings, for psytrance with Attenborough and for never missing a Cherry. To my parents, for unquestioning support and undying patience. Especially to Tony, my Dad, for listening at the right time, many times. To Hugh and José, for bringing a little magic to the hood and for making me feel at home when so very far from it. For teaching me to play chess and to drink tea like a lady. To Arturo for reasoning, whether good or bad. To Alex, for surprising openers. To others who were brilliant, vital and complicated, and to whom I simply do not know what to say. To Alice, for being my partner in crime and my rock of ages. Finally, to Stan; should there lie within these pages any worthy idea, any fragment of scientific progress that may someday prove to be of value, then it is that my friend, which I dedicate to you.

Charlie J. Daniels
Somewhere between Switzerland and France
22nd August 2017

Abstract

Dissolution dynamic nuclear polarisation is an emerging clinical technique which enables the metabolism of hyperpolarised ^{13}C-labelled molecules to be dynamically and non-invasively imaged in tissue. The first molecule to gain clinical approval is [1-^{13}C]pyruvate, the conversion of which to [1-^{13}C]lactate has been shown to detect early treatment response in cancers and correlate with tumour grade. As the technique has recently been translated into humans, accurate and reliable quantitative methods are required in order to detect, analyse and compare regions of altered metabolism in patients. Furthermore, there is a requirement to understand the biological processes which govern lactate production in tumours in order to draw reliable conclusions from this data.

This work begins with a comprehensive analysis of the quantitative methods which have previously been applied to hyperpolarised ^{13}C data and compares these to some novel approaches. The most appropriate kinetic model to apply to hyperpolarised data is determined and some simple, robust quantitative metrics are identified which are suitable for clinical use. A means of automatically segmenting 5D hyperpolarised imaging data using a fuzzy Markov random field approach is presented in order to reliably identify regions of abnormal metabolic activity. The utility of the algorithm is demonstrated on both *in silico* and animal data. To gain insight into the processes driving lactate metabolism, a mathematical model is developed which is capable of simulating tumour growth and treatment response under a range of metabolic and tissue conditions, focusing on the interaction between tumour and stroma. Finally, hyperpolarised ^{13}C-pyruvate imaging data from the first human subjects to be imaged in Cambridge is analysed. The ability to detect and quantify lactate production in patients is demonstrated through application of the methods derived in earlier chapters. The mathematical approaches presented in this work have the potential to inform both the analysis and interpretation of clinical hyperpolarised ^{13}C imaging data and to aid in the clinical translation of this technique.

Contents

List of Figures

Chapter 1

Background

1.1 Metabolism in cancer

Abnormal metabolism is a prominent feature of almost all cancers and as such, has been an active driver of basic research since its importance was first observed by Otto Warburg in the late 1920s. The rapid proliferation of cancer cells creates additional demand on both the energy and molecular synthesis requirements of the cells compared to normal tissue. The alternative metabolic pathways which must therefore be accessed in order to fulfil these additional needs separate malignant from healthy cells, providing a clear target for therapeutic agents and molecular imaging probes. Reprogramming of energy metabolism is so widely observed in malignant cells that this feature has been identified as one of the key hallmarks of cancer [1]. Although metabolic phenotypes may be heterogeneous between and even within cancers, there are typical features which allow for broad clinical exploitation, the most common of which is aerobic glycolysis. Commonly referred to as the 'Warburg effect', this particular feature of cancer cells not only inspired a wealth of chemotherapeutic agents, but is also behind the success of molecular imaging techniques such as ^{18}F-fluorodeoxyglucose positron emission tomography (^{18}F-FDG PET) and hyperpolarised imaging with ^{13}C-pyruvate for the detection and monitoring of disease.

1.1.1 Anaerobic glycolysis

The Warburg effect is a phenomenon observed almost ubiquitously in which cancer cells generate a high proportion of their energy through anaerobic glycolysis, even in the presence of adequate oxygen for oxidative phosphorylation. In 1929, Otto Warburg observed that cancer cells taken from mouse ascites produced around half of their adenosine triphosphate (ATP) from glycolytic metabolism, compared to less

than 1% in healthy liver and kidney cells [2]. This seemingly inefficient form of energy production produces just 2 ATP per glucose compared to a possible 38 from mitochondrial respiration. In order to maintain energy requirements, cellular glucose uptake is heavily upregulated to maintain sufficient levels of ATP production; this leads to the production of large amounts of lactate which is pumped out of the cell thereby acidifying the extracellular environment. This microenvironmental acidification has been shown to promote tumour invasion and aggressiveness [3], making tumour pH and anaerobic glycolysis popular targets when considering potential therapies.

Despite its low ATP yield, aerobic glycolysis may not be as inefficient as it appears and there is mounting evidence that this alternative metabolic pathway pays an important role in healthy tissues. Lactate production is a well known feature of exercising muscle cells [4] and there is growing evidence that other healthy cells, for example in the brain [5, 6] and gut [7], regularly utilise anaerobic metabolism when rapid energy production is required. Upregulated glucose uptake is also known to occur at sites of inflammation, with recent evidence pointing to high levels of glycolytic activity from activated T-cells rapidly expanding during an immune response [8]. A simple systems biology approach by Vazquez *et al* considers the limited spatial capacity which a cell may dedicate to different metabolic pathways; for rapidly proliferating cells capable of rapid glucose uptake, the Warburg effect is shown to be the most efficient method of energy production in terms of solvent capacity [9].

1.1.2 Other metabolic changes in cancer

The abnormal use and production of lactate is one of the most clinically important and ubiquitous hallmarks of cancer, however there are a number of other commonly observed metabolic changes which separate healthy from malignant tissue. Cancer cells must not only produce high levels of ATP, but synthesise the macromolecules needed in order to rapidly divide. Increased glutamine uptake has been widely observed in many cancers [10, 11, 12]. DeBerardinis *et al* used ^{13}C spectroscopy to demonstrate that the increased uptake of glutamine by *in vitro* glioblastoma cells far exceeded the cells' requirements for protein and nucleotide synthesis [13]. Not only did the rate of glutamine to lactate metabolism produce sufficient NADPH to support fatty acid synthesis, but the increased glutamine was found to heavily supplement reduced glucose entering the TCA cycle as a carbon source, facilitating the production of many important precursors for biosynthesis. This over-reliance on glutamine metabolism has been termed 'glutamine addiction' and has been shown to be caused by mutation of the Myc oncogene [14].

One of the products of excessive glutamine metabolism, citrate, is used for another process shown to be upregulated in tumours; that of fatty acid synthesis [15]. Since high levels of fatty acids are required for rapid proliferation, identifying means of limiting their production may slow cancer growth significantly. A study by Thupari *et al* showed increased levels of fatty acid synthase enzymes in human breast cancer cells [16]. They demonstrated that inhibition of this enzyme led to apoptosis in the tumour cells but not in normal proliferating tissue, highlighting the enzyme acetyl-CoA carboxylase as a potential therapeutic target in this process. High levels of fatty acid synthase have been shown to be present in tissue exhibiting advanced disease [17] and increased levels of the enzyme correlate with poor prognosis [18].

The rapid biosynthesis of nucleotides, fatty acids, proteins and their necessary precursor molecules demanded by cancer cells, causes differential metabolite uptake to be displayed across cancers. Metabolic flux shows high heterogeneity between and within tumours and is heavily influenced by microenvironmental conditions, with many molecules providing useful clinical targets for probing disease. Non-FDG PET imaging is a good example of how these metabolic changes may be clinically exploited. Uptake of ^{11}C-choline has been shown to occur across multiple different grades of prostate cancer; for identifying low grade tumours it therefore provides an advantage over FDG which shows little or no uptake at low grades [19]. Limited success with this tracer has been also been demonstrated for imaging lymph node metastases [20]. [^{18}F]fluoro-L-dihydroxyphenylalanine ([^{18}F]FDOPA), a labelled dopamine precursor, has proven a useful tracer in the detection of neuroendocrine tumours [21] and of low-grade brain tumours, both of which demonstrate upregulated dopamine uptake [22]. Although the exact mechanisms driving metabolic changes are often poorly understood, identifying the differential uptake of a molecule between cancer and normal tissue provides a means for identification and stratification of tumours, as well as opportunities for therapeutic targeting of these pathways [23]. Figure 1.1 highlights some of the main differences between the metabolic processes utilised by normal and malignant cells.

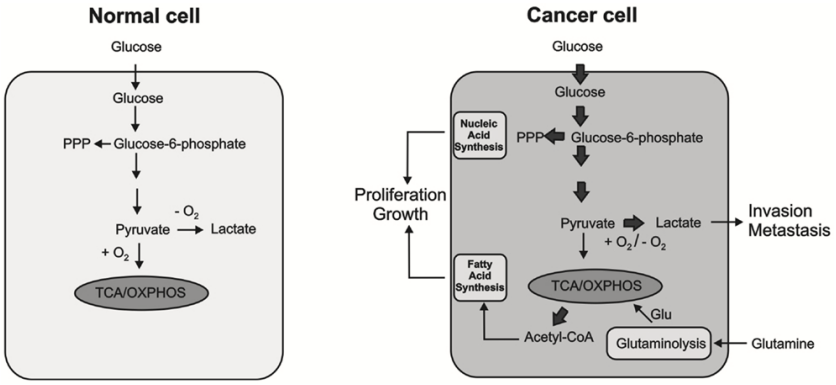

Figure 1.1: Glucose metabolism and energy production pathways in normal (left) and malignant (right) cells. Large arrows denote upregulated processes in cancer cells, either to synthesise the necessary molecules and ATP required for rapid proliferation, or for other advantageous means. Reproduced from Jozwiak *et al*, 2014 [24].

1.1.3 Environmental drivers of metabolic changes in cancer

Although there are certainly commonalities in the metabolic features of cancers, heterogeneity between and within tumours remains an active area of both basic research and clinical concern. Within a single tumour, multiple clonal populations displaying divergent metabolic phenotypes are likely to co-exist as a consequence of accelerated genetic evolution [25, 26]. Although a full discussion of genetic heterogeneity is beyond the scope of this work, there exists a second strong driver of differential phenotypes within and between tumours; that of the tumour microenvironment. The metabolic phenotype expressed by a given cell will, in general, depend on its access to nutrients, its interactions with neighbouring cells and the chemical concentrations and gradients of various growth factors, cytokines, hormones and other important signalling molecules. It is crucial therefore, to consider not the tumour alone, but the tumour-host ecosystem with its multiple complex feedback mechanisms when interpreting metabolic data. The interaction between the tumour and the most commonly involved host cells is described below in the context of ovarian cancer, however it is worth mentioning here one of the most important modulators of the tumour environment which is the vascular system.

High vascularity has been consistently linked to poor prognosis and increased proliferation rates in many different cancers [27, 28, 29]. Tumour angiogenesis and its most important driver, vascular endothelial growth factor (VEGF) are therefore common therapeutic targets, with both anti- and pro-angiogenesis agents trialed in recent years [30, 31, 32]. Although a strong tumour vascular system provides access to vital nutrients such as glucose for fast proliferation, it also increases the delivery rate of

chemotherapy agents and facilitates the removal of acid from the system. The build up of lactate generated by high aerobic glycolysis damages the surrounding stroma and is known to be a key potentiator of invasion and agressiveness [33]. Tumour vascularity is often disorganised, heterogeneous and inefficient, leading to regions of hypoxia within the tumour. This not only promotes an acidic, glycolytic phenotype, but stabilises the production of hypoxia-inducible transcription factors (HIF); this in turn increases VEGF and therefore angiogenesis [34]. The positive feedback mechanisms at play here highlight the complexity and compromises which take place to generate a heterogeneous metabolic tumour environment.

1.1.4 Lactate shuttling and intratumoural cooperation

The propensity of tumours towards lactate production via anaerobic metabolism has been well documented and known for many years. However, it is only recently that the potential function of this excess lactate as an alternative fuel source has been suggested. This is well known to occur in healthy tissue; the 'cell-cell lactate shuttle' theory [35], describes how cells with insufficient oxygen supply, such as in exercising muscle fibre, may produce lactate which is then transported out of the cell via the cell membrane channel protein monocarboxylate transporter 4 (MCT4) and can be taken up by neighbouring cells to be utilised as a fuel source. There are numerous examples of lactate shuttling throughout the body; the transfer of lactate produced by astrocytes, shown to be taken up by neurones for energy production, is one notable example [36]. The same process has now been suggested to occur in cancer, creating a coupled metabolism between heterogeneous regions of the tumour.

Hypoxic areas rely heavily on aerobic glycolysis for energy production, however the lactate produced by these cells diffuses down the lactate gradient towards well oxygenated cells which then can take up the lactate by MCT1 transporters. From here it enters the oxidative phosphorylation pathway to produce ATP, thereby preserving glucose for the anaerobic cells which require it in large quantities [37]. To support this theory, Sonveaux *et al* showed that when MCT1 is inhibited, the tumour is forced to use glucose which, when in short supply, causes the cells to necrose [38]. These results point to cooperation between environmentally distinct tumour regions, in order to optimise available resources for the whole tumour. Lactate has also been identified as a signalling molecule involved in the activation of HIF-1α regardless of oxygen levels; HIF-1α is then responsible for a whole cascade of growth, angiogenic and metabolic changes in the cell [39, 40].

1.1.5 Tumour-stroma coupling and the reverse Warburg effect

Rather than being a purely intra-tumoural effect, lactate shuttling may take place between the tumour and cells known as cancer associated fibroblasts (CAFs). Fibroblasts are a common stromal cell type which become activated in normal tissue as part of the wound healing process. These cells can be recruited by tumours and utilisted for a multitude of purposes, primarily the secretion of useful growth factors and matrix degredation proteins. In a similar mechanism to the intratumoural lactate shuttling described above, peripheral CAFs have been shown to take up lactate produced by hypoxic tumour cells, deacidifying the tumour microenvironment. Koukourakis *et al* found that while colorectal cancer cells had high levels of LDH5 and MCT1 for lactate production and extrusion respectively, the CAFs showed increased LDH1 for lactate oxidation, reduced glucose consumption and increased MCT1/2 for lactate transportation [41]. In a computational model by Capuani *et al*, this type of tumour-stroma metabolic coupling via a lactate shuttle was demonstrated to be energetically favourable under a broad range of conditions given simple physiochemical constraints [42]. An evolutionary game theory model by Basanta *et al* had similar findings, demonstrating the advantages of tumour-stroma coupling in prostate cancer through lactate exchange [43].

In a recently identified phenomenon termed the 'reverse Warburg effect', cancer cells may induce metabolic changes in adjacent stromal fibroblasts to increase their rate of anaerobic glycolysis; this provides lactate for aerobically respiring cancer cells to metabolise and fuel rapid growth [44]. Wiechen *et el* analysed complementary DNA strands from normal and cancerous ovarian tissue, showing that this process is most likely to be to be mediated by a loss of caveolin-1 (Cav-1), a probable tumour-suppressor gene underexpressed in many cancers including breast and ovarian [45, 46]. There is very strong evidence that loss of stromal Cav-1 in breast cancer correlates with increased risk of recurrence and poor survival [47], and Cav-1 expression has been shown to correlate with histological grade and aggressiveness in serous ovarian carcinoma, with parallel changes between stromal and perivascular Cav-1 also observed [48].

Martinez-Outschoorn *et al* propose that the reverse Warburg effect is caused by tumour cells secreting hydrogen peroxide, which has the effect of inducing oxidative stress in the neighbouring stroma [49]. They demonstrated that this oxidative stress causes autophagy and mitophagy in the stromal cells, leading to their producing energy rich nutrients including lactate, fatty acids and glutamine, which mitochondrially

respiring tumour cells feed on. In a further study by Pavlides *et al*, the subsequent loss of stromal Cav-1 by autophagy was shown to feed back, inducing further oxidative stress which leads to aerobic glycolysis and inflammation [50]. More controversially, Martinez-Outschoorn went on to suggest that the 'traditional' Warburg effect is an *in vitro* phenomenon, not representative of *in vivo* metabolism. Co-cultured fibroblasts and tumour cells were shown by fluorescence-activated cell sorting analysis to respectively decrease and increase their mitochondrial activity compared to in single cell-type cultures, with the reverse effect observed for glucose uptake [49]. This has obvious implications for the analysis of ^{18}F-FDG PET data, as these results would imply that the increased glucose uptake by CAFs, rather than tumour, creates the image contrast. Although a large amount of further evidence demonstrating this effect will be necessary before the well-established paradigm of the Warburg effect is reconsidered, it would appear that fibroblasts do have a role to play in the apparent metabolic phenotype of cancers.

1.2 Biology of ovarian cancer

Ovarian cancer is the fifth highest cause of cancer-related mortality in women, making it the most lethal gynaecological malignancy in the western world [51]. Despite relatively low incidence compared to other cancer types, ovarian cancer has a disproportionately high mortality rate which is due in part to the majority of cases, around 65%, going undiagnosed before the cancer has reached an advanced stage and has spread throughout the peritoneal cavity; at this point 5-year survival is less than 30% [52]. Although serum markers such as CA125 have been trialled as early predictors for ovarian cancer [53], there are currently no effective screening programs in place. Furthermore, although most patients are symptomatic from stage I, symptoms are common to many gastrointestinal and genitourinary conditions and go unnoticed in the majority of cases [53]. Around 10% of ovarian cancer cases are related to mutations in the DNA repair genes BRCA1 and BRCA2, with woman bearing these mutations having a much higher probability (10% to 60%) of developing breast or ovarian cancer during their lifetime [54]. Prophylactic mastectomy and oophorectomy are often offered to these women as a preventative measure. Following presentation, standard of care treatment generally involves platinum-based chemotherapy, followed by de-bulking surgery to remove the majority of masses from the peritoneal cavity with possible follow-up chemotherapy. Despite this, the majority of patients relapse within a year [55].

1.2.1 Carcinogenesis and histological types

Although it was believed for a long time that ovarian cancer emanated from the ovarian surface epithelium, this has been challenged by recent evidence. It is now thought that ovarian carcinomas have their origin in Müllerian-duct derived tissues, such as those comprising the fallopian tubes and fimbriae, based on the observation that the tumour cells share histological and protein expression profiles with these tissues and with cells of the endocervix and uterus, but have little in common with the ovarian epithelium [56, 57]. This was first formalised by Dubeau in 2008, who argues that the fimbriae cause inflammation by physically rubbing against the surface of the ovary during ovulation making them a likely site for metaplasia [58]. This is consistent with pre-neoplastic changes [59], and with p53 mutations [57], both seen in the fimbriae of oophorectomy patients with BRCA mutations.

Ovarian cancer is a complex and heterogenous disease displaying many sub-types. By far the most common type seen in ∼90% of cases, is epithelial cell ovarian cancer which can be divided into four main histological subtypes: serous, endometrioid, mucinous and clear cell, with serous representing around 60% of cases [60]. Gonadal-stromal and germ cell cancers make up the remaining 6% and 4% of cases respectively. The diversity between subtypes of epithelial ovarian cancer in terms of their molecular and gene expression profiles is huge; clear cell ovarian carcinoma, for example, has more in common with renal cancer than with serous ovarian cancer. Despite subtypes sharing little more than an anatomical location in terms of their biology, similar treatment strategies are often applied. Although 80-90% of serous and endometrioid cases respond to the most commonly given drug cisplatin, response is only seen in 5% of patients with the remaining two subtypes; a similar result is seen for other platinum-based chemotherapies [61].

1.2.2 Metastasis

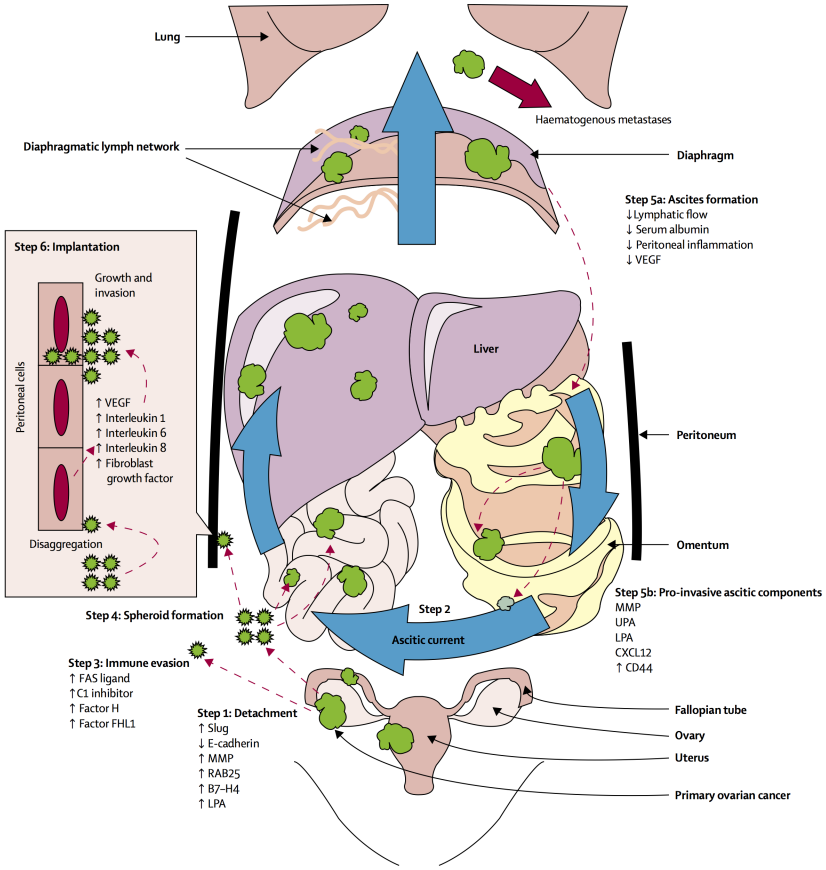

Figure 1.2: Mechanisms of transcoelomic metastasis in ovarian cancer. Step 1: Epithelial ovarian cancer cell (green) detaches after altered gene expression. Step 2: peritoneal or ascitic current (blue arrows) facilitates peritoneal, lymphatic, and haematogenous metastasis. Step 3: immune evasion by complement inhibition and secretion of FAS ligand. Step 4: spheroid formation. Step 5: ascitic components stimulate further metastatic progression. Step 6: peritoneal activation and implantation. B7-H4=Immune costimulatory protein B7-H4; CXCL12=ligand of chemokine (CXC motif) receptor 4 (CXCR4); FHL1=factor H-like protein 1; LPA=lysophosphatidic acid; MMP=matrix metallopeptidase; VEGF=vascular endothelial growth factor. Reproduced from Tan *et al* [62]

Despite the histological diversity present in ovarian cancer, metastatic patterns are highly predictable and common amongst all types. The most frequently involved site (83-100% of cases) is the peritoneum and in particular the omentum, a large fat pad extending from the stomach across the bowel, which has metastases present in 80% of all serous ovarian cancer cases [63]. Other common sites are the lymph nodes (50-60% of cases), with the paraaortic lymph nodes more commonly involved than the

pelvic nodes, the genitourinary and gastrointestinal systems and the liver [64]. The peritoneum has a natural circulation of fluid, facilitating transcoleomic metastasis by transporting detached malignant cells throughout the cavity (see figure 1.2). There is mounting evidence that this is not purely a passive process, but involves adaptive behaviour on behalf of the tumour cells. Upregulation of pathways responsible for preventing apoptosis upon detachment from the extracellular matrix (ECM) may be the first step towards dissemination from the primary site [62]. An alternate theory has been also put forward; according to the metaplasia theory, peritoneal metastases may in fact be independent instances of carcinogenesis based on evidence of genetic heterogeneity between primary and peritoneal implants [65]. Although this theory provides an explanation for the high proportion of cases displaying bilateral ovarian involvement (57.5% of serous carcinomas) [60], it is unlikely to be the full story due to the pattern of metastasis duly following the peritoneal flow.

Peritoneal metastases are frequently associated with the accumulation of malignant ascites, raising the question as to whether the tumour cells are responsible for the production of this ascites, producing a favourable growth medium in which they can proliferate. The ascites is thought to accumulate through a combination of reduced lymphatic drainage due to tumour cell blockage, tumour angiogenesis and microvessel hyperpermeability in the peritoneal lining [66]. VEGF, a glycoprotein over expressed in ovarian cancer, has been found in high concentrations in cell-free malignant ascites, and has been shown to cause leakage of protein from the omentum into the fluid and driving osmosis. VEGF is upregulated by hypoxia, inducing angiogenesis and vessel permeability, with high levels linked to aggressive cancer and poor prognosis [67]. Many additional supernatants found in ascites fluid are thought to have similar protumoral properties. Amongst other factors, high concentration lysophosphatidic acid has been found in malignant ascites, which promotes growth and metastasis by upregulating protease expression and angiogenic factors, and inhibiting apoptosis [68].

1.2.3 Stromal interaction

The observed proportion of stroma from histological analysis of ovarian cancer ranges from around 7% to 83% (median 50%) of total tissue composition, with this estimate proving fairly consistent across histotype and grade [69]. The relative abundance of stromal cells, along with the tumour microenvironmental composition, has been shown to have significant prognostic value and correlate negatively with overall survival alluding to a beneficial symbiotic relationship between tumour and associated stroma. However, the nature of this relationship depends highly on stromal cell

type; where omental fibroblasts have been shown to increase cancer cell adhesion and invasive behaviour, mesothelial cells derived from the omentum actually inhibited aggressiveness [70].

CAFs evidently play a crucial role, although their exact origin is unknown. They may stem from the recruitment of normal tissue fibroblasts, senescent fibroblast promotion or recruitment of mesenchymal stem cells, a differentiation event stimulated by the lysophosphatidic acid abundant in malignant ascites [71]. CAFs have been found in the omentum of patients without metastasis, which may suggest that these cells arrive prior to tumour cells in order to prime the environment for metastasis; there is abundant evidence that the CAFs produce factors promoting adhesion, angiogenesis, lymphangiogenesis and other growth factors important for metastasis to occur [72, 73, 74]. Interestingly, normal stromal cells have actually been shown to inhibit tumour growth, but were not able to survive long-term at the tumour site [74]. In a mouse model by Granot *et al*, injected CAFs labelled with MRI-visible tracer were observed to migrate towards the ovarian tumours and to align around the outer rim, colocalising with the angiogenic neovasculature on the tumour nodules and stabilising the vasculature [75]. It appears that tumour cells can recruit and phenotypically alter the adjacent stroma to support their growth via transforming growth factor-β1 (TGF-β1) and that subsequent over expression of hepatocyte growth factor (HGF) and matrix metalloproteinase-2 (MMP-2) drives invasiveness [73].

The omentum, a highly vascular organ within the peritoneal cavity and comprised mainly of adipocytes, is the most common site for ovarian cancer metastases. In addition to fibroblasts, there is mounting evidence to support the theory that in a range of cancers including ovarian, tumours may recruit adipocytes to become cancer associated adipocytes (CAAs), inducing phenotypical changes within them in order to promote tumour growth [63]. A recent study by Nieman *et al* showed that co-injecting human omental adipocytes with human ovarian cancer cells into mice offered a proliferative advantage compared to the cancer cells alone, with tumours growing on average three times larger [76]. Metabolic changes in both tumour and adipocytes were observed in the *in vitro* co-culture, with the CAAs showing increased lipolysis, providing vital fatty acids to the tumour cells, which in turn showed reduced lipogenesis. The authors suggest FABP4 as the key mediator of this interaction.

1.2.4 Immune involvement

The presence or absence of tumour-infiltrating T-cells in immunohistochemical analysis of ovarian cancer tissue has been shown to be predictive of overall survival, with

38% of patients with T-cells present surviving five years compared to just 4.5% of patients who had no T-cell infiltration [77]. For patients with complete clinical response following surgery and platinum chemotherapy, these numbers were 73.9% and 11.9% respectively. The presence of T-cells was also found to independently correlate with delayed recurrence, and negatively correlated with increased levels of VEGF. An important step in the metastatic pathway is the avoidance of an immune response during transit to the metastatic site; the presence of immunomodulatory factors in the ascites suggests that host immune response plays a role in its production [62]. One way in which ovarian cancer cells have been shown to gain this immune privilege is through the recruitment of regulatory T-cells (T-regs), which migrate preferentially to the ascites and tumour site due to the tumours production of chemokine CCL22 [78]. From there, the T-regs suppress the immune response allowing further tumour growth; imunohistochemical analysis of ovarian cancer tissue by Curial *et al* demonstrated that increased T-reg populations in and around the tumour site correlate with poor survival [78].

1.2.5 Therapy and resistance

Current standard-of-care treatment for ovarian cancer involves the administration of platinum-based chemotherapy followed by de-bulking surgery. Initially, patients can be divided into three cohorts; non-responders, or platinum-refractory; those who relapse within 6 months, termed platinum-resistant; and those who are platinum-responsive. The majority of platinum-responsive patients will also generally relapse, but unusually, those with a long interval may be rechallenged with the same drug in a phenomena known as platinum-sensitive recurrence [79]. The mechanism behind this, and indeed behind the gradual build up of platinum resistance which follows are not well understood.

Platinum-based agents such as cisplatin have multiple mechanisms of action, however the best understood is through the generation of distorting lesions on the DNA, which induces activation of DNA repair mechanisms and ultimately apoptosis [80]. BRCA-positive patients, who already have defective DNA repair mechanisms, will in general display a greater response to platinum-based treatments than similar cancers in BRCA-negative patients, however in both cohorts acquired chemoresistance is a very common problem [81].

A multitude of molecular mechanisms for aquired platinum-resistance have been identified and studied [82], however the mechanisms associated with platinum-sensitive

recurrence are less well documented. Steg *et al* provide the following plausible explanation; the chemo-naive tumour contains a heterogeneous population of chemo-sensitive, quiescent stem cells, and chemo-resistant cells. Platinum administration will target the first of these populations, leaving a much smaller tumour bulk comprising merely the latter two. The quiescent cells then over time may rapidly repopulate the tumour with further treatment-sensitive cells, a model supported by their evidence that post-chemotherapy tumours have higher proportions of cancer stem cells than tumours at recurrence long after treatment, which have a similar stem cell density to the primary [83]. Tumour cells may also resist initial treatment by entering a quiescent state triggered by unfavourable microenvironmental factors, for example hypoxia and nutrient depletion. Long after treatment when conditions become favourable again, they are able to repopulate the tumour with treatment-sensitive cells [84]. Autophagy may be a key initiator of this dormant state; in a study by Lu *et el*, they demonstrate how ARHI, a tumour suppressor gene responsible for autophagy-induced cell death, can switch to promoting dormancy of the tumour cells under certain microenvironmental conditions [85]. Finally, the ECM may also play a role in protecting cells from chemotherapy. Contact with particular components of the ECM, in particular collagen VI, has been shown in several studies to confer resistance to cells, with collagen VI production additionally shown to be upregulated in platinum-resistant cells [86]. The ECM demonstrates further involvement by acting as a regulator for cell dormancy and for the establishment of stem cell populations [87]. Response to treatment may therefore be highly dependant on the spatial location of the cell within the ECM.

1.3 Mathematical oncology

A small but rapidly growing area of cancer research, mathematical oncology describes the process of using formal mathematical techniques to study the behaviour and dynamics of cancer within a theoretical framework. This is certainly not a new idea; mathematical models have been applied to problems in cancer since the 1950s. However, the vast quantity of experimental biological and clinical data generated in recent years, particularly in genetics metabolomics and proteomics, has provided an increased need for complex analysis techniques to be developed [88]. Systems biology saw widespread adoption across many fields as a means of studying a large number of complex interactions within a biological system. Where linear thinking and reductionist approaches failed, systems biology instead provided insight into the emergent and non-intuitive functions and behaviours of a system, through a rigorous analysis

of the system as a whole [89]. Given the recent shift in thinking towards cancer as a complex ecosystem, combined with a need to explain large and growing data sets, it is perhaps unsurprising that mathematical oncology has enjoyed a resurgence within the last fifteen years or so.

Mathematical modelling of cancer allows the complexities of the biology to be translated into a set of rules defined through mathematical formalism. Although the discipline has received criticism in the past for the simplifications of biological components that this process necessarily demands, in reality many experimental set-ups, *in vitro* cell culture for example, require similar simplifying assumptions in order for conclusions to be drawn. By performing mathematical analysis on biological models, a set of predicted outcomes and dynamics with clear limitations is obtained. There are two main classes of model; the first are data driven models, which seek to fit and explain phenomenological experimental data so that future data may be utilised for predictive purposes. The second are theoretical, aiming to provide a mathematical framework which describes the underlying biological processes. This can then be used to explore system dynamics and to make predictions for experimental verification. Both approaches have been successfully applied to common problems in oncology, advancing knowledge and providing testable predictions for, for example, radiotherapy [90], breast cancer [91, 92], tissue invasion [93, 94, 95], metastasis [96] and prostate cancer [97, 98]. Given the huge range of different mathematical approaches which may be applied to clinically relevant questions, the breadth of the field is quite significant. The following sections will therefore focus on mathematical oncology as applied to just three aspects of cancer; growth, metabolism and the interaction with the host immune system.

1.3.1 Simple models of cancer growth

Some of the earliest examples of mathematical modelling being applied to cancer describe the growth of tumours under various constraints [99]. Simple early models such as that by Speer *et al* fit clinical data to models to predict growth patterns [100]. Growth was assumed to obey the commonly invoked Gompertzian law:

$$N(t) = N(0)exp\{\ln(\frac{N_{th}}{N(0)})[1 - exp(-bt)]\} \tag{1.1}$$

where N is the cell count, N_{th} is maximum tumour cell count, and b is a parameter controlling the curve shape. The step-wise behaviour seen in the breast tumour growth data fit the model if spontaneous changes in growth rate were included. A

later model by Norton proposed a correction, in which kinetic heterogeneity is treated as an intrinsic property of neoplasia [101]. This second model provided better fits to individual cancers and gave different predictions for optimal chemotherapy scheduling. Other simple descriptions of tumour growth apply logistic, power law and exponential functions to fit clinical data of tumour proliferation. Each has its success; exponential growth is particularly good at modelling small population growth, tending to a power law relation at large sizes, logistic functions are simple to apply within mathematical frameworks and provide a very good approximation of most clinical data. In general, there is no one accepted growth law amongst the mathematical oncology community, with choice depending largely on context.

Early modelling of avascular tumour spheroids shed light on the size and growth rate limits of such systems. Ward *et al* used a partial differential equation (PDE) model, incorporating nutrient diffusion through the spheroid, where cells took two states; alive or dead. They demonstrated that following initial exponential growth, the system underwent two retardation periods; the first due to nutrient limitations and the second from contraction of necrotic cells [102]. Tindall *et al* built on this model by examining the relative contributions from apoptosis of nutrient-deprived proliferating cells to necrosis from quiescent cells, setting limits on the critical oxygen partial presssure required to maintain cell integrity [103]. Models such as that by Delsanto *et al* operated at multiple scales, bridging the gap between the microscopic tumour spheroid with complex interactions between individual cells, and the macroscopic scale of larger tumour growth [104]. They use a PDE model of the tumour spheroid, taking the hydrostatic pressure at the spheroid wall as an output metric. This is used to model macroscopic implantation and subsequent growth of the spheroids into tissues with varying ECM pressure.

Mathematical models of larger tumours must incorporate some kind of vascular system and often include a description of angiogenesis. An early paper by Anderson *et al* presents two different treatments of tumour induced angiogenesis in a model with both discrete and continuous elements [105]. Nonlinear PDEs are used to describe the response of endothelial cells to diffusable angiogenic factors released by the tumour. At the sprout tips, a discretised version of the model is used to develop a biased random walk which allows anastomosis, mitosis and branching to be explicitly incorporated. Xu *et al* also utilise a PDE approach for their model of tumour growth with angiogenesis [106]. Tumour, capillaries, nutrient and angiogenic growth factor are explicitly modelled, with sprouting of capillaries dependant on both threshold concentrations of nutrients and spatial distance from previous branches. Finally,

Swanson *et al* incorporate angiogenesis into a model of macroscopic glioma growth by treating the vessels as a continuous density which responds to local concentrations of growth factors [107]. A similar approach to vasculature modelling is used by Gallaher *et al* in a comparative study of breast versus lung tumour growth dynamics [108].

Continuous models of tumour growth must either incorporate complicated discrete dynamics at the individual vessel level, or else treat the vasculature as a continuous density, with local nutrient concentrations proportional to this density. Agent based models, which treat each cell as an individual evolving on a grid according to a set of pre-defined deterministic and/or stochastic rules, are a popular way of circumventing the continuum problem and have been used extensively in mathematical oncology [109, 110, 111]. Although generally unable to withstand the rigorous mathematical analysis of dynamical stability that can be applied to differential equation models, agent-based models are flexible and intrinsically spatial, making them a valuable tool for investigating the processes that govern tumour heterogeneity. A simple cellular automata (CA) model by Kansal *et al* demonstrates brain tumour growth on a 3D grid with just four tunable parameters [112]. Their model is able to replicate the growth dynamics of macroscopic tumours from medical data, demonstrating the formation of a spontaneous layer structure from proliferating cells, quiescent cells, then a necrotic core. Monteagudo *et al* take a different approach, using the CA framework to investigate how several hallmarks of cancer affect tumour initiation from a cancer stem cell population [113]. CA models have also been successfully applied to avascular growth of small tumours [114], the growth of small cell lung cancer [115] and pathogenesis in breast cancer [116].

1.3.2 Mathematical modelling of cancer metabolism

Cellular metabolism is a natural candidate for study with a systems biology approach. The cycles and networks which make up metabolic processes operate under a clear set of physiological and biochemical constraints and, whilst often too complex to study intuitively, their structured and deterministic nature is well suited to analysis through computational modelling. The abnormal metabolism that is such a well recognised hallmark of cancer has therefore generated a wealth of mathematical modelling studies focusing on the role of metabolism in tumours [117].

A specific form of PDEs known as 'reaction-diffusion' equations lend themselves very well to modelling the interaction between the tumour and environmental nutrients. The 'reaction' term describes the local production and uptake of a particular metabolite; most commonly, the concentrations of glucose, oxygen and lactate are

modelled. The 'diffusion' term then accounts for the movement of these molecules within the simulation domain, either through free diffusion or, in some cases, in a preferred direction. The same types of equations can simultaneously be used to model the interactions and movements of various cells types. An early model by Venkatasubramanian *et al* extends the simple growth model of the tumour spheroid to explicitly include cellular glycolytic metabolism by modelling the movement and usage of oxygen, glucose and lactate in addition to living and dead cell populations [118]. Cascari *et el* used a similar framework with many more metabolites, including bicarbonate, CO_2 and free protons into the stoichiometrics governing the spheroid metabolism [119].

The glycolytic production of lactate and subsequent acidification of the cellular environment can have profound consequences on tumour growth dynamics [120]. Gatenby and Gawlinski use a reaction-diffusion model to demonstrate that acid production is a key driver of invasive behaviour [121]. Their model predicts a hypocellular gap at the tumour-host interface, caused by the acidic death of the host cells, which they are able to experimentally demonstrate both *in vitro* and *in vivo*. This gap reduces the interstitial pressure at the tumour boundary, aiding fast growth and invasion toward the host tissue. Webb *et al* applied a reaction-diffusion approach to the study of intracellular environmental acidification, predicting a reversed pH gradient in tumour cells [122].

Hybrid models, which treat cells as discrete grid points in an agent-based model, but use reaction-diffusion PDEs to describe the movement and use of nutrients across the domain, have produced some of the most complex yet enlightening simulations of metabolism in tumours. An early model by Alarcon *et al* uses a simple CA model of tumour cells, whose growth dynamics are determined by the local oxygen concentration [123]. Oxygen is provided by a heterogeneous, static vascular network and its concentration at each point in the domain is calculated at each time step by finding the PDE steady-state solution. Their model predicts that normalising the vasculature by increasing its homogeneity would be an effective means of targeting tumour growth. A model of tumour growth and invasion through ECM degradation by Anderson used a similar hybrid system to model individual tumour cells and continuous oxygen [124]. Patel *et al* incorporate a more complete treatment of glycolytic metabolism and environmental acidification into a hybrid model. They demonstrate the importance of lactate production for invasion and predict the existence of an optimal tumour vascularity to achieve this [125]. Later models begin to include phenotype switching or clonal evolution to examine how the nutrient environment drives

metabolic heterogeneity through evolution [126, 127]. One example by Robertson-Tessi *et al* demonstrates very elegantly the non-linear evolution of the tumour cells towards an aggressive glycolytic phenotype [128]. Figure 1.3 shows some of the results from this model, both in real cellular space and in pheonotype space.

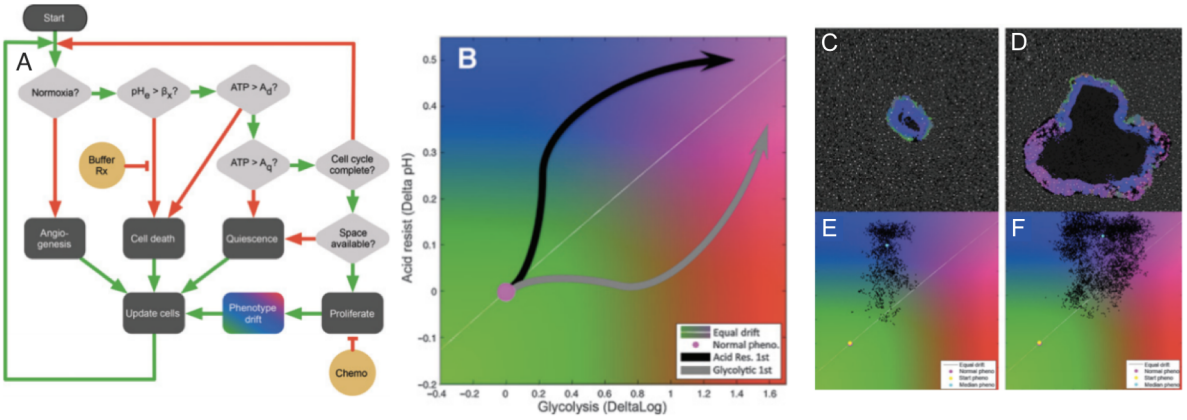

Figure 1.3: Hybrid model of tumour growth and metabolism with phenotypic drift; A. Network showing the decision process for each cell, with green arrows denoting met and red unmet conditions; B. Colourmap of phenotypic drift space with acid resistance (y-axis) and glycolysis (x-axis); C-F. Model results with spatial tumour growth (top) and phenotypic maps (bottom) 285 days after an anti-angiogenic treatment is applied to the left column tumour. Adapted from Robertson-Tessi *et al*, 2017 [128].

Another type of mathematical modelling which has been gathering momentum in cancer research is that of evolutionary game theory. These models may be spatial or non-spatial in design and use a set of axioms to define pay-offs for individuals based on a particular behavioural or evolutionary strategy. Although most commonly applied to study of the genetic or phenotypic evolution of cancer populations, there have been some interesting examples of game theory models with a metabolic focus. Kianercy *et al* developed a non-spatial game-theoretic model of lactate shuttling between hypoxic and normoxic tumour cells, using the overall ATP production as the strategic reward [129]. Their model predicts stable states with both strong and weak coupling, depending on the strategy-switching rate of the hypoxic cells. A similar model by Basanta *et al* examines metabolic coupling between tumour and stroma in prostate cancer within a 2D spatial domain [43].

1.3.3 Mathematical modelling of the tumour-immune interaction

In recent years, the role of the immune system in the prevention, control and treatment of cancer has become a key focus of both experimental biology and clinical research with immunotherapies. However, study of the immune-tumour interaction is not a new topic in mathematical oncology. The 'predator-prey' like dynamic of the immune system in the presence of tumour antigens has historically lent itself well to mathematical analysis; simple ordinary differential equation (ODE) models with few equations are able to determine critical transitions between behaviours such as control or outgrowth [130]. Pillis *et al* present a simple but rigorous three equation system of tumour, antigen and effector cells, which they are able to validate with patient data to predict immunotherapy response [131]. More complex ODE systems with many equations describing the dynamical behaviour of various cells and signalling molecules have provided insight into the complex feedback mechanisms between the many different immune cell types [132]. A PDE model by Matzavinos *et al* explores the conditions required for the immune system to recognise and remove an early malignancy by introducing a lymphocyte population into a model of tumour spheroid growth [133].

Optimal control is a mathematical optimisation method for deriving the laws by which a system may be optimally manipulated within a set of constraints. It has been utilised frequently in recent models of the tumour-immune interaction, generally with the objective of maximising the effectiveness of treatment through controlled timing within the wider tumour-immune system temporal dynamics [134, 135]. Recent developments and successes in immunotherapy have inspired a wealth of mathematical modelling studies seeking to optimise treatment strategies for administering immunotherapies [136, 137, 138] or concurrent chemotherapy and immunotherapy [139, 140] through the application of optimal control theory, generally to an ODE system. These models tend to be impressive in their complexity and in their predictions, however these should be viewed with caution. The highly sensitive control of such systems requires accurate measurement of clinical parameters, which inevitably introduces large sources of error when these theories are clinically implemented.

1.4 Physics and development of hyperpolarised ^{13}C imaging

1.4.1 Historical development

In the early 1950s, Albert Overhauser first described the process by which the nuclei of a solid metal may be polarised in a static magnetic field [141]. The theory stated that by heating or exciting a set of electron spins, a coupled set of nuclear spins could simultaneously be cooled. Despite some controversy over the apparent violation of Boltzmann statistics, Overhauser's theory of dynamic nuclear polarisation (DNP) was demonstrated experimentally in solid lithium later that year [142]. It was soon shown that this behaviour was not unique to metals [143], but that the effect could also be induced in paramagnetic materials and in both liquid and solid states [144, 145]. Research on the subject continued slowly with the first MR sensitive nuclei (^{1}H, ^{2}H and ^{13}C) being polarised in 1974 [146]. A theoretical rethink was required to explain this behaviour and as a result, an extension of Overhauser's theory for non-metals termed the 'solid effect' was developed by Abragam in 1978 [147]. Along with the cross effect and thermal mixing, these four models are thought to account for the levels of DNP observed in a variety of circumstances [148] and have been developed extensively in the literature over time, although theories remain incomplete in some respects today [149, 150].

With hyperpolarisation proving a useful tool for signal magnification in nuclear magnetic resonance (NMR) and due to the many and varied technical challenges of its implementation, DNP research within NMR chemistry and the physical sciences grew steadily following its beginnings in the 1950s. However, it was not until the early 2000s that the full potential of DNP in the biomedical sciences began to reveal itself. Within the NMR community, DNP of ^{13}C-labelled organic molecules become a developed science, with much of the optimisation work for hyperpolarising several organic compounds well documented [151]. It was however, the development of dissolution DNP by Klaes Golman's group in 2003 that allowed hyperpolarised molecules to be brought into the liquid phase at biologically compatible temperatures, leaving the arena of cryogenics for the first time and showing that the nuclei retained their polarisation in solution [152, 153]. In the same year, the first endogenous metabolite, ^{13}C-labelled urea, was hyperpolarised and dissolved for injection into a rat using dissolution DNP [154]. The rat was imaged with ^{13}C magnetic resonance spectroscopy (MRS) providing the first *in vivo* liquid state hyperpolarised imaging experiment. From here, the concept of *in vivo* dynamic metabolic imaging proceeded to grow

through pre-clinical research. DNP has also progressed rapidly both in the academic sciences and the commercial sector, with the first sterile clinical hyperpolariser patented in 2011 and appearing on the market shortly after [155]. Approximately ten years after Golman's first animal studies, the first human study was carried out successfully at UCSF in 2010 to 2011, using a non-sterile prototype hyperpolariser and carrying out the pyruvate polarisation process in clean room conditions [156]. The technical difficulties involved were not inconsiderable and although no further human imaging studies were published until 2017, many sites worked on technical developments during this time to refine the process for clinical use.

1.4.2 Thermal mixing and the solid effect

Spin is an intrinsic quantum property of certain particles and atoms which allows them to interact with magnetic fields. For spin-1/2 particles such as electrons, protons and ^{13}C nuclei, the spin can exist in two eigenstates which become non-degenerate once a magnetic field is applied; i.e. aligned, or anti-aligned with the field. Boltzmann's thermodynamic relation states that for spin-1/2 nuclei in a magnetic field B, the ratio of spins pointing up $n_{\uparrow}$, to those pointing down $n_{\downarrow}$ is given by:

$$n_{\uparrow} = n_{\downarrow} e^{\frac{\gamma \hbar B}{k_B T}} \tag{1.2}$$

Where $\hbar$ and k_B are constants and γ is the gyromagnetic ratio of the nuclei. This means that in a 3 T field at room temperature, 0.001% of ^{1}H nuclei will be polarised and MR visible, whilst the rest will cancel each other out. However, since 62% of the atoms in the human body are ^{1}H, it is still possible to get good signal to noise (SNR) by manipulating this small excess, explaining the feasibility of non-hyperpolarised ^{1}H MRI. Because ^{13}C has a lower gyromagnetic ratio, it has only 0.00026% polarisation at room temperature. Furthermore, the isotope has a natural abundance of just 1.1%, with ^{13}C making up 0.13% of the body's atoms. This means that the ^{1}H signal is about 24000 times higher than that of natural abundance ^{13}C, which is why imaging ^{13}C in the body requires some additional signal-boosting techniques.

With hyperpolarisation, it is possible to align nuclei beyond these natural thermal populations and with current hyperpolarisers, to increase the polarisation by approximately 100,000 fold, from 0.00026% to ∼20-40%. This requires the application of microwave radiation, low temperatures and high magnetic field as well as a source of free electrons from an electron paramagnetic agent (EPA) or free radical. A basic schematic is shown in figure 1.4.

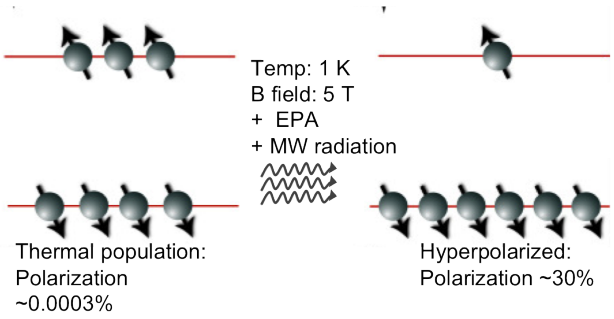

Figure 1.4: Visual representation of ^{13}C spins before and after the hyperpolarisation process. Figure adapted from [157].

In the high magnetic field and low temperature, the electron spins align to become almost 100% polarised. A simple schematic of the possible energy levels and the transitions between them is shown in figure 1.5, where ω_e is the electron paramagnetic resonance (EPR) frequency and ω_n is the nuclear Larmor frequency. Upon the application of saturating microwave radiation detuned from the EPR frequency by $\pm\omega_n$, the corresponding forbidden transition resonant to this offset which requires both a nuclear and electronic spin transition, can be forcefully driven causing a non-thermal population build up in one of the lower energy levels. Over time, a net nuclear polarisation builds up. The consequence of having two possible transitions at $\omega_e \pm \omega_n$ is that polarisation will actually occur at two resonant frequencies; the hyperpolariser should be carefully tuned to only one of these frequencies, allowing polarisation build up in the lower state only. The dominant mechanism at work during DNP of ^{13}C-

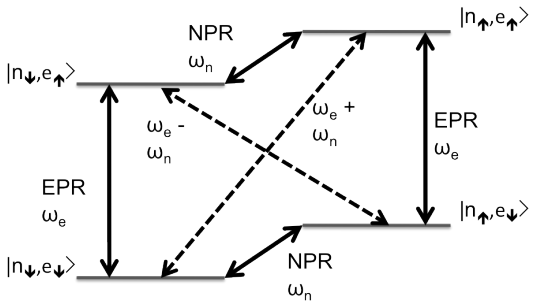

Figure 1.5: Simple energy level diagram for the transitions involved in DNP. Solid lines represent allowed transitions and dashed lines show forbidden transitions. Electron paramagnetic resonance (EPR) frequency = ω_e, nuclear paramagnetic resonance (NPR) frequency = ω_n.

labelled molecules is believed to be thermal mixing, with smaller contributions via the solid effect [158]. Thermal mixing occurs when the EPR line width of the electrons (the frequency range over which transitions between their up and down states can be

induced), is greater than the Larmor frequency of the nuclei ω_n. When this condition is not fulfilled then the solid effect is dominant [159]. Both have been described in full in the literature, with the above description providing a simplified explanation of the solid effect. Unlike the solid effect, thermal mixing is actually a three-spin process which is best described as three spin reservoirs in thermal contact- the nuclear Zeeman (NZ), electron Zeeman (EZ) and electron dipolar (ED) reservoirs [148]. The off-resonance microwave radiation causes a polarisation gradient across the ED reservoir, equivalent to cooling it. Because this system is in thermal contact with the NZ reservoir, this is also cooled via an energy conserving three-spin process and nuclear polarisation is allowed to build up.

1.4.3 Chemical doping agents and glassing agents

The basic requirements for DNP by the mechanism described above are:

- An external static B field of high strength
- Saturating microwave radiation of the correct resonance frequency
- Cryogenic temperatures, allowing for full electron polarisation
- A source of free unpaired electrons
- Polarisable molecules containing one or more nuclei of non-zero spin

The first three can be termed engineering problems and will be dealt with in a following section, but the last two have been considered in depth by NMR chemists for many years. Unlike the metals in which Overhauser first described DNP, the small organic molecules of interest do not have a reservoir of free electrons with which nuclear spins may exchange. This requires them to be chemically doped with a free radical source known as an electron paramagnetic agent (EPA). Metal ions such as chromium(V) and organic radicals, particularly nitroxides and trityls, have all been proven successful for this task [160, 161, 162], however the choice of EPA for a particular system depends on two main criteria [163]. First, the EPA must be chemically stable and completely soluble in the material to be polarised, or its solvent if one is required, since a homogeneous distribution of free electrons within the solution is critical to the process. For the vast majority of biological applications an organic radical is used. Secondly, the electron paramagnetic resonance (EPR) linewidth is required to be greater than the target molecule's nuclear Larmor frequency. In other words, the range of frequencies over which the free electron spins may be excited must

be large enough to incorporate the change in energy when a nuclear spin flip occurs if hyperpolarisation is to proceed via thermal mixing. It is worth noting that the solid effect does not require this condition to hold and as such, polarisation of ^{1}H nuclei is seen in samples by this mechanism.

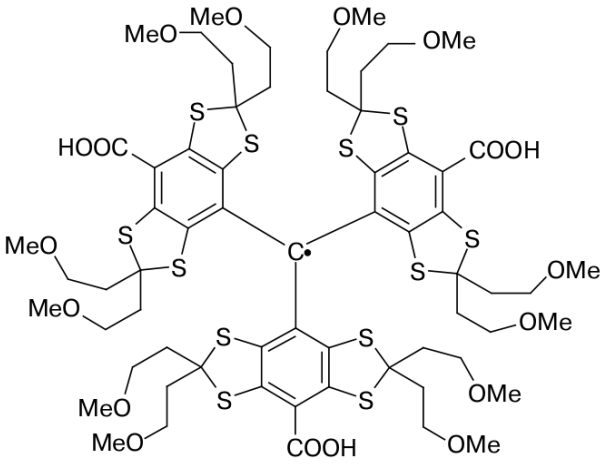

Figure 1.6: Structure of trityl radical OX063 used as standard EPA for hyperpolarisation of [1-^{13}C]pyruvate. Figure adapted from J. H. Ardenkjaer-Larsen *et al*, 2008 [158].

Since the Larmor frequency of many nuclei of interest including ^{2}H, ^{17}O and ^{13}C is very low, for example the ^{13}C frequency is just 35.8 MHz at 3.35 T, there is little constraint on the EPR linewidth. Organic trityl radicals (figure 1.6), which display a range of hydrophobicities are therefore favoured for most applications involving ^{13}C-labelled molecules and have even been proven more efficient than the larger EPR linewidth nitroxides. The trityl OX063 (tris(8-carboxyl-2,2,6,6-tetra(2-(1-methoxy-2,2-d2-ethyl))-benzo[1,2-d:4,5-d]bis(dithiole-4-yl)methyl sodium salt) has a very short linewidth of around 63 MHz at 3.35 T [158], yet it is now used as standard for most preclinical research with [1-^{13}C]pyruvic acid at an optimal doping concentration of 15 mM [164].

Doping the ^{13}C-pyruvate and radical mixture with Gd^{3+} has been shown to affect polarisation build up under a range of conditions, with the potential to provide a significant increase in polarisation [158, 165]; however, the relationship between polarisation and Gd^{3+} concentration is complex. At constant field strength B, a monotonic increase in polarisation, followed by a plateau, then a monotonic decrease in polarisation can be observed as Gd^{3+} concentration is increased [166]. In the thermal mixing

regime, the theoretical maximum polarisation P_{max} is given by:

$$P_{max} = tanh(\frac{\hbar\omega_N\omega_e}{4Dk_BT_L}\frac{1}{\sqrt{\eta(1+f)}}) \tag{1.3}$$

where $\hbar$ is Planck's constant, k_B is Boltzmann's constant, ω_N and ω_e are the nuclear and electron Larmor frequencies, D is the EPR linewidth, T_L is the lattice temperature, η is the ratio of the electronic Zeeman and dipolar spin-lattice relaxation times T_Z/T_D and f is the nuclear polarisation 'leakage' or decay factor. Since ω_N, ω_e and T_L are all fixed by the limitations of the DNP hardware and gadolinium is likely to have little effect on the EPR linewidth D, $(T_Z/T_D)(1+f)$ remains as the factor influenced by Gd^{3+} doping; it should be minimised in order for maximum polarisation to occur. Gd^{3+} has been shown to lower the electronic Zeeman spin-lattice relaxation time T_Z in trityl systems [158]. At low concentrations, this effect is much larger than the simultaneous increase in nuclear polarisation leakage and the overall polarisation in the system increases. However, as the concentration increases, the relative sizes of these two effects gradually switch and beyond a threshold concentration, increasing Gd^{3+} doping will begin to decrease the total polarisation that can be achieved.

For medical applications, the high toxicity associated with heavy metal ions such as Gd^{3+} can be greatly reduced using a gadolinium chelate as is current practice with contrast enhanced MRI, however its use is restricted where possible. The effect of Gd^{3+} doping on polarisation is dependant on numerous chemical and hardware factors. One study has demonstrated that the enhancement visible at 3.35 T was negligible at higher fields; at 4.6 T the additional polarisation gained by Gd^{3+} doping was far outweighed by that caused by increased field strength [164]. Since most current clinical hyperpolarisers have static B fields of 5 T, it seems uncertain as to whether Gd^{3+} doping will be used in clinical practice.

It is essential for the EPA to be distributed evenly throughout the sample for the electron spin and nuclear Zeeman reservoirs to be in good thermal contact. For many molecules liquid at room temperature or dissolved in aqueous solution, crystal domains will begin to form as the temperature is lowered towards those required for DNP. The formation of these domains causes the EPA to separate out, leading to poor thermal contact and poor polarisation. As a result, it is necessary to choose molecules which form amorphous solids, or dissolve those that do not in glassing agents to retain distribution of the EPA [167]. There are some examples of endogenous small molecules which form amorphous solids such as [1-^{13}C]pyruvic acid and 2-keto-[1-^{13}C]isocaproic acid [163]. This is one of the contributing factors to the success of pyruvate as a hyperpolarisable molecule; amorphous solid forming molecules like these

are a minority. Suitable solvents must be found for most molecules of interest, which must not only dissolve the molecule and EPA at high enough concentrations but must also be well tolerated *in vivo*. Solvents currently being used include ethanol, glycerol and dimethyl sulphoxide which is used as a glassing agent for another promising clinical molecule, [1,4-$^{13}C_2$]fumaric acid [168].

1.4.4 Technical considerations and hardware

From simple Boltzmann statistics, the fractional polarisation of spin-1/2 nuclei with a gyromagnetic ratio γ and at temperature T in a magnetic field of strength B is given by:

$$P = tanh\{\frac{\gamma\hbar B}{2k_B T}\} \tag{1.4}$$

This means that for electrons with $\gamma = 2.8 \times 10^4$ MHz/T in a field of 5 T, 99% of the spins will be polarised at a temperature of around 5 K. For ^{13}C nuclei with $\gamma = 10.705$ MHz/T, the required temperature for 99% polarisation drops to 0.0018 K explaining the requirement for indirect methods of polarisation. For full electron polarisation within a sample, temperatures must be maintained at around 1 K which requires a vacuum. The sample must also be in a magnetic field of 3 T or higher, in range of a microwave source and for clinical application, a sterile environment is also required. In 2011, the first automated clinical hyperpolariser was developed to fulfil these requirements [155]. Produced and developed by GE Healthcare, the SPINlab clinical hyperpolariser allows multiple samples to be simultaneously hyperpolarised to ∼40% in a liquid helium-filled environment maintained at 0.8-1 K. The inner helium sample pot in which polarisation occurs is in 5 T magnetic field and a wave guide is used to direct microwave radiation to the sample. A schematic of the cryostat is shown in figure 1.7. Liquid helium is an expensive resource and so to prevent frequent refilling, there is a condenser and charcoal sorb which are used for collecting and re-condensing any liquid helium which boils off.

In addition to the hyperpolariser, a sterile device capable of withstanding the extremely cold conditions within the cryostat is required to contain the sample. The current solution to this problem is the sterile fluid path, which consists of a sample vial capable of holding ∼2 ml of ^{13}C-pyruvic acid (or other agent), which is connected to a syringe containing up to 60 ml of dissolution media via a co-axial tube. This dissolution media is heated and pressurised to 130 °C and when dissolution is required it flows down the inner tube to the vial, dissolves the hyperpolarised pyruvate, then flows back through the outer tube into into an exit tube connected to a syringe. Along

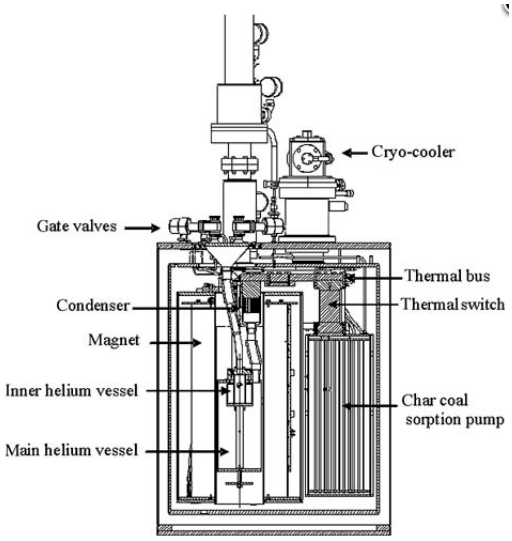

Figure 1.7: Schematic of the clinical hyperpolariser cryostat. Figure taken from J. H. Ardenkjaer-Larsen *et al*, 2011 [155]

this exit tube is a filter to remove the EPA and a collection vessel containing sodium hydroxide and a buffer to neutralise the solution to physiological pH. Attached to this vessel are appendages allowing a quality control module to monitor pH, volume, pyruvate and EPA concentrations, temperature and polarisation to ensure these parameters are all within physiologically safe bounds. The final step of the process is the transfer of the hyperpolarised solution to a sterile Medrad syringe, ready for automated injection into the patient

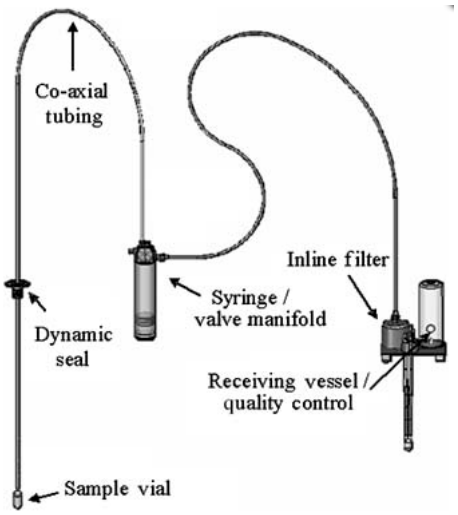

Figure 1.8: Schematic of the sterile fluid path designed for use with the SPINlab clinical hyperpolariser. Figure taken from J. H. Ardenkjaer-Larsen *et al*, 2011 [155]

For imaging and spectroscopy following injection of the hyperpolarised media, a 3 T clinical MR scanner is required. The size of the chemical shift between different metabolites is dependant on, and increases with B_0 magnetic field; a 1.5 T imaging magnet does not provide great enough chemical shift to resolve all metabolites of interest. It should be noted that the majority of studies detailed below use a similar system to that described above, the pre-clinical "Hypersense" polariser, which is a partially automated machine. Most studies in which the Hypersense is used report a [1-^{13}C]pyruvate polarisation of around 20% [169, 170], although the theoretical maximum is certainly higher. These pre-clinical studies are often undertaken using animal imaging magnets which tend to have higher B_0 fields than clinical magnets, ranging from 3-10 T.

1.4.5 ^{13}C-labelled molecules for the clinic

Even after a satisfactory EPA and glassing agent have been found and conditions optimised for sufficiently hyperpolarising a particular molecule, there are still many factors remaining which determine its success as an *in vivo* imaging agent. When hunting for candidate clinical molecules, it is sensible to look first at endogenous molecules and metabolites, as this largely overcomes the issue of toxicology and eases the way through acquiring legal and ethical approval. The fact that a molecule is endogenous however, is not enough to claim that it will be safe when injected in the large quantities required for imaging. Most will need to be injected in supraphysiological concentrations to give the necessary signal-to-noise and may be poorly tolerated or even toxic at this level. The hyperpolarised molecules must be diluted for injection and often large volumes are required to safely introduce the required amount of the hyperpolarised molecule. Solutions to be injected will also need to be adjusted to physiological pH and osmolality; hypotonic solutions are particularly dangerous as the osmotic pressure can cause lysis of blood cells. The addition of neutralising agents, EDTA to chelate impurities and simple salts for osmotic balance can usually overcome these issues.

The next set of criteria depend on the physical properties of the molecule. The T_1 relaxation time must be sufficiently long that dissolution, QC testing, injection and then circulation of the molecule to the tissues of interest can all occur before the polarisation has decayed to a level undetectable by the imaging method being deployed. The polarisation is non-renewable; it is irreversibly lost when sampled for imaging and the T_1 is strongly affected by movement through a magnetic field, such as into the bore of a 3 T MRI scanner, and reduced greatly upon injection by

ferromagnetic haemoglobin in the blood [171]. [1-^{13}C]pyruvate for example, has a T_1 of ∼60 s *ex vivo* which more than halves to 20-30 s *in vivo*. This means that around two half-lives have passed before the hyperpolarised pyruvate even reaches the target tissue. When designing a labelled molecule, there are factors to take into consideration to maximise the T_1 and the position of the ^{13}C label within the molecule is particularly important. Magnetisation is predominantly lost via interaction with nearby ^{1}H nuclei, either within the molecule itself or in surrounding water molecules. A labelled carbon at the end of a chain of carbon atoms will be more open to interactions with external water hydrogens than one protected in the centre of a molecule and will have a correspondingly shorter T_1. Furthermore, the greater number of hydrogen atoms bonded to the labelled carbon, the more likely that polarisation will be lost to them. Loss to surrounding hydrogens can be avoided by deuterating the molecule, or by using deuterated water as the solvent, although this can be expensive and there are some concerns regarding the toxicity of heavy water [172]. Often there is a trade off required in the positioning between maximising T_1 and ensuring the labelled carbon undergoes sufficient change of environment during the reactions of interest that its chemical shift is detectable with the available MR imaging hardware. Any products are also required to have a T_1 long enough to allow detection.

The final key to clinical success is choosing a metabolite which is part of a biologically interesting reaction. The ability to provide useful information about a pathological metabolic alteration which cannot be gained by any other currently technology is crucial if hyperpolarised ^{13}C imaging is to find its place in clinical practice. The molecule of choice should be part of a rapid enzymatic reaction, fast enough for products to be detected before polarisation decay, or a reporter for a relevant cellular function [173]. Furthermore, there must be a detectable and quantifiable change in the metabolic process with pathology. With so many conditions to be satisfied, suitable metabolites for hyperpolarised metabolic imaging are rare. The current best candidate molecules for clinical use are discussed further in section 1.6.3.

1.5 Hyperpolarised ^{13}C MR imaging and spectroscopy

1.5.1 Basic principles of MRS/NMR physics

Any nucleus with a non-zero spin possesses a nuclear magnetic moment. This means that in the presence of a magnetic field, these spins will precess around the z-axis, defined as direction of the static magnetic field, with a frequency known as the Larmor frequency; $\omega_L = \gamma B$ where γ is the gyromagnetic ratio, specific to particular nuclei

and B is the magnetic field strength. This is shown diagrammatically in figure 1.9 Spin-1/2 nuclei such as ^{1}H and ^{13}C can exist in just two eigenstates; aligned or anti-aligned with the direction of the field as discussed in section 1.4.2. This concept is important for understanding the transition states involved in hyperpolarisation, however in descriptions of NMR it is more normal to refer to the vector sum of magnetic moments from many nuclear spins. This vector sum is free to point in any direction as it is rotated by applied fields during NMR experiments. This classical treatment is quite sufficient for a discussion of NMR; the full quantum treatment gives the same result for the large numbers of spins which we will universally be dealing with.

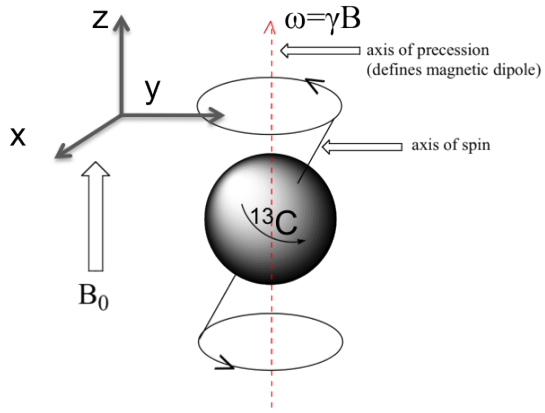

Figure 1.9: Classical depiction of a nuclear magnetic spin rotating in a static magnetic field along the z axis. Rotation, or Larmor frequency ω is given by the product of the field strength B with the gyromagnetic ratio γ.

Exciting the spins with a radio frequency (RF) pulse at the resonant Larmor frequency drives a rotation of the spins away from the z-axis and into the transverse plane. This angle away from the z-axis is known as the flip angle, with a 90° flip angle rotating the spin fully into the transverse plane and 180° causing a complete inversion, often used for refocussing. Following an RF excitation, the spins relax back towards the z-axis with a longitudinal relaxation time T_1. As they relax they continue to precess and in doing so emit a RF signal at the Larmor frequency called the free induction decay (FID), which is picked up by RF receive coils for analysis. This sequence describes the basic FID pulse-and-acquire sequence sometimes used for spectroscopy. Nuclei in different chemical environments will have a slightly different precession frequencies, called their chemical shift, which allows them to be distinguished from one another. Fourier transforming the FID signal, an exponential decay

series in the time domain, produces a series of Lorentzian peaks at each of the different chemical shift frequencies present in the molecular mix being sampled. From the relative size and distribution of the peaks, it is generally possible to discern the concentrations and species of molecules present.

1.5.2 MRI and spatial resolution

It is easy to see how dynamic MRS data can be built up by repeating the above sequence over time, however to image the distribution of metabolites we also require spatial localisation. This is achieved by the application of magnetic gradients along the x, y and z axes. Since the Larmor frequency ω of each spin is dependant on the magnetic field strength B as $\omega_L = \gamma B$, by spatially varying the field it is possible to spatially vary the Larmor frequency of spins within the field. An RF pulse of the desired bandwidth may then be applied which selectively excites only those spins in the location specified by the pulse frequency.

In order to image an axial slice, a field gradient is applied along the z axis. In general, it is desirable to selectively excite a slice of some particular thickness, corresponding to a particular frequency range. Figure 1.10a shows the desired slice shape for exciting spins with a Larmor frequency between $-\Omega$ and Ω and is given by a top hat function in the frequency domain. Fourier transforming this function will produce the necessary input RF signal in the time domain; a sinc pulse as depicted in figure 1.10b and commonly used for slice selection in practice.

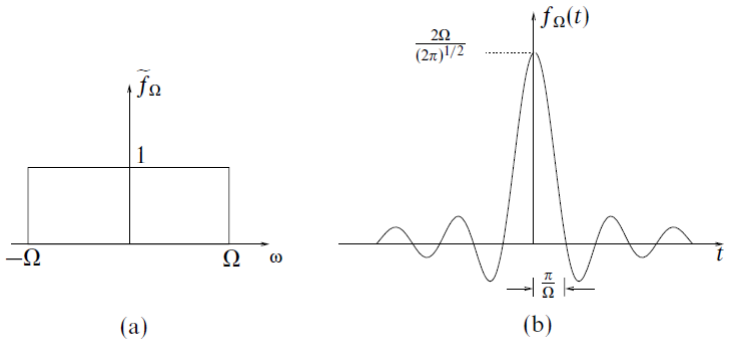

Figure 1.10: Fourier relation ship between desired excitation range and the RF pulse which must be applied. a) Slice to be selected in the frequency domain for spins with a Larmor frequency between $-\Omega$ and Ω, given by a top hat function, and b) Fourier transform into the time domain gives the RF pulse shape to be applied in order to achieve this selection i.e. a sinc pulse.

Spatial encoding in the x-y plane is now required in order to build up a picture

of where each spin is and this is done by further application of x and y gradients to perform frequency and phase encoding. Here, the concept of k-space is generally useful for understanding how the space is sampled. A position in the x-y plane in real space corresponds to a position in k-space via a 2D Fourier transform:

$$\tilde{G}(k_x, k_y) = \frac{1}{2\pi} \int \int G(x, y) e^{-i(k_x x + k_y y)} dx dy \tag{1.5}$$

Where $G(x, y)$ represents the spatial B field gradient as a function of real space and $\tilde{G}(k_x, k_y)$ is its Fourier transform in k-space.

These k-space points are a slightly abstract concept, with each point representing a spatial frequency. The imaging plane can be imagined as a box. We can set up standing waves inside the box along both the x and y directions; standing waves of different wavelengths represent the different spatial frequencies. If we know with what amplitude each standing wave contributes to the overall image, we can build up the picture by overlaying the waves, with areas of constructive and destructive interference providing the contrast for the image. The low spatial frequencies, or long wavelength waves, provide large-scale contrast and big features of the image. As we move to higher spatial frequencies these start to build up the fine contrast and detail. These k-space points are exactly those spatial frequency waves and as we scan across k-space all we do at each point is measure the amplitude with which that spatial frequency contributes. The lowest spatial frequency is at the centre of k-space, with higher frequencies moving outward in each direction. The choice of low and high spatial frequencies to be sampled in a particular scanning sequence determine the levels of contrast and spatial resolution in the final image respectively. Scanning across k-space collecting signal from each spatial frequency, then Fourier transforming that signal, produces the corresponding image in real space. By manipulating the x and y gradients over time, it is possible to move around k-space in a number of ways. Standard MRI images tend to be built up by scanning one line at a time, but 'flyback' trajectories, which cross back and forth across each line of k-space points, and even non-Cartesian trajectories such as spirals and rosettes are available. Figure 1.11 shows the gradient required to produce a spiral k-space trajectory and the relationship between k-space point and applied gradient. The spiral trajectory provides the advantage of sampling the centre of k-space first before moving outwards. This means that the bulk of the contrast information is gathered very quickly, making it an excellent choice for fast imaging, but it misses the fine detail that other trajectories which sample further out into k-space may be able to provide.

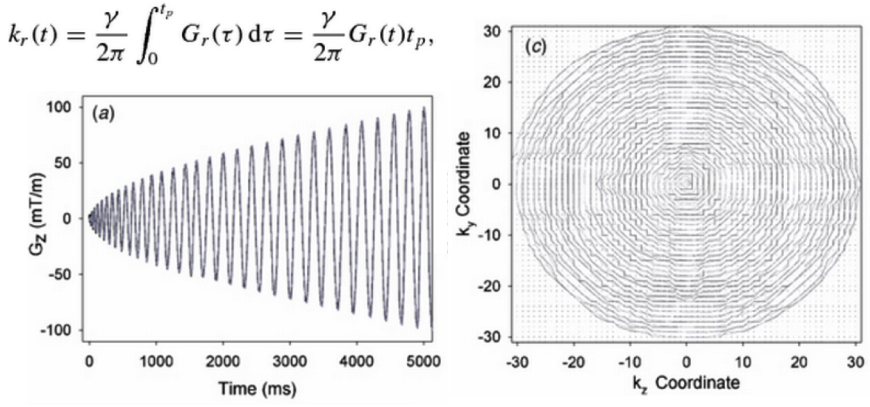

Figure 1.11: Relationship between k-space and applied gradients in polar co-ordinates for a spiral acquisition in the sagital plane. Figure adapted from Han *et al*, 2010 [174].

1.5.3 Non-renewable polarisation

One of the main problems associated with hyperpolarised MR is the irreversible polarisation and therefore signal loss as the nuclei relax exponentially over time back to thermal equilibrium. This can only be overcome by keeping the time from dissolution to imaging minimal, using fast spectroscopy sequences and rapid single-shot imaging techniques. These fast imaging sequences will be discussed in the next section. The RF pulses which are applied to the nuclei during image acquisition also reduce the overall polarisation. For example, after a pulse with a 90° flip angle, there is an equal probability of the nuclear spin relaxing to align or to anti-align with the external B field, thus the spins will cancel each other out and the polarisation will reduce to zero. The effect that the flip angle has on the polarisation can be calculated as follows and is easier to visualise with a quantum treatment. The general state of a nuclear spin in three dimensions can be fully described as:

$$|A(\theta,\phi)\rangle = [\cos(\theta/2)|\uparrow\rangle + e^{-i\phi}\sin(\theta/2)|\downarrow\rangle] \tag{1.6}$$

Here θ is the rotation away from the external B field, the flip angle, and ϕ is the azimuthal angle. The triangular brackets are standard quantum mechanics notation describing the two eigenstates of the spin; aligned and anti-aligned. The probability P' of a spin relaxing to the down state $|\downarrow\rangle$ corresponding to a loss of polarisation, is found by taking the mod-square of its amplitude:

$$P'(\theta) = \sin^2(\theta/2) = \frac{1}{2}[1-\cos(\theta)] \tag{1.7}$$

The actual polarisation loss will be twice this as those spins lost will cancel out the signal from an equal number which recovered, thus the new polarisation fraction P

is given by:

$$P(\theta) = 1 - [1 - \cos(\theta)] = \cos(\theta) \tag{1.8}$$

It is therefore generally advantageous to use small flip-angles for dynamic hyperpolarised imaging in order to retain signal, however a compromise is needed as the receive signal also depends on the flip angle; flip angles of 5° - 15° are generally used. For a sequence with constant flip angle and n repeats, the polarisation over time will then be:

$$P(t) = P(0)e^{-t/T_1} \cos^n(\theta) \tag{1.9}$$

The number of flips n is equivalent to the total time over the repeat time t_R. To simplify calculations during analysis, it can be useful to define an effective T_1 which takes all polarisation losses into account:

$$\frac{1}{T_{1,eff}} = \frac{1}{T_1} - \frac{\ln\cos(\theta)}{t_R} \tag{1.10}$$

Although the non-renewable nature of the polarisation places certain limitations and constraints on hyperpolarised imaging, there are circumstances in which this feature may be exploited. Johansson *et al* describe a method by which they may measure the blood flow; by repeatedly measuring tissue signal, each time intentionally destroying all polarisation, they are able to measure the flow of hyperpolarised tracer to the region in each time increment. If the arterial tracer concentration is simultaneously obtained, a quantitative blood flow estimate may be derived [175]. A further example can be seen in the spectral-spatial imaging method from Schulte *et al*, discussed in more detail in section 1.5.4.2. By repeatedly destroying all lactate polarisation in a region, its build up over each time increment may be measured [176].

1.5.4 Hyperpolarised imaging techniques

Choosing an imaging sequence for hyperpolarised carbon involves a large degree of compromise when it comes to spatial, temporal and spectral resolution. Extra information from one aspect of the acquisition generally comes at the cost of another, leaving the eventual choice of sequence quite subjective; different methods have been favoured by various research groups, and each used successfully. The most commonly used acquisition methods can be roughly divided into two groups; those with a spectroscopic focus and those with an emphasis on spatial imaging.

1.5.4.1 Spectroscopy-based sequences

The main advantage of using any spectroscopy based sequence is the acquisition of full spectra within single or multiple voxels. This allows for the direct detection and quantification of all ^{13}C molecules present within a particular bandwidth and as such, is a popular choice for research focusing on quantitative analysis. This full spectral information does however, come at the cost of spatial and often temporal resolution.

Perhaps the simplest to implement, free induction decay (FID) pulse and acquire sequences have been used in many excellent papers to date [177, 178]. An RF pulse is used to excite the nuclei over the desired frequency range and the resulting FID signal is measured to produce a spectrum of peaks corresponding to the amounts of each ^{13}C metabolite present. This can be repeated every few seconds in order to acquire dynamic spectra which can be used for quantitative analysis. Spatial resolution is generally very poor, although large voxels of around 1 cm can be selected by application of slice selective gradients.

Chemical shift imaging (CSI) allows for greater spatial resolution, yet at the expense of dynamic information. The addition of phase encoding x and y gradients, along with a slice selective z-gradient allows for spatial bounding, producing a grid of voxels containing localised spectra. The slow phase encode gradients mean that dynamic acquisition and imaging of multiple slices is slow and inefficient and often not implemented, but CSI has still been used to good effect by some groups and although poor, temporal resolution may even be sufficient for kinetic analysis [179, 156].

Echo-planar spectroscopic imaging (EPSI) uses a fast flyback k-space trajectory to sample multiple voxels in a faster time frame than CSI and is used often [170, 180]. It still requires phase encoding along one direction and so limited time resolution is available for 2D acquisitions.

1.5.4.2 Fast imaging sequences

Fast imaging sequences are generally unable to produce spectra for each voxel, with the focus on high spatial resolution images for multiple metabolites and time points. Spiral CSI uses a spiral trajectory to efficiently sample k-space from the centre outwards [181]. It has the potential to be single shot, in which the entirety of k-space is sampled over a single readout gradient, although in practice multiple excitations are often needed to overcome gradient limitations in the hardware. Although ^{13}C spectra are available with this method, they are generally not able to capture all metabolites

of interest within the narrow bandwidth used, causing some aliasing of the peaks as a result. Use of these spectra for quantitative analysis is therefore limited.

A more advanced method IDEAL spiral CSI has since been suggested which uses a FID acquisition at the beginning of each scan to provide chemical shift information with which to separate out each metabolite upon reconstruction via a simple discrete Fourier transform [182]. A single-shot spiral then follows each RF excitation, with echo time shifts between each excitation providing spectral encoding. This provides not only a more robust version of spiral CSI, but full spectra are also acquired at the beginning of each time point albeit over the whole image slice.

An interesting method entitled spatio-temporal encoding (SPEN) has been developed which may allow for fast dynamic imaging with spectral and spatial resolution without even requiring Fourier transform during reconstruction [183, 184]. A chirped frequency-swept pulse is played out over an encoding gradient, followed by deconvolution of the encoded information during a acquisition gradient. It is theoretically possible to extract the full spatial and spectral information from the same FID, with 2D and multiple slices. Unfortunately, this sequence is not yet thought to be clinically viable as its implementation is overly complicated for routine use.

Finally, a further approach mentioned in the previous section uses spectral-spatial (SPSP) excitations to selectively excite a single resonance frequency followed by single shot spiral acquisition [176]. The SPSP pulse is simultaneously slice selective and tuned to a particular metabolite. By shifting this frequency, separate metabolites can be consecutively imaged. Further more, because each excitation is metabolite specific, different flip angles can be used on different molecules allowing polarisation to be retained in one metabolite whilst another is interrogated.

It is difficult to directly compare imaging methods in a quantitative way since resolution, particularly spatial resolution, depends strongly on the hardware used. A rough summary is provided in table 1.1.

1.6 Early animal studies

1.6.1 Proof of concept and angiography

Prior to the development of dissolution DNP, there was a lot of interest in the application of hyperpolarised ^{13}C to MR angiography, vascular and perfusion imaging [185, 186]. ^{13}C was an exciting new contrast agent; unlike the current standard Gd^{3+} chelates, it was the agent itself rather than the effect it had on its environment that could be imaged, making for simpler interpretation. Focus was on non-endogenous,

Table 1.1: Direct comparison of popular ^{13}C hyperpolarised imaging and spectroscopy methods

Imaging method	Temporal resolution	Spatial resolution	Full spectra obtained?	Robustness and ease of implementation
FID pulse and acquire	Good	Poor/none	Yes	Very easy to implement and very robust
CSI	Poor	Poor, limited by scan time	Yes	Very easy and very robust, no 3D
EPSI	Poor for 2D, okay for 1D	Poor	Yes	More efficient, still robust and easy to implement
Spiral CSI	Good	Good	None	Prone to artefacts, very sensitive to gradient errors
IDEAL spiral CSI	Good	Good	Some spectra	More robust than spiral CSI, but harder to implement
SPSP	Good	Good	No, but FID can be interleaved	Prone to artefact if frequency drift occurs, but highly customisable and very efficient

soluble molecules chosen for their long T_1 which were polarised often by para-hydrogen induced polarisation as well as DNP. Even when dissolution DNP provided Golman *et al* with the first images using the ^{13}C-labelled endogenous agent [1-^{13}C]urea in 2003 (figure 1.12) the full potential went initially unnoticed, with the researcher suggesting ^{13}C-labelled glucose for follow up work. The concept of metabolic imaging followed shortly with [1-^{13}C]pyruvate taking an early lead.

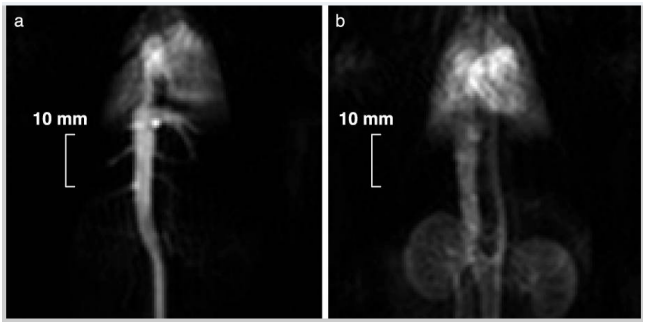

Figure 1.12: First Hyperpolarised [1-^{13}C]urea coronal projection images of a rat acquired a) 0 s and b) 2 s after injection. Figure taken from Golman *et al*, 2003 [154].

1.6.2 [1-^{13}C]pyruvic acid

Chosen for its hugely significant role in enzymatic reactions pertaining to a range of pathological changes, as well as its good physical capacity for polarisation, [1-^{13}C]pyruvic acid has been the subject of numerous important studies and has since

progressed to being the first hyperpolarised molecule to be imaged in humans. [1-^{13}C]pyruvic acid, which is injected as the salt [1-^{13}C]pyruvate after pH neutralisation, is part of three main pathways of interest. These comprise reduction to [1-^{13}C]lactate by the enzyme lactate dehydrogenase (LDH) requiring the cofactor NADH, a reaction prevalent in tumour and ischaemic environments; transamination with glutamate by alanine transaminase (ALT) to [1-^{13}C]alanine and α-ketoglutarate and finally the irreversible carboxylation to [^{13}C]bicarbonate in rapid equilibrium with $^{13}CO_2$. In a paper from 2006, Golman is first to suggest pyruvate for metabolic imaging and goes on to demonstrate the ability to image these reactions in real time *in vivo* using a chemical shift imaging (CSI) technique [187]. Rats were injected with 0.79 mM/kg of hyperpolarised [1-^{13}C]pyruvate and pigs with 0.2 mM/kg. In both cases researchers were able to produce dynamic images and quantitatively determine relative concentrations of the products [1-^{13}C]lactate and [1-^{13}C]alanine in the animals. Imaging of ^{13}C-bicarbonate produced via the carboxylation pathway was achieved in a clinical 3 T MR scanner a year later [188].

1.6.2.1 Pyruvate in tumours

The Warburg effect, believed to be a fundamental process at work in the vast majority of tumours, describes the propensity of tumours to produce energy through aerobic glycolysis, leading to large pools of lactate within and around the tumour site [2]. The conversion of pyruvate to lactate within the glycolytic pathway is reversible, meaning that there is constant exchange between the two even if there is no net flux. By imaging changes in the observed ^{13}C-lactate level after doping *in vitro* cells with different quantities of non-labelled lactate, it has been shown that the exchange of the ^{13}C-label between the injected pyruvate and the large endogenous lactate pool in the tumour is the dominant factor affecting the signal observed by hyperpolarised imaging [169, 189, 190]. These studies demonstrated the potential of ^{13}C imaging for the detection and diagnosis of tumours, offering a level of specificity for detecting cancers only possible due to the the almost ubiquitous Warburg effect. Elevated [1-^{13}C]lactate levels were observed in both primary and metastatic tumours in mice and have been observed in a range of cancers including prostate, lymphoma, renal cancer and glioma [191, 192, 189, 177].

Using a murine model for prostate cancer, the transgenic adenocarcinoma of mouse (TRAMP) model, Albers *et al* showed that elevated lactate could be quantified sufficiently accurately for tumours to be graded [193]. Normal and TRAMP mice with high and low Gleason grade prostate tumours were imaged with a fast spectroscopic

sequence following injection of hyperpolarised pyruvate. The mice were subsequently dissected and histologically analysed to allow grading of the tumours. A correlation coefficient between Gleason grade of the tumour and lactate signal from the imaging of 0.95 was observed, indicating sensitivity enough to allow tumours to be confidently graded without biopsy.

Clinically, the response of a tumour to treatment is currently analysed with standard anatomical imaging techniques such as CT, using the size of the tumour as the main indicator. This requires a long timescale for changes to become visual and can sometimes be misleading, with some tumours initially growing larger even after successful treatment. Hyperpolarised [1-^{13}C]pyruvate has been used to non-invasively detect treatment response within 24 hours [169]. Dynamic MR spectroscopy was used to measure pyruvate and lactate signal after hyperpolarised pyruvate injection in mice with lymphoma and the apparent rate of conversion k_P was calculated. This was carried out before and then 24 hours after treatment with chemotherapy. Figure 1.13 shows an example of the dynamic spectra, and pyruvate and lactate time courses obtained in the experiment. It was found that the rate k_P decreased by $\sim$25% in this time, showing a clear change in tumour metabolism following treatment. A later study on response to radiotherapy in rats with glioma [177] had similarly rapid results. Researchers looked at the ratio of ^{13}C-labelled lactate in the brain to the maximum pyruvate signal in the bloodstream, finding a reduction of 34% just 72 hours after whole brain irradiation with 15 Gy. Other papers have since focused on using hyperpolarised imaging with pyruvate to assess the effectiveness or specificity of a drug [194, 195]; treatment with MEK inhibitor U0126 causing a decrease in pyruvate to lactate conversion in the breast but an apparent increase in the prostate, highlighting the complexity of such a system.

The ability to rapidly detect if a particular drug has had an effect on a tumour is of great clinical interest. Chemotherapy drugs are often detrimental to patient well being and extremely expensive, so knowing quickly whether it will be effective or not could be exceedingly valuable. This application of hyperpolarised imaging has perhaps the most obvious clinical worth of those investigated so far.

1.6.2.2 Cardiac metabolism

Pyruvate has also been successfully applied to the analysis of cardiac metabolism [196, 197]. The main pathway of interest in this case, is the irreversible conversion of [1-^{13}C]pyruvate to acetyl-CoA by the enzyme pyruvate dehydrogenase (PDH), producing ^{13}C-bicarbonate as a detectable by-product in rapid pH-dependant flux with

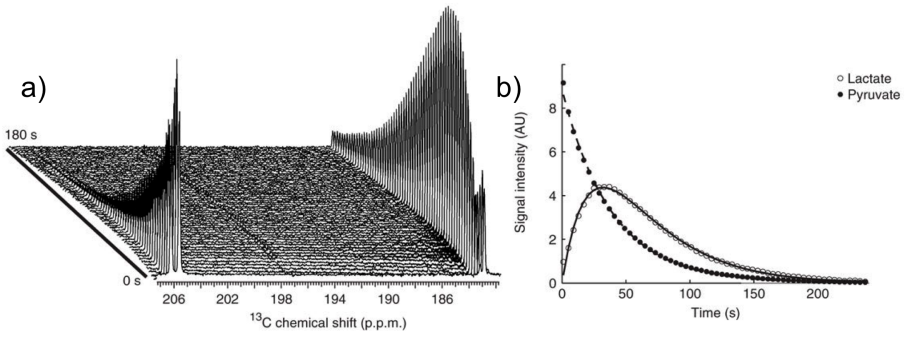

Figure 1.13: Dynamic MR spectroscopy data showing pyruvate and lactate signal over time in a murine lymphoma model: a) full ^{13}C spectra acquired every 4 s over 180 seconds, with [1-^{13}C]lactate (left peak) and [1-^{13}C]pyruvate (right peak) clearly visible; b) corresponding relative pyruvate and lactate signal intensity over time. Figure adapted from Day, 2010 [169].

carbon dioxide. Schroeder *et al* used rats with streptozotocin-induced type 1 diabetes to look at the role of cardiac PDH activity in diabetes and heart failure [178]. Around 30% of energy in the heart is produced through glycolysis of pyruvate by PDH. PDH exists in both activated and inactivated states in the heart, the ratio of which are strongly determined by environmental factors. The increased activity of PDH in the heart has been linked to high blood insulin levels; researchers used hyperpolarised [1-^{13}C]pyruvate to image and compare the amount of break-down product ^{13}C-bicarbonate, an indicator of PDH activity, in the hearts of 1 day fasted and normally fed rats. The depleted ^{13}C-bicarbonate in the fasted rat heart by 74% supported the connection of PDH to insulin level and demonstrated the sensitivity of the technique. When tested in the diabetic rat model, bicarbonate was also lowered compared to the control rats by 65%, and a negative correlation between its production and the blood glucose level of the rat was found.

Reduced ^{13}C-bicarbonate was also observed in the myocardium of pigs following an induced ischaemic episode [179]. A balloon catheter was introduced into the left circumflex artery of the pig and inflated for 0, 15 or 45 min to model different levels of ischaemia, then re-perfused before imaging with ^{13}C-pyruvate. Before and after images of the pig hearts clearly show damage to the myocardium with some areas producing little or no bicarbonate after the ischaemia. Not only does this study demonstrate the feasibility of ^{13}C-pyruvate imaging for detecting damage to the heart on a metabolic level following trauma, but it overcomes the signal to noise difficulties with imaging a large animal, an encouraging step towards use in humans.

1.6.2.3 Other applications

In a study similar to that above by Schroeder *et al* [178], the same diabetic rat model was used to look at metabolic changes in the kidney associated with the disease [198]. The kidneys of the diabetic and normal control rats were imaged using hyperpolarised MRS and blood oxygen-level dependant (BOLD) sequences. It was found that unlike the cardiac study, the bicarbonate/pyruvate ratio was found to be unchanged, whereas the lactate/pyruvate ratio increased by 149% in the diabetic rats. This, along with decreased oxygen levels detected by the BOLD imaging, indicates a pseudohypoxic condition in the diabetic kidney. Laustsen *et al* suggest that these ratios, along with the bicarbonate/lactate ratio could be used as quantitative metrics for monitoring disease by imaging metabolic changes in diabetic patents.

It has been proposed that inflammation may also cause similar metabolic changes to those seen in ischaemia [199]. Hyperpolarised ^{13}C-pyruvate was injected into isolated perfused rat lungs in which a state of acute inflammation had been induced by administration of bleomycin. Lungs were removed and imaged at 7 or 21 days and the level of lactate was observed to increase by 330% in the acute inflammation condition on day 7 compared to healthy controls. The researchers attribute this effect to elevated glycolysis in the inflamed tissue and suggest further investigation with hyperpolarised imaging for inflammatory diseases.

In addition to the tumour environment, the metabolism of pyruvate to lactate is altered in ischaemic conditions. Low oxygen levels cause normal body metabolism to proceed anaerobically leading to the production of lactate; a reaction which can be probed with hyperpolarised pyruvate through exchange with the lactate pool. Pullinger *et al* examined the effects of ischaemia on the isolated perfused rat lung [200]. Each lung was imaged twice, with the order of the normoxic and hypoxic imaging sessions reversed for half of the samples to eliminate time degradation as a cause of lactate build up. Their theory was validated, with higher lactate signal observed for the ischaemic condition in both groups.

1.6.3 Fumarate and other molecules

Another endogenous molecule which has shown excellent potential for clinical translation is [1,4-$^{13}C_2$]fumarate. It has been suggested that the production of [1,4-$^{13}C_2$]malate from [1,4-$^{13}C_2$]fumarate may be a sensitive marker for tumour necrosis. In a paper by Gallagher *et al*, a murine lymphoma model was used to image the conversion of fumarate to malate *in vivo* [168]. The tumour region was imaged before and

then 24 hours after the administration of etoposide, which induced a significant level of tumour necrosis. It was found that the production of ^{13}C-labelled malate increased 2.4 fold following drug administration; possibly due to leaking of the conversion enzyme fumarase into the extracellular space after induced apoptosis or cell death. In addition to the pyruvate-lactate exchange reaction, the production of malate from fumarate may also be an indicator of tumour response to treatment. The potential use of [1,4-$^{13}C_2$]fumarate in acute kidney injury has been investigated by Clatworthy *et al* [201]. Acute kidney injury is difficult to discern from glomerulonephritis using current imaging methods or biomarkers, however only the former is caused by tubular necrosis. Mouse models of each disease were injected with hyperpolarised [1,4-$^{13}C_2$]fumarate before undergoing MRS. A significant increase in [1,4-$^{13}C_2$]malate production was seen in the acute kidney injury mouse model, but not in the glomerulonephritis or normal mice, suggesting that this may be a tool for differential diagnosis of the disease in patients. It is likely that ^{13}C-fumarate will be an early, if not the second molecule to be imaged in humans and is currently undergoing review at the University of Cambridge for its use in patient studies.

Although it is known that pH is altered in many disease states such as cancer, ischaemia and inflammation, there is currently no good way to measure pH levels across body tissues [202]. Bicarbonate is in fast equilibrium with CO_2, with the relative levels of each strongly pH dependant. It has been shown that by injecting hyperpolarised ^{13}C-bicarbonate into a murine lymphoma model and analysing the conversion to CO_2, it is possible to image the spatial distribution of reduced pH at the tumour site [165].

Other molecules which have been successfully hyperpolarised and investigated as *in vivo* metabolic probes include [5-^{13}C]glutamine [203], [1-^{13}C]glutamate [204], [1-^{13}C]acetate [205], [1-^{13}C]α-ketoglutarate [206], ^{13}C-glucose [207] and ^{13}C-succinate [208]; a brief summary of each of these is provided in table 1.2.

1.7 Early human studies with hyperpolarised ^{13}C

1.7.1 Neurological potential

The lactate/pyruvate ratio in the brain is already used as a clinical indicator of damage in traumatic brain injury and there have been numerous studies using ^{13}C-labelled molecules to probe neurochemistry and metabolism. Most of the research efforts to image ^{13}C-pyruvate metabolism in the brain have so far focused on its role in glioblastoma, however there are many neurological disorders which would be expected to

Table 1.2: Possible candidate metabolites clinical translation with ^{13}C hyperpolarised imaging

Metabolite	Product(s)	*In vivo* T_1	Clinical relevance
[1−^{13}C]pyruvate	[1−^{13}C]lactate [1−^{13}C]alanine ^{13}C-bicarbonate	29 s	Indicator of tumour metabolism (Warburg effect) [191, 192, 177], areas of ischaemia or inflammation [200, 199], metabolic changes due to diabetes [198]
[1,4-$^{13}C_2$]-fumarate	[1,4-$^{13}C_2$]malate	24 s	Increased malate production as a marker for necrosis [168, 201]
^{13}C-bicarbonate	$^{13}CO_2$	10 s	Measurement of pH [165, 202]
[1−^{13}C]acetate	[1-^{13}C]- acetylcarnitine	15 s	AcetylCoA synthetase activity in cancer [205]
[5−^{13}C]glutamine	[5-^{13}C]glutamate	20 s	Indicator of tumour metabolism [203]
^{13}C-succinate	^{13}C-glutamate ^{13}C-glutamine	6 s	Early detection of brain tumour [208]

demonstrate metabolic changes. Ischaemia and inflammation are both obvious candidates for imaging with hyperpolarised pyruvate. Although imaging has been shown feasible in a rat glioma model [209, 177], the abnormal vasculature and compromised blood-brain barrier still left questions unanswered regarding use in the non-cancerous brain. A proof of concept study in 2014 looked at the feasibility of imaging the healthy primate brain prior to testing possible experimental set-ups for human studies [210]. Pyruvate was able to cross the blood brain barrier in cynomolgus healthy monkeys and its conversion to lactate inside the brain was successfully imaged, opening up the possibility of using [1-^{13}C]pyruvate for studying neurometabolism further. A study to image multiple sclerosis in patients is now under way at Addenbrooke's hospital Cambridge, where it is believed that the plaques visible during active disease will show increased conversion to lactate, due to the inflammatory response that causes the lesions. Human imaging in stroke patients is also planned, where the neuroprotective production of lactate may indicate salvageable tissue in the ischaemic penumbra.

1.7.2 Advancement to the clinic: first human studies

In 2013, Nelson *et el* performed the first hyperpolarised ^{13}C metabolic imaging study in patients with prostate cancer [156]. The study used hyperpolarised dissolution DNP of [1-^{13}C]pyruvate in a pre-clinical Hypersense polariser and hyperpolarisation carried out in clean room conditions, to assess the safety and feasibility of the technique. No dose limiting toxicity or adverse effects were seen in the initial tests and

a weight-dependant dose of 0.43 mL/kg of pyruvate was chosen for the experiment. A small number of the 31 patients were chosen to undergo 1D or 2D spatially localised dynamic hyperpolarised MRS. Spatial locations were chosen which included both a region of known tumour and of healthy tissue for each patient so that comparisons could be drawn, and the rate k_P of pyruvate to lactate flux was calculated in each case by fitting of the dynamic data to a simple one-way kinetic model; this parameter was shown to be lower in the healthy tissue. The majority of patient data acquired consisted of single time-point MRS over a 9 voxel array. By analysing the [1-^{13}C]pyruvate/[1-^{13}C]lactate ratios in each voxel, researchers were able to detect bilateral cancers, later confirmed by biopsy, that were not detectable with the conventional anatomical images that were also acquired. Their work provides an early indication that the sensitivity of hyperpolarised imaging may be sufficient to allow for very early tumour detection.

The difficulty of the clean-room approach taken by the UCSF team was one of a number or reasons why publications on human imaging were halted for the next four years. Although a number of conference abstracts were presented in the field, some containing early human data [211, 212, 213] it was not until 2017 that the second human study of ^{13}C-pyruvate in the healthy human heart was published. Cunningham *et al* imaged the metabolism of [1-^{13}C]pyruvate to [1-^{13}C]lactate and ^{13}C-bicarbonate in the healthy human heart in four volunteers at Sunnybrook Hospital Toronto [214]. Bicarbonate production was clearly observed in the myocardium whilst lactate signal was more diffusely seen in the blood, muscle and tissues. The same dose as the previous study of 0.1 mmol/kg was given with no adverse effects; a result echoed in early unpublished human studies at other sites.

A very recent third publication from UCSF images one prostate cancer patient before and six weeks after treatment with androgen deprivation therapy [215]. A marked change in the k_P value as derived from a single large tumour-containing voxel is noted, with a pretreatment k_P of 0.025 s^{-1}, dropping to 0.007 s^{-1} following treatment. Although this is a single patient study and the time window of six weeks is far longer than might be hoped for detecting treatment response with hyperpolarised imaging, it nevertheless marks an important first demonstration of potential for the technique.

1.8 Quantitative analysis of dynamic ^{13}C spectra

1.8.1 Enzyme kinetics and the Michaelis-Menten approach

The temporal resolution of many hyperpolarised imaging and spectroscopy techniques is sufficient that dynamic data may be produced, describing the relative concentrations of metabolites over time. This allows for a range of potential quantitative analysis to be applied and for values of rate constants governing the dynamics to be derived. By far the most widely investigated reaction is the reversible conversion of pyruvate to lactate by the LDH enzyme, requiring one molecule of NADH for each pyruvate molecule metabolised. The enzyme kinetics of the reaction have been well probed with ^{1}H NMR *in vivo* [216] and later also with hyperpolarised ^{13}C NMR [217]. The reaction can be summarised as follows:

$$[\mathrm{P}] + [\mathrm{NADH}] + [\mathrm{LDH}] \underset{\mathrm{k_{21}}}{\overset{\mathrm{k_{12}}}{\rightleftharpoons}} \underset{\text{Enzyme complex}}{[\mathrm{P}][\mathrm{LDH}]} \underset{k_{32}}{\overset{k_{23}}{\rightleftharpoons}} [\mathrm{L}] + [\mathrm{NAD^+}] + [\mathrm{LDH}] \tag{1.11}$$

where letters in square brackets represent concentrations of metabolites and LDH enzyme, and k_{ij} are reaction rates for each step. One simplifying assumption which may be made is that the backwards reaction rate $k_{32} = 0$. In this case, the reaction model simplifies to one-way conversion and obeys Michaelis-Menten dynamics if the following assumptions are made. First, the formation of the pyruvate/LDH complex is in fast exchange, or $k_{12} \approx k_{21} \gg k_{23}$, and is also in steady state. Second, it must be assumed that the pyruvate concentration is much greater than the LDH concentration and can therefore be considered constant. The rate of lactate production k_P is then given by:

$$k_P = \frac{[LDH]_T k_{32}[P]}{[P] + ([k_{23} + k_{21}]/k_{12})} = \frac{V_{max}[P]}{[P] + K_M} \tag{1.12}$$

where V_{max} is the maximum speed at which the reaction can occur and K_M is the Michaelis-Menten constant, representing the concentration of pyruvate at which the reaction rate is half of its maximum. It is often desirable to reduce the complexity of a reaction down to these simple parameters, which describe clear and measurable quantities; many enzymatic reactions are very successfully described by this equation. However, the numerous assumptions made do not necessarily apply to every exchange reaction meaning such simplifications are not always possible or appropriate.

1.8.2 The modified Bloch equations

When dealing with hyperpolarised metabolites, it is not the concentrations that we are able to measure but rather that fraction of each species which is polarised and

thus visible. We are also unable to directly measure LDH in any way, so it is sensible to simplify the equation 1.11 to:

$$\mathrm{P} \underset{\mathrm{k_L}}{\overset{\mathrm{k_P}}{\rightleftharpoons}} \mathrm{L} \tag{1.13}$$

The polarisation is being lost over time at a rate defined by the $T_{1,eff}$ as described in section 1.5.3. It is then possible to define two coupled differential equations, known as the modified Bloch equations [218], to describe how the visible magnetisation of these metabolites changes in time:

$$\frac{dP}{dt} = k_L L - k_P P - \rho_P P \tag{1.14}$$

$$\frac{dL}{dt} = k_P P - k_L L - \rho_L L \tag{1.15}$$

The ρ_i are equivalent to the inverse of the $T_{1,eff}$ for each species. This set of equations can be easily extended to include other metabolites, or to account for intra- and extracellular compartmentalisation, and provide a starting point from which the majority of hyperpolarised ^{13}C kinetic modelling approaches are derived. Both equations have bi-exponential solutions, which tend to zero when t becomes large. These solutions can then be fit to experimental data, generally by using a least-squares fitting method to find values for each of the four parameters k_P, k_L, ρ_P and ρ_L. Generally of greatest interest is the pyruvate to lactate conversion rate constant k_P; the tighter the constraints placed on the other three variables, the more accurately the rate constant can be determined.

By setting the backwards rate k_L to zero, an approximation of the modified Bloch equations can be made which allows analysis of hyperpolarised data via a Michaelis-Menten model as described above. This simple and popular model has been applied with some success by multiple groups [219, 220, 221, 222]. However, researchers have at times underestimated the complexities involved, with both Harris and Whitney concluding that the transport of pyruvate into the cell was in fact flux-limiting, contrary to implicit assumptions with the one-way model that this step is instantaneous. Another example of the pitfalls of this approach is highlighted in a paper by Zierhut *et al* [170], in which dynamic data from healthy rats and TRAMP mice (prostate cancer model) is fit to a Michaelis-Menten type model with apparently good results. However, when the T_1 of pyruvate is estimated by the fit, the variance is enormous, with data from two mice giving a three-fold difference. Since the T_1 is a largely physical property of the molecule and the data were obtained in the same magnetic field and roughly the same biological environment, these erratic values would indicate that

their model is under constrained, most likely due to the use of separate equations pre- and post-peak, which would explain the visually good fits. Additionally, the steady state approximation necessary for Michaelis-Menten statistics is unjustified, as the reaction is nowhere close to equilibrium. A paper reviewing this model found it to provide the worst fits to data out of several models tested [223].

1.8.3 Two and three compartment models

There has been some debate over whether it is necessary to include contributions from intracellular and extracellular lactate separately, giving rise to both two and three-compartment models; the two-compartment model is described by equations 1.14 and 1.15 and has been used successfully in numerous papers without requiring the assumptions detailed above [169, 222]. It was shown in a ^{13}C diffusion study by Schilling *et al* [224], that although it was a reasonable assumption to treat all pyruvate as extracellular, transport of lactate into and out of the cell produces separate intracellular and extracellular pools which undergo exchange. With subscripts i and e denoting intracellular and extracellular respectively, the three-compartment model can be described by the rate equation:

$$\mathrm{P} \underset{\mathrm{k_{Li}}}{\overset{\mathrm{k_{Pi}}}{\rightleftharpoons}} \mathrm{L_i} \underset{\mathrm{k_{ei}}}{\overset{\mathrm{k_{ie}}}{\rightleftharpoons}} \mathrm{L_e} \tag{1.16}$$

Which gives the following set of differential equations:

$$\frac{dP}{dt} = k_{Li}L_i - k_{Pi}P - \rho_P P \tag{1.17}$$

$$\frac{dL_i}{dt} = k_{Pi}P - k_{Li}L_i + k_{ei}L_e - k_{ie}L_i - \rho_i L_i \tag{1.18}$$

$$\frac{dL_e}{dt} = k_{ie}L_i - k_{ei}L_e - \rho_e L_e \tag{1.19}$$

Pyruvate may only be converted to intracellular lactate; it must first be transported into the cell where NADH and LDH are available before the reaction can commence. The intracellular pyruvate pool may be neglected due to the rapid speed at which pyruvate is converted upon entering the cell. In a comprehensive review of six different two and three compartment kinetic models [223], dynamic hyperpolarised data were obtained from isolated glioblastoma cells as well as mass spectrometry (MS) data from pyruvate exposed to cells taken at 0, 3 and 10 min. Pyruvate, intracellular and extracellular lactate were measured and used for comparison. Both data sets were fit simultaneously to the six models. Surprisingly, they found that all six models were

able to provide good fits to the hyperpolarised data, with or without the MS data. When the hyperpolarised and MS data were used together to calculate the kinetics, it was only the bi-directional three compartment and bi-directional two compartment models which were able to produce a good fit. When the hyperpolarised data were fit to each model without the MS data, only the two-compartment bi-directional model produced a fit compatible with the MS data. It is interesting that all of the models with a uni-directional component were unable to describe both data sets simultaneously; the implication here is that the fully bi-directional models fit the data due to a more accurate description of the reaction, rather than simply by having more fitting parameters.

1.8.4 Arterial input function

None of the above models account for the influx of pyruvate to the imaging site which occurs clinically; each one assumes that the pyruvate is injected instantaneously. Although this may be a reasonable approximation for *in vitro* data, in animals and particularly in patients, a large volume of fluid must be injected over a finite time. The pyruvate will then wash through the imaging site as a bolus after a few seconds, with a flow profile known as an arterial input function (AIF). Mathematically, this results in an extra term in equation 1.14 for the rate of change of incoming pyruvate, with the simplest possible description being the addition of a constant representing constant inflow. For a more accurate description of the flow profile, a Gaussian or gamma-variate function can be better used to model the pyruvate bolus moving through the site. The gamma-variate is commonly used approximation of the AIF, which describes a fast initial flux starting from zero with a slow tail off. One paper uses a directly measured AIF from a catheter placed in the femoral artery of rats, along with simultaneous pyruvate injection and dynamic hyperpolarised data acquisition [225]. They then compare fits to the hyperpolarised data with a two-site model incorporating the measured AIF, various box-car function AIFs (constant inflow for a defined period) or using a simple precursor-product model. All of the box-car functions gave poor fits. Additionally they find that unless the effects of blood flow and substrate delivery are of direct importance, it is better to make no assumptions about the shape of the AIF by using the precursor-product model. Although the measured AIF gave an excellent fit to the data, and by fitting it to a gamma-variate function parameters could be ascribed biological relevance, it would be very impractical to use this method for AIF measurement on a patient since arterial catheterisation carries potential risk. Non-invasive measurements of the AIF, or of parameters which

could be used to build up a representative gamma-variate input, could yet be of use to provide better models for more complicated reactions involving three or more metabolites, or for situations when blood flow is of great importance to the results.

1.8.5 Model-free approaches

There has been much debate between groups over which kinetic model best describes dynamic hyperpolarised data with no clear outcome. The two-site one-way model is certainly the most popular, yet in comparison papers has been shown multiple times to provide the worst fits [223, 225, 226, 227]. The three-site models would appear to give a better scientific description, yet these too have been found lacking. Arterial input functions are difficult to measure and modelling cerebral metabolism brings further problems with regards to metabolites crossing the blood brain barrier [209, 228] and the possibility of new models being required in order to account for this slow transit. In the light of all this it would be highly desirable, particularly in a clinical setting, to find some simple quantitative parameter capable of characterising the observed reaction without the need for complicated models. There have been several suggestions as to what this parameter could be.

In a paper by Hill *et el*, they suggest calculating the area under curve (AUC) for each of lactate and pyruvate, then taking the ratio of these to provide a simple quantitative parameter [226]. They demonstrate mathematically that, providing that the input function only depends on pyruvate, this AUC ratio is completely independent of what exact function is used. They go on to prove that this ratio is also directly proportional to the rate k_P, and is equal to:

$$\frac{L_{AUC}}{P_{AUC}} = \frac{k_P}{\rho_l + k_L} \tag{1.20}$$

When compared to fits from both two and three compartment models, the AUC ratio was found to correlate well with the k_P values, providing a slightly better correlation with those obtained from the two compartment model. This is an indication that the AUC ratio may provide a simple and robust alternative to the derivation of rate constants.

A different approach called $FmR\alpha$ analysis was developed by Pagès and Kuchel [229]. This involves the determination of two geometric values from the data which they call α and β. They begin with two assumptions; that the T_1 is equal for pyruvate and lactate and that the reaction is one-way, i.e $k_L = 0$. From here, they define β to be the ratio of the two curves at the maximum of the lactate signal, i.e. at $t = t_{max}$

and show this to be $\beta = L(t_{max})/P(t_{max}) = k_P T_1$. The next step is to determine two points in the rise and fall of the lactate signal such that the width between them is equal to T_1; this is the fall-minus-rise time at height α, or $FmR\alpha$, where $L(t_1) = L(t_1 + T_1)$. α is defined as $L(t_1)/L(t_{max})$. Since α varies slowly with β, it can be approximated as 0.8. $\beta/FmR\alpha$ is then equal to the rate constant k_P. The method was tested against previously published *in vivo* data fitted to the same unidirectional model. Correlation was reasonable but not good, possibly due to limitations in the one-way model both sets of values were derived from.

Other researchers, particularly when the emphasis has been on collecting spectroscopic data, have used the ratio of lactate-to-pyruvate peak heights as determined from the spectra [177, 156]. This is a good parameter to utilise in the absence of dynamic data and has been shown to correlate well with the Gleason grade of tumours [193].

There are numerous other model-free approaches to hyperpolarised data analysis which could prove clinically valuable for quick assessment of patient data. Whether they will be able to provide biologically meaningful values, or just an arbitrary but still clinically useful measure, is yet to be fully discussed. Also to be established is the robustness of each approach and the correlation both to measured biological parameters and to each other. It is highly desirable that a clinical standard of quantitative analysis presents itself so that patient data from different groups and sites can be compared; it is clear that further investigation and comparison of the various potential approaches is required.

1.9 Molecular imaging with ^{18}F-FDG PET

The most similar imaging modality to hyperpolarised MRI with ^{13}C-pyruvate is ^{18}F-Fluoro-deoxyglucose positron emission tomography (^{18}F-FDG PET). The two techniques may be thought of as complementary, providing similar yet distinct metabolic data (see [230] for a full comparison). As PET/MR becomes a more widely available technology, the potential for simultaneous hyperpolarised ^{13}C/^{18}F-FDG PET is becoming apparent and clinical feasibility studies are already being performed; for example, Gutte *et al* successfully imaged 10 canine cancer patients using a clinical "hyperPET" set-up [231]. ^{18}F-FDG PET is a metabolic imaging technique which uses uptake of a radioactive glucose-based tracer as a marker of abnormal metabolism. Tumours and areas of inflammation are particularly glucose avid, showing up as areas of bright contrast on the images. After the tracer is taken up into the cells by glucose

transporters it is phosphorylated by the enzyme hexokinase, however the labelling prevents the tracer from progressing any further through glycolysis, or being transported out of the cell. Instead, it remains in the cytoplasm and emits positrons (β^+ radiation) which may meet an endogenous nearby electron and annihilate to produce two 511 KeV photons. A cylinder of photo-detectors surrounding the scanner detects simultaneous incidences as coming from the same annihilation event. By using a technique called time-of-flight correction to account for the different journey times of photons released simultaneously but detected in different locations, it is possible to calculate their spatial origin and to generate a 3D map of glucose uptake through out the whole body.

PET is intrinsically semi-quantitative in nature, as the image contrast is directly based on the number of photons detected to have originated in each voxel. In standard clinical practice, PET contrast is quantified by a parameter called the standardised uptake value (SUV), which is defined for each voxel as the ratio of the observed activity to the injected activity. These quantities are measured in MBq/ml or MBq/g and are corrected for the radioactive decay of the tracer between injection and imaging and the weight of the patient, such that the SUV can be read as the unitless deviation of any particular voxel from the averaged expected uptake, assuming uniform tracer uptake across the body. The SUV_{max} and SUV_{mean} define the highest voxel within and average over voxels within a region of interest respectively, and are the quantities most commonly utilised clinically in the analysis of PET images. In most cases a single static 3D image is acquired, however it is also possible to acquire multiple images over time. Although the SNR is reduced with this approach, capturing the glucose uptake timecurve at each voxel allows for the derivation of quantitative parameters by fitting kinetic models to the 4D data [232].

PET imaging is generally combined with CT, or more recently MRI, taken on the same machine in order to anatomically reference the images, particularly as the resolution of PET itself is poor (5×5 mm) and images suffer from being very noisy. There are several factors in the physics of PET which combine to produce this: the emitted positron will travel a few millimetres from the source before annihilating; the photons are not produced perfectly orthogonally and are subjected to further scattering effects before reaching the detectors and the individual photodetectors have a finite size within which they are not able to further spatially locate the point of photon impact. The patient may also move during the scan, either voluntarily or involuntarily, and normal uptake in the body organs, particularly in the brain, gut and urinary system, often obscure nearby regions of pathological uptake. Although a

wealth of approaches exist to reduce the effect of these sources of noise and error, any attempt to derive quantitative results from PET images must bear these limitations in mind.

1.9.0.1 ^{18}F-FDG PET in oncology

^{18}F-FDG PET is an established clinical tool for the diagnosis, grading and treatment response monitoring of many cancers [233]. The increased uptake observed to occur in tumours of the glucose-analogue tracer ^{18}F-FDG, is due to a combination of increased rate of cellular glucose metabolism and an increased number of glucose transporter proteins on the cell surface (primarily GLUT1 and GLUT4). The almost ubiquitous occurrence of these factors in tumour cells make ^{18}F-FDG PET feasible in most cancers, however additional factors such as tumour size, anatomical location and the availability of competing, cheaper means of detection mean that PET is only used routinely for certain applications. Nevertheless, it still provides a highly sensitive and specific tool for imaging a range of cancers.

^{18}F-FDG PET has been successfully applied for diagnosis and staging in a wide range of diseases. It has been shown to provide a significant benefit over CT alone for distinguishing between benign and malignant pancreatic lesions [234] and offers sufficiently sensitive detection of bone metastasis in Hodgkin's lymphoma to negate the use of an invasive bone marrow trephine biopsy [235]. Use of PET imaging for the staging of lymphoma has been shown to be superior to other standard methodologies including physical examination, radiography and laboratory testing [236]. It has also demonstrated significant benefit over other means of cancer detection and staging for non-small cell lung cancer [237], recurrent colorectal cancer [238] and head and neck cancer [239].

^{18}F-FDG PET offers a significant benefit for the imaging of gynaecological cancers such as cervical and ovarian [240]. In recurrent metastatic ovarian cancer, PET imaging has been shown to significantly aid the detection of lesions not visible on anatomical CT or MRI alone [241] and to improve site-specific radiation planning, as well as aid in the selection of optimal surgical candidates [242]. Furthermore, Avril *et al* were able to accurately predict patient response to neoadjuvant chemotherapy after just one cycle from sequential FDG PET [243]. They demonstrated the improved accuracy of this approach over clinical or histopathologic response criteria including changes in tumor marker CA125. The benefits of using ^{18}F-FDG PET to detect early treatment response have further been demonstrated in Hodgkin's lymphoma [244], non-small cell lung cancer [245] and esophageal squamous cell carcinoma [246].

1.9.0.2 ^{18}F-FDG PET for imaging the immune response

Increased glucose uptake is known to occur in activated immune cells during an inflammatory response; ^{18}F-FDG PET therefore provides a means of imaging such a response. Often, the high metabolic activity of the immune cells is viewed as a hinderance which obscures signal from sites of oncological interest, however there are several situations in which ^{18}F-FDG PET may be usefully deployed for directly probing immune cells. Standard clinical applications range from autoimmune diseases to infections, such as rheumatoid arthritis [247], sarcoidosis [248], HIV and AIDS related infection [249, 250] and fever of unknown origin [251]. Recently, the role of glycolytic metabolism in activated T-cells has been elucidated [252]. The rapid proliferation of these cells initiates metabolic reprogramming remarkably similar to that seen in tumours, demonstrating high levels of ATP production through glycolysis and elevated glucose and glutamine uptake [253]. This clearly has profound implications for tumour imaging with both ^{18}F-FDG PET and hyperpolarised ^{13}C-pyruvate, particularly as the use of immunotherapies gains clinical popularity.

1.10 Image segmentation in PET and MRI

Clinical imaging research commonly makes use of regions or volumes of interest (ROI or VOI) for delineating anatomical features, or for the analysis and quantification of areas that are pathologically abnormal in comparison to normal tissue. For example, radiation treatment planning relies heavily on accurate delineation of the tumour volume to avoid damage to normal tissue, and many commonly used metrics for assessing disease progression and treatment response rely on region determination and the subsequently derived quantitative parameters based on these regions; the SUV_{mean}, commonly used in the clinical interpretation of PET images, is a good example of such a metric. Accurate and robust quantification of imaging data is imperative in order to make reliable inter- and intra-patient comparisons therefore any ROI used in this analysis must be accurate, robust and repeatable.

There are four main approaches which are applied to the problem of image segmentation, which vary considerably in complexity. The first is manual delineation; this is used very commonly by clinicians for defining ROIs on anatomical images, however it is time consuming making it unsuitable for processing large date sets, prone to human error and has poor repeatability [254, 255]. Also frequently applied, particularly in clinical PET analysis, is a thresholding approach whereby the user defines

some inclusion criteria for the ROI based on image contrast [256]. Although iterative and adaptive thresholding methods have been developed over the past decade [257, 258], these methods are still ultimately quite susceptible to noise and variability. Unsupervised image segmentation methods use a more complex, statistical decision process, generally accounting for background noise and other user supplied information when defining the ROI. They have the benefit of being completely repeatable and require very little user interaction once the algorithm has been set up [259]. Finally, supervised segmentation methods using machine learning techniques have been rapidly gaining popularity. Initially requiring very large data sets to train algorithms, supervised methods can become very accurate over time and eventually require no additional user input [260]. They are well suited to the detection of subtle anatomical features on MRI or CT images which would not be possible with other methods.

Unsupervised and statistical segmentation techniques are particularly well suited to molecular and functional imaging data due to their enhanced capability to appropriately handle the noise, partial voluming effects and artefacts which are common to these modalities. The reminder of this section will therefore focus on unsupervised segmentation in PET and functional MRI, motivated by the potential application of these techniques to hyperpolarised ^{13}C data.

1.10.1 Edge-detection approaches for image segmentation

Variational methods rely on detecting the location of gradients in image contrast to determine the boundaries between regions. A common starting point is a Sobel edge detection or watershed transform, which determine the lines of maximum gradient across the whole image. The water shed transform treats the image contrast as a topography with pixel intensity representing height; the transform can be thought of as the dividing lines between different catchment basins for rain falling on the landscape. Although an early study applying this technique to PET images found little benefit over thresholding methods [261], Greets *et al* were able to produce more accurate results by first applying denoising and deblurring edge-conserving filters, along with constrained iterative deconvolution, to images [262]. Active contour methods are also a means of edge detection which seek to iteratively minimise an objective function defining the contour. Hsu *et al* demonstrate the success of this approach, combined with a genetic algorithm for objective function parameter optimisation, for segmenting the liver [263]; it has also been used to delineate PET tumour volumes in conjunction with an adaptive region-growing algorithm [264]. Known colloquially as "snake" methods, many variational methods struggle with discontinuities and more recently,

the level-set method was proposed to overcome some of these limitations [265]. Starting with some initial contour, an evolutionary PDE is solved iteratively to balance the forces between image gradient and contour curvature. The resulting segmentations have been successfully utilised for both PET and fMRI [266, 267, 268, 269].

1.10.2 Clustering methods

Clustering methods are a form of unsupervised classification learning which have been widely applied to medical image segmentation. The k-means algorithm is perhaps the simplest; a known number K of initial cluster centres are chosen, either randomly or manually, from the N image voxels. For each voxel, a vector of features x_j such as the intensity are defined based on which the algorithm will attempt to classify the voxels. Voxels are initially assigned to the most similar cluster centroid, with the aim to minimise the objective function for each cluster:

$$J(x, c) = \sum_{j=1}^{N} \sum_{k=1}^{K} \parallel x_j - c_k \parallel^2 \tag{1.21}$$

where c_k are the cluster centroid feature vectors. New centroids are then calculated as the mean for each cluster and voxels are reassigned. This iterative process continues to convergence. Although this method has shown some successful applications in MRI, [270, 271], an adaptation known as fuzzy c-means (FCM) clustering has been far more widely applied in molecular imaging problems [272]. By incorporating fuzzy as opposed to binary logic, large voxels, which may cover elements from more than one real biologically distinct segment, are permitted to belong to multiple classes simultaneously during the iterative procedure. Fuzzy logic is a popular way of acounting for poor image resolution and partial voluming; the fuzzy c-means algorithm has been applied to many problems in PET imaging such as whole body attenuation correction [273], brain lesion detection [274] and heterogeneous tumour quantification [275]. It has also been successfully applied to brain tumour delineation in MR [276].

1.10.3 Statistical image segmentation

Statistical image segmentation methods generally make use of a Bayesian inference to exploit statistical differences between the region of interest and the background. These methods are particularly well suited to noisy data, as the noise can be explicitly modelled for each segment and therefore taken into consideration when classifying each voxel. Gaussian mixture models work on the principle that any distribution, such

as image voxel intensities within an image, can be described as a mixture of Gaussian (normal) distributions representing the image classes. The segmentation task is then to use Bayesian expectation maximisation (EM) to determine as to which class each voxel belongs. Aristophanous *et al* apply this approach, with three mixed Gaussian distributions representing tumour, background and uncertain classes, to the definition of lung tumor volumes from PET [277]. One notable approach for segmenting PET imaging is suggested by Hatt *et al*. They use a Bayesian EM framework with two hard classes and two fuzzy classes, which additionally accounts for the spatial relationship between voxels based on the premise that voxels of the same class are more likely to be adjacent that separate. They demonstrate the superiority of this approach over a range of competing methodologies, particularly in the delineation of tumours <2 cm in size [278].

An extension to the above approach uses the same Bayesian framework, but incorporates a specific form of prior called a Gibbs prior defined for each permutation of the segmentation map $\mathbf{x}$ as:

$$p(\mathbf{x}|\beta) = \frac{1}{Z}e^{-U(\mathbf{x}|\beta)} \tag{1.22}$$

where β is a temperature parameter and Z is the partition function, defined as the sum over all permutations of $\mathbf{x}$. There are a number of key advantages to this approach; the term $U(\mathbf{x}|\beta)$ in the exponent may be made up of multiple additive terms, making it possible to incorporate prior information from different sources. One of these terms defines the spatial relationship between voxels; in 2D, this is known as a Markov random chain (MRC) and in 3D, a Markov random field (MRF). As with the Gaussian mixing model, normal distributions are used as the joint distributions to model noise explicitly for each class. MRFs, and MRCs, have been extensively applied to segmentation problems in MRI [279], [280], [281], [282], CT [283], [284] and PET imaging [285], [286], [287]. More recently, studies have extended the approach to include a temporal component, notably to handle time activity curves in PET [285] and in 4D MRI for both brain [288] and cardiac imaging [289]. Descombes *et al* have a particularly interesting approach, utilising a 4D MRF model to examine blood flow profiles in fMRI as a means of providing additional temporal information to their segmentation process [290].

Chapter 2

A comparison of quantitative methods for clinical imaging with hyperpolarised ^{13}C-pyruvate

Dissolution dynamic nuclear polarisation (DNP) enables the metabolism of hyperpolarised ^{13}C-labelled molecules, such as the conversion of [1-^{13}C]pyruvate to [1-^{13}C]lactate, to be dynamically and non-invasively imaged in tissue. Imaging of this exchange reaction in animal models has been shown to detect early treatment response and correlate with tumour grade. Early human DNP studies are now under way at multiple sites worldwide, and for widespread clinical translation, simple and reliable methods are necessary to accurately probe the reaction in patients. However, there is currently no consensus on the most appropriate method to quantify this exchange reaction. In this study, an *in vitro* system was used to compare several kinetic models, as well as simple model-free methods. Experiments were performed using a clinical hyperpolariser, a human 3 T MR system, and spectroscopic imaging sequences. The quantitative methods were compared *in vivo* by using subcutaneous breast tumours in rats to examine the effect of pyruvate inflow. The two-way kinetic model was the most accurate method for characterising the exchange reaction *in vitro*, and the incorporation of a Heaviside-step inflow profile was best able to describe the *in vivo* data. The lactate time-to-peak and the lactate-to-pyruvate area under the curve ratio were simple model-free approaches which accurately represented the full reaction, with the time-to-peak method performing indistinguishably from the best kinetic model. Finally, extracting data from a single pixel was a robust and reliable surro-

gate of the whole region-of-interest. This work has identified appropriate quantitative methods for future work in the analysis of human hyperpolarised ^{13}C data.

2.1 Introduction

Functional and molecular imaging is increasingly used as a routine clinical tool in many areas of oncology. The advent of molecularly-targeted drugs, combinational therapies and personalised medicine has resulted in an increasing requirement for specific imaging methods to monitor drug efficacy; consequently, new imaging methods to probe tumour biology are required that demonstrate both intra- and inter-patient repeatability. Dissolution dynamic nuclear polarisation (DNP) is a new imaging test which has the potential to image tissue biology. The technique increases the signal-to-noise (SNR) of molecules containing one or more ^{13}C nuclei by more than 10,000-fold above thermal levels; this process is undertaken outside of the animal or patient, and the hyperpolarised molecule is subsequently injected intravenously [152]. When combined with ^{13}C-magnetic resonance spectroscopic imaging (MRSI), this increase in SNR allows real-time *in vivo* metabolism of the molecules to be imaged non-invasively [291].

There are now many ^{13}C-labelled probes which have been successfully hyperpolarised using DNP and these have been used to interrogate many aspects of tissue biology and metabolism that occur in a wide range of disease processes [168, 165, 203, 204, 207, 208]. [1-^{13}C]Pyruvate is the most extensively studied of these probes; the major reaction of pyruvate is its conversion into [1-^{13}C]lactate, which is catalysed by the enzyme lactate dehydrogenase (LDH) and requires the reduced form of nicotinamide adenine dinucleotide (NADH) as a cofactor. Hyperpolarised [1-^{13}C]pyruvate may also form [1-^{13}C]alanine, [1-^{13}C]bicarbonate, and [1-^{13}C]pyruvate-hydrate in a pH-dependent reaction [173]. These reactions have been well characterised *in vivo* in pre-clinical animal models of disease [193, 189, 191, 198, 200] and there are now a number of sites worldwide that are developing the technique for human use [156].

The success of hyperpolarised ^{13}C-labelled pyruvate as a cancer imaging biomarker is largely dependent on the phenomenon of aerobic glycolysis within tumours known as the Warburg effect [2]. There is a high lactate concentration within most cancers, even in normoxic conditions, and the hyperpolarised ^{13}C signal may rapidly exchange between the injected [1-^{13}C]pyruvate and the endogenous lactate pool. Imaging of this exchange reaction in animal models has been shown to detect early treatment

response [169, 177] and correlate with tumour grade [170]. The results from the only clinical study performed to date, have shown that labelled lactate may be present in small tumours that are not visible with standard proton imaging techniques [156].

The sensitivity of ^{13}C-MRSI to small changes in metabolic rate offers the potential to non-invasively monitor metabolic alterations in patients. However, for any novel imaging technique to be widely adopted, it must be repeatable, reproducible and will ideally utilise simple and robust quantitative methods for analysis. Current clinical approaches for the analysis of dynamic contrast-enhanced MRI and positron emission tomography (PET) can offer insight into quantitative imaging with DNP. For example, the maximum standardised uptake value (SUV_{max}) is a very simple and powerful routine clinical tool to quantify metabolism in PET imaging with ^{18}F-fluorodeoxyglucose [292]. For each voxel of a PET image, the SUV is defined as the tissue radioactivity concentration divided by the injected radiation per unit body weight, correcting for decay from the time of injection. The SUV_{max} is the voxel of highest SUV within a region of interest while the SUV_{mean} is the average over that region. A number of methods have been employed to quantify the pyruvate-lactate exchange reaction measured using DNP, many of which involve fitting kinetic models of varying complexity to imaging or spectroscopy data to produce the forward reaction rate constant k_P as a quantitative marker [169, 170, 220, 219]. Simple methods for estimating k_P from the time course of pyruvate and lactate have been suggested [229], as well as methods using model-free parameters such as the area under the metabolite curve (AUC) [226], or ratios of the metabolite signal peaks [194, 178]. However, there is currently no consensus on the best method to characterise the pyruvate-lactate reaction, either for research purposes or for more routine clinical use.

In this chapter, both *in vitro* and *in vivo* dynamic hyperpolarised data are used to comprehensively compare a range of kinetic models and simple analysis parameters. A clinical hyperpolariser and imaging sequences were used with a 3 T MR system, as well as a pyruvate concentration similar to the blood pyruvate concentration anticipated in future patient studies. The aim was to determine which quantitative parameters are most appropriate to describe the dynamic time-course data acquired, testing for accuracy, simplicity and robustness in each case. Each analysis was also applied *in vivo* to rats with subcutaneous tumours, which were imaged with the same spectroscopic imaging sequence, to examine the effect of pyruvate inflow on kinetic model accuracy.

2.2 Materials and methods

2.2.1 *In vitro* experiments

Research grade fluid paths (GE Healthcare, Milwaukee, WI, USA) were filled with 100 μl of [1-^{13}C]pyruvic acid doped with 15 mM of an electron paramagnetic agent (EPA or Trityl radical AH111501, GE Healthcare, Milwaukee, WI, USA) and 30 ml of dissolution fluid containing 1 g/L ethylenediaminetetraacetic acid (EDTA, GE Healthcare, USA). Samples were polarised using a clinical hyperpolariser (SPINlab, GE Healthcare, USA) at approximately 0.9 K and 5 T for an average of 101 minutes (range 83-149 min) to an average polarisation of 21% (range 10-38%) at the time of measurement using a benchtop NMR polarimeter (Oxford Instruments, Abingdon, UK). Following rapid dissolution, 1.4 ml of neutralisation medium containing 0.72 M NaOH, 0.4 M TRIS buffer and 0.1 g/L EDTA (GE Healthcare, USA) was added to the solution. The final pH ranged from 6.7-7.4 with an average of pH 7.2.

Imaging phantoms consisted of 15 ml Falcon tubes filled to 14 ml with 5-times concentrated phosphate buffered saline at pH 7.2 and containing the coenzyme NADH at 4.4 mM (Sigma-Aldrich, UK). L-lactate dehydrogenase from rabbit muscle (Sigma-Aldrich, UK) was added in quantities varying from 0 to 120 U, a range chosen to incorporate the expected range of k_P in human blood based on the only published study to date (mean $\pm$ SD of 0.045 $\pm$ 0.025 s^{-1}) [156]. 1 ml of the above 60 mM hyperpolarised solution was added simultaneously to the three tubes making up each set immediately before imaging, giving a final pyruvate concentration of $\sim$4 mM. This is similar to the final blood concentration in the rats ($\sim$3 mM) and that expected in patients ($\sim$1.5 mM). If uniform distribution of this is achieved in the body in the timescale of the half-life of hyperpolarisation, then the tissue concentrations would be lower. Neither pyruvate nor NADH were rate limiting. The time between dissolution and imaging was approximately 35 s.

2.2.2 *In vivo* experiments

Four adult female Fischer 344 rats (Charles River, Sulzfeld, Germany; 165 $\pm$ 6 g body weight) bearing subcutaneous mammary adenocarcinomas were imaged [176, 293]. Tumours were induced by implanting 1×10^6 MAT B III cells (syngenic breast cancer cell line), and imaging was performed 12-16 days after cell implantation. Animals were anaesthetised with 1-3% isoflurane and monitored for ECG, breathing, and temperature, and kept warm on a heating pad with circulating warm water. The time delay between dissolution and injection was 15-20 s. The animal study was

approved by the local governmental committee for animal protection and welfare (Tierschutzbehörde, Regierung von Oberbayern).

[1-^{13}C]Pyruvic acid doped with 15 mM of the trityl radical OX063 and 1 mM gadoteric acid (Guerbet, France) was polarised in a HyperSense DNP polariser (Oxford Instruments, UK) for approximately 45 min at 1.4 K and 3.35 T to a polarisation of approximately 25%. Dissolution fluid, containing 80 mM NaOH, 80 mM Tris buffer, and 0.1 g/L EDTA dissolved in water, was heated to 185 °C and used to rapidly dissolve the polarised sample. The final solution contained 80 mM [1-^{13}C]pyruvate at pH 7.6 and physiological temperature and osmolarity. This was injected into a tail vein inside the MRI scanner at a rate of approximately 0.2 mL/s and at a dose of 2.5 mL/kg. Dynamic imaging was performed from the time of injection.

2.2.3 Spectroscopic imaging

All imaging was carried out on a clinical 3 T MRI system (Signa HDx, GE Healthcare, USA) using imaging sequences from the multinuclear spectroscopy (MNS) research pack version 2.0 (GE Global Research, Munich, Germany). Enzyme phantoms were imaged in sets of 3 using a ^{13}C-^{1}H multi-nuclear receive/transmit coil (GE Coils, Aurora, Ohio, USA). First, four 90° non-localised spectral-spatial pulses with TR = 1 s centred on the lactate Larmor frequency were applied [176]; this was found to be the optimum number for removing signal from any lactate labelling prior to commencement of the experiment whilst retaining maximum pyruvate polarisation. These were immediately followed by a 3 min IDEAL (iterative decomposition with echo asymmetry and least-squares estimation) spiral chemical shift imaging (CSI) acquisition [182] acquired using a single 20 mm axial slice. Each excitation is followed by a single-shot spiral image encoding module, with echo-time shifting of 1.12 ms between excitations. Seven time-shifted echoes plus a single free induction decay (FID) spectrum are acquired in total for each time step, with the chemical-shift information from the FID providing prior knowledge for the reconstruction. Other parameters were TR 500 ms, flip angle 5°, FOV 80 mm, nominal matrix resolution 32×32 and 4 s time resolution.

Animals were imaged on a similar clinical 3 T MRI system (Signa HDx, GE Healthcare, USA) using a rat-sized ^{13}C-1H multi-nuclear birdcage coil. The same IDEAL spiral CSI acquisition was performed through four axial 10 mm slices over 1 min with a temporal resolution of 4 s. ^{13}C-pyruvate is replenished by inflowing blood *in vivo*, so a larger flip angle of 10° was used. All other parameters were consistent with the *in vitro* experiments. Single metabolite k-space data was first reconstructed

by matrix inversion with off-resonance correction, followed by Cartesian regridding for spatial reconstruction [182]. Gaussian k-space filtering was applied during post-processing on both data sets, resulting in an effective image resolution of 5×5 mm. For anatomical reference, standard gradient echo proton images were acquired from the same slice geometry and FOV (resolution 256×256, slice thickness 3 mm, spacing 7 mm, TE 10 ms, TR 500 ms).

2.2.4 Data analysis

Imaging data was exported into Matlab (Mathworks, Natick, Mass. USA) for analysis using custom built software. Images were partially noise-corrected by subtracting the average squared background noise from the power images [294]; the effect of this correction on the images is demonstrated in figure 2.1. Dynamic time-course data for pyruvate and lactate were extracted from the images, using two methods for comparison. In the first, a region of interest (ROI) was defined by thresholding the $t = 0$ pyruvate image at 40% of the maximum pyruvate signal within each phantom for the *in vitro* data, or by outlining the tumour boundary based on the anatomical proton image for the *in vivo* data. This ROI was applied to all subsequent images in the series and the pixels within the ROI were averaged to produce the relative signal strengths of each metabolite at each time point. The second method defined a pixel-of-interest (POI) as the pixel within each phantom, or within the rat on the tumour bearing image slice, which demonstrated the highest lactate signal after averaging over all time points. Dynamic data from these two extraction methods was separately analysed using each of the methods detailed below.

2.2.4.1 Kinetic modelling

The exchange reaction between pyruvate and lactate, along with the irreversible hyperpolarised signal loss due to spin-lattice relaxation and applied RF excitation, can be characterised by the following coupled differential equations:

$$\frac{dP(t)}{dt} = k_L L(t) - k_P P(t) - \rho P(t) \tag{2.1}$$

$$\frac{dL(t)}{dt} = k_P P(t) - k_L L(t) - \rho L(t) \tag{2.2}$$

Where P and L are the relative pyruvate and lactate signal intensities, k_P and k_L are the forward and backward reaction rate constants respectively and ρ is the effective relaxation time given by:

$$\rho = \frac{1}{T_{1,eff}} = \frac{1}{T_1} - \frac{1}{t_R}\ln(cos\theta) \tag{2.3}$$

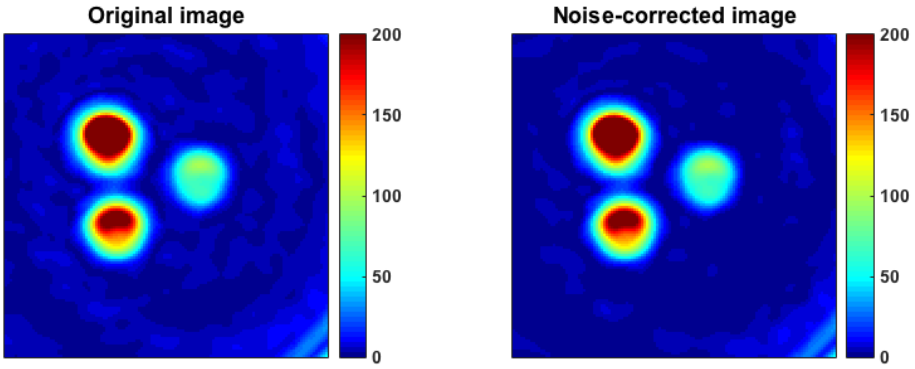

Figure 2.1: The same ^{13}C-lactate image before (left) and after (right) applying noise correction for comparison. Image is taken from phantom experiments and shows an axial slice through 3 phantoms containing 20, 40 and 60 U LDH at t = 6 s.

Where T_1 is the relaxation time of pyruvate in the medium or tissue, t_R is the known repetition time of the applied RF pulses and θ is the flip angle. To reduce the number of parameters to be fitted, it is assumed throughout that the pyruvate and lactate relaxation rates are equal, which in the limit of fast exchange between metabolites can be shown to be a good approximation [295], and use the above expression to correct for RF flip angle. Each model variant was applied to yield the forward reaction rate constant k_P, the T_1 decay constant, their standard errors and other fitting parameters where appropriate. Constrained fits were carried out in Matlab using the *fmincon* function unless otherwise stated. Solutions were found by minimising the negative log of the maximum likelihood function, which for N data points is given by:

$$f(\mathbf{K},\sigma) = \sum_{i=1}^{N} \frac{(L_i - L_i^{data})^2}{2\sigma^2} - \ln(1 - exp\{\frac{-(P_i - P_i^{data})^2}{2\sigma^2}\}) + \ln((P_i - P_i^{data})^2) \quad (2.4)$$

Here $\boldsymbol{K}$ is the vector of free parameters to be fit, σ^2 is the lactate variance, L_i and P_i are the model estimates of the metabolite signal strengths and L_i^{data} and P_i^{data}, the measured values for the ith data points. This likelihood function is derived from a Bayesian extension to least squares minimisation which addresses the disproportionately large early pyruvate signal, as described by Hill *et al* [226]. It incorporates a lower-bound prior on the pyruvate noise which acts to reduce the impact of any large early pyruvate residuals which can otherwise dominate the fit. Due to the sensitivity of the optimisation algorithm to the initial values of P and L, a Monte Carlo method was used to randomly vary these inputs over 1000 runs for each model fit. Inputs

were allowed to vary over a Gaussian distribution centred, with a standard deviation of 5%, on the measured value of P or L at t=0.

The two-site exchange model For the *two-way differential model*, the above set of differential equations were solved simultaneously to fit the pyruvate and lactate time course data with k_P, k_L and ρ as free parameters. The equations may also be solved analytically to give the following solutions:

$$P(t) = \frac{1}{k_P + k_L}\{P(0)(k_L e^{-\rho t} + k_P e^{-(k_P+k_L+\rho)t}) + L(0)(k_L e^{-\rho t} - k_L e^{-(k_P+k_L+\rho)t})\} \tag{2.5}$$

$$L(t) = \frac{1}{k_P + k_L}\{P(0)(k_P e^{-\rho t} - k_P e^{-(k_P+k_L+\rho)t}) + L(0)(k_P e^{-\rho t} + k_L e^{-(k_P+k_L+\rho)t})\} \tag{2.6}$$

These equations themselves may then be fit directly to the data in the *two-way integral model*, which is computationally faster than applying the full differential fit but may be more sensitive to the initial values of the parameters. For the *in vitro* data, the latter two models are virtually identical apart from the fitting algorithms used, however they require different approximations for metabolite inflow when used *in vivo*. A popular simplification of the model is to set the backwards reaction rate constant k_L to zero [170, 220, 219, 221, 222]. This is argued to be a reasonable assumption since k_L is often around 10-fold smaller than the forward rate constant k_P and, depending on the model used, may not be a mathematically distinct parameter. To investigate the validity of the *one-way model*, the above integral solutions with k_L=0 were also applied to the data.

Ratiometric model A ratiometric model has been suggested by Li *et al* [295]. Briefly, when the ratio is taken of the above integral solutions, ρ can be eliminated as a parameter; this new model can be fit to the ratio of the lactate-to-pyruvate data to solve for the rate constants k_P and k_L. Prior to fitting with the *nlinfit* function in Matlab, ratio data was smoothed by averaging over every three data points. The lactate data was used to weight the fit towards the region in which the rate constants are stable and was subsequently derived as a single unknown by inputting the k_P and k_L obtained from the ratiometric fit into the differential kinetic model.

2.2.4.2 Model-free methods

Fall minus rise at height α approach Pagès and Kuchel suggest a method for estimating k_P and ρ from graphical features of the time-course which they call the

FmRα (Fall minus Rise at height α) approach [229]. They suggest parameter β to be the ratio of the lactate-to-pyruvate signals for the time at which the lactate signal is maximal, then show this to be mathematically equal to the product of k_P and $T_{1,eff}$. Furthermore, they show that an estimate for $T_{1,eff}$ can be obtained from the width of the lactate curve at a specific height α. Although they suggest it is sufficient to use a consistent value of $\alpha = 0.8$, α was calculated here explicitly in each case to avoid incurring a non-physical correlation between k_P and T_1.

Lactate/pyruvate peak ratio The *in vitro* $T_{1,eff}$ is only affected by physical factors such as magnetic field and temperature. Since these factors are controlled for, the $T_{1,eff}$ is not expected to show a large variation. The above parameter β, which will be refered to here as the L/P peak ratio, could therefore be expected to correlate with LDH concentration and as such, was investigated as a potential parameter of interest.

Area under the curve ratio The ratio of the lactate-to-pyruvate area under the curve (AUC) has been shown by Hill *et al.* to be independent of the shape of the pyruvate inflow [226] making it an excellent candidate for analysis of *in vivo* data. If it is assumed that only the pyruvate has an explicit input function and that the concentration of both metabolites is zero at $t = 0$, then using the two-way, two-site model, the AUC ratio can be shown to be proportional to k_P. For *in vitro* data this ratio was calculated in two ways: firstly taking the AUC ratio of the available data (AUC data) and secondly fitting bi-exponential solutions extrapolated back to $t = 0$ (AUC fit).

Time-to-peak measurements Finally, this work suggests a new approach that examines the time difference from the start of the lactate build up to its peak, as has been used in DCE-MRI. Starting from the two-way model, the rate equations can be solved analytically to find the time at which the lactate reaches its maximum by differentiating the lactate solution, and solving for t when this is zero. The time-to-peak (TTP) is then given by:

$$TTP = \frac{1}{k_P + k_L} \ln(1 + T_{1,eff}(k_P + k_L)) \tag{2.7}$$

The TTP should show a roughly inverse correlation with LDH concentration. A bi-exponential function was fitted to the time-domain lactate data and extrapolated back to find the predicted start time of the increase in lactate signal from zero. Schematic

diagrams of each of the models and model-free methods described above are presented in figure 2.2a-f.

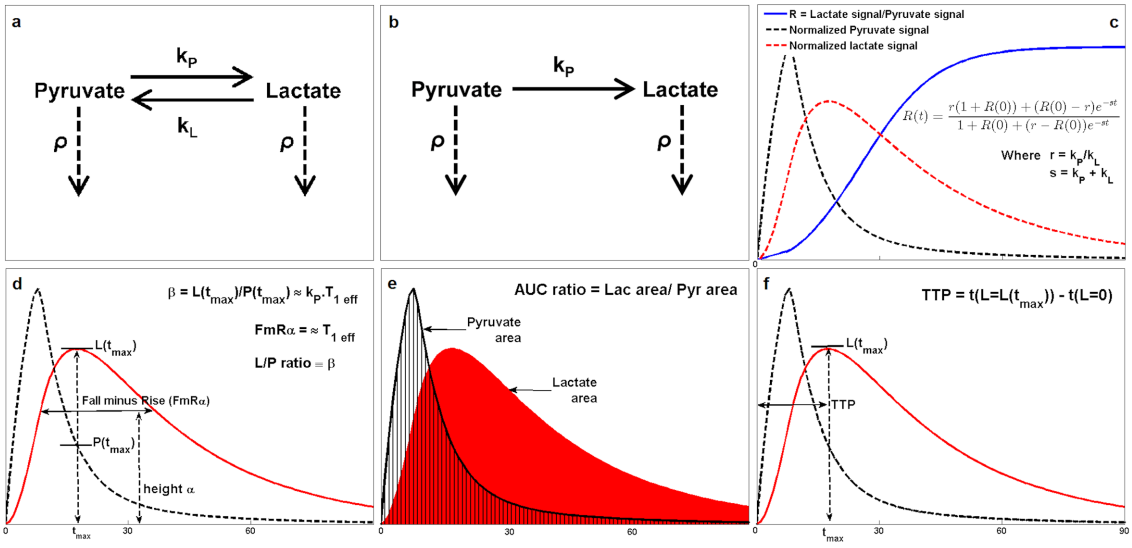

Figure 2.2: Schematic diagrams for each of the models and model-free methods proposed. a: Interactions accounted for in the two-way differential/integral models where k_P and k_L are the forwards and backwards reaction rate constants respectively and ρ is the inverse of the effective spin-lattice relaxation, $T_{1,eff}$; b: Interactions for one-way integral model; c: Example metabolite timecourses demonstrating the ratiometric model; d: FmRα approach and L/P ratio method; e: Lactate-to-pyruvate area under the curve ratio; f: Lactate time-to-peak.

2.2.4.3 *In vivo* imaging

in vivo analysis of pyruvate metabolism is complicated by the flow of injected metabolites in the bloodstream, tissue diffusion and cellular transport. For full modelling of this data, a pyruvate inflow function (PIF) must be included to describe the large initial pyruvate peak as the injected bolus reaches the tissue of interest. In the interest of simplicity, each of the four model variants was fitted only to data from the pyruvate peak onwards, which in each case occurred at the third data point. Each of the model-free methods was implemented on the entire dataset. A common way to approximate the PIF is to use a box-car or trapezoidal function, and an alternative is to fit a piece-wise integral solution. The latter involves splitting the pyruvate profile into two segments described by separate equations; the first for constant pyruvate inflow, and the second describing signal decay and conversion to lactate [170, 296, 297, 225]. Here, a Heaviside-step function is used to incorporate a continuous PIF into the pyruvate

two-way differential equation with the same characteristics as a box-car function:

$$\frac{dP(t)}{dt} = k_i \left(1 - \frac{1}{1 + e^{-2(t-t_e)}}\right) + k_L L(t) - k_P P(t) - \rho P(t) \tag{2.8}$$

Where k_i is the pyruvate flow rate and t_e is the time at which the inflow ceases. This was compared to the piece-wise one-way integral model described by Zierhut *et al.* [170] in two ways: fixing t_e at the peak of the pyruvate curve or fitting for it as an extra parameter.

2.2.5 Statistical analysis

The quantitative parameters derived using each method were tested for their correlation with the known *in vitro* LDH concentration. These correlations were generally linear. Both Pearson (linear) and Spearman (rank) correlation coefficients and their two-tailed p-values were calculated, so that it was possible to compare all methods directly whilst making no assumptions about the nature of the dependences. In order to determine whether one analysis approach was significantly better than another, Steiger's z-test for dependant correlations was implemented pair-wise on both the Pearson, then Spearman coefficients produced by each method, and the two-tailed p-values calculated (significance p <0.05) [298]. In addition, a simple linear regression model was applied in each case to calculate the adjusted R^2 values both with and without a robust bi-square weighting function applied to the data. The difference in R^2 with and without the weighting, denoted the 'instability factor, provides a crude indicator of how much the fit is dominated by outliers and therefore how robust a particular method may be. The mean, range and standard deviation (SD) of T_1 values obtained from all phantoms taken together were also analysed for each quantitative method to assess goodness of fit. Since the T_1 is expected to be highly consistent *in vitro*, a large range and high SD suggests that a model is not fully describing the data or is under-parametrised.

To assess how well each model was able to fit the *in vivo* data, the corrected Akaike Information Criteria (AICc) were calculated [299]. The AICc uses the minimised likelihood function values to examine how well each model was able to describe the data, whilst imposing a penalty for each extra free parameter to guard against over-fitting; a low AICc denotes higher model accuracy. The relative likelihood that each model is correct as compared to the model with the lowest AICc was then calculated. To investigate model-free parameters *in vivo*, correlation coefficients and R^2 values were again calculated, however because the enzyme activity was an unknown, they

were compared against k_P values derived using the most likely model with ROI or POI data as appropriate. The ROI and POI results were combined when calculating correlation coefficients due to the small size of the dataset.

2.3 Results

2.3.1 *In vitro* modelling

Thirty-three 15 ml phantoms containing 0 U ($n = 2$), 20 U ($n = 5$), 40 U ($n = 6$), 60 U ($n = 6$), 80 U ($n = 6$), 100 U ($n = 5$) and 120 U ($n = 3$) of LDH enzyme were imaged in sets of three, for which representative images can be seen in figure 2.3a. Ringing artefacts, noise spikes and other interference were visible in some images, however since it was of particular interest to test the quantitative analysis methods for robustness against such common artefacts, none of the data was excluded. The quantitative parameters obtained with each analysis method were tested for their correlation with the known scale of phantom LDH concentrations. The two-tailed p-values calculated from the Pearson and Spearman correlation coefficients were all highly significant (p <0.001).

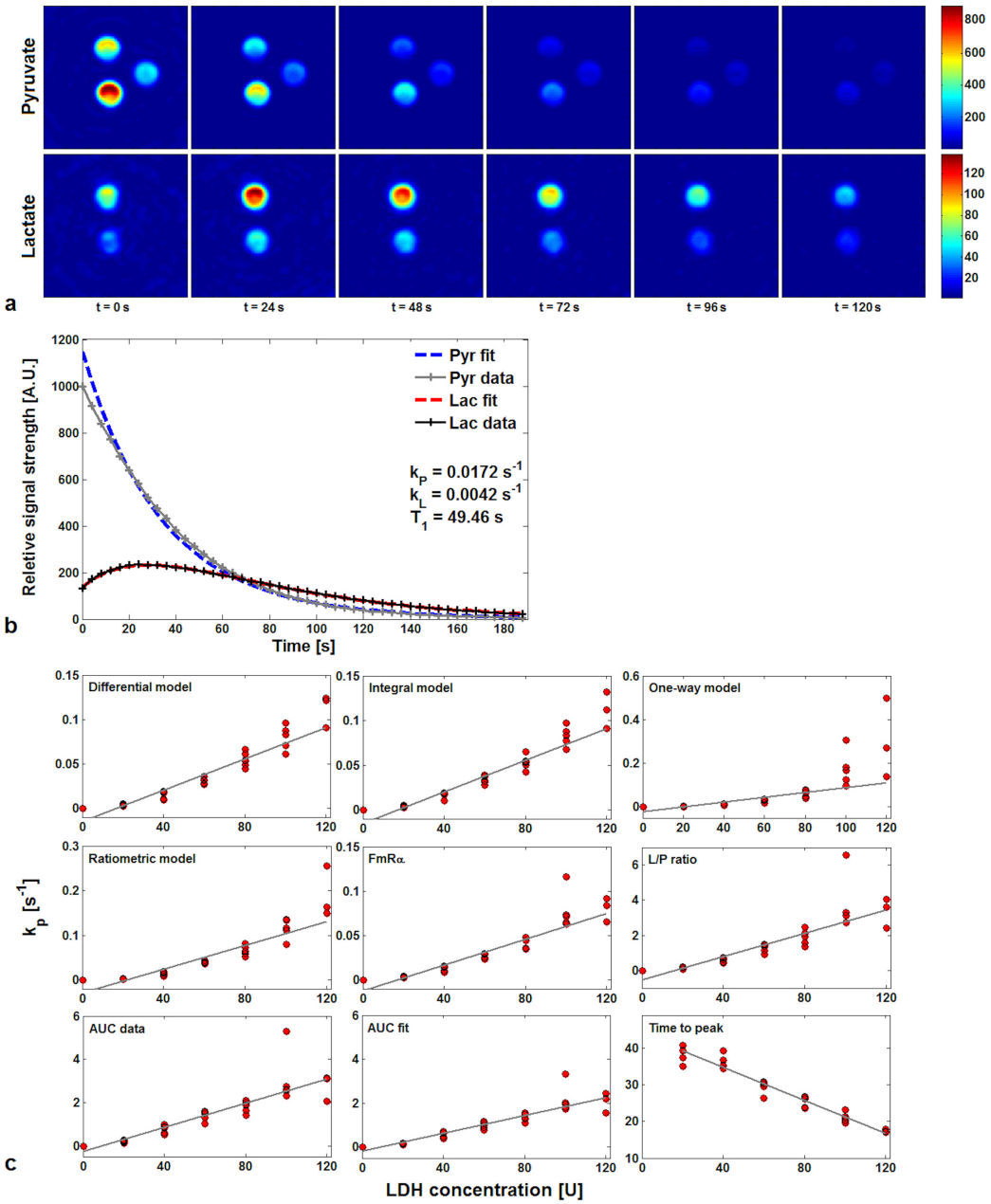

Figure 2.3: Representative data from the in vitro study. a: IDEAL spiral CSI axial images of pyruvate and lactate in three phantoms, displayed at 24 s intervals. Phantoms contain 40, 0 and 20 U of LDH enzyme (clock-wise from top), colour bar shows arbitrary signal units scaled to the brightest point in the time curve for each metabolite. b: Pyruvate and lactate time-courses (solid lines) extracted from the 40 U phantom using the ROI method and fitted using the differential two-way kinetic model (dashed lines). c: Correlation with LDH enzyme concentration of the forward reaction rate constants k_P derived from four model variants (differential, integral, ratiometric and one-way models). Note that the scale for k_P varies between plots.

Table 2.1: Summary of the analysis for the in vitro data are shown by comparing the calculated exchange rate constants with the known enzyme concentration. Calculations have been performed using both the ROI and POI approaches.

Region of interest	Pearson coeff.	Spearman coeff.	Adj. R^2	Adj. R^2 robust	Instability	T_1 mean	T_1 range	T_1 SD
k_P Differential	0.950	0.984	0.900	0.917	0.017	52.4	13.2	3.04
k_P Integral	0.952	0.986	0.903	0.931	0.028	52.5	13.5	2.97
k_P One-way	0.942	0.982	0.883	0.907	0.025	58.4	21.7	5.99
k_P Ratiometric	0.896	0.986	0.796	0.891	0.095	57.3	26.9	5.46
k_P FmRα	0.920	0.981	0.842	0.923	0.082	47.7	21.9	4.36
L/P ratio	0.854	0.969	0.721	0.905	0.184	-	-	-
AUC data	0.877	0.966	0.761	0.945	0.184	-	-	-
AUC fit	0.916	0.974	0.833	0.944	0.110	-	-	-
TTP	-0.971	-0.964	0.940	0.946	0.006	-	-	-
Pixel of interest	Pearson coeff.	Spearman coeff.	Adj. R^2	Adj. R^2 robust	Instability	T_1 mean	T_1 range	T_1 SD
k_P Differential	0.925	0.982	0.852	0.946	0.094	53.8	12.4	3.75
k_P Integral	0.919	0.982	0.840	0.939	0.100	54.0	15.8	4.23
k_P One-way	0.767	0.924	0.574	0.923	0.348	60.2	26.6	7.78
k_P Ratiometric	0.915	0.984	0.831	0.852	0.020	58.6	30.4	6.63
k_P FmRα	0.922	0.981	0.846	0.942	0.096	46.4	21.8	4.81
L/P ratio	0.858	0.976	0.727	0.921	0.195	-	-	-
AUC data	0.880	0.971	0.766	0.926	0.160	-	-	-
AUC fit	0.898	0.976	0.801	0.943	0.142	-	-	-
TTP	-0.963	-0.964	0.926	0.921	0.005	-	-	-

The results of the analyses are summarised in table 2.1. For the model-based approaches, application of Steiger's z-test to the Pearson coefficients for the ROI data demonstrated the ratiometric method to be significantly poorer than the other three models, which were not found to be significantly different. However, the POI data showed the one-way model to be worse than the other methods tested. In both cases, the differential and integral models are better able to constrain the T_1 compared to the other three methods, which suggests that they are more closely modelling the data. A fit with the differential model is shown in figure 2.3b. The variation in k_P between the integral and differential versions of the two-way model is a function of the algorithm used for fitting the data, but this difference was shown to be insignificant ($p > 0.2$). Despite the simplicity of the FmRα approach, k_P values obtained from the FmRα analysis were not significantly different from those obtained by modelling methods, other than the ROI integral model.

In contrast, the model-free methods showed greater variation with the TTP proving to be significantly better, and the L/P ratio significantly worse, than other meth-

Table 2.2: Significance matrix for in vitro data from region-of-interest (ROI) data (top) and pixel-of-interest (POI) data (bottom). Matrix shows p-values from applying Steiger's z-test for comparing the relative strength of correlations pairwise to Pearson coefficients; the Pearson coefficients test the correlation between quantitative parameters produced by each method, and known enzyme concentration. * indicates the better ranking (high 1-9 low) analysis method of the two is significantly so (significance level p <0.05).

ROI analysis	Pearson	Raw rank	k_P Integral	k_P One-way	k_P Ratiometric	k_P FmRα	L/P ratio	AUC data	AUC fit	TTP
k_P Differential	0.9503	3	0.762	0.664	0.001*	0.075	0.001*	0.007*	0.098	0.156
k_P Integral	0.9518	2	-	0.604	0.000*	0.050*	0.000*	0.005*	0.075	0.183
k_P One-way	0.9415	4		-	0.032*	0.402	0.011*	0.051	0.336	0.219
k_P Ratiometric	0.8956	7			-	0.380	0.322	0.643	0.539	0.001*
k_P FmRα	0.9201	5				-	0.000*	0.010*	0.722	0.010*
L/P ratio	0.8541	9					-	0.078	0.000*	0.000*
AUC data	0.8766	8						-	0.000*	0.000*
AUC fit	0.9158	6							-	0.007*
TTP	-0.9705	1								-
POI analysis	Pearson	Raw rank	k_P Integral	k_P One-way	k_P Ratiometric	k_P FmRα	L/P ratio	AUC data	AUC fit	TTP
k_P Differential	0.9254	2	0.206	0.000*	0.640	0.753	0.003*	0.073	0.173	0.054
k_P Integral	0.919	4	-	0.000*	0.860	0.763	0.007*	0.129	0.303	0.035*
k_P One-way	0.7666	9		-	0.002*	0.000*	0.048*	0.026*	0.003*	0.000*
k_P Ratiometric	0.9147	5			-	0.780	0.173	0.375	0.647	0.020*
k_P FmRα	0.9223	3				-	0.000*	0.024*	0.103	0.048*
L/P ratio	0.8575	8					-	0.103	0.001*	0.001*
AUC data	0.8795	7						-	0.074	0.003*
AUC fit	0.8983	6							-	0.010*
TTP	-0.9633	1								-

ods tested. The AUC from the extrapolated fits also performed well, being indistinguishable from the modelling approaches. When p-values were calculated from the Spearman coefficients, the results largely supported those from the Pearson coefficients with the exception of the TTP, which performed least well. Table 2.2 shows full significance matrices for both ROI and POI data from the pair-wise application of Steiger's z-test.

The sensitivity of k_P may be examined in terms of the offsets of the fit lines at the origin. The cause of these offsets is two-fold; firstly there is a positive skew caused by the divergent k_P values produced at high LDH concentrations and secondly, sensitivity limitations at very low concentrations cause an initial monotonic but non-linear rise in k_P with increasing LDH. The relative sensitivity of each model to these features is characterised by the difference in the two correlation coefficients; they are accounted for well by the Spearman coefficients, which allow regions of monotonic non-linear increase, but will incur a penalty with the Pearson coefficients which enforce linearity.

2.3.2 *In vivo* modelling

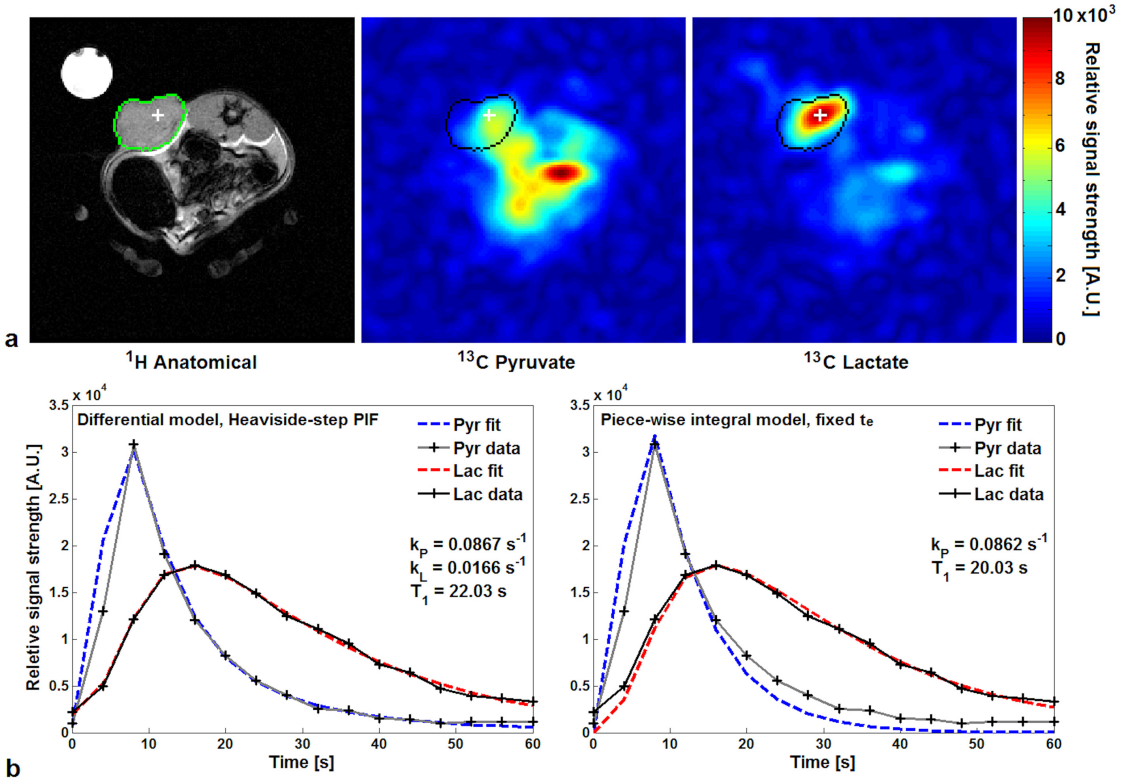

Figure 2.4: *In vivo* data from a rat (rat 1) with a subcutaneous implanted mammary adenocarcinoma. a: proton anatomical reference image and hyperpolarised ^{13}C-pyruvate and ^{13}C-lactate images at $t = 20$ s; color bar in arbitrary signal units. b: Pyruvate and lactate time-courses (solid lines) extracted from the thresholded tumor ROI and fits (dashed lines) from the differential kinetic model with a Heaviside-step PIF (left) and the fixed t_e piece-wise model (right) for comparison.

Each of the four models tested *in vitro* were fit to both ROI and POI derived time course data from four rats with subcutaneously implanted tumours. An additional three models were tested which incorporated a PIF. The corrected Akaike Information Criterion scores (AICc) and the relative likelihood of each model correctly describing the observed data were then calculated; the results of this, along with the T_1 mean, range and SD are shown in table 2.3. The T_1 values obtained were slightly higher than those previously estimated in healthy rats of ∼15 s, but consistent with other rodent tumour T_1 values [170, 187]. The *in vivo* results were similar to those found *in vitro*, with the differential and integral models statistically indistinguishable from each other, but significantly more likely than the one-way or ratiometric models to accurately describe the data. Models incorporating a PIF were applied to a larger

number of data points than the remaining models to include data prior to the pyruvate peak. For this reason, the relative likelihood values for the PIF models were calculated separately to compare just these three, as shown in table 2.3.

Table 2.3: Summary of statistical analysis from calculating the corrected Akaike Information Criterion for each model, separately fitted to ROI and POI data from four rats with subcutaneously implanted tumours. The relative likelihoods for models incorporating a PIF were calculated separately against each other. The lowest section shows correlation coefficients for model-free parameters against k_P values from the differential Heaviside-step PIF model. * p <0.05; ** p <0.001.

Region of interest	Average AICc	Relative likelihood	T_1 mean	T_1 range	T_1 SD
k_P Differential	368.9	0.257	25.7	7.51	2.78
k_P Integral	367.5	1	25.4	7.60	2.90
k_P One-way	403.3	2.95×10^{-16}	23.2	5.98	2.26
k_P Ratiometric	388.8	5.87×10^{-10}	27.1	8.54	3.03
k_P Differential, PIF	469.0	1	24.6	6.90	2.61
k_P Piece-wise, fixed t_e PIF	495.9	2.12×10^{-12}	22.2	5.71	2.24
k_P Piece-wise, variable t_e PIF	499.2	2.12×10^{-12}	22.2	5.78	2.28
Pixel of interest	Average AICc	Relative likelihood	T_1 mean	T_1 range	T_1 SD
k_P Differential	436.1	1	25.0	4.75	1.83
k_P Integral	436.2	0.880	25.2	4.84	1.89
k_P One-way	449.5	1.51×10^{-6}	22.8	5.18	1.97
k_P Ratiometric	469.0	5.28×10^{-15}	27.6	2.47	0.91
k_P Differential, PIF	527.8	1	23.9	4.59	1.73
k_P Piece-wise, fixed t_e PIF	533.7	2.97×10^{-3}	22.5	5.82	2.13
k_P Piece-wise, variable t_e PIF	536.4	1.90×10^{-4}	22.0	5.53	2.15
Combined ROI and POI	Pearson	Spearman	Adj. R^2	Adj. R^2 robust	
k_P FmRα	0.797*	0.714	0.574	0.497	
L/P ratio	0.636	0.548	0.305	0.637	
AUC	0.888*	0.905*	0.754	0.733	
TTP	-0.970**	-1.00**	0.930	0.920	

The differential model with the Heaviside-step PIF provided the lowest AICc of the three, fitting the data significantly better than the piece-wise models. Interestingly, the penalty for allowing the end of inflow time t_e to vary as an extra free parameter within the piece-wise model, was greater than the improvement this made to the fit. It has been stated by previous users of the model that t_e should correspond to the injection length starting from t_0 [170, 297], which in the case of the rats was around 2 s. The fitted t_e calculated here was 8-10 s, which corresponded to the pyruvate peak time instead. For this reason, t_e was then fixed at the pyruvate peak time, as was the centre of the downslope for the Heaviside-step function used in the differential model. Figure 2.4b shows fits of the differential PIF model as compared to the fixed t_e piece-wise model to ROI time courses from one animal (rat 1).

In the absence of a gold standard as a comparator, it was difficult to assess the model-free parameters *in vivo*. However the differential model with a Heaviside-step PIF was used as a surrogate standard given its low AICc. Based on comparison to these calculated k_P values, the TTP significantly out-performed the other approaches and the L/P ratio performed least well, being the only method to produce no significant correlation coefficients. The AUC also correlated very well with k_P, with both correlation coefficients having p <0.005. Parameter maps for k_P were generated for each of the four rats and are shown in figure 2.5: *in vivo* parameter mapping derived from the model-based methods were largely similar and two representative examples are shown using the one-way and two-way non-PIF integral models. Unfortunately, many of the model-free parameter mapping methods were very sensitive to noise in regions of low lactate, rendering them difficult to interpret which is an inherent limitation of some of these more simplified approaches. A visual inspection of the two sets shows that both models were able to distinguish the implanted tumours from normal tissue, however the two-way maps appeared to better highlight the full tumour and offered higher contrast-to-noise, showing increased sensitivity over the one-way model. k_P values were capped at 0.25 s^{-1}, a value chosen to be suitably above those previously reported in rat tumours ($\sim$ 0.1 s^{-1}) [293]; only one rat (rat 4) had an area of very high activity greater than this. The mean tumour k_P and range were both higher with the two-way than the one-way model, and in general, the k_P maps demonstrated significant intra-tumour heterogeneity.

2.4 Discussion

Metabolic imaging with hyperpolarised ^{13}C-labelled molecules is an emerging clinical tool to non-invasively detect real-time metabolism. In order to utilise this dynamic data - either as a research technique or ultimately as a clinical tool - mathematical analysis methods are required which are sensitive to detecting the small changes in metabolism that occur during tumour growth and following treatment, whilst being insensitive to noise and artefacts. Many of the approaches used to analyse the metabolism of hyperpolarised pyruvate are analogous to the methods used in other areas of MRI research (such as DCE-MRI), as well as those used with PET. In this work, a comprehensive analysis is performed of the main quantitative techniques used to analyse hyperpolarised data, as well as some novel approaches, with the aim of determining which are the most appropriate as research tools and which may have potential for clinical application in the future. Imaging data is utilised for this study

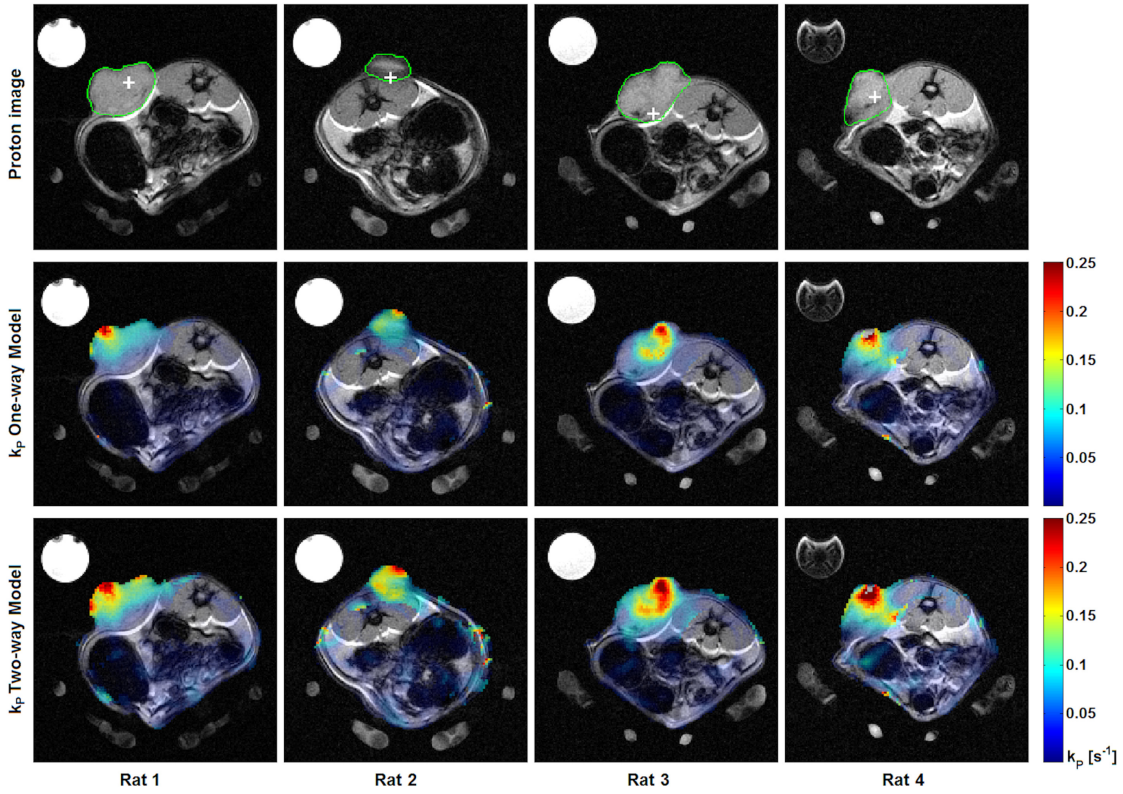

Figure 2.5: Functional parameter mapping in four rats with subcutaneous mammary adenocarcinomas demonstrating intratumoural heterogeneity. a: Grey scale anatomical proton images showing the outline of the implanted tumours defining the region-of-interest (green) and pixel-of-interest (white cross) which were used for modelling. b: False-colour functional maps of k_P calculated using the one-way integral model superimposed over the grey scale anatomical imaging. c: Similar colour maps using a two-way integral model. The maximum k_P has been limited to 0.25 s^{-1} in both cases.

rather than spectroscopic data, as this will be more applicable to patient studies and two methods of extracting the dynamic time course data from these images are compared.

The approaches studied can be divided into two groups: model-based and simpler model-free analyses. Of the four kinetic model variants, the differential and integral two-way models performed best, showing strong correlation with *in vitro* LDH enzyme concentration and producing the most accurate modelling *in vivo* (as determined by a low AICc). Furthermore, the T_1 values produced by these models, which are expected to be constant *in vitro*, had the smallest ranges and standard deviations of those tested implying good parameterisation. The one-way model is a very popular approach

because it allows for the use of Michaelis-Menten kinetics in order to solve for real, as opposed to apparent, reaction rate constants. However, this requires an assumption which is not fulfilled by the hyperpolarised exchange reaction: that the reaction has reached chemical equilibrium [300]. The one-way model was found to be unstable at higher enzyme concentrations within the physiological range, producing divergent k_P values almost three times higher than those given by the two-way models (figure 2.3c). This divergence was also seen in some of the *in vivo* data sets (figure 2.5, rat 4), and is likely to be a consequence of the approximation $k_L = 0$ which becomes less valid with increasing enzyme activity or in the presence of large pools of lactate which are freely exchanging with the pyruvate. A previous comparative study by Harrison *et al.* [223] demonstrated the shortcomings of the one-way model by showing that results from fitting to hyperpolarised data were incompatible with those from mass spectrometry data. This suggests an inconsistency between the model and the underlying biology; the breakdown of the model at high enzyme activity that is observed here provides further evidence against the use of the one-way model.

The effect of explicitly modelling the pyruvate inflow within both the differential and integral (piece-wise) models was examined. Kazan *et al* suggest modelling the PIF with a gamma-variate function which, although an excellent descriptor for the flow profile, requires accurate measurement of the arterial input function either with an invasive arterial line, or by image acquisition from a large vessel which may be difficult to obtain from human hyperpolarised data [225]. The choice was made here to look at incorporating simpler functions. From calculations of the AICc, the differential model with a Heaviside-step PIF was significantly more likely to correctly describe the data than either variant of the piece-wise model. The fitted pyruvate inflow end-time t_e in this model correlated poorly with the measured injection length; this mismatch is indicative of the difficulty in fitting theoretical arterial input functions to hyperpolarised data with a low SNR and temporal resolution. Complicated inflow functions introduce several additional free parameters which over-fit noisy data and increase the error of the derived rate constants. With the current resolution limitations for clinical hyperpolarised imaging, simple approximations for pyruvate inflow, such as those used in this study, are therefore required.

The above methodologies are desirable when accurate fitting is required for research purposes, however kinetic modelling can be computationally intensive and time consuming. Four model-free methods were tested as potential candidates for providing simple, robust parameters that are fully representative of the metabolic exchange

reaction. Such approaches may allow easy intra-patient and inter-patient comparison across clinical sites. The FmRα method described by Pagès and Kuchel [229] provided a better correlation with LDH concentration and tighter constraints on T_1 than two of the modelling methods. However in this study it was necessary to calculate α explicitly in each case, rather than using a constant value as suggested by the authors, to produce realistic results. Simpler still, and producing similar statistical results, is the AUC ratio described by Hill *et al.* [226], which is independent of the PIF. The lactate-to-pyruvate ratio at the time of maximum lactate signal was consistently the poorest method for describing the data. The final approach using TTP showed the strongest correlation with enzyme concentration *in vitro* of any analysis and the strongest correlation with k_P values derived using the differential PIF model *in vivo* of any model-free method. The small size of the *in vivo* dataset means it is not possible to claim significance of the TTP over the AUC and so further testing of these two methods on larger *in vivo* data sets is required. Nonetheless, these preliminary results along with the *in vitro* results suggest that the TTP may prove to be a very robust quantitative marker which is able to provide an equivalent assessment of metabolism to fitting a full PIF kinetic model.

Finally, two methods for extracting dynamic time course data from the images were defined and assessed for their effect on quantification. Data extracted using the region-of-interest (ROI) method provided universally stronger correlations with the *in vitro* enzyme concentrations than the pixel-of-interest method, although this was not significant in the majority of cases. Averaging results over a tumour ROI may provide a more sensitive measure of metabolic change in that region which is robust to experimental noise, however it tells nothing of the local heterogeneity nor allows for tumours outside the region to be detected in the way that pixel-by-pixel analysis could. Furthermore, determining the anatomical limits of a tumour is subjective, and therefore difficult to reproduce accurately, even if performed by the same operator using the same dataset [301, 302]. These findings suggest that extracting data from a single POI is sufficiently robust to provide a metric that reports on the whole area, and may provide a simple and reproducible method for analysing the data objectively over time. This approach is analogous to the SUV_{max} used routinely in the analysis of clinical PET data. Under normal conditions, the POI (representing the highest lactate concentration over time) will lie within the boundaries of the tumour. Although unlikely, theoretically the POI could lie outside the tumour margin if it was so poorly vascularised that the time required to perfuse the tumour was long compared to the half-life of the polarised pyruvate signal, or if the systemic

lactate level was very markedly elevated. Since single pixel analysis was shown to be sufficiently robust, parameter mapping of k_P was performed in the rats. This showed marked intratumoural heterogeneity with some areas of low exchange within the tumours and regions of high activity extending beyond the tumour boundary. Due to the spatial resolution of the ^{13}C images, it is not possible to determine whether these findings are due to artefact from partial voluming or whether there is underlying biological heterogeneity due to changes in metabolism or vascularity, although a highly heterogeneous vasculature is a known feature of the subcutaneous tumour type studied here [303]. Future human studies comparing histology to these k_P maps will be required to further understand this heterogeneity.

The rate constant k_P is generally considered to be the gold standard for quantification of hyperpolarised data, but several of the simpler non-model based approaches used here appeared to provide a good approximation to the reaction. A good probe for tumour biology should be repeatable, reproducible, quantitative, highly sensitive and highly specific. The results of this study show that k_P is a robust biomarker of LDH activity. However, at low LDH concentrations the modelling is more susceptible to noise, and at high LDH concentrations greater divergence was demonstrated which may relate to undersampling. Importantly, this work has shown that these modelling methods performed well in the physiological range and further research is required from human studies to validate this. Variation in k_P may occur secondary to other factors such as SNR, which is dependent on polarisation [304, 305], pyruvate concentration [297] and imaging protocol [306]. Therefore the optimisation and standardisation of each of these is an important step for multi-center comparison, or if k_P is to be considered as a clinical tool.

2.5 Conclusion

For accurate kinetic analysis of the hyperpolarised pyruvate-lactate exchange reaction *in vivo*, the two-way differential model with a Heaviside-step PIF centred on the pyruvate peak was best able to characterise the data with the fewest free parameters. If the data prior to the pyruvate peak are not included in the analysis, the two-way differential and integral models performed equally well and were significantly better than the one-way model in the presence of high enzyme activity or when applied to the pixel-by-pixel analysis. As a simple parameter for clinical quantification of hyperpolarised imaging data, the TTP performed best both *in vitro* and *in vivo*, providing excellent correlation with model-derived k_P values. Extracting data from

an averaged ROI may provide the most sensitivity to small changes in metabolism, however the POI approach is sufficiently robust to be applied pixel-by-pixel allowing tumour heterogeneity to be probed. This work provides a basis for analysing data from future human trials in hyperpolarised ^{13}C imaging.

Chapter 3

Unsupervised segmentation of 5D hyperpolarised ^{13}C MRI data using a fuzzy Markov random field model

Hyperpolarised MRI with ^{13}C-labelled compounds is an emerging clinical technique allowing *in vivo* metabolic processes to be characterised non-invasively. Accurate quantification of ^{13}C data, both for clinical and research purposes, typically relies on the use of region-of-interest analysis to detect and compare regions of altered metabolism. However, it is not clear how this should be determined from the five-dimensional data produced and most standard methodologies are unable to exploit the multidimensional nature of the data. In this chapter, a solution to the novel problem of ^{13}C image segmentation using a hybrid Markov random field model with continuous fuzzy logic is proposed. The algorithm fully utilises the multi-dimensional data format in order to classify each voxel into one of six distinct classes based on its metabolic characteristics. Bayesian priors fully incorporate spatial, temporal and ratiometric contextual information whilst image contrast from multiple spectral dimensions are considered concurrently by using an analogy from colour image segmentation. Performance of the algorithm is demonstrated on *in silico* data where the superiority of the approach over a reference thresholding method is consistently observed. Application to *in vivo* animal data from a pre-clinical subcutaneous tumour model illustrates the ability of the MRF algorithm to successfully detect tumour location whilst avoiding image artefacts. This work has the potential to assist the analysis of human hyperpolarised ^{13}C data in the future.

3.1 Introduction

With the increasing use of functional and molecular imaging techniques in medicine, there has been a significant increase in the size and the complexity of the data acquired. A major challenge in medical imaging is to determine the optimal use of these large data sets. For example, automated lesion identification and segmentation could greatly assist the interpretation of radiological images but is often hampered by the intrinsically noisy nature of most molecular imaging techniques when compared to conventional anatomical imaging. Hyperpolarised imaging with ^{13}C-labelled compounds is an emerging clinical technique allowing *in vivo* metabolic processes to be characterised and quantified non-invasively. The method is based on dynamic nuclear polarisation (DNP); endogenously occurring metabolites labelled with one or more ^{13}C atoms are hyperpolarised at a cryogenic temperature and within a high magnetic field, before being rapidly dissoluted using a heated fluid [152]. The molecules are able to retain liquid state polarisation for a sufficient length of time to spectroscopically image both the substrate and its metabolic breakdown products with magnetic resonance spectroscopic imaging (MRSI), following their intravenous injection into an animal or human [187].

The conversion of hyperpolarised [1-^{13}C]pyruvate to [1-^{13}C]lactate is the most intensively studied exchange reaction to date and the first molecule to be translated into the clinic. Preclinical oncological studies have shown increased lactate exchange correlating with tumour grade [170], a change in this exchange rate to be a marker of treatment response [169] and a first-in-man study in prostate cancer has demonstrated the feasibility for human imaging [156]. [1-^{13}C]pyruvate may also be metabolised to produce [1-^{13}C]alanine and ^{13}C-bicarbonate. The ability to rapidly detect small changes in metabolism *in vivo* can be applied to a number of areas within medicine including oncology, neurology [209] and cardiology [196], with a recent pilot study successfully imaging pyruvate metabolism in the healthy human heart [214].

By utilising the change which occurs in the ^{13}C frequency as metabolites interconvert, multiple metabolites can be simultaneously imaged in 3 spatial dimensions and at multiple time points with a resolution of a few seconds to generate intrinsically co-registered 5-dimensional data. Accurate and robust quantification of multidimensional ^{13}C data is imperative in order to make reliable inter- and intra-patient comparisons and many methodologies have been suggested for this purpose. Most commonly, the forward exchange rate constant k_{PL} is derived by fitting variations on the following coupled differential equations to pyruvate and lactate timecourse data

[169], [170], [219]:

$$\frac{dP}{dt} = I(t) - k_{PL}P + k_{LP}L - \rho_P P \tag{3.1}$$

$$\frac{dL}{dt} = -k_{LP}L + k_{PL}P - \rho_L L \tag{3.2}$$

where $I(t)$ is a function describing the pyruvate inflow, k_{LP} is the backwards exchange rate constant and ρ describes the polarisation loss for each metabolite due to both thermal T_1 decay and through radiofrequency excitation during sampling. Simple model-free analyses have also been shown to accurately quantify lactate exchange [226], [307]. Both the lactate/pyruvate area under the curve (AUC) ratio and the lactate time-to-peak show excellent correlation with the exchange rate model approach, albeit by producing parameters less easily linked to the underlying biological reaction [307].

Clinical imaging research has conventionally made use of regions or volumes of interest (ROI or VOI) for the analysis and quantification of areas that are pathologically abnormal in comparison to normal tissue. A VOI must be accurate, robust and repeatable, however commonly used manual delineation and thresholding techniques both often suffer from high variability, as well as susceptibility to noise and image contrast [254], making statistical segmentation methods important for the reliable processing of large imaging datasets.

Unsupervised segmentation of ^{13}C data offers a unique challenge due to its low spatial resolution, high noise, susceptibility to artefacts and its inherent 5-dimensionality, making analysis of this data using spatial contrast alone very difficult. Simple segmentation methods such as thresholding are made unsuitable by the rapidly changing temporal dynamics and spectral interdependency, whilst supervised learning methods are hampered by the lack of clinical data currently available to enable training. The use of a fuzzy Markov random field (MRF) model is proposed here, which provides a framework for segmentation which fully incorporates spatial, temporal and spectral information whilst effectively handling the low image quality currently associated with hyperpolarised MRI.

Image segmentation describes the problem of sorting a set of image pixels or voxels into a number of distinct classes. For a set $S = \{1, 2...s\}$ of image pixels, indexed by j, the MRF model considers two random fields; the observed, noise-corrupted field $Y = (Y_j)_{j \in S}$ and the underlying ground-truth field $X = (X_j)_{j \in S}$. Here, the vector of real, positive image pixel intensity values is a realisation, defined here as a particular observed configuration, $Y = \mathbf{y}$ of Y and the objective is to uncover the field

$X = \mathbf{x}$ representing the "true" image by means of iteratively optimising an objective function. Here, the realisation $\mathbf{x}$ represents the assignment vector of one of the set $\Omega = \{1, 2..., q\}$ of classes to each pixel j.

In addition to being an efficient approach for many problems, a main advantage of using an MRF model for medical image segmentation is the ability to formally incorporate multiple forms of contextual information. Modelling of local interactions between spatially and/or temporally adjacent pixels vastly reduces the influence of noise on the segmentation, as each pixel is classified based not only on its own contrast, but on the contrast of its neighbours. MRFs, and the closely related Markov random chains, have been extensively applied to segmentation problems in MRI [282], computed tomography (CT) [283] and positron emission tomography (PET) imaging [287].

A powerful way of accounting for poor image resolution is to incorporate fuzzy logic into the segmentation process. Rather than pixels being assigned to a 'hard' Boolean class, i.e. definitely tumour or definitely background with $x_j = 0$ or 1, pixels are assigned a fuzzy membership level to each class. This is similar to, although distinct from, the probability of belonging to each class and instead provides a measure of uncertainty on the true content of the pixel. Similarities between PET and hyperpolarised ^{13}C imaging include low resolution and large partial volume effects [202]. Incorporation of fuzzy logic into PET segmentation algorithms proved successful in handling these challenges by providing a more realistic description of the blurred boundaries between regions of different classes when compared to a hard Boolean approach. This is particularly apt for both PET and ^{13}C, as each large pixel is likely to contain elements of both tumour and background.

Two methodologies for applying fuzzy logic in medical image segmentation have dominated the literature; the fuzzy c-means (FCM) approach [273], [274] and the Markovian approach [308], [287]. Chatzis *et al* have proposed a hybrid FCM-MRF which combines the flexibility of the FCM model with the capacity to incorporate higher dimensional prior information of an MRF model [309]. Their framework is used as a starting point, with this work extending it to handle the 5D data produced by hyperpolarised ^{13}C MRI, using an analogy with colour image segmentation to fully incorporate the spectral dimension, in order to segment and quantify regions of interest. The primary focus is to detect the metabolism of [1-^{13}C]pyruvate to [1-^{13}C]lactate, however the capability of identifying [1-^{13}C]alanine and ^{13}C-bicarbonate production is also included.

The performance of the algorithm is initially demonstrated here on an *in silico* dataset as well as *in vivo* animal data from rats with subcutaneously implanted tumours. This work demonstrates the feasibility of applying a fuzzy MRF approach to the novel and challenging problem of hyperpolarised ^{13}C image segmentation in order to automatically detect regions of altered metabolism, thereby providing a useful tool to delineate tumour from normal tissue.

3.2 Theory

3.2.1 The MRF framework

Given a set of 2D or 3D image voxels $S = \{1, 2, ...s\}$, the objective of the MRF segmentation algorithm is to find the correct classification for each voxel which minimises a Bayesian-derived objective function, separating the image into segments displaying similar features. The input information is the observed data; the measured voxel intensity values are a realisation $Y = \mathbf{y}$, where Y is the set of all possible measurements, and the desired output is to find the correct configuration $X = \mathbf{x}$ of assigned class labels. Y and X are the 'emitted' and 'hidden' random fields respectively, where a random field is defined as having a strictly positive probability distribution:

$$p(\mathbf{x}) > 0 \qquad \forall \mathbf{x} \in X \tag{3.3}$$

An MRF is defined as any random field for which the joint probability distribution is a Gibbs (Boltzmann) distribution:

$$p(\mathbf{x}|\beta) = \frac{1}{Z} e^{-U(\mathbf{x}|\beta)} \tag{3.4}$$

Here β is the inverse temperature parameter, which is maximised at each iteration of the algorithm; in physical terms, this is equivalent to actively 'cooling' the system such that it converges to a state of minimum energy. In further analogy to statistical mechanics, Z is the partition function, defined as the sum of the numerator over every possible realisation of $\mathbf{x} \in X$.

Exact computation of the partition function becomes computationally expensive to the point of being intractable for systems with a large number of sites; it is therefore simplified here by the commonly used mean-field approximation [310]. Under this approximation, the site of interest is decoupled from the field by averaging over its external interactions with each other site to produce a single mean effect and $p(\mathbf{x}|\beta)$

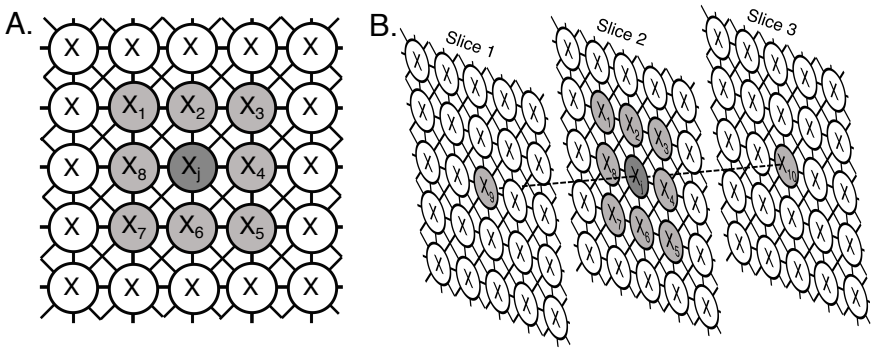

Figure 3.1: Graphical depiction of image pixels x as nodes in a Markov random field and the connections between them. A. shows the 8-neighbourhood in 2D (shown in gray) and B. the 10-neighbourhood for 3D segmentation which form the cliques on which the state of each pixel x_j will depend.

is given by:

$$p(\mathbf{x}|\beta) = \prod_{j=1}^{s} p(x_j|\hat{\mathbf{x}}_{c_j}, \beta) \tag{3.5}$$

where $\hat{\mathbf{x}}_{c_j}$ is an estimate of the class labels in the clique c_j obtained from the previous iteration of the algorithm.

The term $U(\mathbf{x}|\beta)$ in (3.4) is the energy function containing the contextual prior information. For the set of voxels $S = 1, 2, ...s$, it is possible to define a set of cliques c_l such that for each site $j \in S$, $j \in c_l$ if and only if $j \neq l$ and $l \in c_j$. This sets up the network of two-way interactions to be considered at each site; figure 3.1 depicts the 8- and 10-connectivity neighbourhoods which form the cliques considered in the 2D and 3D contexts respectively. A main advantage of MRF models is the straightforward incorporation of additional prior information by linearly adding terms to form the energy function $U(\mathbf{x}|\beta)$. Three terms are considered here with equal weighting: a spatial term $U_S(\mathbf{x}|\beta)$ utilising the network discussed above; a temporal prior $U_T(\mathbf{x}|\beta)$ testing for an expected shape profile; a ratiometric prior $U_R(\mathbf{x}|\beta)$ which tests for expected metabolite ratios. In accordance with Bayes' theorem, the joint probability of the Gibbs prior distribution for the hidden field $p(\mathbf{x})$, and the emitted field distribution $p(\mathbf{y})$ is given by:

$$p(\mathbf{x}, \mathbf{y}) = p(\mathbf{y}|\mathbf{x})p(\mathbf{x}) \tag{3.6}$$

It is reasonable to assume that the full conditional distribution can be written as the product of contributions from each individual site and that the distributions are of

multivariate Gaussian form:

$$p(\mathbf{y}|\mathbf{x}) = \prod_{j=1}^{s} p(\mathbf{y}_j|x_j) = \frac{e^{(\mathbf{y}_j-\boldsymbol{\mu}_{x_j})^{\mathrm{T}}\boldsymbol{\Sigma}_{x_j}^{-1}(\mathbf{y}_j-\boldsymbol{\mu}_{x_j})}}{\sqrt{(2\pi)^n|\boldsymbol{\Sigma}_{x_j}|}} \tag{3.7}$$

where $\mathbf{y}_j$ is the vector of measured intensity values of dimensionality n, $\boldsymbol{\mu}_{x_j}$ is the vector of means over each dimension of $\mathbf{y}_j$ defined for a given class x_j and $\boldsymbol{\Sigma}_{x_j}$ is the corresponding covariance matrix.

Substituting (3.5) and (3.7) into (3.6), then taking the negative log, provides a convenient form of the posterior probability as the objective function to be minimised. Given the set of possible classes $\Omega = \{1, 2, ...q\}$ where each x_j may take values 1 to q, the full negative log-likelihood function under the mean-field approximation takes the form:

$$L(\mathbf{x}|\mathbf{y}) = -\sum_{j=1}^{s} \log p(\mathbf{y}_j|x_j, \boldsymbol{\mu}_{x_j}, \boldsymbol{\Sigma}_{x_j}) - \sum_{j=1}^{s} \log p(x_j|\beta) \tag{3.8}$$

where the voxel-wise priors are given by:

$$p(x_j|\beta) = \frac{e^{-U(x_j|\beta)}}{\sum_{i=1}^{q} e^{-U(x_j=i|\beta)}} \tag{3.9}$$

3.2.2 The hybrid fuzzy c-means MRF model

Fuzzy c-means clustering is a simple and commonly used algorithm for separating a set of s voxels into q partitions by minimising the objective function:

$$L_\lambda = \sum_{j=1}^{s}\sum_{i=1}^{q} R_{i,j}^{\lambda} D_{i,j} \tag{3.10}$$

The 'dissimilarity function' $D_{i,j}$ describes the likelihood of voxel j belonging to a given class i, and $R_{i,j}$ is the 'fuzzy membership function', which describes the certainty of j belonging to each class i and exhibits the following properties:

$$R_{i,j} =]0, 1[\qquad \sum_{i=1}^{q} R_{i,j} = 1 \tag{3.11}$$

The parameter λ controls the level of fuzziness. Following the rationale set out by Chatzis *et al* [309], it is instructive to consider a variant of the above function which is regularised by relative entropy [311]:

$$L_\lambda = \sum_{j=1}^{s}\sum_{i=1}^{q} R_{i,j} D_{i,j} + \lambda \sum_{j=1}^{s}\sum_{i=1}^{q} R_{i,j} \log\left(\frac{R_{i,j}}{P_{i,j}}\right) \tag{3.12}$$

This version of the fuzzy objective function reverts to hard partitioning when λ=1 and the fuzzy membership function is redefined with $R_{i,j} = \{0, 1\}$. In this special case, it is possible to make a direct comparison with equation (3.8) and thus to define:

$$D_{i,j} = -\log p(\mathbf{y}_j | x_j = i, \boldsymbol{\mu}_i, \boldsymbol{\Sigma}_i) \tag{3.13}$$

$$P_{i,j} = p(x_j = i | \beta) \tag{3.14}$$

In this way it is possible to incorporate the MRF multivariate conditional distribution, as well as the MRF priors containing the desired contextual information, into the clustering framework provided by the fuzzy c-means objective function. This hybrid model can be iteratively minimised over the parameters $\beta, \boldsymbol{\mu}$ and $\boldsymbol{\Sigma}$ in order to find an optimal solution for R; the hard classification field $\mathbf{x}$ is then defined simply as the class for which R is maximised at each voxel.

3.2.3 Application to hyperpolarised ^{13}C data

The novel approach proposed in this chapter is to adapt and apply the hybrid fuzzy clustering MRF framework described above to the problem of segmenting the 5D data produced by hyperpolarised ^{13}C MRSI. Although the exact form of the data may differ depending on the imaging sequence used, it will in general consist of a set of 2D (single slice) or 3D (multi-slice) images, acquired at multiple time points and at multiple frequencies. The spectral dimension may either be acquired as a continuous spectrum, or at a number of discrete frequencies corresponding to target metabolites. The second case is considered here, which provides a separate series of images for each metabolite.

Four metabolites are considered; pyruvate (P), lactate (L), alanine (A) and bicarbonate (B), therefore at each voxel j in the 3-dimensional imaging volume, the observed intensity vector $\mathbf{y}_j$ is given by:

$$\mathbf{y}_j(t) = [P_j(t), L_j(t), A_j(t), B_j(t)] \tag{3.15}$$

To reduce the dimensionality of $\mathbf{y}_j(t)$ from $[4 \times T]$ to $[4 \times 1]$, where T is the number of imaging time points, the data were time-averaged. Only images from time points at which the total carbon signal present was greater than the minimum value plus 0.2 times the standard deviation were included in the time average. This protocol effectively removed noise images whilst retaining as much useful signal as possible. Based on the animal data, total carbon SNR was approximately 4 at this cut-off with individual metabolite SNRs considerably lower. The overall objective of the segmentation was to automatically identify regions of differing metabolism, therefore the set

of classes $\Omega = \{1, 2, 3, 4, 5, 6\}$ into which voxels were sorted was defined as follows: 1. background (no pyruvate inflow); 2. no conversion of pyruvate; 3. low conversion rate of pyruvate into lactate; 4. high conversion rate of pyruvate into lactate; 5. conversion of pyruvate into alanine; 6. conversion of pyruvate into bicarbonate. If at any point during the iterative minimisation process membership of one of these classes falls to zero, then it is removed from further calculations and $q \rightarrow q - 1$.

In conventional colour image segmentation, a multivariate Gaussian conditional distribution, as in equation (3.7), may be used to describe the separate intensities from each of the relevant dimensions of a chosen colour space; e.g. red, green and blue. Analogous with this approach, the time-averaged data here is treated as a single image with intensity contributions from four different 'colours', i.e. the four different metabolites. The conditional distribution at each voxel is then modelled by (3.7), where $\mathbf{y}_j = [P_j, L_j, A_j, B_j]$, $\boldsymbol{\mu}_i$ is the vector of corresponding means for each metabolite in relation to class i and $\boldsymbol{\Sigma}_i$ is their covariance matrix. For a given voxel j, its weighting in the calculation of the noise parameters $\boldsymbol{\mu}_i$ and $\boldsymbol{\Sigma}_i$ is dependant on its fuzzy membership to class i as given by $R_{i,j}$.

The energy function $U(x_j|\beta)$ in equation (3.9) is comprised of three parts incorporating the spatial, temporal and parametric prior information respectively:

$$U(x_j|\beta) = -\beta \left\{ U_S(x_j) + U_T(x_j) + U_R(x_j) \right\} \tag{3.16}$$

It is in general possible to incorporate any number of terms into the energy function; the three included in this work are described below.

3.2.3.1 Spatial priors

The first term in the energy function $U_S(x_j)$ describes the spatial dependency of the MRF system, and the connectivity between voxels. An 8 or 10-connectivity network is used depending on whether the image to be segmented is 2D or 3D as depicted in figure 3.1. The spatial energy is calculated as follows:

$$U_S(x_j) = -\frac{\sum_{l \in c_j} \delta(x_j - x_l)}{\text{card}(l \in c_j)} \tag{3.17}$$

where δ is the Dirac delta function defined as follows:

$$\delta = \begin{cases} 1 & \text{if } x_j = x_l \\ 0 & \text{otherwise} \end{cases} \tag{3.18}$$

The function *card* is simply the count of voxels in the clique c_j. As x_j takes each class label $1, 2, ...q$, U_S will take a minimum value of -1 when the labels of all voxels

in clique c_j match that of $x_j = i$ and a maximum value of 0 when no labels coincide. For the purpose of this calculation, the hard class labels of each voxel in the clique are defined as that which maximises the current value of the fuzzy membership function:

$$x_l = \arg\max_{i=1}^{q}(R_{i,l}) \tag{3.19}$$

This results in imposing a penalty on $x_j = i$ for not being of the same class as its immediate surroundings, therefore reducing the influence of random noise and fulfilling the requirement that voxels containing similar tissue types or metabolic features are more likely to be adjacent than separate. The spatial priors also prevent small regions of noise being picked up as false positives by making it energetically unfavorable to have many small ROIs.

3.2.3.2 Temporal priors

Although the algorithm uses a time-averaged version of the data, the temporal information is preserved through its incorporation into the prior on each voxel. The changes in the local concentrations of each of the four metabolites of interest can be described by the following set of ordinary differential equations:

$$\frac{dP}{dt} = I(t) - (k_{PL} + k_{PA} + k_{PB})P + k_{LP}L - \rho_P P \tag{3.20}$$

$$\frac{dL}{dt} = -k_{LP}L + k_{PL}P - \rho_L L \tag{3.21}$$

$$\frac{dA}{dt} = k_{PA}P - \rho_A A \tag{3.22}$$

$$\frac{dB}{dt} = k_{PB}P - \rho_B B \tag{3.23}$$

where $I(t)$ is the pyruvate inflow profile, k_{AB} is the rate of metabolic conversion form metabolite A to metabolite B, and ρ_A is the rate of polarisation loss of metabolite A. Values for ρ can be estimated from the known thermal decay rates and imaging parameters, whereas the k terms are unknowns to be solved. Nevertheless, the solutions to these equations have distinct expected forms, which are of similar shape regardless of the exact values of the conversion rates.

Measured temporal profiles for the relative concentrations of each metabolite at voxel j are stored in $\mathbf{y}_j(t)$. To assess whether these time profiles are likely to represent real signal, their shape is compared to a set of trial functions which form the solutions to the above differential equations [307]. Six trial functions are used for each metabolite, varying the k_{AB} and, for pyruvate, the inflow speed contained in the function $I(t)$. Both the measured signal and trial functions are normalised to [0,1],

the positions of the peaks are aligned and the R^2 is calculated to test goodness of fit to each of the six trial functions. The highest R^2 is then selected for inclusion in the temporal prior function.

For a given voxel j, the priors for each class i for metabolite X can then be defined as follows:

$$P_{X,i,j} = \frac{f_i(R^2_{X,j})}{\sum_{i=1}^{q} f_i(R^2_{X,j})} \tag{3.24}$$

Here, the function $f_i(R^2_{X,j})$ takes two different forms dependant on the expectation of that metabolite in each class. When no signal is expected from a particular metabolite, $f^-_{X,j} = 1 - (R^2_{X,j})^3$, whereas $f^+_{X,j} = (R^2_{X,j})^3$ if signal is required for inclusion of a voxel into a particular class. The cube is used to produce a sharper distinction between signal and noise. Explicitly, where each column in the row vector is a class 1 to 6, then the following apply:

$$P_{P,j} = [f^-_{P,j}, f^+_{P,j}, f^+_{P,j}, f^+_{P,j}, f^+_{P,j}, f^+_{P,j}] \tag{3.25}$$

$$P_{L,j} = [f^-_{L,j}, f^-_{L,j}, f^+_{L,j}, f^+_{L,j}, f^-_{L,j}, f^-_{L,j}] \tag{3.26}$$

$$P_{A,j} = [f^-_{A,j}, f^-_{A,j}, f^-_{A,j}, f^-_{A,j}, f^+_{A,j}, f^-_{A,j}] \tag{3.27}$$

The polarisation decay rate of bicarbonate is too fast to define appropriate test functions, therefore only pyruvate, lactate and alanine are included in the temporal prior. Finally, the normalised contribution to the energy function is given by:

$$U_T(x_j = i) = -\frac{P_{P,i,j} P_{L,i,j} P_{A,i,j}}{\sum_{i=1}^{q} P_{P,i,j} P_{L,i,j} P_{A,i,j}} \tag{3.28}$$

3.2.3.3 Parametric priors

The final contribution to the energy function considers ratios of the metabolites observed at each voxel and also utilises the full temporal data set. Using the time curve for each metabolite, it can be shown that the ratio of Areas Under the Curve (AUC) for lactate and pyruvate is equal to [226]:

$$R_{LP} = \frac{AUC_{Lactate}}{AUC_{Pyruvate}} = \frac{k_{PL}}{k_{LP} + \rho_L} \tag{3.29}$$

What is striking about this result is that it is completely independent of the pyruvate inflow function $I(t)$. Furthermore, since $k_{PL} \gg k_{LP}$ and ρ_L is expected to be consistent, this simple metric correlates reasonably well with the forward rate conversion constant k_{PL} [307].

AUC ratio maps were calculated for lactate, alanine and bicarbonate, relative to pyruvate. Values >2 were set to this maximum value, the upper limit expected from a true signal, to avoid random noise in the background region skewing the results. Each map was then normalised by dividing by its maximum value. Individual metabolite priors were then constructed from the ratio maps:

$$P_{XP,i,j} = \frac{f_i(R_{XP,j})}{\sum_{i=1}^{q} f_i(R_{XP,j})} \tag{3.30}$$

The following main changes to the functions f_i used in the temporal case are noted. Firstly, the background class 1 is noise so does not depend on the AUC ratios; this was set such that $P_{XP,1,j} = 1/6$ after normalisation. Secondly, the low lactate class, class 3, requires a negative quadratic response as the lactate/pyruvate AUC increases. The normalised ratiometric contribution to the energy function is given by:

$$U_R(x_j = i) = -\frac{P_{LP,i,j}P_{AP,i,j}P_{BP,i,j}}{\sum_{i=1}^{q} P_{LP,i,j}P_{AP,i,j}P_{BP,i,j}} \tag{3.31}$$

Although there are multiple parametric approaches which could be included as prior information, the AUC ratio was chosen because of its rapid calculation speed, insensitivity to pyruvate inflow profile, full usage of temporal data and its dual treatment of metabolite signals, which separates metabolic conversion from perfusion. It is the latter of these which provides the most important additional information for the segmentation process.

3.2.4 Initialisation

Given that each class in the ^{13}C segmentation is required to exhibit specific predefined metabolic properties, initialisation was performed using a Bayesian maximum posterior likelihood method using thresholded, time-averaged metabolite images to estimate initial class means and variances and incorporating previously calculated ratiometric and temporal maps for the Bayesian priors. Estimates for the background class noise parameters $\boldsymbol{\mu}_1$ and $\boldsymbol{\sigma}_1$, the 4-metabolite mean and standard deviation vectors respectively, were obtained from the final metabolite images in the time series, by which time all the signal has decayed. These parameters were then used to determine whether each voxel in the time-averaged data set, with measured signal intensity $\mathbf{y}_j = [y_{P,j}, y_{L,j}, y_{A,j}, y_{B,j}]$, contained signal significantly above the noise level.

The following initial thresholding was used to find mean and variance estimates for each class, where L_{max} is the maximum lactate signal intensity in the time-averaged image:

1. Background class: $y_{P,j} < \mu_{P,1} + 5\sigma_{P,1}$
2. No exchange: $j \notin 1, 5, 6$ and $y_{L,j} < \mu_{L,1} + 5\sigma_{L,1}$
3. Low lactate exchange: $j \notin 1, 4$ and $y_{L,j} \geq \mu_{L,1} + \quad 5\sigma_{L,1}$
4. High lactate exchange: $j \notin 1$ and $y_{L,j} \geq \mu_{L,1} + 5\sigma_{L,1} + \quad 0.8(L_{max} - \mu_{L,1} + 5\sigma_{L,1})$
5. Conversion to alanine: $j \notin 1, 3, 4$ and $y_{A,j} \geq \mu_{A,1} + 5\sigma_{A,1}$
6. Conversion to bicarbonate: $j \notin 1, 3, 4, 5$ and $y_{B,j} \geq \mu_{B,1} + \quad 5\sigma_{B,1}$

From these initial voxel groupings, mean $\boldsymbol{\mu}'_i$ and covariance $\boldsymbol{\Sigma}'_i$ are calculated for each class as the inputs into a multivariate normal distribution, $\mathcal{N}(\boldsymbol{\mu}'_i, \boldsymbol{\Sigma}'_i)$. The final initialisation is given by the class which for each voxel maximises the Bayesian posterior:

$$x'_j = \arg\max_{i=1}^{q} \frac{P'_{i,j}\mathcal{N}_j(\boldsymbol{\mu}'_i, \boldsymbol{\Sigma}'_i)}{\sum_{k=1}^{q} P'_{k,j}\mathcal{N}_j(\boldsymbol{\mu}'_k, \boldsymbol{\Sigma}'_k)} \tag{3.32}$$

Where $P'_{i,j}$ is an initial prior constructed in the same way as $P_{i,j}$ but with the spatial term omitted. An initial estimate of 3 was used for the temperature parameter β and the fuzziness parameter λ was set to 3 throughout. This value was chosen to provide a satisfactory trade-off between underestimating the region size and producing false positives; λ may be optimised further when additional clinical data becomes available.

3.2.5 Iterative determination of the hidden field x

Having defined the constituent parts of the objective function (3.12) and the procedure for initialisation in the context of the segmentation of ^{13}C imaging data, it is possible to define the iterative process with which the hidden field $\mathbf{x}$ is determined. The procedure for the most part follows that described by Chatzis *et al* [309] and is outlined below.

The full objective function to be minimised at each iteration w is given by:

$$L_\lambda^{(w)} = \frac{1}{2}\sum_{j=1}^{s}\sum_{i=1}^{q} R_{i,j}^{(w)}\{n\log(2\pi) + \log(|\boldsymbol{\Sigma}_i^{(w)}|) + (\mathbf{y}_j - \boldsymbol{\mu}_i^{(w)})^{\mathrm{T}}\boldsymbol{\Sigma}_i^{(w)^{-1}}(\mathbf{y}_j - \boldsymbol{\mu}_i^{(w)})\} + \lambda\sum_{j=1}^{s}\sum_{i=1}^{q} R_{i,j}^{(w)}\log\left(\frac{R_{i,j}^{(w)}}{P_{i,j}^{(w)}}\right) \tag{3.33}$$

Therefore at each step, the priors $P_{i,j}$, the noise parameters $\boldsymbol{\mu}_i$ and $\boldsymbol{\Sigma}_i$, the fuzzy membership function $R_{i,j}$ and the temperature parameter β must all be updated. Given some initial estimate of the hidden field $\mathbf{x}^{(w)}$ at iteration w, the priors $P_{i,j}^{(w)}$ are calculated as follows:

$$P_{i,j}^{(w)} = \frac{e^{\beta^{(w)}\{U_S(x_j=i|c_j^{(w)}) + U_T(x_j=i) + U_R(x_j=i)\}}}{\sum_{k=1}^{q} e^{\beta^{(w)}\{U_S(x_j=k|c_j^{(w)}) + U_T(x_j=k) + U_R(x_j=k)\}}} \tag{3.34}$$

Here $c_j^{(w)}$ denotes the current estimate of the hard class labels for voxels in the clique c_j. These are determined by choosing the value for each $x_l \in c_j$ which maximises the fuzzy membership function $R_{i,j}^{(w)}$ according to equation (3.19). Only the spatial term in the energy function $U(x_j|\beta)$ is updated, along with the temperature parameter β, at each iteration.

Given initial estimates of the noise parameters at w, $D_{i,j}^{(w)}$ is defined as the negative-log of the multivariate Gaussian conditional distribution, equation (3.7):

$$D_{i,j}^{(w)} = \frac{1}{2}\{n\log(2\pi) + \log(|\boldsymbol{\Sigma}_i^{(w)}|) + (\mathbf{y}_j - \boldsymbol{\mu}_i^{(w)})^{\mathrm{T}}\boldsymbol{\Sigma}_i^{(w)^{-1}}(\mathbf{y}_j - \boldsymbol{\mu}_i^{(w)})\} \tag{3.35}$$

The value of the fuzzy membership function can now be computed for the subsequent iteration $w+1$:

$$R_{i,j}^{(w+1)} = \frac{P_{i,j}^{(w)} e^{-\frac{D_{i,j}^{(w)}}{\lambda}}}{\sum_{k=1}^{q} P_{k,j}^{(w)} e^{-\frac{D_{k,j}^{(w)}}{\lambda}}} \tag{3.36}$$

This function is derived by minimising the objective function L_λ with respect to $R_{i,j}$ subject to the constraint:

$$\sum_{i=1}^{q} R_{i,j} = 1 \qquad \forall j \in S \tag{3.37}$$

This can be achieved by introducing a Lagrange multiplier ψ_j to enforce the constraint at each voxel $j \in S$ and then setting the partial derivative of the resulting Lagrangian equal to zero:

$$\frac{\partial}{\partial R_{i,j}}\{L_\lambda - \sum_{j=1}^{s}\psi_j(\sum_{i=1}^{q} R_{i,j} - 1)\} = 0 \tag{3.38}$$

Similarly, setting the partial derivative of L_λ with respect to each of $\boldsymbol{\mu}_i$ and $\boldsymbol{\Sigma}_i$ to zero, yields the following update functions for the noise parameters at $w+1$:

$$\boldsymbol{\mu}_i^{(w+1)} = \frac{\sum_{j=1}^{s} R_{i,j}^{(w)}\mathbf{y}_j}{\sum_{j=1}^{s} R_{i,j}^{(w)}} \tag{3.39}$$

$$\boldsymbol{\Sigma}_i^{(w+1)} = \frac{\sum_{j=1}^{s} R_{i,j}^{(w)}(\mathbf{y}_j - \boldsymbol{\mu}_i^{(w)})(\mathbf{y}_j - \boldsymbol{\mu}_i^{(w)})^{\mathrm{T}}}{\sum_{j=1}^{s} R_{i,j}^{(w)}} \tag{3.40}$$

The final step is to find the new value for the inverse temperature $\beta^{(w+1)}$ according to:

$$\beta^{(w+1)} = \arg\max_{\beta} \sum_{j=1}^{s}\sum_{i=1}^{q} R_{i,j}^{(w)} \log(P_{i,j}^{(w)}) \tag{3.41}$$

Maximising β in this way fine-tunes the system to become maximally sensitive to the value of the energy function $U(\mathbf{x}|\beta)$, therefore globally forcing the system into

the state of lowest energy based on the definition of $U(\mathbf{x}|\beta)$. There is now sufficient information to calculate the updated value of the objective function $L_\lambda^{(w+1)}$. This was compared at each step with the value of $L_\lambda^{(w)}$ and convergence was defined as having reached a stable value of $\Delta L_\lambda = |L_\lambda^{(w+1)} - L_\lambda^{(w)}|/L_\lambda^{(w)} < c_T$ with c_T, the convergence threshold, set at 0.1.

In summary, the full iterative procedure for the segmentation of ^{13}C imaging data is as follows:

1: **Input:** 5D ^{13}C imaging data
2: Calculate temporal coherence maps and value of temporal energy function $U_T(\mathbf{x})$ for each voxel j in the 3D volume
3: Calculate AUC ratio maps and parametric energy function $U_R(\mathbf{x})$
4: Use initialisation procedure to establish initial estimates of $R_{i,j}^{(0)}$, $x_j^{(0)}$, $\boldsymbol{\mu}_i^{(0)}$ and $\boldsymbol{\Sigma}_i^{(0)}$, and thus calculate $L_\lambda^{(0)}$
5: Set iteration number $w = 1$
6: **while** $\Delta L_\lambda > c_T$ **or** $w < 150$ **do**
7: Calculate the new temperature parameter $\beta^{(w)}$ using $R_{i,j}^{(w-1)}$ and $P_{i,j}^{(w-1)}$ with equation (3.41)
8: Update the values of fuzzy membership function $R_{i,j}^{(w)}$ from $D_{i,j}^{(w-1)}$ and $P_{i,j}^{(w-1)}$ using the formula given by (3.36)
9: Calculate the updates to the noise parameters $\boldsymbol{\mu}_i^{(w)}$ and $\boldsymbol{\Sigma}_i^{(w)}$ using (3.39) and (3.40) respectively
10: Calculate the current realisation of $x_j^{(w)}$ from fuzzy membership function $R_{i,j}^{(w)}$ using equation (3.19)
11: Calculate the current value of voxel-wise priors $P_{i,j}^{(w)}$ using $x_j^{(w)}$ and $\beta^{(w)}$
12: Find the new value of the objective function $L_\lambda^{(w)}$
13: Calculate $|L_\lambda^{(w)} - L_\lambda^{(w-1)}|/L_\lambda^{(w-1)}$ and test for convergence
14: $w \rightarrow w + 1$
15: **end while**
16: **Return:** Hidden field $\mathbf{x}$ of voxels segmented into q classes

The fuzzy MRF algorithm was written and implemented in Matlab (MathWorks, Natick, MA, USA). The algorithmic runtime is dependent on the image size, number of image slices and number of classes detected during the initialisation process. For 128×128 single slice images, the computational runtime is 42-117 s for 4-6 classes as measured with a 2.2 GHz Intel Core i7 processor and 8 GB RAM. This stated time is for processing the raw reconstructed 5D image tensor, including all parametric map calculations. Computational complexity scales linearly with the number of image

slices but in practice, this is rarely greater than 4. The algorithm was not optimised for speed, so further reductions in this runtime will be possible.

3.3 Data acquisition and analysis

3.3.1 *In silico* data generation

In order to quantitatively assess the accuracy of the segmentation algorithm, an *in silico* ^{13}C dataset consisting of 27 sets of images was generated. Each set had the following properties, chosen to resemble those of the animal data: 2 spatial dimensions, with 128×128 voxels in each image; 16 time points and 4 s temporal resolution; 4 metabolites. Each set contained regions corresponding to classes 1-6. Metabolite signals were generated by solving equations (3.20-3.23) at each voxel location over time with the following parameterisation; $\rho_P = \rho_L = \rho_A = 0.064$; $\rho_B = 0.131$; $k_{PL} = 10k_{LP}$; and the pyruvate inflow function:

$$I(t) = k_I \left(\frac{1}{1 + e^{-(t-t_s)}} - \frac{1}{1 + e^{-0.4(t-t_e)}} \right) \tag{3.42}$$

Where t_s is the inflow start time and t_e the inflow end time. These were set to increase gradually with distance from a main 'supply vessel' with a fixed difference of 4 s, and the inflow rate k_I decreased from a maximum value at this same point. To evaluate the performance of the segmentation under different conditions, three parameters were varied across the dataset. Firstly, to assess the detection of differently sized metabolic regions of interest, the mean radius of the high lactate conversion region was ascribed values of 3, 6 and 9 voxels and the surrounding low conversion zone mean radius set to be 2.4 times larger. Alanine and bicarbonate regions had a variable size between these two. Secondly, to assess the effects of variable metabolic conversion rates, each k_{PX} was varied across the entire image, decreasing outwards from a centre point which took values; $k_{PL,max}$ = 0.01, 0.03, 0.05; $k_{PA,max}$ = 0.008, 0.012, 0.016; $k_{PB,max}$ = 0.01, 0.014, 0.018. k_{PX} maps were set to zero everywhere except within the test regions. For the lactate map, the outer low conversion region had a multiplier of 0.14 applied to the k_{PL}. Finally, the effect of varying the SNR, qualitatively equivalent to differing initial polarisation, was investigated by varying the inflow rate k_I over arbitrary units of 9000, 12000 and 16000, corresponding to a mean pyruvate SNR of approximately 20, 30 and 40 within the high conversion zone. To mimic the partial voluming and noise corruption characteristic of *in vivo* data, image resolution was first reduced to 32×32, the nominal matrix resolution of the imaging, by grouping

the pixels into 4×4 bins and taking the mean. Random Gaussian noise with a variable random mean of 220-410 and variance of 1.1-6.3×10^4 was then applied to each image, before artificially increasing the resolution to 128×128 using the *imresize()* function in MATLAB with the default bicubic interpolation kernel. The noise parameters were chosen by measuring the mean and variance of pixels in real images containing only noise such as those from the end of an acquisition. This procedure produced signal spread and patterns of noise similar to the *in vivo* data.

3.3.2 *In vivo* data acquisition

The segmentation algorithm was tested on previously published data from four tumour-bearing adult rats with subcutaneous mammary adenocarcinomas [293], [176]. Briefly, [1-^{13}C]Pyruvic acid was hyperpolarised to approximately 25% in a Hypersense hyperpolariser (Oxford Instruments). The final solution contained 80 mM [1-^{13}C]pyruvate at pH 7.6 and physiological temperature and osmolarity. This was injected into a tail vein inside the MRI scanner at a rate of approximately 0.2 ml/s and at a dose of 2.5 ml/kg and dynamic imaging was performed from the time of injection.

Animals were imaged in a clinical 3 T MRI system (Signa HDx, GE Healthcare) using a ^{13}C-^{1}H multinuclear birdcage coil. IDEAL spiral CSI acquisition [182] was performed through four axial 10 mm slices over 1 min with a temporal resolution of 4 s and a flip angle of 10°. Other parameters were: repeat time (TR) 500 ms; field of view 80 mm and nominal matrix resolution 32×32. Gaussian k-space filtering was applied during post-processing, interpolating from a real resolution of about 5×5 mm^2 to an effective image resolution of 0.625×0.625 mm^2. For anatomical reference, standard gradient echo proton images were acquired from the same slice geometry and FOV (resolution 256×256, slice thickness 3 mm, spacing 7 mm, echo time (TE) 10 ms, TR 500 ms).

3.4 Results

3.4.1 Statistical results on *in silico* data

The fuzzy MRF segmentation algorithm was applied to each of the 27 4-dimensional *in silico* image sets described above. The data set was designed to test the limits of the algorithm and asses its ability to distinguish two separate regions: region A was defined as the total area of lactate production (class 3 + class 4); region B, high lactate production region only (class 4). In both cases, all other classes are considered

background with the known input k_{PL} map for each *in silico* image providing the gold standard for comparison. Performance of the algorithm was compared to that of thresholding the time-averaged lactate image at 40, 50, 60, 70 and 80% of the maximum lactate value; a comparison standard chosen for its clinical applicability. The same time-averaging as for the MRF segmentation was applied. To quantify performance, the Precision (positive predictive value) and Recall (sensitivity) for this binary case were calculated; these can be combined to produce the balanced F-score for the segmentation as follows:

$$Precision = \frac{tp}{tp + fp} \tag{3.43}$$

$$Recall = \frac{tp}{tp + fn} \tag{3.44}$$

$$F = \frac{2PR}{P + R} \tag{3.45}$$

where tp stands for "true positives", the count of voxels correctly identified as tumour when compared to the gold standard, fp are "false positives" and fn are "false negatives". The F-score for the full segmentation into six classes was calculated using the averages of the precision and recall over each class, with instances where the algorithm failed to detect a region still included in this score. As an additional measure of accuracy, the classification error (CE) was calculated in addition to the F-score. It is defined as:

$$CE = \frac{100(fp + fn)}{\text{no. pixels in region}} \tag{3.46}$$

where fn are "false negatives", pixels incorrectly labelled as background, and a CE closer to zero denotes a more accurate segmentation. The results from calculating both metrics over each region A and B for all segmentations are shown in table 3.1. The mean values for all 27 images, as well as the maximum and minimum in each set, are given.

In every instance, the MRF segmentation performs, on average, better than thresholding for binary segmentation of both tumour regions A and B. In almost every case, the MRF method produced the highest minimum and maximum F-scores, as well as the lowest minimum and maximum classification errors, suggesting that it is a more robust methodology than thresholding the lactate image at any level. Exceptions to this are the maximum lower CEs produced by the high threshold levels for the small region B. In general, both the MRF algorithm and the reference thresholding methods were better able to detect region B than A due to class 3 being very close to the noise floor as evidenced by figure 3.2C and I. Considering the full segmentation

Table 3.1: Comparison of performance between MRF algorithm and different thresholding levels (as % of maximum lactate) for the detection of two separate regions A and B.

		MRF	40%	50%	60%	70%	80%
F-score	Mean	0.694	0.490	0.402	0.329	0.251	0.155
(A)	Min	0.284	0.028	0.048	0.247	0.182	0.081
	Max	0.938	0.840	0.630	0.548	0.462	0.317
F-score	Mean	0.895	0.758	0.864	0.870	0.788	0.571
(B)	Min	0.613	0.006	0.011	0.120	0.692	0.355
	Max	1.000	1.000	0.997	0.982	0.949	0.844
CE	Mean	43.70	497.8	214.4	89.98	85.65	91.54
(A)	Min	12.09	29.87	62.64	63.32	72.73	82.25
	Max	83.47	6795	3662	344.6	90.02	95.80
CE	Mean	27.30	2157	700.5	71.95	34.814	59.42
(B)	Min	0.000	0.000	0.694	3.472	9.722	28.57
	Max	126.5	32030	17230	1463	47.14	78.45

Table 3.2: F-scores and classification errors for each of the six classes, excluding instances where a class is empty. Exclusions by class; class 4, 8; class 5, 1; and class 6, 7 out of 27 images.

F-score	Class 1	Class 2	Class 3	Class 4	Class 5	Class 6
Mean	0.947	0.975	0.475	0.400	0.583	0.812
Min	0.919	0.932	0.011	0.000	0.527	0.714
Max	0.974	0.991	0.598	0.552	0.639	0.921
CE	Class 1	Class 2	Class 3	Class 4	Class 5	Class 6
Mean	10.41	5.053	58.84	75.91	43.62	45.31
Min	5.157	1.839	20.14	31.31	15.99	16.92
Max	17.49	14.37	246.9	136.7	79.41	80.23

into 6 classes, the mean F-score was 0.798 with a range of 0.547-0.882. Figure 3.2A illustrates the variation in calculated F-score as the simulation parameters are varied. Low scores indicate that one or more classes failed to be detected. In 8 instances, only the inner high lactate region was detected and marked as class 3 with class 4 empty. Although this is damaging to the statistical results, it is technically not an incorrect result to see low lactate production labelled as such; the k_{PL} was just 0.01 in all but one of these cases. In a clinical setting, it is advantageous that the algorithm can correctly detect a area of low conversion to lactate whilst separating the region

from a noisy, very low conversion background. Background lactate is often present, particularly in organs such as the brain or in the muscles, but should be ignored by the segmentation. There were no cases in which region B was not detected at all and no false positives. In 1 case the alanine class and in 7 cases the bicarbonate class failed to be detected. Lower sensitivity to these metabolites has been chosen to avoid false positives which, although not detected in the *in silico* data, are common for *in vivo* data. Table 3.2 shows class by class F-score and CE results. Empty classes are omitted from the mean calculations.

3.4.2 *In vivo* results

Application of the MRF segmentation algorithm to *in vivo* imaging was demonstrated on 5D data from four rats with subcutaneous implanted tumours. Figure 3.3 shows the single-slice segmentation results for three rats alongside the corresponding ^{13}C-pyruvate, ^{13}C-lactate and ^{1}H anatomical images. The same time-averaging is used for these images as for the segmentation algorithm. In each case, the tumour location is correctly detected and dual-labelled between low and high lactate classes demonstrating the feasibility of the algorithm to identify tumour heterogeneity.

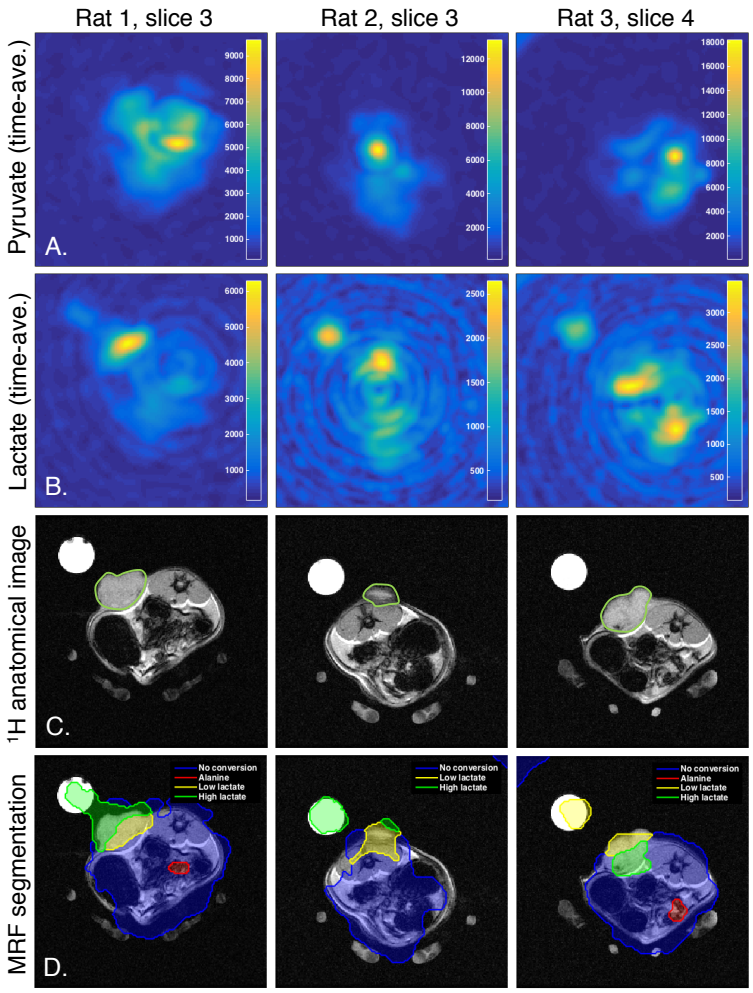

Figure 3.3: A single axial image slice centred on the tumour is shown for 3 rats. A. Time-averaged pyruvate over each slice; B. Time-averaged lactate; C. Anatomical reference image with tumour location outlined in green; D. MRF segmentation results showing background class 1 (no colour) no-conversion class 2 (blue), low conversion class 3 (yellow), high conversion to lactate class 4 (green) and alanine class 5 (orange). Class 6 is empty. Lactate phantom in upper left corner.

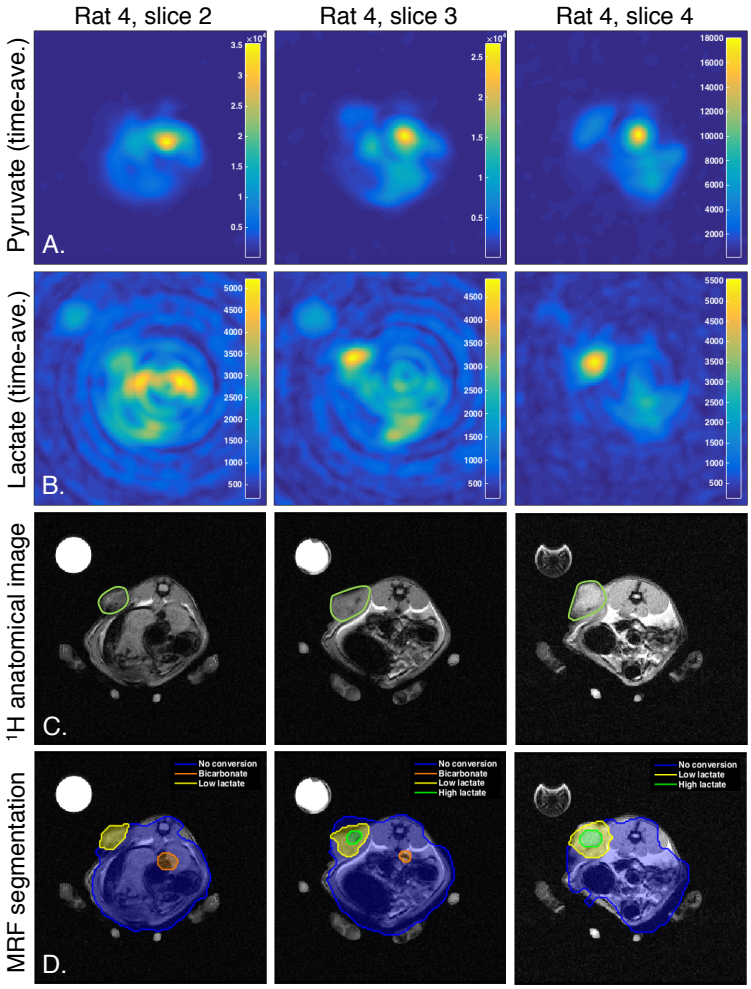

Figure 3.4: Three consecutive tumour-bearing slices from rat 4 are shown, with slice 1 cranial in orientation. A. Time-averaged pyruvate over each slice; B. Time-averaged lactate; C. Anatomical reference image with tumour location outlined in green; D. MRF segmentation results showing background class 1 (no colour) no-conversion class 2 (blue), low conversion class 3 (yellow), high conversion to lactate class 4 (green) and bicarbonate class 6 (orange). Class 5 is empty. Lactate phantom in upper left corner.

The only false positives to be detected were the lactate phantoms; the close proximity to the large tumour in rat 1 has caused joining of these regions, highlighting a current limitation of the algorithm. Although the alanine detected in rat 1 is likely to be a false positive from an overlying artery, in rat 3 it points to real signal from the muscle. Four image slices were acquired for each animal, however only one rat had a tumour which spanned multiple slices allowing for a demonstration of the 3D capabilities of the algorithm. The resulting segmentation of the three tumour-containing slices for this rat are shown in figure 3.4. Poor image quality due to artefacts is a

common problem with current ^{13}C imaging methods; it is therefore crucial to demonstrate the ability of the proposed MRF algorithm to distinguish high contrast artefacts from real tissue metabolism. Despite the low spatial resolution and spiral artefact, particularly in the lactate image where the artefact intensity is comparable to that of the tumour, the algorithm performs well and correctly identifies the tumour in each slice with no false positives. A small area of bicarbonate production was also detected (shown in orange on figure 3.4D); while this may be real, it may also be artefactual, caused by signal overspill from the very high pyruvate signal in the overlying artery. Finally, it is worth noting that the lactate phantom, seen as the bright circle in the top left of figure 3.4C-D, has been correctly classified as part of the background despite the increased lactate signal it generates. Taken together, the *in silico* and *in vivo* results suggest that the model is able to distinguish areas of low from high metabolism. Future correlation of hyperpolarised images with histology will determine how accurately this variation corresponds to true biological variation.

3.5 Conclusion

A fuzzy Markov random field approach has been presented as the first example of a segmentation algorithm designed for handling 5D hyperpolarised ^{13}C data. The method fully utilises the multi-dimensional format of the data in order to classify each voxel into one of six distinct classes based on its metabolic characteristics. Conversion of ^{13}C-pyruvate into downstream metabolites ^{13}C-lactate, ^{13}C-alanine and ^{13}C-bicarbonate, in addition to no-conversion and no-perfusion regions, are considered in this work, however the approach could be applied to other hyperpolarised ^{13}C-labelled molecules in the future. Unlike a hard classification algorithm, the suggested approach uses continuous fuzzy logic to effectively analyse the low resolution, noisy images by retaining information about the true contents of each voxel throughout the segmentation process. Contextual information on each voxel is handled by Bayesian priors describing spatial, temporal and ratiometric dependencies, whilst the use of a multivariate Gaussian conditional distribution allows image contrast from multiple spectral dimensions to be considered concurrently.

When tested on an *in silico* dataset which varied parameters such as the SNR, metabolic conversion rate constant and lesion radius, the MRF approach significantly out-performed the reference thresholding methodology at all five thresholding levels tested. There were no cases in which the algorithm failed to detect the region of high metabolic conversion of pyruvate to lactate and only a small number in which the

low conversion region was not detected despite the lactate signal being barely visible above the noise floor in these image sets. Application to *in vivo* data from rats with subcutaneously implanted tumours demonstrated the ability of the algorithm to successfully segment regions of varying metabolic activity in three spatial dimensions. The anatomical tumour location was correctly identified in each occasion, whilst detection of high lactate signal from imaging artefacts was avoided.

Since the algorithm takes imaging parameters including the TR, temporal resolution and flip angle as inputs, it should be robust to changes in these parameters. Future work will look more closely at these and other dependencies by testing the algorithm for robustness against different spatial resolutions and image sequences, as well as developing the capability to effectively handle sequences with multiple or variable flip angles. Another avenue for future development will be incorporating prior information from the co-registered anatomical ^{1}H images into the segmentation process to improve accuracy. In the anatomical rat images used in this work, background and lactate phantoms form clearly defined regions which may be detected using existing segmentation algorithms tailored to proton MRI. Although this may not be appropriate for all human applications, (deep tissue imaging of the liver or ovaries for example) there are certainly areas such as the brain where the clear division between tissue and background would allow for easy incorporation of proton image derived priors. The capability to automatically detect and exclude phantoms as part of the MRF segmentation is a further point for development.

The method of applying Gaussian white noise to corrupt the *in silico* dataset is intended to be as general as possible, thereby making the results applicable to multiple imaging sequences. However, this comes at the expense of generating artefacts more closely aligned to those produced by the IDEAL spiral sequence used to collect the *in vivo* data. A useful extension of this work would be to examine the effects of the spiral artefact on the segmentation by generating data in the following way. Begin by Fourier transforming the uncorrupted metabolite data generated into the frequency domain; add Gaussian noise; Fourier transform back and zero-fill the truncated data to artificially increase the resolution back to 128×128. This methodology should better simulate the effects of the point spread function and spiral artefact and would provide a controlled means of testing the accuracy of the MRF segmentation in the presence of these effects.

Hyperpolarised imaging with ^{13}C-labelled compounds is an established research field and an emerging clinical technique allowing metabolism to be characterised *in vivo*. Highly accurate quantification of the multidimensional data produced is an

ongoing research objective and the success of this technique as a clinical tool depends on the ability to detect and quantify these changes in metabolism. ROI or VOI analysis is an integral part of this process and the fuzzy MRF approach presented here is capable of efficiently providing this analysis in a way that is repeatable and accurate. This novel methodology for analysing pyruvate metabolism could be applied to other metabolites and clinical imaging in the future and provides a first solution to the problem of hyperpolarised ^{13}C image segmentation.

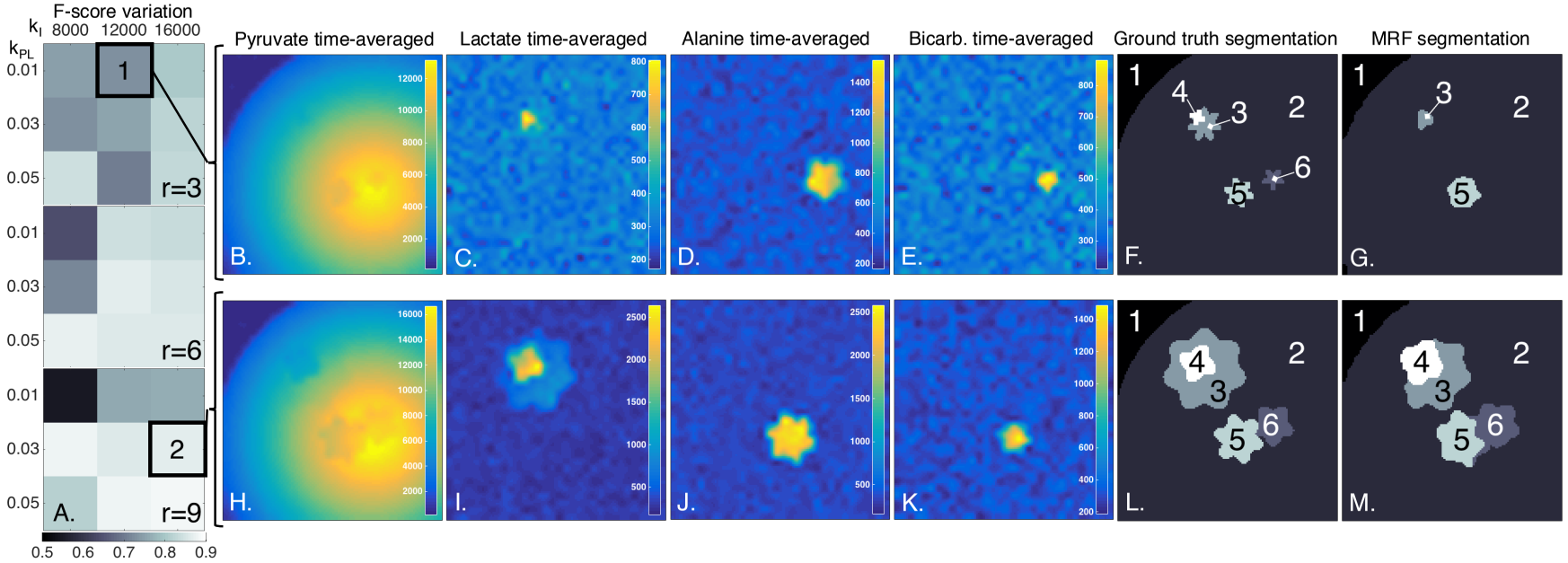

Figure 3.2: Performance of the MRF algorithm on *in silico* data. Part A. Variation in F-score as the inow constant k_I and rate constant k_{PL} are increased for a mean inner lesion radius of 3 (top), 6 (middle) and 9 (bottom) image voxels. Further images from two representative sets labelled 1 (B-G) and 2 (H-M) on part A are shown. These are: the time-averaged pyruvate (B, H); time-averaged lactate (C, I); time-averaged alanine (D, J); time-averaged bicarbonate (E, K); ground-truth segmentation (F-L) and MRF segmentation (G, M). The numbers 1-6 labelling the latter two of these denote the six classes.

Chapter 4

A mathematical model of tumour-stroma metabolic coupling in metastatic ovarian cancer

Ovarian cancer is a highly heterogeneous and metabolically active disease which is often already metastatic by the time of diagnosis. Metastatic patterns are predictable, but the common locations are varied in terms of their microenvironmental conditions and cellular composition. The interaction between stroma and tumour cells in ovarian cancer has been shown to dramatically affect outcome, with cancer associated fibroblasts repeatedly implicated as an important driver of invasive and aggressive behaviour. Furthermore, it has been suggested that metabolic coupling may exist between these two cell types, resulting in a symbiosis which aids cancer growth. Ovarian cancer has been the subject of a number of ^{18}F-FDG-PET studies to date and is due to be imaged with hyperpolarised ^{13}C-pyruvate as part of a study at Addenbrooke's Hospital in Cambridge. In order to accurately interpret metabolic imaging data, it is crucial to understand the way lactate is used and produced by both tumour cells and fibroblasts in this complex disease. This chapter presents a mathematical model of tumour growth in a range of tissue environments, focusing on the role of cancer associated fibroblasts and the different metabolic coupling regimes which may exist between them and the tumour. Platinum-based chemotherapy is simulated to explore how the metastatic environment may affect treatment response and the subsequent presentation of the tumour on metabolic imaging data.

4.1 Introduction

The increased production of lactate which is observed in the vast majority of cancers forms the basis of metabolic imaging techniques such as ^{18}F-FDG-PET and hyperpolarised ^{13}C-pyruvate MRI. These imaging modalities rely on the detection of regions exhibiting abnormally high metabolic conversion or cellular uptake of the exogenous tracer in order to make quantitative estimates of changes in metabolism compared to that of surrounding healthy tissue. Previous chapters have focused on defining the analytical techniques required to accurately and robustly quantify the pyruvate-lactate exchange reaction from reconstructed hyperpolarised ^{13}C images. However, there is an implicit assumption that the observed lactate originates solely from the tumour cells and any observed changes to the metabolic exchange rate represent a fundamental change in the tumour, either due to treatment response or progression. Although ^{18}-FDG-PET is a less direct measure of glycolytic metabolism, detecting glucose transport and phosphorylation, it is frequently deployed clinically as a means of monitoring treatment response [312, 243, 242, 313]. Preclinical studies with ^{13}C-pyruvate have similarly showed that a drop in the observed labelled lactate is indicative of a positive response to treatment [169, 177].

Recently, the notion that lactate in the tumour environment is produced solely by the tumour cells has been challenged by many studies examining the interaction between tumour cells and the surrounding stroma, and the metabolic coupling which can occur between them [314, 315]. Cancer associated fibroblasts (CAFs) may be particularly interesting in this regard due to a phenomenon termed the "reverse Warburg effect" which describes the observation that fibroblasts are capable of producing and utilising lactate in a symbiotic relationship with the tumour cells [44, 316, 49, 317]. Understanding the mechanism by which lactate is both generated and utilised by the tumour and surrounding stroma, before, during and following treatment, is crucial for the successful interpretation of metabolic imaging data; this work uses a mathematical model in order to investigate the dynamics and consequences for treatment response and imaging of tumour-stroma metabolic coupling.

Ovarian cancer has been chosen here as a model system for this study for a number of reasons. Firstly, it is a heterogeneous and metabolically active cancer which has been the subject of a number of PET studies of treatment response [241, 243, 242, 318]; secondly, a clinical study imaging hyperpolarised ^{13}C-pyruvate in ovarian cancer is also under way which will shortly provide detailed insight into the metabolism of pyruvate and lactate in these tumours. Thirdly, the importance of CAFs and the

stromal microenvironment in the development and progression of ovarian cancer has been repeatedly demonstrated [75, 69, 319, 320]. Finally, ovarian cancer commonly metastasises to a range of heterogeneous tissue environments, making it a good candidate disease for such an environmental diversity study.

Ovarian cancer is a complex and heterogeneous disease with poor survival. Early stage disease can often be effectively managed through a combination of drug and surgical treatments, however early detection remains problematic and symptoms are generally ambiguous with common gastrointestinal and genitourinary conditions [53]. Therefore, many patients are already at an advanced stage with widespread metastases at the time of diagnosis, making ovarian cancer the eighth highest cause of cancer-related mortality in women [321]. Current standard-of-care treatment for ovarian cancer involves the administration of platinum-based chemotherapy followed by de-bulking surgery. Allthough most patients will generally relapse, they may be again treated with the same drug in an unusual phenomena known as platinum-sensitive recurrence [79]. The mechanism behind this, and indeed behind the gradual build up of platinum resistance which follows, are not well understood; however explanations favour post-platinum re-population by quiescent tumour stem cells [83], or by cells which resist treatment though entering a quiescent state triggered by unfavourable microenvironmental factors [84].

Despite the histological diversity present in ovarian cancer, metastatic patterns are highly predictable and common amongst all subtypes. The peritoneum has a natural circulation of fluid, facilitating transcoleomic metastasis by transporting detached malignant cells throughout the cavity [62]. The most frequently involved site is the peritoneum and in particular the omentum, a large fat pad extending from the stomach across the bowel, which has metastases present in 80% of all serous ovarian cancer cases [63]. This is followed by the lymph nodes, genitourinary and gastrointestinal systems and the liver [64], which together provide a diverse range of tissue compositions and microenvironmental conditions into which malignant cells in the form of exfoliated tumour spheroids from the primary site can implant and develop.

The stromal microenvironment has been shown to play a critical role in determining the clinical outcome of many cancers including ovarian [314]. The proportion of stromal cells found in ovarian tumours is highly variable, and ranges from around 10-80% [69]; this stromal abundance has been shown to have significant prognostic value, correlating negatively with overall survival. Fibroblasts are the most commonly observed intratumoural stromal cell type and may be recruited and phenotypically altered by adjacent tumour cells to become CAFs through the action of

microRNAs and TGFβ signalling [319, 320]. CAFs have been shown to increase invasiveness and tumour cell motility by degradation of extracellular matrix proteins [67, 73], and to drive angiogenesis [72]. There is abundant evidence that CAFs also produce factors promoting adhesion, lymphangiogenesis and other growth factors important for metastasis and the subsequent development of an aggressive phenotype [322, 319, 72, 73, 74].

Metabolic coupling is a form of symbiosis between CAFs and tumour that has recently been gaining attention. The propensity of tumour cells to undergo glycolytic metabolism has been well documented [2] and has the effect of acidifying the extracellular environment by the fermentation of glucose into lactate. Microenvironmental acidification has been shown to promote tumour invasion and aggressiveness [3], making tumour pH and anaerobic glycolysis popular targets when considering potential therapies [38]. Upregulated glycolysis also forms the target of molecular imaging techniques such as ^{18}F-fluorodeoxyglucose positron emission tomography (^{18}FDG-PET) which detects cellular glucose uptake and hyperpolarised imaging with ^{13}C-pyruvate, a more specific probe for lactate production.

Excess lactic acid creates a favourable environmental niche for the tumour, however it may be also used as an energy source when nutrients are scarce. This phenomenon, termed 'cell-cell lactate shuttle' theory, is already known to occur frequently in healthy tissue and describes how cells with insufficient oxygen supply, such as exercising muscle fibre, may produce lactate which is then transported out of the cell via monocarboxylate transporter 4 (MCT4), a membrane protein which is widely expressed in glycolytic tissues [35]. This lactate can be taken up by neighbouring cells to be utilised as a fuel source; lactate produced by astrocytes for example, is taken up by neurons for rapid energy production in the brain where it can be used instead of glucose as a substrate for oxidation [36]. The same process has been suggested to occur in cancer, creating a coupled metabolism between heterogeneous regions of the tumour.

Peripheral CAFs have also been shown to take up lactate produced by hypoxic tumour cells; this deacidifies the tumour microenvironment but reduces competition for glucose, aiding tumour glycolysis [41]. Computational and evolutionary game theory models have shown this type of tumour-stroma lactate shuttle to be energetically favourable under a broad range of conditions given simple physiochemical constraints [42, 43, 129]. Furthermore, tumour cells may induce increased anaerobic glycolysis in the surrounding CAFs, generating a two-way lactate shuttle which allows heterogeneous tissue regions to make optimal use of available nutrients [44]. The process,

often called the 'reverse Warburg effect', has been shown to be mediated by the loss of stromal caveolin 1, a protein involved in cell cycle progression and metabolism and the expression of which has been shown to negatively correlate with histological grade and aggressiveness in serous ovarian carcinoma [48].

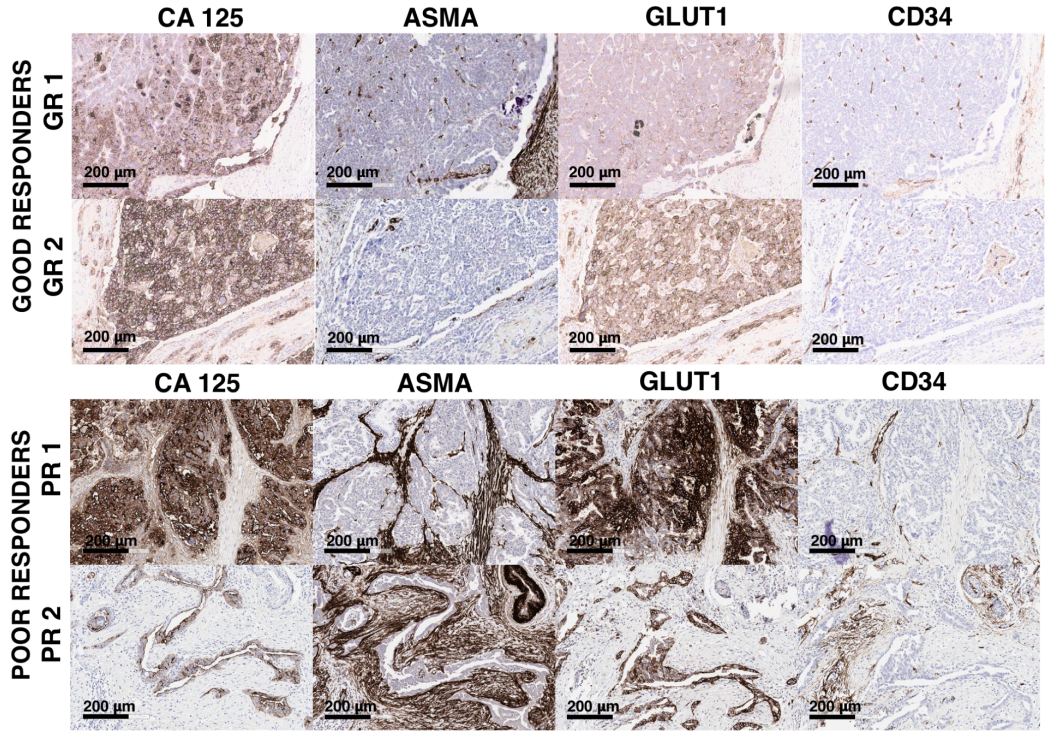

Figure 4.1: Histology data from the primary tumours of four ovarian cancer patients, with good responders (top) and poor responders (bottom). Four stains are shown, where brown staining shows positive regions and blue indicates background. Stains shown from left to right: CA125 (ovarian cancer marker); Alpha-smooth muscle actin (active fibroblasts); GLUT1 (glucose transporter protein 1); CD34 (vessels).

Tissue composition is clearly an important driver of tumour outcome and one which may be probed clinically through histological analysis of biopsy-derived tissue. Histology data was obtained from the primary tumours of 15 ovarian cancer patients at Addenbrooke's hospital and although this cohort is too small to make any quantitative claims, it is instructive to discuss here some observed trends. Figure 4.1 shows data from two good and two poor responders to re-treatment with platinum chemotherapy following relapse with ovarian cancer. The good responders show greater tissue homogeneity, with diffuse but even staining for ovarian cancer marker CA125, little infiltration of active fibroblasts (ASMA) and weakly elevated GLUT1. In contrast, the poor responders show very high levels of GLUT1 over and around ovarian cancer cells, with dense active stroma tightly surrounding the tumour, clearly

indicating a much more metabolically active tissue. Perhaps the most striking difference between the two sets is in the CD34 staining, a marker of vasculature. The good responders show well-spaced, homogeneously distributed vessels throughout the tissue, whereas the poor responders have both regions of very dense staining and large areas with no staining. These tumours are likely to have both hypoxic and highly metabolically active regions; it is likely that the more aggressive coupled metabolic phenotypes emerge as a response to heterogeneous vasculature such as this.

By its mechanistic nature, cellular metabolism lends itself well to study through computational and mathematical approaches which make it possible to explore a broad range of physiological conditions and constraints in a simulated tumour. Simple spatial differential equation models have been successfully utilised to investigate glycolytic metabolism in tumour spheroids [119, 118], and the effects of tumour acid production and microenvironmental pH on growth dynamics [121, 122, 120]. Such models generally use reaction-diffusion type equations to model the movement of acid and nutrients through the cellular environment. More complicated partial differential equation (PDE) models with many cellular and chemical compartments have been used to demonstrate various aspects of metabolic or environmental dynamics; notably, Kim *et al* model the recruitment of fibroblasts via the release of cytokines by the tumor [323]. Further examples of PDE models studying the tumour-stroma interaction have focused on angiogenesis [107] and tumour response to chemotherapy [324].

Although there have been numerous mathematical modelling attempts to demonstrate either the advantages of metabolic coupling or the spatial interaction between the tumour and host cells, there is currently no work in which these two approaches are combined. This work presents a spatial mathematical model to investigate the role of CAFs under differing environmental and metabolic regimes in ovarian cancer, with the objective of understanding qualitatively how the tumour environment may affect treatment response on both a cellular and metabolic level. Growth of a small tumour 'seed', such as that which remains following standard-of-care debulking surgery for ovarian cancer, is allowed to grow to a clinically detectable size before platinum-based chemotherapy is simulated. Multiple environments are simulated for the same seed in order to examine how different metastatic locations may effect outcome. Several vascular densities are considered as well as four metabolic environments: in the first, no fibroblasts are recruited by the tumour; secondly, CAFs are recruited but may only respire aerobically; thirdly, recruited CAFs are able to utilise lactate as a fuel source in partial metabolic coupling with the tumour; finally, CAFs are allowed to

produce, metabolise and exchange lactate with the tumour cells in metabolic symbiosis. Although this model was built with ovarian cancer as a model system, the findings are more widely applicable to other solid tumours.

4.2 Methods

A mathematical model was built to explore *in silico* the effects of metabolism and tissue environment on growth and treatment response in metastatic ovarian cancer. The reactive stroma has been demonstrated in the literature to play an important part in modulating the microenvironment to promote angiogenesis, aggressiveness and invasiveness in ovarian cancer, with CAFs repeatedly implicated as the primary driver. For this reason, it was decided that the interaction between the tumour, CAFs and vasculature should be the primary focus of the model. It was also important to include a detailed treatment of cellular metabolism in the model, with separate equations for the three important metabolites: oxygen, glucose and lactate.

For this purpose, a 1D spherically symmetric partial differential equation (PDE) model was chosen, which models the tumour growing in the centre of a sphere surrounded by normal tissue. Interactions between tumour cells, CAFs, non-reactive stromal cells and vascular endothelium are considered, with dead cells also included in the equations. Concentrations of three nutrients - glucose, oxygen and lactate - are modelled explicitly in addition to the cell densities, as well as the concentration of the drug cisplatin; a platinum-based chemotherapy agent used frequently for the treatment of ovarian cancer. The scale of the model was chosen to correspond to that of metabolic imaging data to enable future comparison, with growth simulations performed over a sphere of tissue 6 cm in diameter. Simulations for growth were run over 200 days. Simulations incorporating treatment were run until the tumour reached a clinically detectable size of 2×10^8 cells, followed by an additional 400 days from the start of treatment. Treatment was simulated as 6 cycles of cisplatin chemotherapy, each cycle consisting of a single 4 hour infusion, spaced 21 days apart.

4.2.1 Model assumptions

Interactions between five cellular compartments are included in the model: tumour, reactive stroma/CAFs, non-reactive stroma, vasculature and necrotic/dead tissue. Given the scale of the model, vasculature is not modelled as discrete vessels, but approximated as a vascular density of epithelial cells with the surrounding nutrient concentrations proportional to this density. Cell densities are set to zero if they drop

below a single cell. Figure 4.2 demonstrates the form of the interactions between each of the cell compartments and the applied chemotherapy drug.

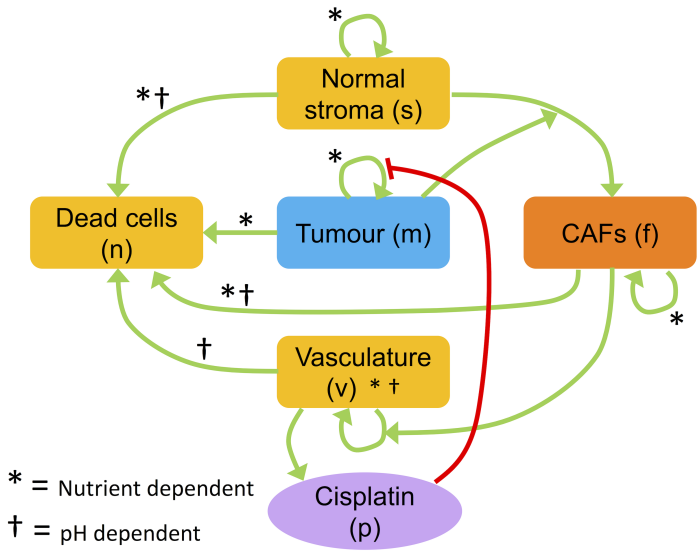

Figure 4.2: Visual representation of the interactions between different cellular compartments and cisplatin chemotherapy. Green arrows represent positive feedback and red denote inhibitory effects on linked compartments. Arrows marked by an asterisk represent interactions dependent on ATP production rates and those with a dagger are pH dependant; both the removal of acid from the system and the level of available nutrients for ATP production are mediated by the vascular compartment.

The following assumptions are used in this model:

- In the presence of tumour cells, CAFs may be recruited from the normal stroma population.
- In the presence of CAFs, tumour cells have increased motility and the vascular proliferation rate increases [72].
- Excluding the vasculature, cells must be producing ATP at 60% of the maximum rate in order to proliferate, and will die if this falls to 20%. Cells between these two thresholds are considered quiescent.
- Lactic acid produced by the tumour changes the local pH, with the change in protons calculated according to $[H^+] = k_{pH}[c_l]$ where $k_{pH} = 2.5 \times 10^{-4}$ is taken as the buffering constant and c_l is the lactate concentration [128].
- Stromal cells begin to die if the pH drops below 6.65, the vasculature below pH 6.6 and CAFs below pH 6.5. Cancer cells are assumed to have adequate resistance to acidic conditions.

- Stromal cells use aerobic respiration only, while tumour cells have an altered metabolic phenotype which allows them to both use and produce lactate. CAFs may take either of these metabolic phenotypes or an alternative third approach which allows lactate to be used in addition to aerobic metabolism.
- Vascular endothelial cells are not included in metabolic calculations as it is assumed they always have access to sufficient nutrients.
- Where available, tumour cells will take up all available glucose up to a maximum allowed rate.
- All cellular metabolism is constrained by the stoichiometry of ATP production.

4.2.2 The PDE system

The full PDE system comprises ten equations with 1D spherical symmetry to describe the change over time in the cell densities of the tumour (m), CAFs (f), non-reactive stroma (s), vasculature (v) and dead cells (n). Additionally modelled are the molar concentrations of oxygen (c_o), glucose (c_g), lactate (c_l) and platinum-based chemotherapy drug (p). In the following equations, the parameters D are diffusion or motility coefficients, μ are proliferation rates, η are acid induced or nutrient deficiency induced death rates and δ are basal death rates. Cells may proliferate only when there is sufficient space, where Ω is the maximum cell density, and $\omega = m + f + s + v + n$ is the current local cell density. The functions of the form $\mathcal{H}(q_A^A - \theta_+)$ are continuous step functions normalised to [0,1]; these smoothly but rapidly turn on or off terms dependant on threshold concentrations of lactate, or threshold ATP production rate, with the mid-point of the transition from zero to one occurring when the argument equals zero.

Tumour cells are considered to move with a non-directional mobility coefficient D_m which may be modulated by the presence of CAFs. Cells proliferate if there is sufficient space and ATP production and may die if ATP production is insufficient, as well as at their basal rate, according to:

$$\frac{\partial m}{\partial t} = \underbrace{\nabla \cdot \{(D_m + D_{mf} f)\nabla m\}}_{\text{Motility}} + \underbrace{\mu_m m(\Omega - \omega)\mathcal{H}(q_A^C - \theta_+)}_{\text{Proliferation}} - \underbrace{\eta_m m\mathcal{H}(\theta_- - q_A^C) - \delta_m m}_{\text{Cell death}} \tag{4.1}$$

Up to 50% of the local healthy stroma may be recruited to produce CAFs at a rate k_{sf} in the presence of tumour cells. CAFs are subject to the same growth and death assumptions as the tumour cells and may additionally die if the pH drops below

a threshold level. The q_A^X in this equation represents ATP production rates for the three possible metabolic phenotypes the CAFs may take, denoted by the superscript as q_A^A, q_A^B or q_A^C. The full equation governing the behaviour of CAFs is given by:

$$\frac{\partial f}{\partial t} = \underbrace{\nabla \cdot \{D_f \nabla f\}}_{\text{Motility}} + \underbrace{m(s-f)k_{sf}}_{\text{CAF recruitment}} + \underbrace{\mu_f f(\Omega - \omega)\mathcal{H}(q_A^X - \theta_+)}_{\text{Proliferation}} - \underbrace{\eta_f f \mathcal{H}(\theta_- - q_A^X) - \eta_l f \mathcal{H}(c_l - H_f) - \delta_f f}_{\text{Cell death}} \tag{4.2}$$

The non-reactive normal stroma obeys the same basic behaviour as the reactive stroma above, with the corresponding equation:

$$\frac{\partial s}{\partial t} = \underbrace{\nabla \cdot \{D_s \nabla s\}}_{\text{Motility}} - \underbrace{m(s-f)k_{sf}}_{\text{CAF recruitment}} + \underbrace{\mu_s s(\Omega - \omega)\mathcal{H}(q_A^A - \theta_+)}_{\text{Proliferation}} - \underbrace{\eta_s s \mathcal{H}(\theta_- - q_A^A) - \eta_l s \mathcal{H}(c_l - H_s) - \delta_s s}_{\text{Cell death}} \tag{4.3}$$

The vasculature is modelled as a vascular density which is able to proliferate at a rate μ_v provided the local oxygen concentration is below the maximum allowed and there is sufficient space. This rate increases in the presence of CAFs. Vasculature may preferentially diffuse, or chemotax, down the oxygen concentration gradient to supply oxygen-starved regions with additional vessels, and vessels will begin to die above their basel rate when the pH drops bellow a threshold level. The full equation for the vascular compartment is given by:

$$\frac{\partial v}{\partial t} = \underbrace{\nabla \cdot \{D_v \nabla v\}}_{\text{Motility}} + \underbrace{(\mu_v + \mu_{vf} f)v(\Omega - \omega)(c_{o,max} - c_o)}_{\text{Proliferation}} + \underbrace{\chi_v \nabla \cdot (v \nabla c_o)}_{\text{Chemotaxis}} - \underbrace{\eta_l v \mathcal{H}(c_l - H_v) - \delta_v v}_{\text{Cell death}} \tag{4.4}$$

The final tissue compartment is that of dead or necrotic cells. When the other four cell types die, they move to this compartment where they remain to take up space until they are eventually reabsorbed:

$$\frac{\partial n}{\partial t} = \underbrace{\eta_m m \mathcal{H}(\theta_- - q_A) + (\eta_f f + \eta_s s)\mathcal{H}(\theta_- - q_A^A)}_{\text{Nutrient deficiency death}} + \underbrace{\delta_m m + \delta_v v + \delta_f f + \delta_s s}_{\text{Basal cell death}} + \underbrace{\eta_l(s\mathcal{H}(c_l - H_s) + f\mathcal{H}(c_l - H_f) + v\mathcal{H}(c_l - H_v))}_{\text{Acid induced death}} - \underbrace{\delta_n n}_{\text{Clearance}} \tag{4.5}$$

Chemical concentrations of three metabolically important molecules - oxygen (c_o), glucose (c_g) and lactate (c_l) - are modelled. These molecules are provided or removed by local vasculature, may diffuse and also be used or produced by cells. The equations for nutrient concentrations over the tissue domain are as follows:

$$\frac{\partial c_o}{\partial t} = \underbrace{\nabla \cdot \{D_o \nabla c_o\}}_{\text{Diffusion}} + \underbrace{v\alpha_o(c_{o,max} - c_o)}_{\text{Vascular supply}} - \underbrace{q_o^A s}_{\text{Stromal uptake}} - \underbrace{q_o^X f}_{\text{CAF uptake}} - \underbrace{q_o^C m}_{\text{Tumour uptake}} \tag{4.6}$$

$$\frac{\partial c_g}{\partial t} = \underbrace{\nabla \cdot \{D_g \nabla c_g\}}_{\text{Diffusion}} + \underbrace{v\alpha_g(c_{g,max} - c_g)}_{\text{Vascular supply}} - \underbrace{q_g^A s}_{\text{Stromal uptake}} - \underbrace{q_g^X s}_{\text{CAF uptake}} - \underbrace{q_g^C m}_{\text{Tumour uptake}} \tag{4.7}$$

$$\frac{\partial c_l}{\partial t} = \underbrace{\nabla \cdot \{D_l \nabla c_l\}}_{\text{Diffusion}} - \underbrace{v\bar{\alpha}_l c_l}_{\text{Vascular removal}} - \underbrace{q_l^X f}_{\text{CAF uptake}} - \underbrace{q_l^C m}_{\text{Tumour uptake}} \tag{4.8}$$

The parameters α ($\bar{\alpha}$) are vascular supply (removal) rates, and the metabolite uptake parameters q_o^X, q_g^X, and q_l^X are defined by the stoichiometry of metabolism and the local nutrient concentrations according to the rules of the particular metabolic regime being played out. Three metabolic phenotypes are considered: aerobic metabolism denoted by the superscript q^A; aerobic or lactate metabolism q^B; aerobic, lactate or glycolytic metabolism q^C. The stromal cells always metabolise aerobically as type A and tumour cells always as type C whereas CAFs may take any of the three phenotypes. Where more than one metabolic pathway is available to a cell, the relative contributions from each type of energy production depends on the local nutrient concentrations according to a set of rules.

In the aerobic type A case, it is assumed that the uptake of both glucose and oxygen is rate limited by the nutrient in scarcest supply, and that near the maximum uptake rate $q_{i,max}$ the cell produces sufficient ATP for proliferation. For the aerobically respiring cells, the mass balance equations for the rate of ATP production q_{ATP}^A are given by:

$$q_o^A = min\{\frac{q_{o,max}c_o}{K_o + c_o}, \frac{6q_{g,max}c_g}{K_g + c_g}\}, \qquad q_g^A = \frac{1}{6}q_o^A \tag{4.9}$$

$$q_{ATP}^A = 7q_g^A + \frac{25}{6}q_o^A \tag{4.10}$$

Nutrient uptake takes a Michaelis-Menten form, with K_i representing the half-max concentration constants. Although aerobic respiration has a theoretical ATP yield of 38 ATP molecules per glucose, this process is not perfectly efficient due to losses as molecules are transported into the mitochondrial matrix. Here, P/O ratios of 2.5 and 1.5 have been assumed for NADH and $FADH_2$ respectively based on the

most recent experimental evidence [325]; this corresponds to an actual aerobic ATP yield of 32 molecules per glucose.

The second metabolic phenotype, type B, is only exhibited by the CAFs and models the lactate shuttle effect whereby CAFs may metabolise the lactate produced by the tumour cells as a carbon source when glucose is scarce. It is assumed that cells will take up oxygen and lactate where available with the rate limited by the scarcer of the two, and that any additional oxygen may be utilised for glucose metabolism. In this case, the oxygen uptake rate is given by:

$$q_o^B = min\{\frac{q_{o,max}c_o}{K_o + c_o},\ 6\frac{q_{g,max}c_g}{K_g + c_g} + 3\frac{q_{l,max}c_l}{K_l + c_l}\}, \qquad q_g^B = \frac{1}{6}q_o^B - \frac{1}{2}q_l^B \tag{4.11}$$

$$q_l^B = min\{\frac{q_{l,max}c_l}{K_l + c_l},\ \frac{1}{3}q_o^B\}, \qquad q_{ATP}^B = 7q_g^B + \frac{5}{2}q_l^B + \frac{25}{6}q_o^B \tag{4.12}$$

In the type C metabolic state, cells are permitted to maximise their energy production through a combination of aerobic, glycolytic and lactate metabolism. In this case, it is assumed that cells will consume glucose where available, and that the rate of aerobic metabolism will then be limited by the available oxygen, with the remaining glucose converted into lactate. However, if sufficient oxygen is available but little glucose, lactate may be metabolised as an alternative carbon source according to the following equations:

$$q_o^C = min\{\frac{q_{o,max}c_o}{K_o + c_o},\ 6q_g^C + 3\frac{q_{l,max}c_l}{K_l + c_l}\}, \qquad q_g^C = \frac{q_{g,max}c_g}{c_g + K_g} \tag{4.13}$$

$$q_l^C = \frac{1}{3}q_o^C - 2q_g^C, \qquad q_{ATP}^C = 7q_g^C + \frac{5}{2}q_l^C + \frac{25}{6}q_o^C \tag{4.14}$$

Constraining $q_l^X = 0$ gives the equivalent relations for the aerobic case. It should be noted here that $q_{l,max}$ and q_l^X are both uptake rates, however q_l^C can be, and generally is, negative, indicating an overall net production of lactate. Figure 4.3 depicts schematically the four different tumour-CAF coupling conditions being simulated.

4.2.3 Application of treatment

After 200 days, 6 simulated cycles of chemotherapy are implemented. In accordance with the standard of care treatment offered to the ovarian cancer patient cohort, treatment is modelled as a single intravenous infusion for 1 hour every 3 weeks. The equation for the cisplatin concentration is:

$$\frac{\partial p}{\partial t} = \underbrace{\nabla \cdot \{D_p \nabla p\}}_{\text{Diffusion}} + \underbrace{v\alpha_p(t)(p_{max} - p)}_{\text{Vascular provision}} - \underbrace{q_p p m}_{\text{Tumour uptake}} - \underbrace{\gamma_p p}_{\text{Elimination}} \tag{4.15}$$

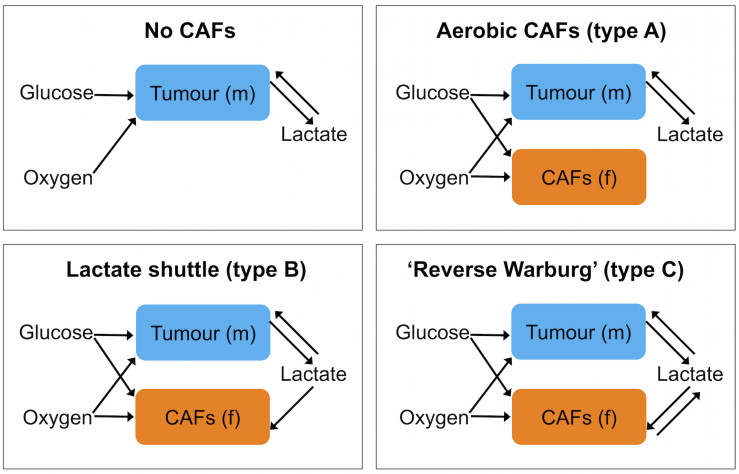

Figure 4.3: Schematic showing the use and production of metabolites in each of the four test conditions for tumour-CAF metabolic coupling. The control condition with no CAFs (top left); aerobic CAFs with no metabolic coupling (top right); partial coupling via lactate a shuttle (bottom left); fully metabolically coupled (bottom right).

Where q_p and γ_p are constant uptake and decay rates respectively and $\alpha_p(t)$ defines the inflow of the drug via the vasculature over time; the temporal flow profile is modelled as a series of six four-hour 'on' periods spaced three weeks apart. The corresponding modification to the tumour cell and dead cell populations under treatment are as follows:

$$\frac{\partial m}{\partial t} = ... - mp\mathcal{H}(q_A^C - \theta_+)q_p\eta_p, \qquad \frac{\partial n}{\partial t} = ... + mp\mathcal{H}(q_A^C - \theta_+)q_p\eta_p \tag{4.16}$$

Here η_p is the chemotherapy-induced death rate, and the drug is assumed to kill only those cells which are proliferating; explicitly, the cells which have an ATP production rate q_A^C above the critical value required for proliferation θ_+.

4.2.4 Non-dimensionalisation

By transforming all variables and parameters into dimensionless form, the set of equations can be scaled such that each variable may vary between a minimum of zero and a maximum of one, corresponding to the maximum allowed value. This not only confines the system to a more numerically tractable space, but allows for easier estimation of any unknown parameters by making clear the scale on which they must operate. By defining new dimensionless parameters as indicated by a tilde, and making appropriate substitutions, the differential equations can be written in dimensionless form. The following non-dimensional variables are defined:

$$\tilde{c_o} = \frac{c_o}{c_{o,max}}, \qquad \tilde{c_g} = \frac{c_g}{c_{g,max}}, \qquad \tilde{c_l} = \frac{c_l}{c_{l,max}} \qquad \tilde{p} = \frac{p}{p_{max}}$$

$$\tilde{m} = \frac{m}{\Omega}, \qquad \tilde{n} = \frac{n}{\Omega}, \qquad \tilde{v} = \frac{v}{\Omega}, \qquad \tilde{f} = \frac{f}{\Omega}, \qquad \tilde{s} = \frac{s}{\Omega}$$

Additionally, characteristic time and length scales T and L respectively can be defined, such that:

$$\tau = \frac{t}{T}, \qquad \rho = \frac{r}{L}, \qquad \tilde{\nabla} = L\nabla, \qquad \tilde{D_i} = \frac{D_i T}{L^2}, \qquad \tilde{D}_{mf} = \frac{\Omega T D_{mf}}{L^2}$$

A value of 1 hour was chosen for T and of 1 cm for L. Substituting into the equations for nutrient concentrations, the following are obtained:

$$\tilde{q_i}^j = \frac{\Omega T q_i^j}{c_{i,max}}, \qquad \tilde{q_p} = \Omega T q_p, \qquad \tilde{\alpha_i} = \Omega T \alpha_i$$

Where i represents the subscript for each of the three nutrients oxygen, glucose and lactate, and j denotes the type of metabolism, aerobic or abnormal. For the cell concentration equations, the following can be defined for each of the general growth, decay and death rates:

$$\tilde{\delta_k} = T\delta_k, \qquad \tilde{\mu_k} = T\Omega\mu_k, \qquad \tilde{\eta_k} = T\eta_k, \qquad \tilde{\gamma_p} = \gamma_p T$$

And for the following which take a slightly different form to the general case:

$$\tilde{\mu_v} = T\Omega c_{o,max}\mu_v, \qquad \tilde{\mu_{vf}} = T\Omega^2 c_{o,max}\mu_{vf}, \qquad \tilde{\mu_{mf}} = T\Omega^2\mu_{mf}, \qquad \tilde{\delta_p} = \frac{\delta_p p_{max}}{\Omega}$$

Finally, the chemotaxis, recruitment and Michaelis-Menten constants are given by:

$$\tilde{\chi_v} = \frac{\chi_v c_{o,max} T}{L^2}, \qquad \tilde{k_{sf}} = k_{sf}\Omega T, \qquad \tilde{K_i} = \frac{K_i}{c_{i,max}}$$

These new dimensionless parameters are substituted into the original equations. If the tildes are omitted from each of the variables and parameters, this leads to equations of very similar form to those described above.

4.2.5 Parameterisation

The PDE system was built in the knowledge that any free parameters would have to be derived from the literature. Although the model is comprised of a very large system of equations, it contains few quantities which are not biologically measurable with well documented values. Parameter values were obtained where possible from human

studies, although it is noted that in some instances only animal or *in vitro* data was available. In the interest of internal consistency, similar parameters were obtained from as few sources as possible; for example, all chemical diffusion parameters are derived from the same study which ensures values are correctly distributed relative to one another.

There were a small number of parameters which were not directly measurable. Firstly, the vascular transport parameters α_o, α_g and α_l were picked to produce the correct observed tissue concentrations of the respective nutrients under steady state conditions with no tumour cells present; it is these tissue concentrations that are referenced for these parameters. The CAF enhanced tumour motility $D_{m,f}$ was chosen such that the motility of tumour cells was doubled at a relative CAF density of 20% in line with experimental observations. The vascular basal death rate δ_v was varied to produce different vascular densities, taking values of 1.25×10^{-7}, 3.60×10^{-9} and 2.56×10^{-9} s^{-1} to produce tissues with 4%, 8% and 12% vasculature by volume at steady state respectively. Finally, the rate of CAF recruitment rate k_{sf} was chosen to produce a qualitatively similar proportion of CAFs as the tissue vascular density was varied, with the objective to produce a CAF density of around 30% at the tumour periphery in accordance with clinical histological findings. k_{sf} values of 2×10^{-15}, 6.2×10^{-14} and 1.82×10^{-13} were chosen for tissue vascular densities 4%, 8% and 12% respectively to achieve this.

Table 4.1 shows the full list of parameters used in the tissue model, with their descriptions, symbols, units, values and literature references given. Parameters describing the behaviour of both the platinum and alkalysing drugs are shown in a separate table 4.2. Values for these parameters were derived from the known pharmacokinetics of cisplatin.

Table 4.1: Descriptions of all parameters used in the tumor growth model, or in the non-dimensionalisation process, with their symbol, unit, value and literature references where appropriate.

Parameter description	Symbol	Units	Value	Ref
Oxygen diffusion	D_o	cm^2s^{-1}	1.32×10^{-5}	[326]
Glucose diffusion	D_g		3.62×10^{-6}	[326]
Lactate diffusion	D_l		6.08×10^{-6}	[326]
Tumour cell motility	D_m		1.0×10^{-9}	[326]
Vascular motility	D_v		1.0×10^{-10}	[327, 324]
CAF motility	D_f		1.7×10^{-9}	[328, 323]
Stroma cell motility	D_s		1.7×10^{-10}	[329, 330]
CAF enhanced tumour motility	D_{mf}	$cm^2s^{-1}cell^{-1}cm^3$	4.0×10^{-17}	[323, 72]
Vascular provision of oxygen	α_o	$cm^3cell^{-1}s^{-1}$	1.82×10^{-8}	[331, 332]
Vascular provision of glucose	α_g		6.06×10^{-11}	[333, 332]
Vascular removal of lactate	α_l		1.00×10^{-10}	[333, 332]
Tumour proliferation	μ_m	$cm^3cell^{-1}s^{-1}$	1.20×10^{-13}	[334, 335]
Vascular proliferation	μ_v		8.02×10^{-14}	[336]
CAF proliferation	μ_f		1.26×10^{-14}	[323, 337]
Stroma proliferation	μ_s		4.38×10^{-14}	[323], [337]
CAF enhanced tumour proliferation	μ_{mf}	$(cm^3cell^{-1})^2s^{-1}$	1.93×10^{-24}	[323, 72]
CAF enhanced vascular proliferation	μ_{vf}		1.75×10^{-20}	[72]
Tumour nutrient-mediated death	η_m	s^{-1}	4.0×10^{-8}	[128]
CAF nutrient-mediated death	η_f		4.0×10^{-6}	[128]
Stroma nutrient-mediated death	η_s		4.0×10^{-6}	[128]
Acid-mediated cell death rate	η_l		$2.24.0\times10^{-6}$	[338]
Tumour cell death rate	δ_m	s^{-1}	1.0×10^{-9}	[334, 335]
Vascular cell death rate	δ_v		Variable	
CAF cell death rate	δ_f		2.42×10^{-9}	[330]
Stroma cell death rate	δ_s		2.42×10^{-9}	[330]
Dead cell re-absorption	δ_n		2.47×10^{-7}	[108]
Vascular chemotaxis	χ_v	$cm^2cm^3mol^{-1}s^{-1}$	9.10×10^{-5}	[108]
Stroma to CAF conversion	k_{sf}	$cm^3cell^{-1}s^{-1}$	Variable	[323]
Max tissue O_2 concentration	$c_{o,max}$	mol cm^{-3}	1.1×10^{-7}	[128], [339]
Max tissue glucose concentration	$c_{g,max}$		5.5×10^{-6}	[128, 340]
Max tissue lactate concentration	$c_{l,max}$		4.0×10^{-5}	[332, 341]
O_2 Michaelis-Menten constant	K_o	mol cm^{-3}	4.8×10^{-9}	[332, 341]
Glucose Michaelis-Menten constant	K_g		4.0×10^{-8}	[332, 341]
Lactate Michaelis-Menten constant	K_g		5.5×10^{-10}	[332, 341]
Max O_2 transport rate	$q_{o,max}$	mol $cell^{-1}s^{-1}$	1.76×10^{-16}	[332, 341]
Max glucose transport rate	$q_{g,max}$		1.33×10^{-16}	[332, 341]
Max lactate transport rate	$q_{l,max}$		1.00×10^{-14}	[332, 341]
Max ATP production rate	$q_{ATP,max}$		9.39×10^{-16}	Calculated
Max cell density	Ω	cell cm^{-3}	1×10^8	[332, 128]
Stromal acid-death threshold pH	H_s	pH	6.65	[342]
Vascular acid-death threshold pH	H_v		6.60	[342]
CAF acid-death threshold pH	H_f		6.50	[342]
ATP proliferation threshold	θ_+	mol $cell^{-1}s^{-1}$	0.6 $q_{ATP,max}$	[343]
ATP death threshold	θ_-		0.2 $q_{ATP,max}$	[343]

Table 4.2: Parameter values for simulated cisplatin treatment.

Parameter description	Symbol	Units	Value	Ref
Cisplatin diffusion	D_p	$\mathrm{cm^2 s^{-1}}$	2.10×10^{-6}	[326]
Drug vascular provision rate	$a_p(t)$	$\mathrm{cm^3 cell^{-1} s^{-1}}$	2.78×10^{-11}	[344]
Max. cisplatin concentration	p_{max}	mol $\mathrm{cm^3}$	Variable	[344, 345]
Tumour cell uptake rate	q_p	$\mathrm{cell^{-1} cm^3 s^{-1}}$	$6.50\times10^{-16} p_{max}$	[344, 345]
Tumour cell kill potency	η_p	cell $\mathrm{mol^{-1}}$	6.00×10^{22}	[80, 344]
Cisplatin decay rate	γ_p	$\mathrm{s^{-1}}$	1.50×10^{-6}	[344, 345]

4.2.6 Numerical methods

The system of nine coupled partial differential equations was solved numerically using a semi-implicit finite-difference scheme. Reaction-diffusion equations of this type are hard to treat due to the inhomogeneous reaction terms and the fact that the processes being described act on very different time scales, making this particular system stiff in both the reaction and diffusion terms. This results in a system which requires impractically tiny time steps to be taken if a standard explicit finite difference scheme is used, else the solution will become unstable as the Fourier modes of the system grow and generate oscillations. On the other hand, using a fully implicit method requires vast matrix manipulations and is extremely computationally demanding. One way of dealing with such a system is to use an implicit integration factor (IFF) scheme in which the linear diffusion terms are treated exactly, and the stiff reaction terms are treated implicitly. Several possible methods are compared by Nie *et al* [346], however they find only the 2nd order IFF method (or weighted combinations with other methods) to be unconditionally linearly stable with increasing time step. The method is further developed in [347] and will be briefly described below.

The system of reaction-diffusion equations in one spatial dimension r, for time $t \geqslant 0$ may be written concisely as:

$$\frac{d\mathbf{u}(r,t)}{dt} = \mathcal{C}\mathbf{u}(r,t) + f(\mathbf{u}(r,t)), \qquad \mathbf{u}(r,0) = \mathbf{u_0} \tag{4.17}$$

Where $\mathbf{u}$ is a vector containing the values of each variable at each radial point r, $\mathbf{u}_0$ is a set of given initial conditions, $\mathcal{C}$ is a matrix operator describing the action of the diffusion (all spatially dependant) terms and $f(\mathbf{u}(r))$ is a vector containing the non-linear (non-spatially dependant) reaction terms. Multiplying the above expression

by an integrating factor $e^{-\mathcal{C}t}$ and rearranging (dropping the dependence on r for convenience), the following is obtained:

$$\frac{d}{dt}(\mathbf{u}e^{-\mathcal{C}t}) = f(\mathbf{u})e^{-\mathcal{C}t} \tag{4.18}$$

The vector $\mathbf{u}$ is known at time t_n and its value at the next time step t_{n+1} must be found, where $t_{n+1} = t_n + \Delta t$. First, both sides of equation 4.18 are integrated from t_n to t_{n+1}:

$$\mathbf{u}(t_{n+1})e^{-\mathcal{C}t_{n+1}} - \mathbf{u}(t_n)e^{-\mathcal{C}t_n} = \int_{t_n}^{t_{n+1}} f(\mathbf{u}(t))e^{-\mathcal{C}t}dt \tag{4.19}$$

Then, making the substitution $\tau = t - t_n$:

$$\mathbf{u}(t_{n+1}) = \mathbf{u}(t_n)e^{\mathcal{C}\Delta t} + e^{\mathcal{C}\Delta t}\int_0^{\Delta t} f(\mathbf{u}(\tau + t_n))e^{-\mathcal{C}\tau}d\tau \tag{4.20}$$

in order to continue, some discrete approximation is needed for the expression under the integrand, $g(\tau) = f(\mathbf{u}(\tau + t_n))e^{-\mathcal{C}\tau}$. The Lagrange polynomial for any set of $k+1$ discrete points t_n and set of numbers g_n is defined as the polynomial of lowest order which is able to connect each of the $k+1$ points to their corresponding numerical values and is always a unique solution. Using this particular notation, the Lagrange interpolating polynomial is defined:

$$p(\tau) = \sum_{j=0}^{k+1} g_j l_j = \sum_{j=0}^{k+1} g_j(\tau) \prod_{m=0, m\neq j}^{k+1} \frac{\tau - t_m}{t_j - t_m} \tag{4.21}$$

The 2nd order solution should be used since it is universally stable, so only two terms are required in the interpolation at $g(0) = f(\mathbf{u}(t_n))$ and $g(\Delta t) = e^{-\mathcal{C}\Delta t}f(\mathbf{u}(t_{n+1}))$; $g(\tau)$ is therefore being approximated by a polynomial which passes through the two limits of the integral, with a solution which will have a truncation error of the order Δt^3. Then:

$$p(\tau) = f(\mathbf{u}(t_n))\frac{\Delta t - \tau}{\Delta t} + e^{-\mathcal{C}\Delta t}f(\mathbf{u}(t_{n+1}))\frac{\tau}{\Delta t} \tag{4.22}$$

Substituting into equation 4.20 and integrating over $p(\tau)$ gives the final equation to be used in the finite difference scheme:

$$\mathbf{u}(t_{n+1}) - \frac{\Delta t}{2}f(\mathbf{u}(t_{n+1})) = e^{\mathcal{C}\Delta t}(\mathbf{u}(t_n) + \frac{\Delta t}{2}f(\mathbf{u}(t_n))) \tag{4.23}$$

The known quantities are on the left of the equation and the unknowns to be found for the next time step are on the right. All terms with any spatial dependence, i.e. all those incorporating a spatial derivative, are contained within the matrix $\mathcal{C}$. If we were only considering diffusion, which acts independently of other variables, the

matrix exponential $e^{\mathcal{C}\Delta t}$ would only need to be calculated once making this algorithm extremely efficient, however since terms such as chemotaxis are included which must be updated at each time step to account for the current local oxygen concentration, this needs to be recalculated each time. Luckily, the fact that $\mathcal{C}$ is sparse can be exploited for speed, using the function *expv.m* [348], which calculates an approximation of the matrix exponential for sparse matrices when the input is of the form $ve^{t\mathcal{C}}$, with v some vector and t a constant.

A central difference approximation was used for discretisation of the spatial terms. For the diffusion terms, the finite difference discretisation of the spherically symmetric Laplacian is of the form:

$$\nabla \cdot D_k \nabla \mathbf{u} = D_k \{ \frac{\partial^2 \mathbf{u}}{\partial r^2} + \frac{2}{r} \frac{\partial \mathbf{u}}{\partial r} \} \approx D_k \{ \frac{\mathbf{u}_{j+1} - 2\mathbf{u}_j + \mathbf{u}_{j-1}}{\Delta r^2} + \frac{2}{r} \frac{\mathbf{u}_{j+1} - \mathbf{u}_{j-1}}{2\Delta r} \} \quad (4.24)$$

Where here the index j on the vector $\mathbf{u}$ represents the discrete spatial coordinate on r, where $j = 1, 2, 3...(N-1)$ with N the total number of spatial grid points with separation Δr. Zero flow boundary conditions (Neumann) were implemented at $r = 0$ and $r = R$, where the spatial derivative of $\mathbf{u}$ goes to zero, as no flow conditions are assumed through the centre of the tumour and steady state at the edge of the tissue boundary where $r = R$. This leads to boundary approximations of the form:

$$\nabla \cdot D_k \nabla \mathbf{u}|_{r=0} \approx 6 D_k \frac{\mathbf{u}_{j+1} - \mathbf{u}_j}{\Delta r^2}, \qquad \nabla \cdot D_k \nabla \mathbf{u}|_{r=R} \approx 2 D_k \frac{\mathbf{u}_{j-1} - \mathbf{u}_j}{\Delta r^2} \quad (4.25)$$

The discretisations and boundary conditions for the other spatially dependant terms, chemotaxis and fibroblast induced motility, were implemented in the same way. Note that the dependence on r in the Laplacian due to the geometry of the problem drops out if we assume zero flux at the tumour core, meaning there is no issue of the solution blowing up at the centre as $r \to 0$.

The simulation was run for 360 days with a time step of $\Delta t = 0.5$ hr and a spatial grid size of $\Delta r = 0.02$ cm. The full finite difference algorithm is as follows:

Data: Input initial conditions for tissue composition $\mathbf{u}_0(r, 0)$;
Define all parameter values;
Define treatment dynamics;
Define matrix $\mathcal{C}$ to incorporate all spatially dependant terms and boundary conditions which will act on the vector $\mathbf{u}$;
for *n = 1; n < No. time steps; n++* **do**
  Update dynamic terms in matrix $\mathcal{C}$;
  Calculate new chemical uptake rates $q_{i,n}$;
  Calculate reaction vector $f(\mathbf{u}(t_n)$;
  Calculate RHS of equation 4.23: $X = e^{\mathcal{C}\Delta t}(\mathbf{u}(t_n) + \frac{\Delta t}{2} f(\mathbf{u}(t_n)))$;
  Make starting approximation $\mathbf{u}'(t_{n+1}) = \mathbf{u}(t_n)$;
  `// Begin fixed point iteration`
  while *Solution not converged || No. iterations <25* **do**
    Calculate chemical uptake rates $q'_{i,n+1}$;
    Calculate reaction vector $f'(\mathbf{u}'(t_{n+1}))$;
    Set up function to be minimised: $Y = X + \frac{\Delta t}{2} f'(\mathbf{u}'(t_{n+1}) - \mathbf{u}'(t_{n+1}) = 0$;
    Calculate Jacobian matrix $\mathcal{J}_{i,j} = \frac{\partial Y_i}{\partial \mathbf{u}'(t_{n+1})_j}$;
    Then using Newton's method: $\Delta\mathbf{u} = \mathbf{u}''(t_{n+1}) - \mathbf{u}'(t_{n+1}) = -Y/\mathcal{J}$;
    Update working value of $\mathbf{u}(t_{n+1})$;
    $\mathbf{u}'(t_{n+1}) \leftarrow \mathbf{u}''(t_{n+1})$;
    Has solution converged? ($\Delta\mathbf{u} \sim 0$?)
  end
  $\mathbf{u}(t_{n+1}) = \mathbf{u}'(t_{n+1})$
end

Algorithm 1: Finite difference algorithm for numerical solution of PDE system

4.3 Results

In order to determine normal tissue conditions, the model was first run over 3000 days with the initial tumour cell and CAF populations set to zero and the vascular density fixed. In the absence of these cell populations the model behaved appropriately and quickly reached a steady state for integer vascular densities of 4-12% of the maximum tissue capacity Ω. In order to produce long-term stability at each of these nine fixed vascular densities, the vascular basal death rate was required to vary; the optimal value of this parameter for each tissue condition was found by solving the steady state system of equations under appropriate constraints. The resulting set of stable normal tissues provided initial conditions to input into the full model. In each case, the tissue was perturbed with an identical tumour of $\sim$1 mm radius and 5.65×10^6 cells at the centre of the simulated tissue sphere. The initial conditions for tumour growth in tissues of 4, 6 and 12% vasculature are shown in figure 4.4.

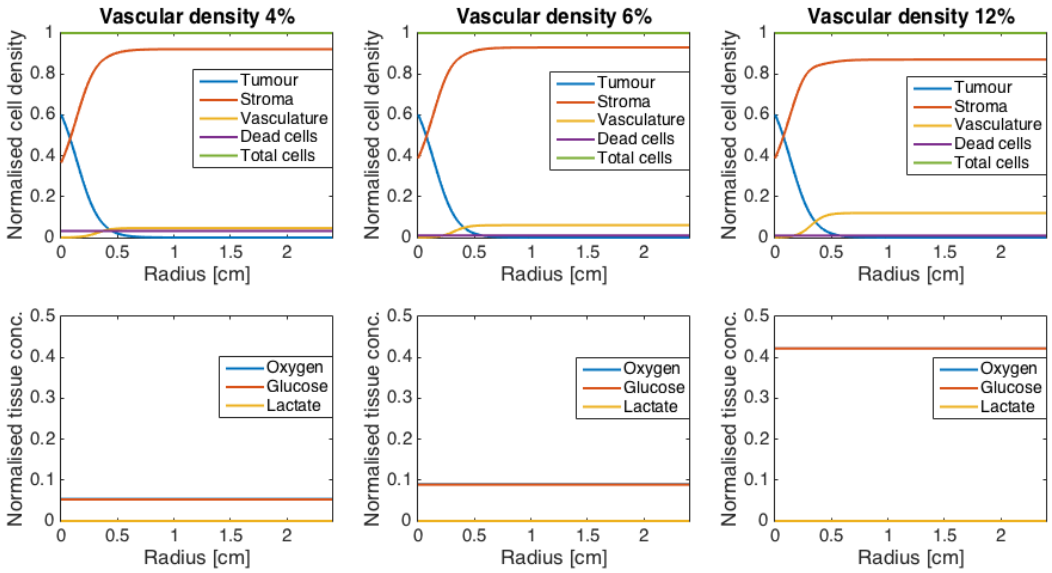

Figure 4.4: Initial cell densities (top row) and metabolite concentrations (bottom row) for used in the PDE model. Initial conditions for three different tissues are shown with vascular densities 4% (left), 6% (centre) and 12% (right). Cell densities are as a proportion of the carrying capacity Ω and metabolites are as a proportion of their respective maximum values $c_{o,max}$, $c_{g,max}$ and $c_{l,max}$.

4.3.1 Growth phase results

Tumour growth was simulated over 200 days from an identical initial population in nine different tissue types with vascular densities from 4-12%. For each tissue, four conditions were tested. In the first, no CAFs are recruited by the tumour with $k_{sf} = 0$; second, CAFs are recruited and respire aerobically with type A metabolism; third, CAFs and tumour are partially metabolically coupled via a lactate shuttle with CAFs exhibiting type B metabolism; finally, CAFs and tumour are fully metabolically coupled, with CAFs showing type C metabolism in analogy with the 'reverse Warburg' effect. Figure 4.5 shows the growth curves for tumours in six representative tissues; results for a vascular density of 8%, and for 10% and 11%, are omitted as they are qualitatively very similar to those of 7% and 12% respectively. As vascular density increases, different metabolic phenotypes of the CAFs become advantageous for maximal growth. Furthermore, there appear to be critical cell numbers at which the most advantageous strategy switches, or at which two previously similar strategies diverge. At around $2{\times}10^7$ cells in tissue with 6% vascularity, the partially coupled type B CAFs are overtaken by the tumour with no CAFs present. Despite providing an initial advantage by redistributing nutrients when they are scarce, the removal of lactate from the tumour environment eventually hinders the invasiveness and there-

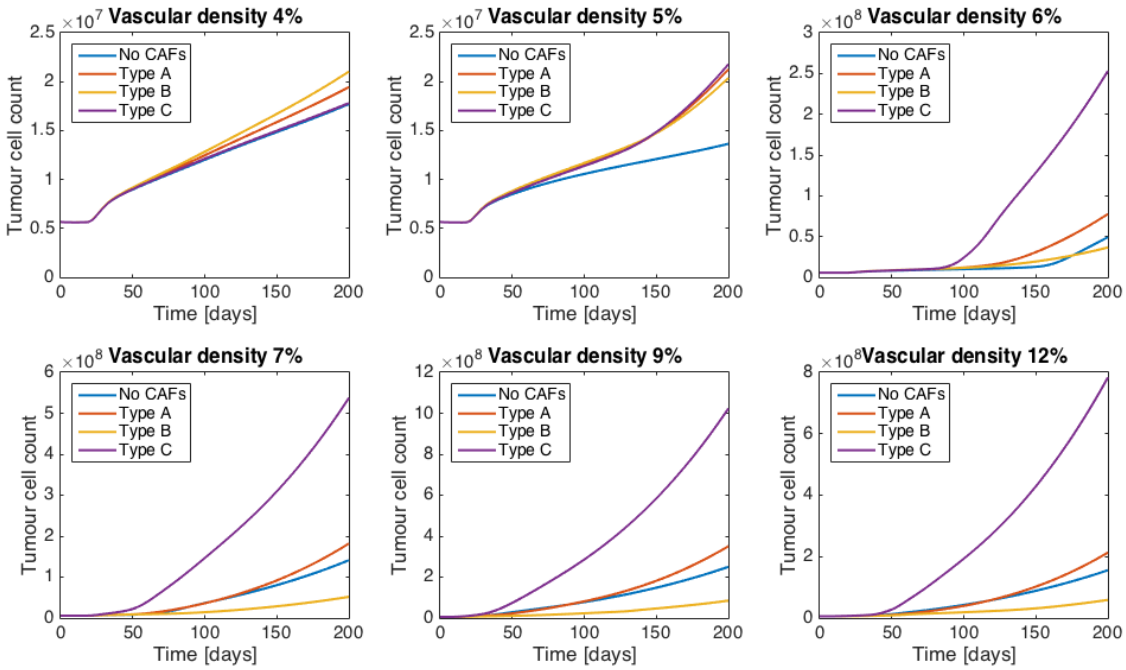

Figure 4.5: Tumour growth over 200 days in tissues with six different representative vascular densities. For each tissue, four metabolic regimes are shown: no CAFs present; aerobically respiring CAFs (type A); partial coupling of tumour and CAFs via a lactate shuttle (type B); full metabolic coupling between tumour and CAFs (type C).

fore growth potential of the tumour. The type B phenotype is the most successful in the tissue with 4% vascular density, and at early times in the 5% tissue, for a similar reason. With insufficient nutrients for growth, it is most beneficial to have CAFs recycle lactate, however as vascular density increases, having CAFs which also produce lactate drives invasion and the type C metabolic coupling becomes by far the most successful once the tumours become established. The higher the vascular density of the tissue, the bigger the advantage of the reverse Warburg phenotype is over the other metabolic regime, with the 12% tissue showing the biggest percentage difference in growth between this and the next most successful phenotype.

The hierarchy of vascular densities is well conserved across conditions, with the 9% vascularity tissue condition clearly optimal for tumour growth across all metabolic conditions. At early times, the tissue conditions are generally comparable; the 4% condition even outperforming other higher vascularity tissues as the poor health of the surrounding stroma offers an initial invasive advantage. Two clear growth stages are evident in figure 4.5; an early 'establishment' stage where growth is slow and tumour vasculature is developing, followed by an exponential growth phase, the onset

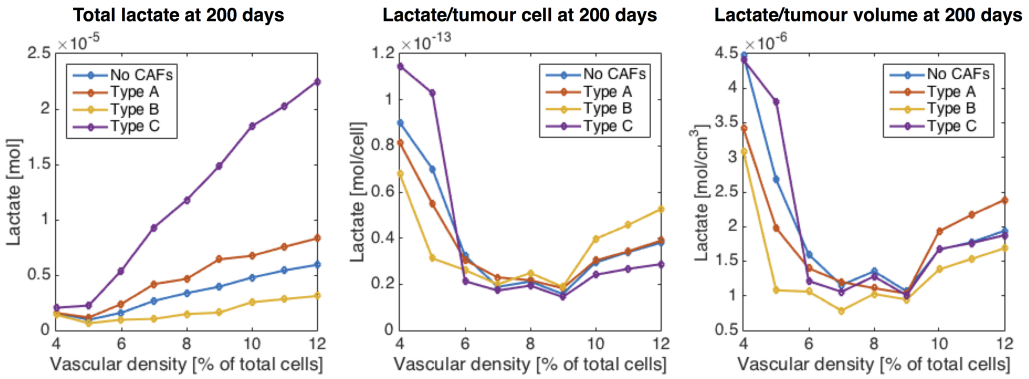

Figure 4.6: Total lactate after 200 days growth in tissues of 4-12% vascular density and under four different metabolic conditions: no CAFs present; aerobically respiring CAFs (type A); partial coupling of tumour and CAFs (type B); full metabolic coupling between tumour and CAFs (type C). The total lactate in the 3 cm radius tissue sphere is shown (left), along with the same total lactate normalised by tumour cell count (centre) and tumour volume (right).

time of which is heavily dependant on tissue vasculature and metabolic phenotype. In the 6% tissue condition for example, exponential growth begins at around 80 days for the type C system and at 160 days for the system without CAFs, whereas at 9% both begin exponential growth at around 40 days. The type B system seems to be the exception to this, producing slower, steadier growth with no clear transition.

It is also of interest to examine the acidity of tumours growing in each different environment. Figure 4.6 shows the total lactate in the tumour environment, summed over the 3 cm radius simulation domain, after 200 days of growth. The total lactate in the tumour environment increases with tissue vascularity rather than with growth rate or tumour size as might be expected, with the type C condition increasing faster with vascularity than the other conditions, followed by the type A, the no CAF and finally the type B condition. When the lactate is normalised by tumour size, either by cell count or by tumour volume, this hierarchy is preserved at low vascularities which, in general, have the highest normalised lactate levels. Although metabolic strategies cross over with slightly noisy trajectories, the general trend is a drop in normalised lactate to a minimum at the optimal tissue condition of 9%, followed by an increase. The order of the four strategies also stabilises and diverges at this point; figure 4.6 (centre) shows almost a clean reversal at high vascular densities compared to that at low. The 9% vascular density mark is clearly a critical point at which the behaviour of the system switches The increase in tumour acidity as vascular density rises may be caused by glycolytic metabolism rising due to increased glucose access, whilst at the

same time, peripheral lactate being carried away by the vasculature limits growth rate by slowing invasion. There are small differences between the graphs in the central and right portions of figure 4.6 depicting different normalisations by cell count or volume respectively. The disparity is due to differences in tumour density that each metabolic regimes produces; while the type B tumours are quite sparse at 200 days, the type A and C are much denser.

4.3.2 Application of treatment

Four representative tissue types were further investigated to examine the tumour response to simulated chemotherapy with cisplatin. Vascular densities of 4% (low), 6% (medium), 9% (optimal) and 12% (high) were chosen, as it was believed that these four were sufficient to represent the full range of vascularities studied in the growth phase in terms of their behaviour. In order to study how the tissue environment may affect treatment response, tumours in each tissue were grown until they reached 2×10^8 cells, corresponding to a clinically detectable tumour of between 2-4 cm diameter depending on conditions. When the tumour reached this critical mass, 6 cycles of cisplatin spaced 3 weeks apart were simulated at a starting dose of 0.90 g. Figure 4.7 shows the tumour response to this treatment in the four tissues.

It is immediately clear that treatment response is at least partly dependant on growth rate; the faster growing tumours in the higher vascularity tissues regrow quickly after treatment, whereas the slower tumours in the 4% tissue are eradicated. The dose required to remove a tumour of a particular metabolic type increased with tissue vascularity; steeply at first, then more slowly past 6% vasculature. As with the total lactate produced, (figure 4.6) it is surprising that the dose required for tumour eradication scales with the vascularity of the tissue rather than with the growth rate of the tumour. The two results together indicate that high acidity offers a protective advantage. As further confirmation that growth rate is not the the most important feature, the top right of figure 4.7 shows the 4% tissue where the type C tumour is the only one to make an, albeit small, recovery despite having the slowest growth rate. To examine the effect of a given metabolic phenotype on treatment response, the tissues were treated at variable doses of cisplatin. Figure 4.8 shows the results of treating tumours in 6% tissue with doses from 1.00 to 1.10 g of cisplatin; a dose range chosen simply to highlight the dynamics. Although the type A tumour has a faster growth rate than the no CAF condition, it is less treatment resistant. Since these two tumours are metabolically similar, it is most probable that the additional vasculature that the CAFs stimulate works against the tumour to increase drug delivery. The

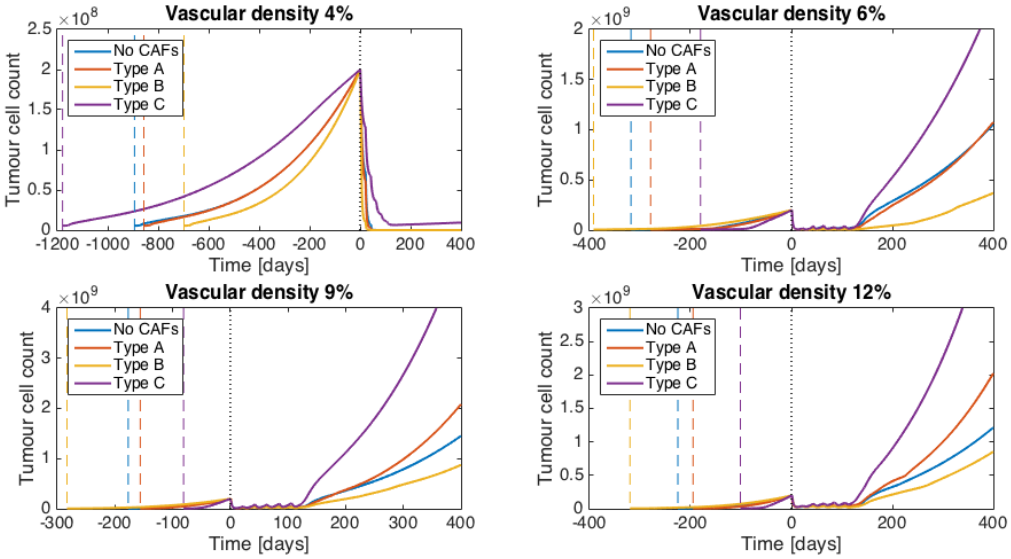

Figure 4.7: Tumour response to treatment at a dose of 900 mg in four different tissues with vascular densities of 4, 6 9 and 12%. Four metabolic conditions are shown for each tissue. Tumours are grown to 2×10^8 cells over various times; dashed lines of matching colour indicate the start of the growth curves for each metabolic condition, with the black dotted line indicating the onset of treatment at day 0 and lasting 126 days.

same order of resistance between metabolic types is seen in the 4% tissue at lower doses, although all of the tumours regrow extremely slowly. Order is also preserved in the 9% tissue; the no CAF and type C tumours can survive a dose of 1.10 g, only the type C survives at 1.20g.

Repeating the above experiment in 12% tissue a very different result is achieved. Since the vasculature is too high for optimal growth, any increase by the CAFs is a disadvantage to the tumour through the angiogenesis they promote. The no CAF condition was therefore the most resistant to treatment despite its slow growth rate. For the remaining three metabolic conditions, a number of competing factors determine their resistance. A poor vascular supply within the tumour provides a niche in which less drug is delivered and more cells are protected through quiescence, however it also slows the regrowth rate so the tumour is less able to repopulate between treatment cycles. CAFs do still offer an advantage in some cases; as both the most acidic and fastest growing tumour, the type C tumours have a large advantage over both type A and B. With the highest inter-tumour vascularity, the type A tumour has the lowest resistance and the type B falls in between.

Figures 4.10 and 4.11 show the spatial distribution of cells and lactate in tumours

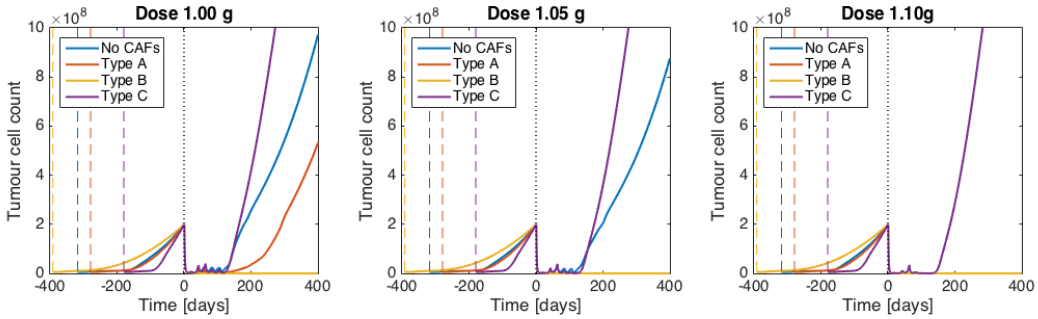

Figure 4.8: Tumour response to increasing doses of cisplatin of 1.00 g (left), 1.05 g (centre) and 1.10 g (right) in 6% vascularity tissue. Tumours are grown to 2×10^8 cells over various times; dashed lines of matching colour indicate the start of the growth curves for each metabolic condition, with the black dotted line indicating the onset of treatment at day 0 and lasting 126 days.

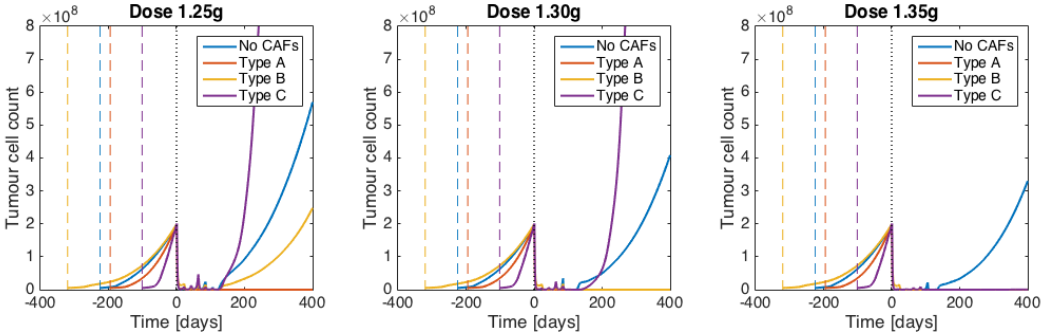

Figure 4.9: Tumour response to increasing doses of cisplatin of 1.25 g (left), 1.30 g (centre) and 1.35 g (right) in 12% vascularity tissue. Tumours are grown to 2×10^8 cells over various times; dashed lines of matching colour indicate the start of the growth curves for each metabolic condition, with the black dotted line indicating the onset of treatment at day 0 and lasting 126 days.

in tissues of 4%, 6% and 12% vascular density. Again, tumours grow to 2×10^8 cells before treatment is simulated. Although the number of cells at the onset of treatment is the same in each case, the distribution of tumours and CAFs are qualitatively very different between tissues. In the 4% tissue, there is no distinct tumour area. Instead, the tumour grows out into the stroma as a diffuse, homogeneous and mixed population comprising tumour, CAFs stroma and vasculature, regardless of the metabolic phenotype of the CAFs. Although the two 4% tumours look similar in terms of their size and density, they are quite different metabolically. In the type B tumour, lactate produced by the tumour sustains the CAFs, aiding growth and motility. In the type C, the two cell types are in direct competition and, since the cell distribution is so homogeneous, there is no real advantage to the coupling and the tumour grows slowest of the four metabolic types. Much of the lactate in this tumour is produced

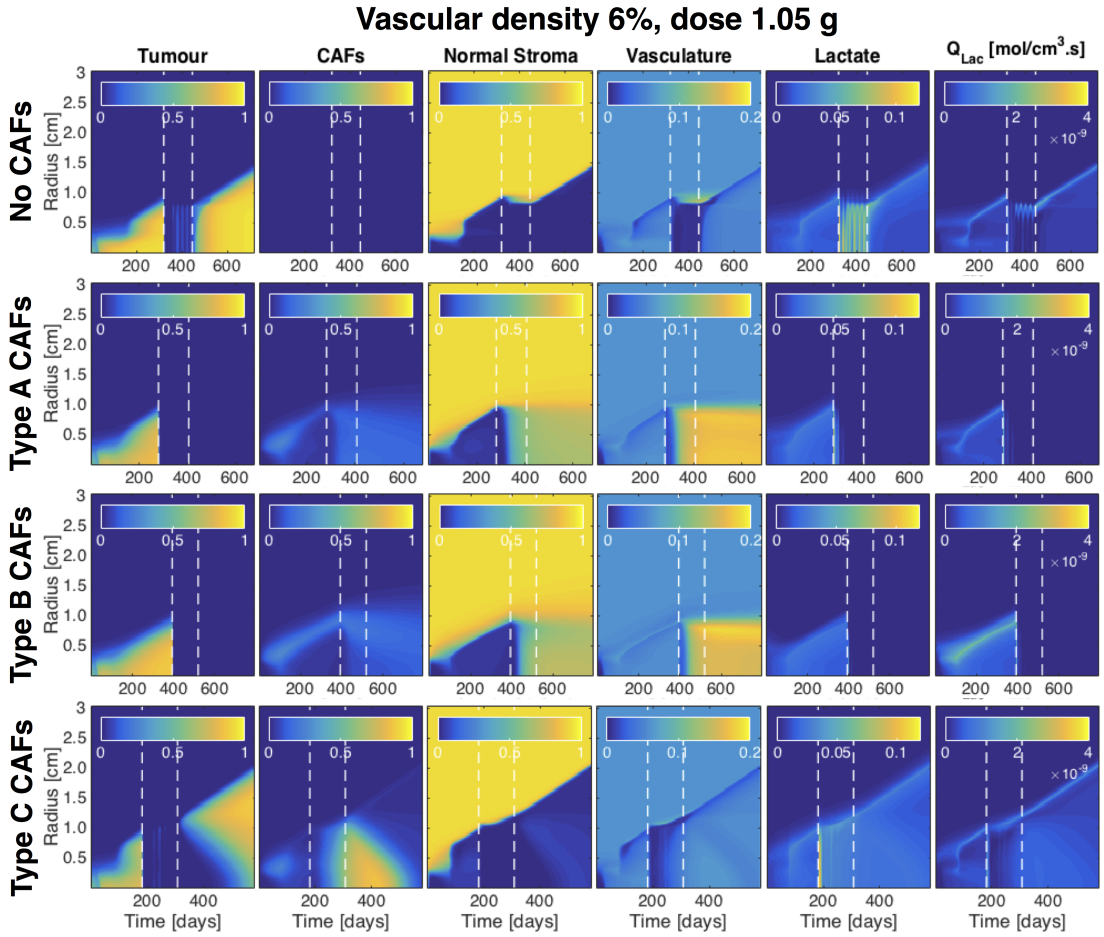

Figure 4.10: Tumour growth and response to a 1.05 g dose of cisplatin over a 3 cm radius sphere of tissue for the four metabolic conditions. Spatial distribution of tumour, CAFs, stroma, vasculature, (as fraction of maximum cell density Ω), lactate (as fraction of $c_{l,max}$) and net lactate production Q_{Lac} are shown.

by the CAFs as can be seen by the matching space that the CAFs and lactate fill, as well as the lack of change to the lactate during the treatment window, as compared to in the type B tumour where there is a significant change.

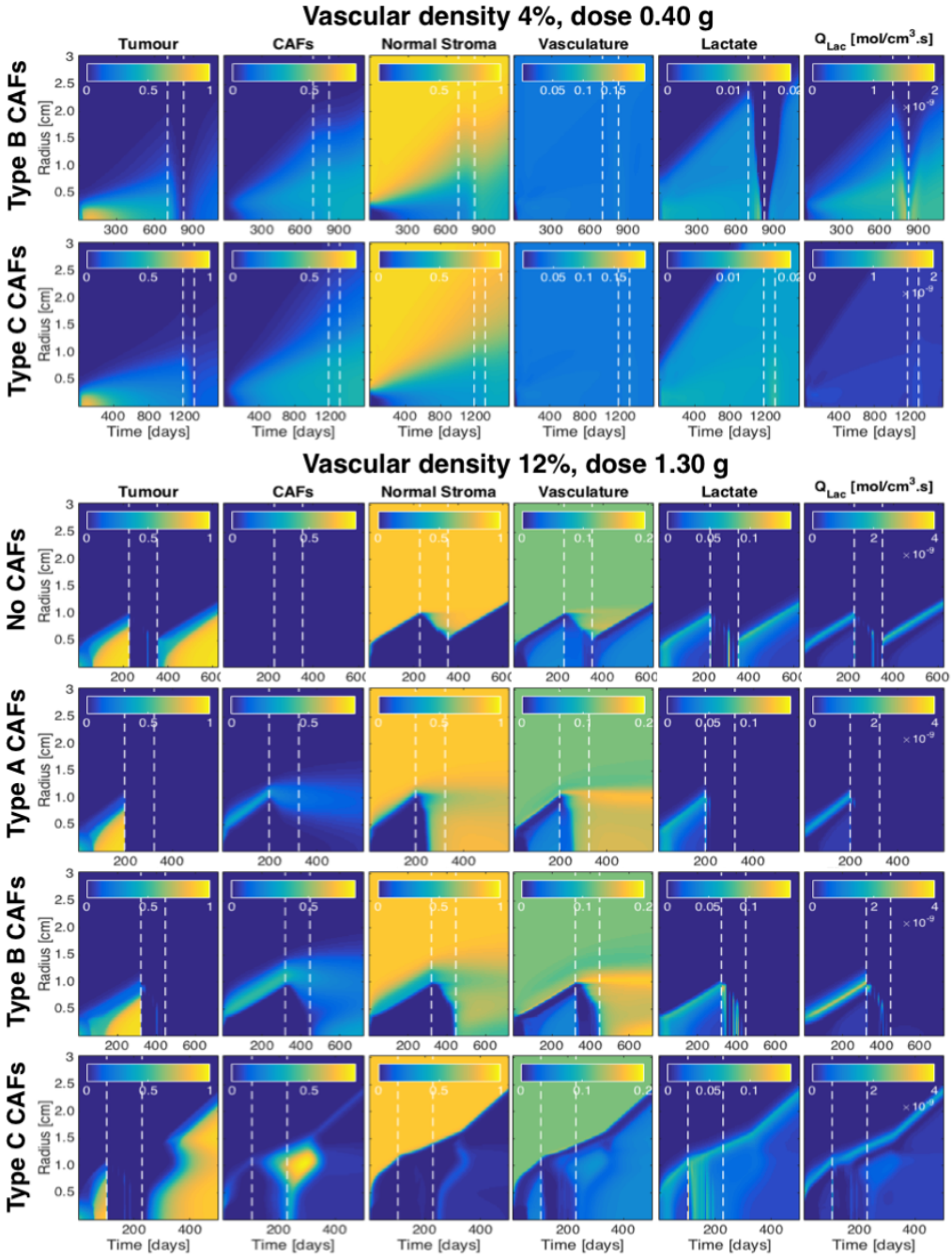

Figure 4.11: Spatial view of tissue distribution and lactate production over the tumour region for the type B and C metabolic phenotypes in 4%, and all phenotypes in 12% vascularity tissue. Spatial distribution of tumour, CAFs, stroma, vasculature (as fraction of maximum cell density Ω), lactate (as fraction of $c_{l,max}$) and net lactate production Q_{Lac} are shown. White dashed lines show treatment window for treatment with 0.40 g and 1.30 g of cisplatin for the 4% and 12% tissues respectively. Lactate and Q_{Lac} images are scaled differently between 4% and 12% images.

All four metabolic phenotypes are shown in figure 4.10. The tumours are more

dense with some visible heterogeneity, however CAFs still spread quite far into the tumour and there is a small population of stromal cells within the tumours also. Again, there is little contrast between the tumour and outside tissue in terms of vascularity, although in the no CAF and type C conditions a gap with very low cell density has opened up at the tumour periphery due to a build up of lactate. It is clearer from this image how the hierarchy of treatment response occurs in the sub-optimal vascularity tissues; the no CAF and type C tumours both utilise this vascular-poor region to resist the treatment. Both also leave large pools of lactate when cells are killed which in turn further damages the vasculature. The bottom row of figure 4.10 clearly shows the tumour regrowing from cells remaining where the vasculature has been destroyed. The same can be seen in the no CAF condition, although it is less obvious. In each tumour, slightly more lactate is produced at the periphery as would be expected from increased access to glucose in this area.

The equivalent set of images is shown for the 12% tissue in the lower half of figure 4.11. The change to the composition of the tumours is remarkable, with clear regions of both tissue and metabolic heterogeneity visible. The acidity of the tumours confines the CAFs fully to the periphery, however their impact on the dynamics of the tumour is by no means marginalised. Metabolic heterogeneity can be seen in the Q_{Lac} images; a leading edge of CAFs with highly glycolytic metabolism produces an advancing front of acid, which kills healthy stroma and vasculature clearing space for invasion. The lactate produced here is used as an energy source for the next layer of the tumour where the blood supply is very poor, then finally low-rate glycolysis occurs again at the core. This layer structure can be seen most clearly in the type B tumour where the peripheral CAFs free up even more glucose for glycolysis. The tumour vascular density is significantly lower than that of the surrounding tissue, varying around 1-7%.

Resisting treatment in high vascularity tissue appears to be more about maintaining an acidic tumourgenic niche than about the level of vasculature. The most resistant no CAF tumour has the highest intratumoural vasculature of the four during the treatment window, however it is the only tumour in which the surrounding stroma does not rebound. The least resistant type A tumour sees the surrounding stromal cells grow quickly to fill the space meaning the few surviving tumour cells are unable to compete. The same thing happens, slightly less quickly, in the type B tumour and very slightly in the type C tumour as well; the regrowth of both the stromal cells and vasculature can be seen surrounding the fibrotic outgrowth of CAFs in the bottom row of figure 4.11, despite the glycolytic acid production from the CAFs. The very

high surrounding vasculature is efficient at removing acid from the system, allowing other cell types to thrive when tumour cells die during the treatment window.

4.4 Discussion

The poor survival rate of ovarian cancer can be largely attributed to the fact that most patients are already metastatic at diagnosis. Since screening programmes have been unsuccessful at aiding the early detection of the disease, it has very poor prognosis. A deeper understanding of tumour growth and its reliance on metabolic phenotype is important to model and predict tumour development. Identifying and exploiting altered metabolism in cancers may allow for the development of new targeted therapies and patient specific treatment strategies. With this objective in mind, this work presents a spatial mathematical model capable of simulating the interaction between the tumour and surrounding tissue on both a cellular and metabolic level. The model has the potential to reproduce the dynamics of human disease *in silico*, allowing for the direct comparison of tumour growth and treatment response outcomes under a wide range of environmental conditions. There are two main factors that have been considered in the model; the vascular density of the tissue in which the tumour grows and the behaviour of CAFs recruited by the tumour, which may engage in different types of metabolic coupling with the tumour cells. Although previous studies have utilised mathematical models to study the tumour interaction with its environment, this is the first model of its kind which fully integrates a cellular tissue interaction model with a detailed study of multiple possible metabolic regimes.

Although metastasis to multiple locations is common in many cancer types, there are a number of features which make ovarian cancer an ideal model system for this study. Metastatic locations are common between patients, yet very diverse in terms of their tissue composition; tumours arriving from the same primary will implant in tissues with high variation in stromal composition and vascularisation such as the omentum and lymph nodes display. Following standard-of-care debulking surgery, small amounts of tumour remain. These fragments may then regrow, simultaneously beginning repopulation of multiple environments such as occurs in the model. Finally, the common phenomenon of platinum sensitive recurrence means that ignoring the gradual build up of genetic resistance, in order to study instead environmentally conferred resistance, is a reasonable first approximation in this instance. Despite these features, the model remains general enough for its predictions to be applicable

to many other metastatic solid tumours in which the involvement of CAFs is known to occur.

One of the key early predictions of this model is that there is an optimal tissue vascularity for tumour growth, which occurs here in the 9% vascular density condition. This is a somewhat arbitrary measure of vascularity for the purposes of the model; treating vascularity as a cell density rather than modelling discrete vessels is a simplification only possible due to the large scale of the simulation domain compared to that of the individula cells. Nevertheless, it clearly demonstrates the trade-off between access to nutrients and the accumulation of acid at the invasive edge, which together, dictate the growth rate of the tumour. This optimal tissue vascularity has been predicted previously in a mathematical modelling study by Patel *et al* [125], has been discussed in a mathematical oncology review of acid-mediated invasion [120] and is seen clinically in the preference of particular cancers for specific metastatic sites which may be particularly well vascularised, such as the omentum. The existence of both anti- and proangiogenic treatments is also indicative of this phenomenon. The model showed that the intratumoural vascularity only correlated with external tissue vascularity up the 9% vascular density condition, after which it anticorrelated. Although many studies exist comparing intratumoural vascularity to proliferation rate, there are none which quantitatively compare tumour growth rate to the vascularity of the external tissue environment. This observation may be relevant for therapies where pro- or antivascular agents are used alone or in conjunction with other therapies, as there is the potential to unintentionally push the tumour vasculature towards a more optimal growth condition.

The tumours can be seen to grow in stages, with growth accelerating following the establishment of vascularity with in the tumour. After 200 days of growth, the total lactate in the tumour area was found to positively correlate with tissue vascularity rather than growth rate, suggesting the most important factor for acid production is access to glucose. The higher the tissue vasculature, the more this lactate production is seen to concentrate at the tumour periphery. Normalising for tumour size at 200 days, it becomes clear that both very high and low vascularity tumours accumulate more lactate per tumour cell; this is likely due to a lack of ability to remove acid at low vascularity and the glycolytic exploitation of plentiful glucose at high vascularity. It is worth emphasising an interesting prediction with regards to ^{13}C metabolic imaging; the tumours with the highest lactate turnover may not necessarily be the fastest growing due to competing environmental constraints. In this case, even though their lactate turnover rate is higher, the 12% vascularity tumours grow slower than the

9% tumours because their invasive potential is reduced through increased removal of acid from the system. Additionally, although the total lactate is high in the low vascularity tissue tumours, figure 4.11 demonstrates that it is at low concentration as the tumours in these tissues are of extremely low cell density compared to tumours in more vascular tissues. Such tumours would likely produce low lactate conversion rates on ^{13}C images despite being quite acidic overall.

The CAFs, through their metabolic coupling with the tumour cells, have a remarkable impact on the growth rate of the tumour, despite being comparably small in number to the other cell types, the effect of which is most clearly visible in figures 4.5 and 4.7. In the very low 4% and 5% vascularity tissues, the type B metabolism, where lactate produced by the tumour may be used by the CAFs as an energy source, provides a huge advantage over the other phenotypes. When nutrients are scarce this phenotype removes competition from the other cells, but at the expense of removing lactate from the system and deacidifying the microenvironment, thereby preserving the healthy tissue and reducing invasion. For this reason, the type B coupling very quickly becomes by far the least efficient, producing the slowest growing tumours in almost all tissues, even though it has a slight advantage when tumours are very small for the 5-6%. In each case, the type A (no metabolic coupling) CAFs demonstrate a small advantage over the no CAF condition due the increased angiogenesis and motility they provide. This growth advantage is stable across all tissues, even when vascularity is higher than optimal.

The type C CAFs with full metabolic coupling, which may both use and produce lactate, offer the biggest growth advantage in every tissue above 4% vascularity; the size of this benefit grows with increasing vascularity. It is clear from these results that a 'reverse Warburg' effect would have very poor outcome for patients in virtually every situation as these tumours grow 2-4 times faster than every other phenotype. This type of metabolism not only allows the cells to perform the most efficient possible metabolism heterogeneously across the tumour, but since the CAFs are largely peripheral, the lactate they produce penetrates deeper into the healthy stroma than with any other phenotype, clearing the path for invasion. The high vascularity tumours have more peripherally concentrated CAFs which in turn, have the most access to glucose, explaining the increasing efficiency of this strategy with tissue vascularity.

By allowing tumours to grow to the same number of cells before simulating chemotherapy, it was possible to examine the differences in treatment resistance caused by the different environmental growth conditions. Although growth rate was a factor in determining resistance, it was not the most important one in this model.

Resistance scaled, almost counter-intuitively to some extent, with tissue vascularity rather than with growth rate, despite the greater drug delivery ability of high vascularity tissues. One reason for this is that above the optimal 9% vascularity tissue, the vascular density within the tumour volume drops, as the increased acid present damages the vessels. In general, the increased angiogenesis conferred by the CAFs reduced treatment resistance, with the no CAF condition proving the most resistant in high vascularity tissues and second to type C in all other tissues. In tissues up to and including the optimal 9% vascular density, survival was largely determined by a trade off between growth rate and drug delivery. Concentrated regions of acidity reduce drug delivery, while angiogenesis increases it, therefore creating the order of resistance seen in figure 4.8. The picture is slightly different above 9% however; since drug delivery is strong, survival of the tumours relies on the creation and maintenance of a tumorigenic niche. The most resistant no CAF case demonstrates this; by maintaining a intertumoural vascular structure as well as an acidic environment, the space remains free for a very small tumour cell population to repopulate unchallenged. The role of the fibroblasts in normal tissue as wound healers suddenly becomes evident; in the other three phenotypes they rebuild vasculature and allow healthy stroma to regrow during the treatment phase. Although the type C CAFs also promote healing, they simultaneously maintain the tumour niche through the acid they produce which provides a resistive advantage over the other two CAF metabolic phenotypes.

There are several further predictions of the model which are worth mentioning for their reproduction of real clinical phenomena. As already alluded to, the normal role of fibroblasts is in healing damaged tissue following injury, a behaviour that can be seen to occur also in the model results. This behaviour applies equally to a tumour site, with cancers often being described as a 'wound that will not heal'. Fibrosis is the growth of active fibroblasts which may often follow cancer treatment, causing large growths at the site; despite the very slow CAF turnover rate, such fibrotic growths can be seen in figures 4.10 and 4.11 in cases where the tumour is completely or partially healed. The type C CAFs in particular cause very large regions of fibrosis, filling the space left behind by the tumour, which raises the question as to whether lactate production may have a role in this particular pathology. A second interesting feature of the model are the regions of both tissue and metabolic heterogeneity which spontaneously emerge, an effect more pronounced in the higher vasculature tissues. These regions, which appear as concentric layers into the tumour, provide evidence for metabolic coupling within the tumour itself regardless of the behaviour of the CAFs. Highly glycolytic cells on the periphery have access to the most glucose, producing

large quantities of lactate which is then used as an energy source by cells in the next layer. The cells in the centre of the tumour are again slightly glycolytic, but far less so than those on the leading edge. The emergence of such structure adds significant weight to the lactate shuttle theory of tumour metabolism [4, 349, 350] and provides insight into the potential benefit the CAFs, particularly type C CAFs, could provide by enhancing further the glycolytic activity at the tumour rim.

There are several predictions of this model which have implications for the use of hyperpolarised [1-^{13}C]pyruvate imaging as a means of determining treatment response. The net lactate output rate of the tumour, Q_{Lac}, is seen to drop during treatment; however for those tumours which are not eradicated, it remains high at the periphery and rises in the core during treatment, even though there is little or no visible mass. If this prediction is correct, probing the tumour with hyperpolarised [1-^{13}C]pyruvate and spatially mapping the conversion rate to lactate should be able to distinguish between tumours which respond and those which regrow, even when anatomical imaging shows little difference. Another interesting result is the build up of lactate that occurs following treatment; an effect best seen for the no CAF and type C conditions in figure 4.10. This release of lactate following treatment is a commonly observed clinical effect; what is perhaps interesting here is that it occurs far more prominently in cases where the tumour is not removed, and is only observed for certain metabolic phenotypes. In each case where this lactate build up occurs, it is accompanied by a drop in Q_{Lac}, at least initially, which then slowly rises for tumours which will regrow following treatment. Monitoring both this extracellular lactate pool size and the metabolic lactate turnover rate simultaneously, may give greater insight into treatment response than is currently available. Although currently not clinically approved, measurements of this type may be available through imaging patients injected with co-polarised [1-^{13}C]pyruvate and ^{13}C-bicarbonate, a marker of extracellular pH, at some time in the future.

Returning to the example histology data from good and poor responders shown in figure 4.1, it is encouraging to observe visual similarities between these images and the model outputs. Considering first the histology data of tissue from the good responders, tumours appear fairly homogeneous with low but even staining for CA125. Vessels are sparsely but evenly distributed and there is some fibroblast infiltration which again appears quite uniform throughout the tissue. The simulation results from the 4% vascular density tissue, which demonstrated the best treatment response, echoes this pattern; figure 4.11 shows each cell type distributed homogeneously within the tumour region. In contrast, simulations of tumours growing in the 12% vascularity

tissue, the poorest responders to treatment, can be seen in 4.11 to produce far more heterogeneous tissue compositions. Tumour cells and vessels form distinct domains and the fibroblasts are densely clustered on the periphery of the tumour; both of these effects are also seen in the histology data for the bad responders.

It is worth noting that the method of varying the vascular basal death rate δ_v is an arbitrary fix to control the target tissue density. This method was used because δ_v proved to be the only single parameter capable of generating a range of stable conditions as it was varied; it is not an accurate model of the physiology. In reality, normal tissue densities are likely to be controlled by VEGF production, which is in turn controlled through HIF1 stabilisation by hypoxia in tissues where oxygen availability is too low. In tumour tissue, vascular growth may be accelerated by HIF1 over-expression resulting in higher levels of VEGF than is warranted by hypoxia and elevated tissue lactate concentration alone. It would therefore be expected that the dynamics governing vascular proliferation and death would be very different in tumour and normal tissue; the simplifying assumptions made here and in controlling the tissue density are noted as limitations of the model.

Although the model is capable of reproducing realistic simulations of human disease, there are a number of limitations to such an approach. The main consideration is the size of the model and the large number of free parameters which have been calculated, derived from the literature or in some cases estimated. Models of this complexity are difficult to parameterise and validate, however this does not necessarily invalidate the results if they are used carefully. Very few parameters are varied between the tissue conditions- only the vascular turnover rate δ_v and the CAF recruitment rate k_{sf}- which allows for comparative if not completely objective conclusions to be drawn. Another limitation is the lack of human data available for validation of the model, with many parameters being drawn from animal or even *in vitro* studies. As more data become available, particularly from *in vivo* human studies of tumour metabolism, it may be possible to refine the model and its parameters to the point where it provides a useful clinical tool for predicting treatment response. A final and more subtle limitation of the model worth mentioning is in the form of its lactate production output metric Q_{Lac}. The way that the model is designed means it is only possible to track the net lactate production rate, but not the rates of use and production individually. Given that the type C tumours are so acidic, it is highly likely that both of these metabolic processes are occurring simultaneously across heterogeneous regions on both the tumour and CAFs. Although the spatial distribution Q_{Lac} is useful in making predictions of how such tumours would present on hyperpolarised

[1-^{13}C]pyruvate images, it is worth noting that future versions of the model could be better able to spatially localise the movement of lactate in the system, thereby improving predictions for metabolic imaging.

4.5 Conclusion

This work presents a spatial mathematical model of tumour growth and treatment response, in which an identical initial tumour population is exposed to a range of different tissue and metabolic environments. The model is unique in its ability to simulate multiple metabolic conditions for comparison, and is capable of reproducing many features and phenomena that are found in human disease. There are two main focal points of the model; the first is the effect of differing vascular density in the native tissue and the second is the interaction with, and metabolic phenotype of, recruited CAFs. The vascular density of the tissue in which the tumour grows effected both the growth rate of the tumour and the preferred CAF phenotype; there was an optimal vascular density for tumour growth at 9%, after which the vasculature removed too much acid and the invasive potential of the tumour was reduced. CAFs capable of metabolising lactate provided a growth advantage in very poorly vascularised tissue, however in general provided the slowest growing tumours. Coupling with CAFs which both produced and utilised lactate as in the 'reverse Warburg effect', produced tumours which had much faster growth rates than any other phenotype and high treatment resistance due to their promotion of an acidic tumorigenic niche. The no CAF condition produced in general the second slowest tumour growth, however it offered high treatment resistance; particularly in highly vascular tissue. The model presented here may be clinically valuable in understanding the tumour interaction with its environment and may prove to be a useful tool in aiding the interpretation of histopathology and metabolic imaging data in order to make informed, patient-specific treatment decisions in the future.

Chapter 5

Initial insights from early human hyperpolarised ^{13}C-pyruvate imaging in the breast and brain

Hyperpolarised imaging with ^{13}C-labelled molecules is an emerging technique with the ability to dynamically and non-invasively probe tissue metabolism. Since the first human study was published in 2014, sites around the world have been refining and optimising the technique for clinical application. The first molecule to be approved for human use is [1-^{13}C]pyruvate, the conversion of which to [1-^{13}C]lactate has been shown to correlate with tumour grade and to detect treatment response in preclinical animal models. Accurate quantification of this exchange reaction is therefore of high importance if hyperpolarised data is to be utilised to inform clinical decisions. Hyperpolarised ^{13}C imaging data is presented from four of the first subjects to be imaged at Addenbrooke's Hospital in Cambridge. Two cancer patients and two healthy volunteers, representing the first healthy brain images to be acquired globally, received dynamic hyperpolarised ^{13}C MRI imaging following injection with 0.4 mL/kg of hyperpolarised ^{13}C-pyruvate solution at ∼250 mM. Previously developed analysis and quantification methods, consisting of a Markov random field segmentation for automatic lesion detection, kinetic modelling and model-free quantification methods are applied to the data. The suitability these methodologies to provide an accurate and objective means of quantifying human ^{13}C imaging data is demonstrated.

5.1 Introduction

Since the initial conception of dynamic nuclear polarisation (DNP) as a method of retaining liquid-state polarisation of ^{13}C-labelled molecules in 2003 [152], the field of hyperpolarised imaging has expanded rapidly. The two proof of concept studies published by Golman *et al* in the same year [186, 154] demonstrated for the first time the feasibility of retaining sufficient polarisation to perform angiography with ^{13}C-labelled urea *in vivo*. This was swiftly followed by the discovery that metabolites of interest, initially [1-^{13}C]pyruvate, could be imaged in real time, along with their metabolic breakdown products, to non-invasively probe cellular metabolism [187]. The potential and versatility of the technique has led to a number of of pre-clinical studies at multiple sites world wide, largely focused on the breakdown of ^{13}C-pyruvate to ^{13}C-lactate as a marker of aerobic glycolysis and a potential indicator of treatment response in oncology [291, 191, 169], as well as other applications including diabetes [198] and cardiac metabolism [178]. Other ^{13}C-labelled probes also demonstrated early success for probing tissue biology in animal models; notably, ^{13}C-bicarbonate to image pH *in vivo* [165], the [1-^{13}C]fumarate to [1-^{13}C]malate reaction as a marker of cellular necrosis [168] and [1-^{13}C]glutamate for imaging tumour metabolism [204, 206].

The clinical potential of DNP has attracted significant interest not only in academia but in industry as well. The technique is particularly appealing since existing MRI technology which is already in clinical use for patient scanning can be re-purposed, requiring only a clinical hyperpolariser and ^{13}C-specific MR coils as additional hardware. GE Global Healthcare became the main corporate driver for hardware innovation and in 2011, published the design and sucessful testing of a prototype sterile hyperpolariser intended for clinical use [155]. This was the first version of what would become the GE SPINlab, the first commercial clinical hyperpolariser of which there are now around 30 worldwide.

The first human study was carried out using a non-sterile prototype system in a clean room at the University of California, San Fransisco (UCSF) in 2013 [156]. In this landmark first-in-man study, the safety and feasibility of the technique was demonstrated in 31 prostate cancer patients who each received a dose of up to 0.1 mmol/kg of hyperpolarised [1-^{13}C]pyruvate. Although there were 10 adverse effects in 8 patients, these were all considered to be minor and the agent was tolerated well in general. The conversion rate of pyruvate to lactate was found to be four to five times higher in the tumour than in the surrounding healthy prostate and in one case, a previously undetectable region of low grade tumour was detected, and later

confirmed by biopsy, via high lactate production in the region. The forward reaction rate constant k_P was found to be 0.045 ± 0.025 s^{-1} for conversion of [1-^{13}C]pyruvate to [1-^{13}C]lactate in tumour voxels and 0.009 ± 0.003 s^{-1} for contralateral voxels containing healthy tissue.

Only two other human study in hyperpolarised ^{13}C imaging has been published to date, both limited to very few subjects. In 2016, a pilot study at Sunnybrook Hospital Toronto imaged the metabolism of [1-^{13}C]pyruvate to [1-^{13}C]lactate and ^{13}C-bicarbonate in the healthy human heart in four volunteers [214]. Bicarbonate production was clearly observed in the myocardium whilst lactate signal was more diffusely seen in the blood, muscle and tissues. The same dose as the previous study of 0.1 mmol/kg was given with no adverse effects. A very recent third publication from UCSF images a single prostate cancer patient before and six weeks after treatment with androgen deprivation therapy [215]. The k_P was derived from a single large tumour-containing voxel, with the pretreatment k_P of 0.025 s^{-1} dropping to 0.007 s^{-1} following treatment. This short case study provides a first glimpse of the potential to image treatment response in human tumours.

Although there are no further published studies, there have been several conference abstracts presented on human imaging over the last two years, mostly from UCSF and Memorial Sloane Kettering (MSK) in New York. In 2016, MSK presented their study of [1-^{13}C]pyruvate metabolism in a breast tumour to the International Society for Magnetic Resonance in Medicine (ISMRM) [211]. At the same conference the following year, they presented a study in prostate cancer investigating metabolic dynamics of pyruvate to lactate conversion and comparing to histological grade [213]. In the same year at ISMRM, UCSF presented imaging data of ^{13}C-pyruvate metabolism in three glioblastoma patients [212], along with a methodology abstract for automated kinetic modelling in human brain tumours using their SIVIC software [351]. They demonstrated the feasibility of a specialised symmetric echo planar imaging sequence for metabolite-specific imaging of hyperpolarised pyruvate and lactate in the human prostate [352] and finally, presented spectroscopic imaging data from patients with liver metastases [353]. Although these were the only two sites to present patient data, there has been a steady increase in both conference papers and published articles on pre-clinical ^{13}C imaging with new applications and new probes, and on technical developments in pulse programming, reconstruction, image processing and quantification from multiple sites worldwide over recent years.

Much of the early translational work in hyperpolarised ^{13}C MRI has been in imaging the abnormally high metabolism of pyruvate to lactate within various oncological

applications. Of the small number of sites with the necessary technical set up and regulatory approval to perform human imaging, two focus purely on cancer. UCSF are currently imaging patients with renal cancer, glioblastoma, prostate cancer and advanced metastases in the liver as well as other organs, while MSK are studying cancer in the prostate and breast. Also popular is the application of ^{13}C-pyruvate to image the heart; both Sunnybrook and Oxford are beginning patient trials in cardiac imaging to asses metabolic changes to damaged myocardial tissue. [1-^{13}C]pyruvate is currently the only ^{13}C-labelled probe to be approved for patient imaging, however a number of other molecules are likely to be available within the next few years. UCSF are currently in the process of approving ^{13}C-urea, [2-^{13}C]pyruvate, [1-^{13}C]lactate and eventually [1-^{13}C]fumarate for use in patients.

Here at Addenbrooke's Hospital Cambridge, work has been under way to achieve clinical translation of hyperpolarised imaging for around five years. In 2013, the 5 T GE SPINlab hyperpolariser was installed in MRIS in a small room adjacent to the clinical 3 T GE sigma MRI scanner, with a small RF-safe hatch between the two to transfer the hyperpolarised agent from the polariser to the patient. This was followed around a year later by the installation of the quality control (QC) unit, which measures the pyruvate concentration, pH, volume, EPA (electron paramagnetic agent) concentration and polarisation of the hyperpolarised pyruvate solution to ensure each of these parameters is within clinically safe bounds prior to injection into a patient via a medrad syringe. While this hardware was being tested, calibrated and optimised, a pharmacy was also being developed for the manufacture of sterile fluid paths on site. These paths consist of closed, helium-flushed tubing, with a vial at one end containing the compound for hyperpolarisation, along with an EPA, which is inserted down into the SPINlab. The remaining two compartments are filled with a dissolution fluid and buffer, all of which must be assembled in perfectly sterile conditions. In order to achieve this, a laminar flow cabinet was set up within which the paths could be filled by trained pharmacists. The quantities of each element going into the fluid paths then required validation and testing to ensure consistent and physiologically safe results after polarisation and measurement by the QC. Sterility checks were additionally performed on the end product.

Technical developments were, and still are, a major part of the preparations for both the collection and processing of clinical data. On the MRI scanner, multinuclear spectroscopy (MNS) research software was installed and calibrated to provide the highly specialised rapid sequences required to scan multiple metabolites at shifted

^{13}C-frequencies. Specialised MR transmit and receive coils duel-tuned to ^{1}H/^{13}C-frequency were acquired from Rapid Biomedical in order to collect carbon and proton images sequentially, without a coil change, for co-registration of the metabolic to anatomical data. Finally, methods for processing, analysing and quantifying the complex 5-dimensional data produced were required; the previous chapters have been directed at solving these problems and developing robust methodologies suitable for clinical use. In order to make clinical decisions such as an assessment of treatment response or the grade of a tumour based on hyperpolarised imaging data, reliable and repeatable methods are required for processing and quantifying the data. The region of interest (ROI) detection algorithm detailed in a previous chapter utilises a Markov random field model to automatically detect regions of specific metabolic activities and is capable of distinguishing low from high lactate production across a tumour. Coupled with the rigorously tested kinetic modelling and model-free parametric mapping approaches defined in chapter 2, this work has the potential to provide clinicians with simple, clear quantitative measures which have the potential to aid such decisions.

Several projects are simultaneously occurring under the umbrella 'MISSION' title at Cambridge, with each sub-project directed to a separate clinical question. In oncology, patient studies are being carried out in glioma, and in breast, ovarian, and liver cancers with patients recruited as fluid paths become available. Approval has also been obtained for neurological applications in multiple sclerosis (MS) and stroke imaging, with Cambridge the only clinical site to be planning studies in this area. It is hoped that hyperpolarised ^{13}C-pyruvate imaging will be valuable in studying the glycolytic metabolism that occurs due to pathological immune response in MS plaques, and in detecting viable tissue regions through their protective lactate production in the recovering post-stroke brain. Although [1-^{13}C]pyruvate is currently the only molecule approved for human use, applications for [1-^{13}C]fumarate approval are being developed. At this point in time, a number of volunteers and patients have received hyperpolarised ^{13}C scans in Cambridge; successful ^{13}C images have been produced from the brains of two healthy volunteers, one glioma patient and one breast cancer patient, as well as from the brain of one MS patient and a liver volunteer. In the remainder of this chapter, the first four of these early imaging trials will be presented as case studies and the methods for analysing, segmenting and quantifying the data set out in earlier chapters will be applied to each in turn to demonstrate their applicability to clinical data. The quantitative methods applied, along with the deeper understanding of lactate metabolism gleaned through the tumour simulation

model detailed in chapter 4, will be valuable in the clinical interpretation of this and future hyperpolarised imaging data.

5.2 Methods

5.2.1 Subject recruitment and patient background

Two healthy volunteers (HV) and two oncology patients, one breast and one glioma case, received hyperpolarised [1-^{13}C]pyruvate spectroscopic imaging scans between September 2016 and January 2017 at Addenbrooke's hospital Cambridge. Subjects were recruited and gave informed written consent under the physiological study protocol 'MISSION' (Molecular Imaging and Spectroscopy with Stable Isotopes in Oncology and Neurology), which was approved by the Cambridge South Research Ethics Committee and sponsored by the University of Cambridge and Cambridge University Hospitals NHS Foundation Trust. Exclusion criteria for both patients and volunteers were as follows: under 18 years of age; uncontrolled diabetes or glucose deranging condition; pregnant or breastfeeding; known allergies to gadolinium or pyruvate; MRI unsuitable (e.g. severely obese, pacemaker, metal implants); BMI below 18.5 or above 32; failure to have full capacity to give informed written consent. Inclusion for cancer patients required them to present with a confirmed, treatment naive tumour of a suitable size for radiological imaging.

5.2.1.1 Breast case

A 61 year old female who was a BRCA gene carrier presented with a symptomatic mass in the left breast. Initial radiological images from dynamic contrast-enhanced MRI showed an irregular, avidly enhancing mass measuring 41×31×36 mm as well as some minor local lymph node involvement. The primary breast mass was confirmed by biopsy to be a grade 3, triple-negative invasive ductal carcinoma, positive for cytokeratin on immunohistochemistry. The patient was recruited and imaged for the hyperpolarised ^{13}C study prior to receiving chemotherapy.

5.2.1.2 Glioma case

A 66 year old male presented after experiencing confusion and vacant spells suddenly whilst on holiday. Initial radiological imaging identified a heterogeneously enhancing lesion spanning the posterior part of the right temporal, and anterior of the adjacent occipital lobes, with an axial size of 58×34 mm. The lesion was later confirmed as

an IDH-wildtype grade IV glioblastoma, exhibiting moderate nuclear pleomorphism, microvascular proliferation and palisading necrosis. The patient was imaged for the hyerpolarised ^{13}C study prior to receiving surgery.

5.2.2 ^{13}C-pyruvate administration

All subjects were injected with with ^{13}C-pyruvate at a dose of 0.4 mL/kg of an approximately 250 mM solution, equivalent to the 0.1 mmol/kg dose administered in human studies at the other sites which have previously published human studies. Sterile fluid paths were filled in a laminar flow cabinet, in clean room conditions, in a pharmacy set up specifically for the purpose. Vials were filled with 1.47 g of [1-^{13}C]pyruvate (Sigma Aldrich) containing the EPA AH111501 [Tris(8-carboxy-2,2,6,6 (tetra(methoxyethyl) benzo-[1,24,5']bis-(1,3)dithiole-4- yl)methyl sodium salt] at 15 mM. A receiver syringe was filled with 17.5 mL of neutralisation medium (600 mM NaOH / 333mM TRIS buffer) and 19 mL of sterile water and the dissolution syringe was filled with 38 mL of sterile water. A Medrad syringe was fitted to the sterile fluid path aseptically to collect the solution for injection following dissolution and filtering. This procedure was expected to produce a solution of approximately 250 mM pyruvate and physiological pH upon dissolution.

Fluid paths were stored at -20 °C and allowed to thaw for at least 60 minutes before lowering into a GE SPINlab hyperpolariser with a quality control module. Samples were polarised for at least 3 hours at 5 T and <1 K prior to dissolution. Upon dissolution, pyruvate and EPA concentration, pH, temperature, volume and polarisation were measured by the QC module to ensure each of these parameters was within the physiological acceptable range for injection; measurements took 35 s from dissolution time. In each case, the temperature was 34-35 °C and the volume was >40 mL. Full QC results for each of the four subjects are shown in table 5.1. Upon acceptance, the Medrad syringe containing the pyruvate solution was passed through a small hatch into the MR scan room, where it was loaded into a power injector and injected intravenously at a rate of 5 mL/s into the subject inside the scanner bore. Pyruvate solution was injected at the correct volume for the subjects weight up to a maximum of 40 mL (details in table 5.1), followed by a 20 mL saline flush. Imaging began at 12 s following the end of the injection with the exception of the breast patient, for whom imaging began after 25 s due to a technical error.

Table 5.1: QC results, individual dose details and total time from dissolution to injection for each subject.

Subject ID	Subject age	Subject weight	Polarisation	pH	Pyruvate conc.	EPA conc.	Volume injected	Actual dose	Total time
HV 1	38	95.8 kg	4.7%	7.5	253 mM	0.8 mM	38 mL	0.100 mmol/kg	56 s
HV 2	43	77.8 kg	24.9%	7.5	250 mM	0.4 mM	31 mL	0.100 mmol/kg	55 s
Breast	61	106 kg	24.1%	7.6	237 mM	0.5 mM	40 mL	0.089 mmol/kg	62 s
Glioma	66	97.7 kg	22.6%	7.9	232 mM	0.6 mM	39 mL	0.093 mmol/kg	58 s

5.2.3 Imaging and data acquisition

Subjects were imaged in a clinical 3 T MRI system (Signa HDx, GE Healthcare) using a ^{13}C-^{1}H multinuclear coil. A 1 minute IDEAL spiral CSI acquisition [182] was performed, with the imaging sequence initiated immediately following the end of the saline flush. Single-metabolite data was collected at the frequencies for pyruvate, lactate, pyruvate hydrate, alanine and bicarbonate. Prior to injection, each subject received ^{1}H anatomical imaging for the purpose of localisation and further ^{1}H imaging was additionally performed on each subject for anatomical reference and/or clinical diagnostic purposes. The imaging parameters differed between subjects and are detailed individually below.

5.2.3.1 Healthy volunteers

Both healthy volunteers were imaged using a single channel dual-tuned ^{1}H/^{13}C transmit/receive birdcage head coil (Rapid Biomedical). Both volunteers underwent 3D BRAVO T_1 imaging for anatomical reference with the following imaging parameters; flip angle 12°, repeat time (TR) = 8 ms, echo time (TE) = 32 ms, inversion time 450 ms, field of view (FOV) 24 cm, acquired resolution 2×2×2 mm, matrix size 256×256. Each volunteer then received the hyperpolarised ^{13}C-pyruvate injection before an axial IDEAL spiral acquisition was performed over 1 minute. Protocols for the ^{13}C imaging are given below for each volunteer.

HV1 was imaged with the following parameters: flip angle 5°, TR = 500 ms, TE = 1.7 ms, time resolution 4 s, FOV 24 cm, slice thickness 2 cm, inter-slice gap 2.5 mm, 4 slices, acquired resolution 6×6×20 mm. In this case, images were collected only for pyruvate and lactate. HV2 was imaged with the following parameters: flip angle 15°, TR = 260 ms, TE = 1.4 ms, time resolution 2.08 s, FOV 24 cm, slice thickness 3 cm, inter-slice gap 3.5 mm, 3 slices, acquired resolution 6×6×30 mm. All five metabolites were imaged. Each time point acquired a full FID spectrum, followed

by seven single shot 40-pt spiral acquisitions which, following Cartesian re-gridding during reconstruction, produced a real resolution of approximately 12×12×20/30 mm. Gaussian k-space filtering was applied during post-processing, interpolating to an effective image resolution of 1.875×1.875×20/30 mm.

5.2.3.2 Breast cancer patient

The patient was imaged using a prototype 8-channel ^{13}C breast coil (Rapid Biomedical) with 2 transmit/receive coils, and 6 receive-only coils. Corresponding ^{1}H anatomical imaging was performed using the standard body coil in an axial orientation. IDEAL spiral imaging was performed with the following parameters: flip angle 10°, TR = 260 ms, TE = 1.4 ms, time resolution 2.08 s, FOV 24 cm, slice thickness 3 cm, inter-slice gap 3 mm. 3 coronal slices were acquired with slice 2 centred on the tumour. Each time point acquired a full FID spectrum, followed by seven single shot 40-pt spiral acquisitions which, following Cartesian re-gridding during reconstruction, produced a real resolution of approximately 12×12×30 mm. Gaussian k-space filtering was applied during post-processing, interpolating to an effective image resolution of 1.875×1.875×30 mm.

5.2.3.3 Glioma Patient

The glioma patient was imaged with the same single channel dual-tuned ^{1}H/^{13}C transmit/receive birdcage head coil as the volunteers. The patient received 3D BRAVO T_1 imaging for anatomical reference both pre- and post-contrast, with gadolinium contrast agent given at a dose of 0.1 mL/kg prior to the second scan. The following imaging parameters were used; flip angle 12°, repeat time (TR) = 8 ms, echo time (TE) = 32 ms, inversion time 450 ms, field of view (FOV) 24 cm, acquired resolution 2×2×2 mm, matrix size 256×256. Sagittal T_2 CUBE images were additionally acquired with the following parameters; flip angle 90°, TR = 2.5 s, TE = 83 ms, FOV 24 cm, acquired in-plane resolution 1×1 mm, slice thickness 1.2 mm, slice spacing 0.6 mm, matrix size 512×512.

The hyperpolarised ^{13}C-pyruvate injection was then administered with imaging begining 12 s post-injection. Axial 3-slice IDEAL spiral acquisition was performed over 1 minute, with slice 1 centred on the tumour. The following parameters were used; flip angle 10°, TR = 260 ms, TE = 1.4 ms, time resolution 2.08 s, FOV 24 cm, slice thickness 3 cm, inter-slice gap 3.5 mm, acquired resolution 6×6×30 mm. Each time point acquired a full FID spectrum, followed by seven single shot 40-pt

spiral acquisitions which, following Cartesian re-gridding during reconstruction, produced a real resolution of approximately 12×12×30 mm. Gaussian k-space filtering was applied during post-processing, interpolating to an effective image resolution of 1.875×1.875×30 mm.

5.2.4 Analysis

Reconstructed ^{13}C data and anatomical image DICOMs were imported into MATLAB (Mathworks) for analysis. For the two data sets from cancer patients, Markov random field (MRF) segmentation was applied in order to automatically detect the tumour volume or region of interest. The algorithm is described in detail in chapter 3 and is specifically designed to handle the 5D data (3D spatial, 1D frequency and 1D time) produced by multi-metabolite ^{13}C dynamic imaging. The algorithm relies on multiple features of this data, including Bayesian priors based on metabolite ratios, temporal profile shape and spatial location of pixels in order to segment the data based on features less vulnerable to noise and variability than image contrast. The breast data was segmented in 3 spatial dimensions and the glioma data was segmented in 2D, with the tumour-containing slice 1 used. The fuzzy parameter λ was set to 2.6 in both cases, with all other details of the algorithm as described in the previous chapter.

5.2.4.1 Kinetic modelling

Dynamic data for the two cancer patients was prepared for kinetic model fitting by spatially averaging over voxels contained within the tumour ROI as detected by MRF segmentation. Data was also extracted for HV2, however in this case the average over all voxels in slice 2 was used. The following two-way differential kinetic model with a continuous Heaviside-step inflow function was fit to the pyruvate and lactate timecourse data:

$$\frac{dP(t)}{dt} = k_i \left(1 - \frac{1}{1 + e^{-2(t-t_e)}}\right) + k_L L(t) - k_P P(t) - \rho P(t) \tag{5.1}$$

$$\frac{dL(t)}{dt} = k_P P(t) - k_L L(t) - \rho L(t) \tag{5.2}$$

where k_P and k_L are the forward and backward conversion rate constants respectively, k_i is the pyruvate inflow rate, ρ is the inverse decay constant and t_e is the inflow end time. The first four of these were fit for as free parameters and the t_e was fixed at the pyruvate peak time. Due to the acquisition beginning after the pyruvate peak for the breast cancer patient, it was not possible to use an inflow function for this fit and the k_i was therefore fixed at zero. Fits were carried out in MATLAB using the

fmincon function and *ode45* solver. The optimisation is sensitive to the initial values of P and L at $t = 0$ which are provided as inputs to the fit. A Monte Carlo method with 1000 runs was therefore used to randomly vary these inputs over a Gaussian distribution centred, with a standard deviation of 5%, on the measured value of P or L. Parameter values were taken from the run with the best fit as determined by the Bayesian objective function described in chapter 2.

The kinetic model chosen for this analysis was determined in chapter 2 to be the most accurate method for quantifying *in vivo* data, however model-free metrics were also assessed and as such, the two leading analyses were also applied to this work. The area under the curve (AUC) ratio is defined as the ratio of two metabolites after summing over all time points. This was calculated for lactate/pyruvate for each subject and additionally for bicarbonate/pyruvate and lactate/bicarbonate for the glioma case. The lactate time-to-peak (TTP) was also calculated. This is found by fitting a bi-exponential function to the lactate data, then using this curve to measure the time interval from where the lactate is equal to zero to the peak maximum.

5.2.4.2 Parameter mapping

Parameter maps were produced for both cancer patients. For the AUC and TTP maps, the methods described above for ROI analysis were applied to the data from the tumour containing slice on a voxel-by-voxel basis. Voxels detected to be part of the background by the MRF segmentation were excluded. k_P maps were also produced in this way, however the kinetic model applied differed to that used for the ROI fit. In order to significantly improve the computational runtime, the number of Monte Carlo runs was reduced to 10 per voxel and a piecewise kinetic model was used:

$$P(0 : t_{max}) = \frac{k_i}{k_P + \rho}(1 - e^{-(k_P+\rho)(t-t0)}) \tag{5.3}$$

$$L(0 : t_{max}) = \frac{k_i}{\rho}(1 - e^{-\rho(t-t_0)}) - \frac{k_i}{k_P + \rho}(1 - e^{-(k_P+\rho)(t-t_0)}) \tag{5.4}$$

$$P(t_{max} : t) = P_{max}e^{-(k_P+\rho)(t-t_{max})} \tag{5.5}$$

$$L(t_{max} : t) = P_{max}(e^{-\rho(t-t_{max})} - e^{-(k_P+\rho)(t-t_{max})}) + L_{max}e^{-\rho(t-t_{max})} \tag{5.6}$$

Here t_{max} is the pyruvate peak time and t_0 is the start time, found by extrapolating the pyruvate curve back to zero. The Monte Carlo sampling was applied to P_{max} and L_{max}, which are the measured metabolite signal at t_{max}. k_P, k_i and ρ are fit for as free parameters.

5.3 Results

Four subjects were successfully imaged with IDEAL spiral CSI following an injection containing 0.4 mL/kg hyperpolarised [1-^{13}C]pyruvate. There were no adverse events and none of the subjects reported any side effects; this finding is in agreement with reports from other sites that the agent is tolerated well at this dose. One of the four subjects HV1 received pyruvate at a low polarisation of 4.7%; the images for this subject are therefore of very low signal-to-noise ratio (SNR) however it was still possible to obtain ^{13}C spectra in which several metabolite peaks can be visualised. Images of pyruvate, lactate and in some cases bicarbonate over time were produced for the remaining 3 subjects, all of whom received injections of pyruvate polarised to >20%. The individual results for each subject are detailed below.

5.3.1 Healthy volunteer 1

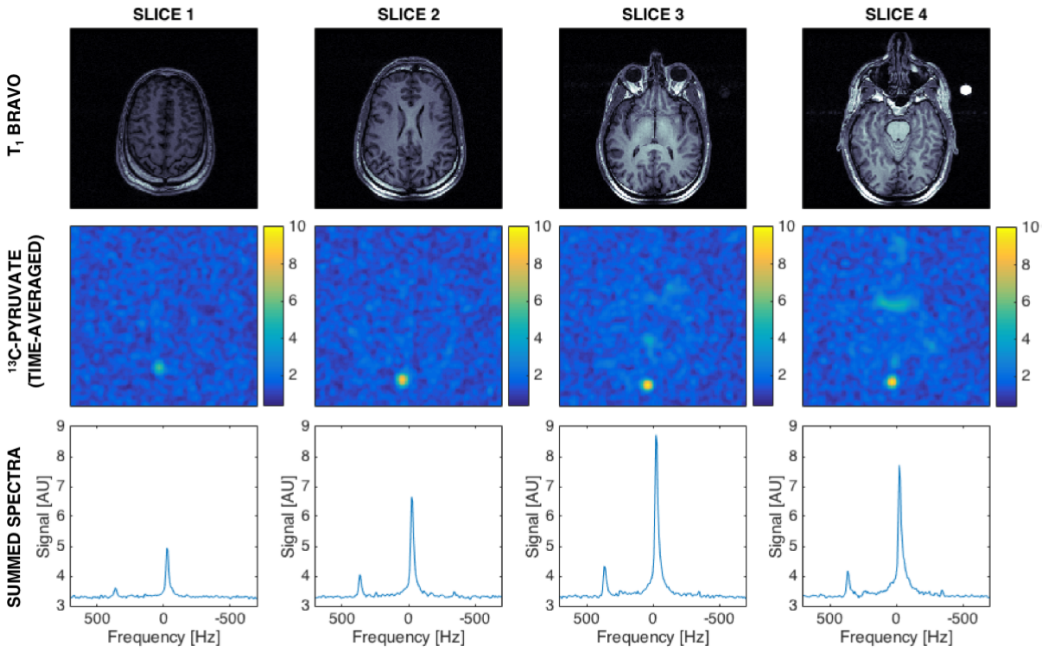

Figure 5.1: Slice by slice ^{13}C-pyruvate and anatomical reference images for healthy volunteer HV1. T_1 BRAVO anatomical imaging (top row), ^{13}C-pyruvate averaged over time points 3-9 (8-32 s) (middle row) and ^{13}C spectra summed over all time points (bottom row) are shown for each images slice 1-4.

Figure 5.1 shows the first healthy volunteer for whom four, 2 cm thick axial slices in the brain were imaged at a time resolution of 4 s and a flip angle of 5°. No

lactate or bicarbonate images were obtained due to poor polarisation, however time-averaging the pyruvate images over images 3-9 in the series (8-32 s) allows some features of the brain to be seen, most notably the sagittal sinus which appears as a bright spot anteriorly. The bottom row of 5.1 shows the ^{13}C spectra, summed over the whole acquisition time, for each whole image slice. The pyruvate peak at ∼0 Hz is prominent for each slice and despite low SNR, the lactate peak at ∼392 Hz can also be clearly seen. Furthermore, slices 2-4 show a small bicarbonate peak at -324 Hz. The appearance of these two metabolites in the healthy brain raises questions about their role in the normal brain and suggests significant normal brain metabolism in the timescale of the experiment. However, it is important to note that the anatomical location of the observed lactate and bicarbonate is unknown. Although it is possible that the metabolites were produced within the brain cells, the signal is more likely to originate from the endothelium, vasculature or extra-cranial tissues, which would not necessitate the ^{13}C-pyruvate crossing the blood brain barrier.

5.3.2 Healthy volunteer 2

The second healthy volunteer (HV2) was imaged with a higher flip angle of 15° and higher time resolution of 2 s as HV1, with the objective of producing higher SNR images of the healthy brain but with the compromise of retaining signal over a shorter time period. To further increase the signal, a larger slice thickness of 3 cm with three slices was used. Figure 5.2 shows the pyruvate lactate and bicarbonate images of the first 40 s for slice 2. Good pyruvate images have been obtained with some signal visible for the other two metabolites, although structural features of the brain are visible only in the pyruvate images. After approximately 16 s no signal can be seen for the lactate or bicarbonate images and the pyruvate signal decays by approximately 36 s. Lower temporal resolution could be effective in extending the time over which signal is visible. Slice by slice data for HV2 is shown in figure 5.3. Metabolite images are time-averaged over time points 1-13 (0-24 s) and spectra are summed over all 30 time points. The pyruvate images clearly show multiple structural elements of the brain, with the venous sagittal sinus visible in each slice, passing through the centre of the image as it traverses over the brain in slice 3. Pyruvate is also visible in the skin and muscle of the head. Unlike the previous healthy volunteer data, the summed spectra show little lactate and almost no bicarbonate, despite the acquisition having higher SNR. It is likely that by not acquiring images at the bicarbonate frequency for HV1, it allowed the metabolite to be visible in the spectra. Little of either metabolite can be seen on the time-averaged images. This may in part be due to noise and

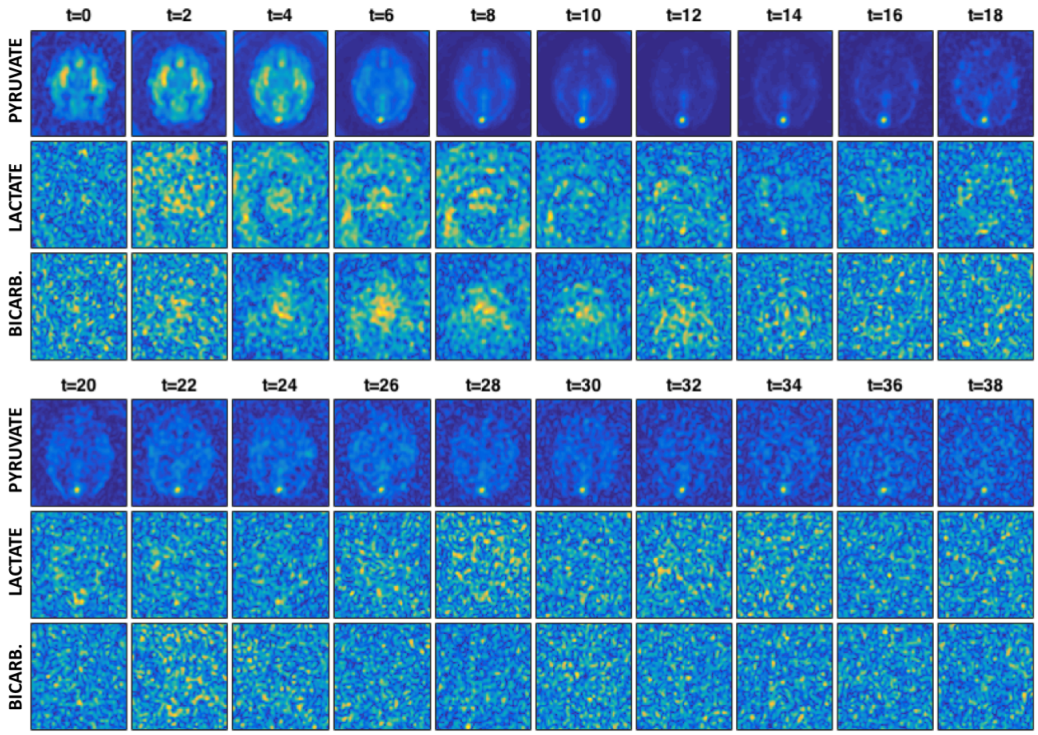

Figure 5.2: Time series of pyruvate, lactate and bicarbonate ^{13}C images for slice 2 in healthy volunteer 2 are shown from t=0 to t=38. Images are individually scaled such that for each image, the colour map takes the highest and lowest pixel values as the dynamic range limits.

artefacts; the spiral artefact is clearly visible in slice 1, being particularly prominent in the lactate image.

Slice 2 was chosen to examine the conversion to lactate in more detail as it was largely free from artefacts and contained the highest overall signal. A two-way kinetic model was fit to the pyruvate and lactate signals averaged over the whole image slice. The fit gives a value of 0.017 s^{-1} for the forward pyruvate-to-lactate conversion rate constant k_P and a T_1 of 18 s. The k_P is in the expected range but the T1 is lower than expected compared to other human results. This is most likely due the model not accounting for the conversion of pyruvate to other metabolites, particularly bicarbonate which is clearly seen to be produced. Also of note is the time at which the lactate curve peaks, which in this case is simultaneous with the pyruvate peak. Figure 5.4 shows the fit to the lactate curve peaking slightly later than the data does which implies that the lactate seen here is not being produced in the brain, a process which would incur a time delay not seen here. This lactate is therefore most likely to have been washed in following its production in other body tissues, potentially in

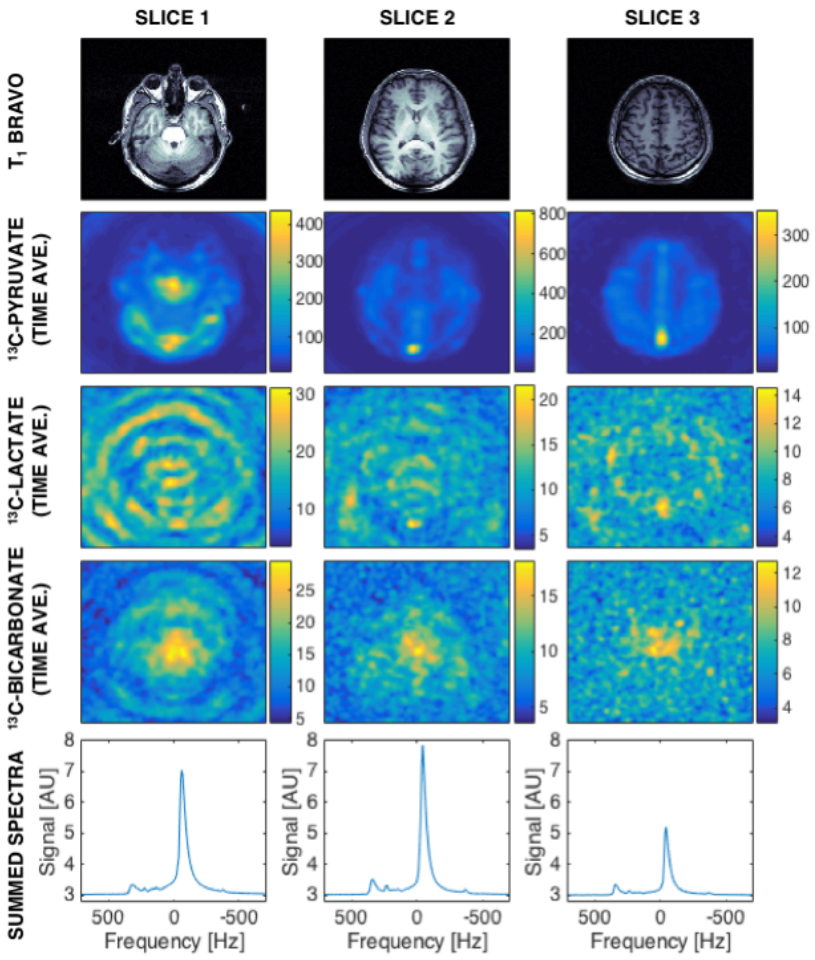

Figure 5.3: Slice by slice ^{13}C images and summed ^{13}C spectra with anatomical reference images for healthy volunteer HV2. T_1 BRAVO anatomical imaging (top row), ^{13}C-pyruvate (second row), ^{13}C-lactate (third row) and ^{13}C-bicarbonate (fourth row) averaged over time points 1-13 (0-24 s), and ^{13}C spectra summed over all time points (bottom row) are shown for each images slice 1-3.

the lungs or endothelium, explaining its simultaneous arrival time with the pyruvate. It is also possible that some of the observed lactate signal is artefactual, caused by spill-over from very high pyruvate signal at this time.

5.3.3 Breast patient

A treatment-naive patient presenting with a triple-negative ductal adenocarcinoma received hyperpolarised ^{13}C imaging in three coronal slices, with slice two centred on the tumour. As a compromise between the two healthy volunteers, a flip angle of 10° was used with a time resolution of 2 s. Figure 5.5A shows the pyruvate and lactate images over time for the tumour-containing slice 2. Unlike the images of

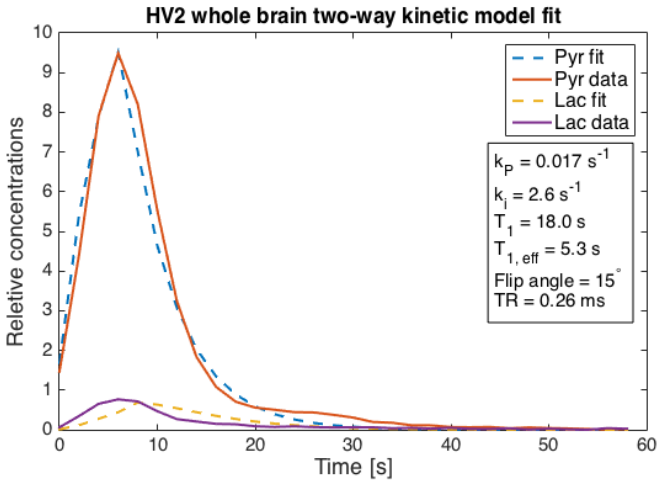

Figure 5.4: Two-way kinetic model fit for pyruvate and lactate summed over the whole of slice 2 for HV2.

the brain, pyruvate can only be seen within the tumour area which is very highly perfused compared to the surrounding tissue comprising mostly fat. A small amount of pyruvate is also visible in the subsequent slice 3, likely from the internal mammary vessels which pass through this area. Given the 3 cm slice thickness, it is not possible to determine whether the lactate seen in slice 3 is from blood or tumour. Given the co-localisation of the lactate signal with that in slice 2, it is most likely to be the latter. In order to automatically determine the tumour region of interest for kinetic modelling, 3D Markov random field segmentation was performed on all 3 slices simultaneously. The results of the segmentation are shown in figure 5.5C along with the time-averaged metabolite images used by the algorithm. The MRF algorithm appears to have correctly identified the region of lactate production in both slices 2 and 3, whilst correctly identifying that slice 1 contains only noise. There were no false positive or false negative regions based on a purely visual inspection of the data and known tumour location. Voxels within the tumour region of interest, as shown in yellow on figure 5.5C, were averaged to produce pyruvate and lactate timecourses to which a two-way kinetic model was fit.

The lactate time-to-peak was also derived, with both results shown in figure 5.6. Since the upstroke of the pyruvate curve was missed due to a late initiation of the ^{13}C imaging sequence, a reduced model was used for the fit which does not contain a pyruvate input function. The fit also appears visually to be very good, with the lactate fitted curve in particular extremely close to the data. A value of 30.4 s was obtained for the T_1 which is very close to that expected in human blood and the k_P was found to be 0.020 s^{-1} which is consistent with values obtained at other sites,

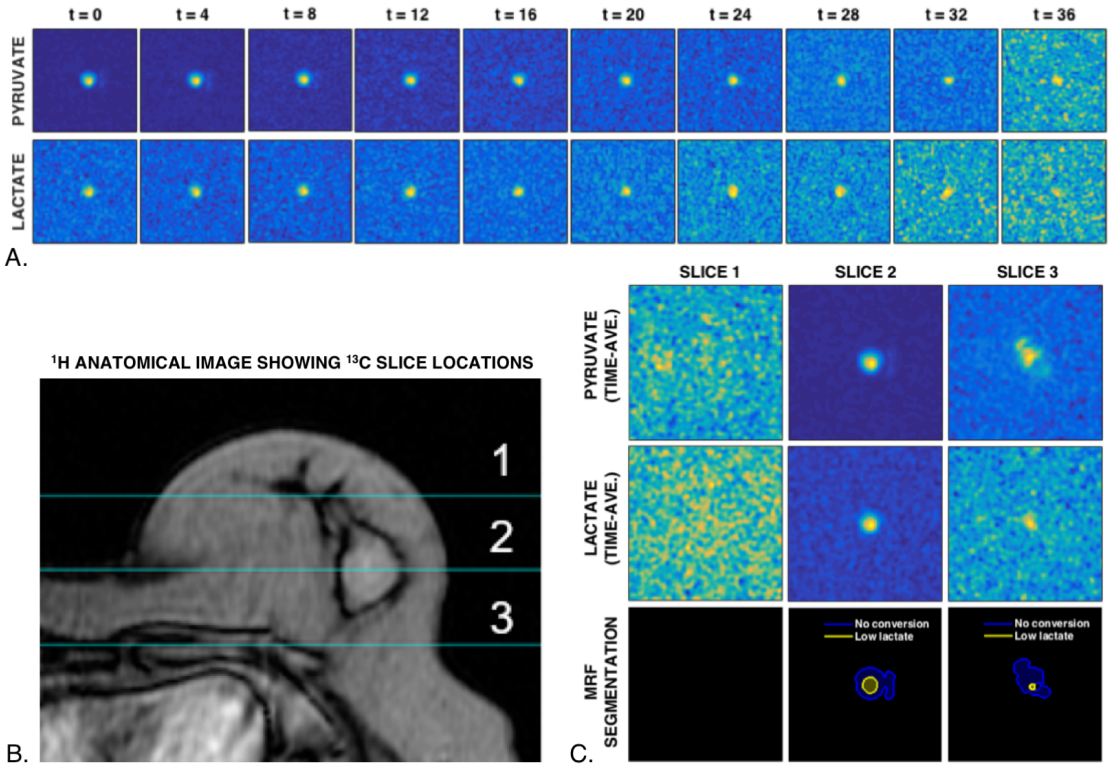

Figure 5.5: ^{13}C and anatomical imaging for breast patient. A. Slice 2 ^{13}C-pyruvate and ^{13}C-lactate images shown for every second time point; B. Coronal ^{1}H anatomical reference image showing the centres of the three ^{13}C image slices; C. Time-averaged pyruvate and lactate as used by the MRF segmentation algorithm, along with the segmentation result for each image slice.

although only slightly higher than in the healthy volunteer HV2. There is no reason to expect k_P values derived from these disparate tissues to be of comparable size; with blood brain barrier transport a rate limiting step, the k_P derived from HV2 could be expected to be considerably lower. The lactate time-to-peak was found to be 7.9 s, although accuracy may be limited by the fact that the much of the early lactate curve data was not acquired. The lactate to pyruvate AUC ratio was also calculated and found to be 0.357.

Parameter mapping was run over all voxels which were not identified as background by the MRF algorithm. The lower part of figure 5.6 shows the voxel-wise k_P, TTP and lactate-to-pyruvate AUC ratios for this region. For all three maps, results are fairly uniform within the tumour boundary, as identified by the automatic segmentation, but more variable outside where there is little or no lactate and increased noise. The tendency for all three maps to give high values towards the edge of the region, when technically values should be much lower outside of the tumour core, is

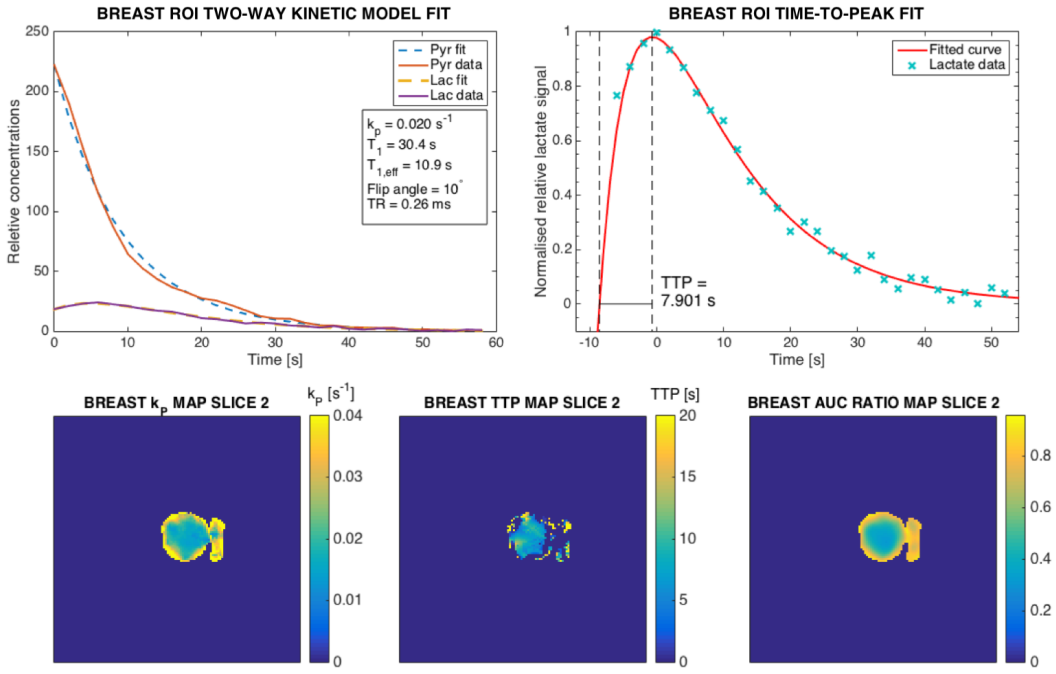

Figure 5.6: Model fits and parameter mapping for breast patient data. Top: two-way kinetic model fit (left) and lactate time-to-peak fit (right) for pyruvate and lactate time courses derived by averaging over the tumour ROI as defined by MRF segmentation. Bottom: voxel-wise parameter mapping over tumour ROI plus non-background vovels. k_P (left), lactate time-to-peak (centre) and lactate to pyruvate area-under-the-curve ratio maps (right) are shown.

caused by two main problems. Firstly; the very high perfusion of pyruvate into the centre of the tumour region skews the results, as the increase in lactate above the noise floor in this region is less than the increase in pyruvate at the tumour centre compared to the edge. The AUC ratio map clearly demonstrates this effect and the k_P map mirrors it. Secondly; this effect is exaggerated by partial voluming and by the manner in which the images are interpolated to artificially higher resolution. These results suggest initially that parameter mapping may only be suitable inside the ROI and that using lower resolution images, closer to the acquired resolution, may give less misleading results.

5.3.4 Glioma patient

Finally, a treatment-naive male presenting with a high grade glioma underwent hyperpolarised ^{13}C imaging in three 3 cm axial slices, with slice one centred on the tumour. As with the breast patient. a flip angle of 10° and time resolution of 2 s was used. Pre- and post-contrast T_1 BRAVO images were also acquired, with the

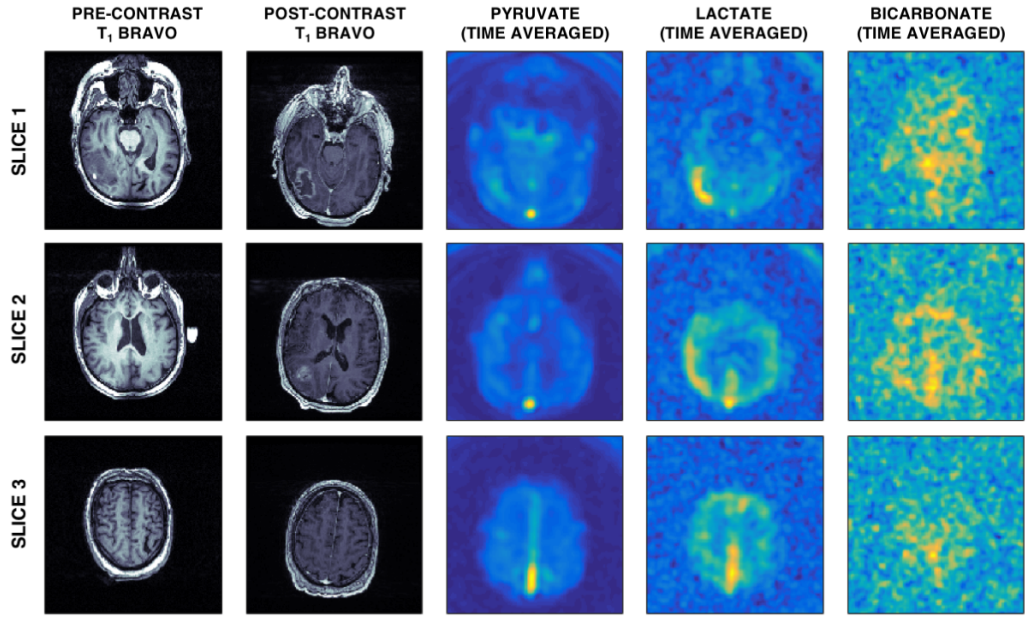

Figure 5.7: Glioma patient ^{1}H and time-averaged ^{13}C images for each slice 1-3. Pre- and post-contrast T_1 BRAVO images (left and centre-left), and time averaged ^{13}C-pyruvate (centre), ^{13}C-lactate (centre-right) and ^{13}C-bicarbonate (right) are shown for each slice. Time-averaging is from MRF segmentation output.

pre-contrast images providing co-registered anatomical images for the ^{13}C data following a translation of 22.5 mm anteriorly. Figure 5.7 shows both sets of T_1 BRAVO images in addition to ^{13}C-pyruvate, ^{13}C-lactate and ^{13}C-bicarbonate images, time-averaged by the MRF segmentation process. The pre- and post-contrast images have been aligned at the tumour centre, although a movement artefact of the patients head between scans prohibits better registration of these two sets. A similar level of brain structure can be seen as in the pyruvate images for HV2, however lactate and bicarbonate are now also clearly visible and unobscured by artefacts. The use of the lower flip angle for this subject may be a contributing factor in the clarity of the images, as other parameters remain similar. Structural elements can be seen in the lactate image as well as the pyruvate image; the visible sagittal sinus in slice 3 confirms the presence of lactate in the vessels as was suggested by the HV2 data. Lactate can also be seen in the tumour and is accompanied by an increase in pyruvate perfusion to the same region. There also appears to be increased lactate production in the neighbouring slice which, being of 3 cm thickness, is likely to cover some of the tumour area.

2D MRF segmentation was performed on slice 1, with the results shown in figure 5.8D alongside time-averaged pyruvate and lactate overlayed onto the proton

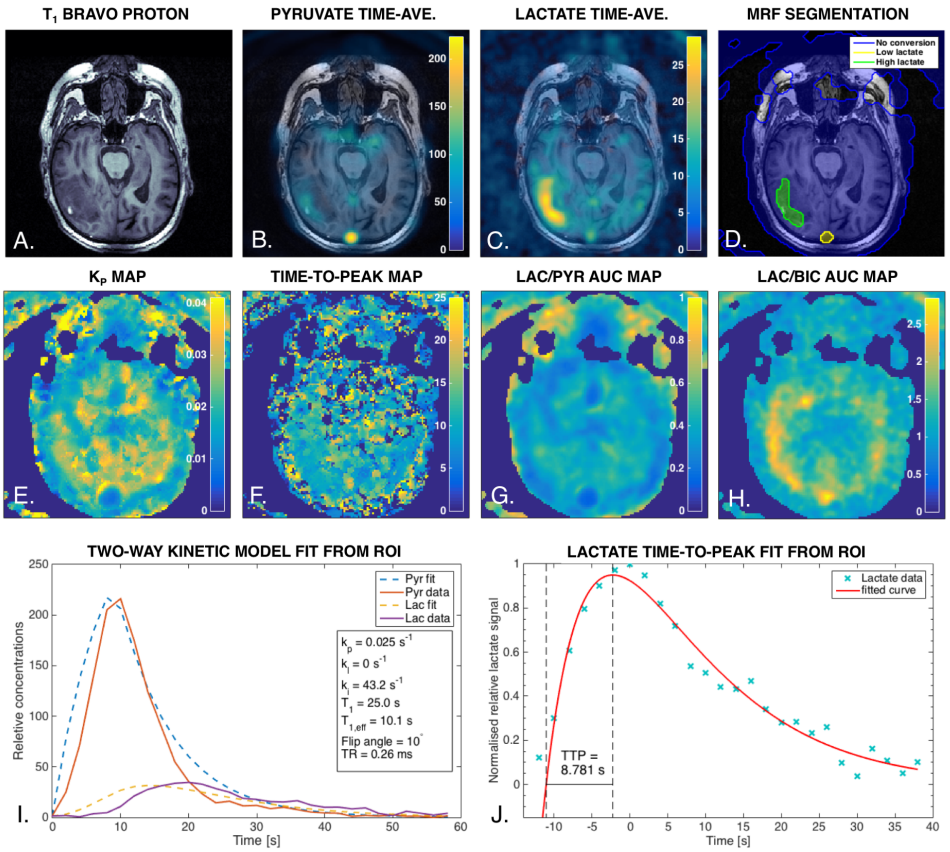

Figure 5.8: MRF results, parameter maps and kinetic model fit results for glioma patient. A. pre-contrast T_1 BRAVO anatomical reference image; B. ^{13}C-pyruvate and C. ^{13}C-lactate overlays, time-averaged as by the MRF algorithm; D. MRF segmentation results showing 'no conversion' class (blue), 'low lactate' class (yellow) and 'high lactate' class (green); E. k_P map; F. lactate time-to-peak map; G. lactate-to-pyruvate and H. lactate-to-bicarbonate AUC ratio maps; I. two-way kinetic model fit and J. lactate time-to-peak fit to voxels averaged over the 'high lactate' class region of interest.

anatomical reference. The segmentation has correctly identified the tumour, placing the region into the 'high lactate' class. Both the MRF and lactate overlay images indicate that the tumour is not uniformly metabolically active; the inner part of the tumour shows no increased lactate production compared to the normal brain, possibly indicating an area of necrotic tissue. The sagittal sinus has also been identified as a region of interest by the MRF segmentation, with the vessel placed in the 'low lactate' class. Although the lactate is objectively higher than much of the rest of the brain, figure 5.8G shows a low lactate-to-pyruvate ratio within the vessel. This information could be used to better inform the algorithm to avoid detecting vessels in the future. Figures 5.8E-G show k_P, time-to-peak and AUC maps, acquired over all

voxels not detected as the 'background' class by the MRF segmentation. Although lactate is clearly visible in the tumour, none of these maps show a clear difference in the vicinity of the tumour, with any potential variation obscured by the general noise level. The main reason for this lack of variation can be deduced from the lactate-to-pyruvate AUC ratio map. The increased lactate seen in the tumour is due to the increased perfusion of pyruvate to the region in the same proportion; the conversion rate is not ostensibly different, nor is the time-to-peak. The higher pyruvate perfusion provides increased SNR in the tumour area, with parameter maps less affected by noise and therefore appearing more uniform within the tumour. Only the lactate-to-bicarbonate AUC ratio map appears to show any real difference between the tumour and contralateral tissue.

The bottom row of figure 5.8 shows the two-way kinetic model fit and time-to-peak fit over the average of voxels within the 'high lactate' class ROI as identified by the MRF segmentation. The k_P is calculated to be 0.025 s^{-1}, which is higher than that of the breast patient and of HV2. The T_1 was found to be 25.0 s which is between the values obtained for the other two subjects and within the range expected *in vivo*. Comparing this kinetic model fit to that of the healthy brain volunteer, an interesting feature is visible. The lactate curve fit has underestimated the peak time of the data, the opposite result as for HV2. This unaccounted for delay, which was not seen with the breast patient, is likely to represent the additional time required for the hyperpolarised ^{13}C-pyruvate to cross the blood brain barrier. Although the blood brain barrier is compromised at the site of the glioma, as is evident from the hugely increased pyruvate perfusion to the region, there is nevertheless a time lag. Any modelling of pyruvate to lactate conversion in the brain may need to take this lag into account in order to achieve accurate fitting. The lactate time-to-peak was found to be 8.78 s; this is longer than in the breast, despite the fact that the k_P is higher in the breast. This again suggests the need to account for the blood brain barrier transit time in the brain and highlights the need for organ-specific standards when reviewing such metrics. The lactate-to-pyruvate, bicarbonate-to-pyruvate and lactate-to-bicarbonate AUC ratios was also calculated for the ROI and found to be 0.390, 0.128 and 3.05 respectively. In order to compare these values with healthy tissue, the 'high lactate' ROI was compared to the contralateral side of the brain. The voxels contained in this mirrored region were averaged to produce normal tissue comparison data. The same model fits were run for the k_P and lactate time-to-peak, with the values 0.024 s^{-1} and 7.33 s obtained respectively. The k_P is lower although not significantly so and the lower time-to-peak is consistent with what may be expected given lactate

data of HV2. AUC ratios were also calculated as follows; lactate-to-pyruvate 0.379; bicarbonate-to-pyruvate 0.247; lactate-to-bicarbonate 1.53. The lactate-to-pyruvate ratio is slightly lower than the tumour result although not significantly so, however the bicarbonate results are quite interesting. Both bicarbonate ratios are very different from the tumour results, echoing the result seen for the lactate-to-bicarbonate ratio map. Although the SNR of the bicarbonate images is low, there appears to be a slight decrease of 12.3% in the bicarbonate produced in the metabolically active tumour region compared to the healthy tissue suggesting that pyruvate metabolism may be shunted away from the TCA cycle into lactate.

The results from all four subjects are summarised below in table 5.2.

Table 5.2: Summary of imaging performed, ^{13}C imaging results and quantitative analysis results for each subject.

Subject ID	Anatomical imaging	^{13}C scan parameters	^{13}C results	k_P fit	k_P value	Other quantification
HV 1	3D BRAVO T_1	Flip angle 5° Time res. 4 s Slices 4 Thickness 2 cm	Pyruvate images only, pyruvate, lactate and bicarbonate visible in spectra.	None	N/A	None
HV 2	3D BRAVO T_1	Flip angle 15° Time res. 2.08 s Slices 3 Thickness 3 cm	Good pyruvate images, some lactate and bicarbonate potentially visible but unconfirmed.	Two-way kinetic model	0.017 s^{-1}	T_1 = 18 s
Breast	Axial T_2 FRFSE FatSat	Flip angle 10° Time res. 2.08 s Slices 3 Thickness 3 cm	Pyruvate and lactate clearly visible.	Two-way kinetic model no inflow	0.020 s^{-1}	T_1 = 30.4 s TTP = 7.9 s $AUC_{L/P}$ = 0.357 s
Glioma	3D BRAVO T_1 pre- and post-gadolinium T_2 CUBE	Flip angle 10° Time res. 2.08 s Slices 3 Thickness 3 cm	Pyruvate, lactate and bicarbonate all clearly visible in images.	Two-way kinetic model	0.025 s^{-1}	T_1 = 25.0 s TTP = 8.8 s $AUC_{L/P}$ = 0.390 s $AUC_{B/P}$ = 0.128 s $AUC_{L/B}$ = 3.05 s

5.4 Discussion

The results presented in this work represent the early successful hyperpolarised ^{13}C images acquired from two cancer patients, as well as the first ever healthy volunteers to be imaged, at Addenbrooke's hospital Cambridge. Firstly, the safety of the approach is demonstrated with no subjects reporting any adverse effects, even of a minor nature. Although side effects have been reported at other sites at the same dose of 0.4 mL/kg of 250 mM [1-^{13}C]pyruvate, these were all considered minor. The results presented here therefore support the general consensus that the agent is safe

and well tolerated. Secondly, the feasibility of simultaneously imaging multiple ^{13}C-labelled metabolites in the human breast and brain, and in healthy and diseased tissue, is demonstrated. [1-^{13}C]Pyruvate images were successfully produced for each subject, with lactate clearly seen in both cancer patients and bicarbonate additionally detected in the spectra of all subject brains and imaged in the glioma case. The ability to detect all three metabolites raises the possibility of using the technique to further understand metabolism in the normal brain, as well as for the detection and characterisation of disease such as cancer, multiple sclerosis and stroke.

Although there has been some debate over whether imaging the human brain with [1-^{13}C]pyruvate is feasible due to the necessity of the agent to cross the blood brain barrier, the early results presented here for the volunteers and glioma patient are encouraging. It is possible to identify many structural features within the brain in the pyruvate images, with the sagittal sinus particularly prominent and other large vessels transiently visible during the passage of the pyruvate bolus. Viewing the glioma patient data which has the highest SNR of the three, pyruvate can also be seen in the skin and muscle, with lactate more clearly confined to the anatomical boundaries of the brain. It is likely that the majority of the hyperpolarised [1-^{13}C]pyruvate does not cross the blood brain barrier; the fit for HV2 shows the two metabolites peaking at a similar time implying that lactate may also be forming in outside of the brain parenchyma, but further work is required to confirm this especially given the high noise levels and visible artefact. Considering the glioma patient data, the long time delay before the lactate peak unaccounted for by the kinetic model is highly suggestive of a delay due to blood brain barrier transit. Although it seems highly likely that transit of ^{13}C-pyruvate occurs where there is compromised integrity of the blood brain barrier, higher SNR data is required in order to judge whether it also crosses into healthy brain cells.

The feasibility of imaging with [1-^{13}C]pyruvate in breast cancer was also demonstrated, with clear images produced of both pyruvate and lactate over time. No other ^{13}C metabolites were detected in the breast. The composition of breast tissue, being mostly fat, lead to an interesting effect in the images where pyruvate was only visible within the tumour and to a much lesser extent, in the internal mammary vessels on the adjacent slice. Adipose tissue has very low metabolic activity compared to the tumour tissue, explaining the absence of metabolite signal outside the tumour ROI. This high, tumour-only pyruvate perfusion made identification of the tumour very obvious; detection of even very small lesions in the breast may be possible with [1-^{13}C]pyruvate due to this perfusion benefit and a comparison with DCE-MRI could

be undertaken in future studies to address this. A potential point of concern here is the potentially misleading results found by parameter mapping with k_P and lactate time-to-peak in the breast. These appeared to show a ring of high activity surrounding the region identified by the MRF segmentation algorithm as lactate producing, with a less metabolically active core. This result is likely not biologically driven, but rather due to the extremely high pyruvate signal at the centre of the tumour and the increase in lactate in this region from the noise floor being proportionally less than the increase in pyruvate. It could potentially represent true signal if the centre of the tumour was very necrotic, however histology would be required to confirm this.

The MRF segmentation produced good results in the breast, correctly identifying the regions of lactate production across multiple slices, even when these areas of lactate were very small. It is not possible to comment on how well the region identified as metabolically active aligned with the anatomical tumour volume; future imaging trials will ensure co-registered anatomical reference images are collected for this purpose, as well as collecting tissue for histological analysis and comparison. The kinetic model fit and lactate time-to-peak fit produced from the average of the MRF-identified ROI were excellent, despite the absence of the pyruvate upstroke from the data. The k_P and T_1 values of 0.020 s^{-1} and 30.4 s respectively are at the centre of the ranges reported by other sites undertaking human subjects, suggesting that kinetic modelling is well suited the breast and that accurate estimates of kinetic parameters can be obtained for clinical assessment of tumour metabolism. The time-to-peak fit appeared visually accurate, but further work is required to more fully understand the quantitative values acquired.

The highest SNR ^{13}C images of pyruvate, lactate and bicarbonate were those acquired from the glioma patient. These images were the least affected by artefacts of the three brain subjects and had the highest SNR, making it possible to see structural features of the brain not only in the pyruvate images, but also in the lactate images. Applying the automatic MRF segmentation algorithm to slice 2 of the glioma data, the tumour was correctly identified, appearing as a metabolically active crescent at the outer edge of the tumour. Since the anatomical tumour boundary appears as an oval on the co-registered T_1 BRAVO image, this mismatch suggests that there is metabolic heterogeneity within the tumour when compared to perfusion alone. This may reflect cell death or metabolic alterations and comparison to histology is required to further evaluate this.

Fitting the two-way kinetic model to the ROI-averaged glioma data produced a k_P value of 0.025 s^{-1}. The researchers at UCSF reported finding the prostate tumour k_P

to be 0.045±0.025 s^{-1}, so this value is with in the range reported for human tumours so far. However, the k_P for the contralateral brain region was 0.024 s^{-1} and that for the whole brain in HV2 was 0.017 s^{-1}; both within the tumour range, but higher than the healthy prostate tissue k_P range of 0.009±0.003 s^{-1} that UCSF report. The relative uniformity of the glioma whole-brain k_P map also suggests lactate formation outside of the tumour. There is growing evidence that lactate production in astrocytes is part of normal brain metabolism; is is possible that imaging with ^{13}C-pyruvate in the brain may be a useful tool to better understand the underlying biology of this process. Furthermore, the use of hyperpolarised ^{13}C-lactate in the future may also be a valuable tool to help probe this process.

Although increased lactate in the tumour could clearly be seen and detected by the segmentation algorithm, there was a similar increase in pyruvate in the tumour due to increased perfusion which rendered the parameter maps quite featureless. Although this data represents a single subject, it raises potential problems in using hyperpolarised pyruvate to image the human brain, suggesting that different quantification methods may be required for analysing the whole brain. Of the metrics tested, only the lactate-to-bicarbonate ratio was significantly different in the tumour to contralateral region; the values being 3.05 and 1.53 respectively. It appears that less bicarbonate is being produced in the malignant compared to healthy tissue due to a shift away from the TCA cycle towards lactate production. It is possible that bicarbonate ratios will provide a useful clinical metric in assessing both healthy and pathological brain metabolism.

The SNR of the ^{13}C images is very heavily affected by the choice of flip angle and repeat time used in the IDEAL spiral CSI acquisition. Each applied radio frequency pulse of flip angle α irreversibly depletes the overall polarisation by $1-cos(\alpha)$, however the signal acquired at the pulse is proportional to $sin(\alpha)$ resulting in a trade off between SNR and polarisation retention. A flip angle of 5° was used for HV1 which produced very poor SNR images, albeit due mostly to poor initial polarisation. For HV2 the flip angle was increased to 15° and the TR was lowered from 500 ms to 260 ms. This produced images with much improved SNR, however most of the signal had decayed after 20 s. Furthermore, the high flip angle applied to the early, very high signal pyruvate may be partly responsible for the large spiral artefact on these images due to truncation of the free induction decay. For both of the cancer cases, the flip angle was set to 10° with the TR fixed at 260 ms. Although helped by the fact that a tumour was being imaged rather than healthy tissue, the images produced are of better quality than HV1 and HV2. Therefore, for future studies, it would seem that

10° provides a good compromise. It is also possible to improve the image quality further at the expense of temporal resolution: e.g. by increasing the TR from 260 to 500 ms and decreasing the time resolution to 4 s. Although this would reduce the accuracy of the kinetic modelling to some extent, the increased signal should allow for a more accurate characterisation of the biology and would be an appropriate compromise at this point in time.

Since the technique of hyperpolarised imaging with ^{13}C is still very much in its infancy, there is much to be done in terms of the validation of results such as those presented here. Test-retest studies, with subjects imaged two or more times on different days, or at different sites, are now crucial to evaluate the repeatability and reliability of the imaging technique and any quantification metrics derived from the data. The images produced are particularly vulnerable physical and physiological variations, such as slight changes in injection and acquisition timing, initial polarisation, pyruvate concentration and patient physiology will all have a dramatic effect on the quality and content of the imaging data.

The quantification methods presented and applied here are specifically aimed at reducing the impact of this variation and at producing the most robust and reliable possible means of quantification. The MRF segmentation algorithm uses each of the five dimensions of the data to segment according to relative, rather than absolute, metabolite intensities. It also utilises features of the data such as temporal shape profiles which can be adjusted for the specific imaging parameters used in the acquisition, and which are less affected by artefacts and changes in SNR. The two-way kinetic model used in this work has been shown to be the most robust model choice when tested on a large *in vitro* data set with known enzyme activity. Although these methods are efficient in reducing the effects of variability in the images, information on the repeatability of measures such as the k_P in human subjects are now required. Repeatability studies should be undertaken before any quantitative measures derived from ^{13}C imaging data can be relied on to evaluate questions such as treatment response in tumours.

5.5 Conclusion

These results represent some of the first subjects to be successfully imaged with [1-^{13}C]pyruvate at Addenbrooke's hospital Cambridge and the first volunteer studies ever to be undertaken. Feasibility of hyperpolarised MRI is demonstrated in the brains of two healthy volunteers and two cancer patients; one breast and one glioma.

In each case, conversion to [1-^{13}C]lactate was observed in the ^{13}C spectra acquired, with lactate images produced for three subjects and ^{13}C-bicarbonate in one volunteer and the glioma patient. An automatic Markov random field segmentation algorithm, previously untested on human data, was applied to the two cancer cases and the tumour region of interest was correctly identified in each case. A two-way kinetic model was fit to dynamic pyruvate and lactate timecourse data taken from these tumour ROIs. The forward reaction rate constants k_P, as well as the decay constants T_1, obtained from this fit were all within the range observed in human tumours by other sites. The exception to this was the high k_P values obtained from fits to healthy brain tissue, implying a low level of lactate production in the normal brain. The results from this early data will be used to refine and improve the hyperpolarised imaging protocol as the number of subjects imaged at Addenbrooke's grows over the following months. The successful application of quantitative methods to this early data is encouraging and will allow for repeatable and robust characterisation and comparison of future patient data.

Chapter 6

Discussion

Dissolution dynamic nuclear polarisation is a new technique which enables the metabolism of hyperpolarised ^{13}C-labelled molecules to be dynamically and non-invasively imaged in tissue using existing MRI technology. As the first human subjects at sites around the world are imaged with ^{13}C-labelled compounds, the early results look promising for the future of the technique. The only molecule approved for human use to date is [1-^{13}C]pyruvate which has been well tolerated with no serious adverse effects reported at the clinical dose that is currently being used. Furthermore, it has been possible to obtain dynamic, multi-metabolite images of [1-^{13}C]pyruvate and its metabolic breakdown products, notably [1-^{13}C]lactate and ^{13}C-bicarbonate, in a range of human organs including the heart, brain, liver, prostate and breast. Although the technique is still in its infancy, the progress that has been made in the last fifteen years is truly remarkable. Since Ardenkjær-Larsen *et al* published their method for obtaining stable liquid-state polarisation in 2003, dynamic nuclear polarisation of ^{13}C-labelled molecules has captured the imagination of pre-clinical biologists, clinicians, industry researchers and large corporations. The ^{13}C research circle that formed from these groups accelerated research output through diverse collaboration and just eleven years later, the first-in-man study from UCSF was published in 2014.

The number of sites with the capability for human hyperpolarised ^{13}C imaging is rising rapidly and it is now important that the community validates the technique and standardises the methodology. By harmonising protocols and analysis methods between and within sites, the repeatability and reproducibility of the technique may be assessed and the potential for multi-centre studies becomes available; these are both important steps on the road to widespread translation. A large proportion of the work presented here was undertaken with the view to aiding and advising the process of clinical standardisation and developing reproducible analysis techniques. The remainder presents a more theoretical approach to the analysis of ^{13}C data, using

mathematical modelling techniques to understand the processes that govern lactate metabolism in both tumours and the cells with which they share their environment. These two very different approaches are complementary, providing both the rigorous technical methods to effectively handle both clinical and research data, as well as providing a thoughtful analysis of the biological processes which generate the observed metabolic dynamics.

This thesis began with a comprehensive analysis of the quantitative methods which have previously been applied to hyperpolarised ^{13}C data and compared these to some novel approaches. The means of quantification studied can be divided into two subsets comprised of model based and model-free methods. Kinetic modelling methods assume that the biological reaction underlying the data can be described by a simple mathematical model; this is then fit to the data in order to derive parameter values such as the forward reaction rate constant k_P. On the other hand, model-free methods derive simple quantitative metrics, such as ratios or curve widths, directly from the data. The aim of this study was to identify the most appropriate methods to apply, for both research and clinical settings, as determined by the correlation of their outputs with the known lactate dehydrogenase (LDH) enzyme concentration in a large *in vitro* dataset. The performance of each approach was then tested on a small *in vivo* dataset from a rat xenograft model.

The most accurate and robust model choice for kinetic analysis of hyperpolarised data was found to be the two-way differential model. Incorporating a Heaviside-step inflow function into this model provided the best means of characterising *in vivo* data, whilst minimising the number of free parameters according to the Akaike information criterion. Of the simple model-free metrics tested, the lactate time-to-peak demonstrated the highest correlation with the *in vitro* LDH correlation and provided excellent correlation with *in vivo* model-derived k_P values. The lactate to pyruvate area-under-the-curve ratio also produced good results. Additionally, this study compared two methods of extracting data from the hyperpolarised images: taking the data from the pixel of highest intensity (POI), or averaging over a region of interest (ROI). Although the ROI method was found to have greater sensitivity to changes in metabolism, the POI approach was sufficiently robust to suggest that pixel-by-pixel parameter mapping can be confidently applied to data of this kind.

In vivo ROIs for the model comparison study were defined by manual delineation of the anatomical tumour boundary. A key reason for this choice, rather than using a thresholding approach, was the observation that parameters derived from ROI

data had high sensitivity to the exact choice of thresholding level if this alternative method was used. This result highlighted the need for a robust, repeatable and objective method of defining an ROI on multi-dimensional hyperpolarised ^{13}C data. Furthermore, it was clear that the chosen method of segmentation should not be based solely on image contrast, should consider multiple metabolite images simultaneously, and should ideally utilise the temporal component of the data.

A Markov random field (MRF) approach was chosen for having the capability to incorporate multiple sources of information into the segmentation decision process. Temporal, 3D spatial and metabolite ratio information for each voxel were stored in Bayesian priors, whilst the intensities from multiple metabolites were treated as components of a single vector, similar to the RGB components in a colour image. All of this information is considered concurrently during the iterative segmentation procedure which sorts voxels into six metabolic classes. The conversion of ^{13}C-pyruvate into ^{13}C-lactate, ^{13}C-alanine and ^{13}C-bicarbonate, in addition to no-conversion and no-perfusion regions, were considered. Finally, continuous fuzzy logic was utilised in order to compensate for low resolution, noisy images by retaining information about the true contents of each voxel throughout the segmentation process.

The proposed MRF segmentation algorithm was tested on an *in silico* dataset with variable SNR, metabolite conversion rates and region sizes, where its superiority over a reference thresholding-based method was demonstrated. The algorithm was consistently able to detect the region in which there was high conversion into lactate with no false positives produced. However, regions with very low SNR were occasionally missed. The fuzzy MRF segmentation was then applied in 2 and 3 spatial dimensions to *in vivo* animal data where, in each case, the anatomical tumour location was correctly identified. In several cases, large artefacts were visible in the lactate images with comparable magnitude to the signal acquired from areas of genuine metabolic activity; however, none of these were falsely detected by the algorithm. This highlights the importance of properly utilising multidimensional data to better inform the algorithm in the presence of noisy, artefact-prone data such as that considered here.

If hyperpolarised imaging is to be used to make clinical decisions, it is of high importance to better understand the biological processes which produce the observed image contrast. Although increased glycolysis is a key hallmark of cancer, there has been significant interest recently in the metabolic interplay between tumours and their environment. Lactate production and metabolism is a feature of many healthy cells, which have the potential to form metabolic couplings with the tumour cells and each other. Cancer associated fibroblasts (CAFs) have been repeatedly implicated

as a driver of aggressive, invasive behaviour and have been shown to exhibit altered lactate metabolism in the presence of tumour cells. The 'reverse Warburg' effect describes an experimentally observed phenomenon in which tumour cells metabolise the lactate produced by CAFs as an alternative energy source. A mathematical model was built to examine the relationship of the tumour with its environment and to simulate different growth and treatment outcomes as both the tissue vascularity and the metabolic coupling between tumour and CAFs was varied. The model presented in the thesis focused on the use and production of lactate in the tumour environment.

It was found that there is an optimal tissue vascularity in which tumour growth rate is maximised; above this, increased access to nutrients is outweighed by the removal of lactate from the system which reduces invasive potential. Lactate production was found to be lowest in the optimal tissue and increasing as vascularity was either increased or decreased. Of the four scenarios simulated, the reverse Warburg coupling, where both tumour and CAFs could use and produce lactate, produced the fastest growing tumours which exhibited high treatment resistance through the promotion of an acidic tumorigenic niche. Partial coupling, where CAFs could only use but not produce lactate, resulted in the slowest growing tumours in all but the most nutrient-starved tissue conditions. Tumours with no CAF interaction were slower growing but more resistant to treatment, particularly in tissues with denser than optimal vasculature. The model is developed with the objective of better understanding the tumour interaction with its environment and aiding the interpretation of combined histopathology and metabolic imaging data in order to make informed, patient-specific treatment decisions.

In the final section, the approaches developed in earlier chapters for the analysis of hyperpolarised ^{13}C data were applied to a small initial dataset comprising two healthy volunteers and two patients; one presenting with a breast tumour and the other with a glioblastoma. Each subject received IDEAL spiral multi-metabolite imaging following the injection of 0.4 mL/kg of 250 mM hyperpolarised [1-^{13}C]pyruvate solution. The agent was well tolerated with no adverse effects reported and its conversion to [1-^{13}C]lactate was observed in the ^{13}C spectra acquired from each subject. Lactate images were acquired for three subjects, with ^{13}C-bicarbonate images additionally produced from one volunteer and the glioma patient.

MRF segmentation was applied to the two oncology cases, correctly identifying the tumour as the highest conversion region in each data set. Voxels contained within these ROIs were averaged to produce pyruvate and lactate timecourse data for quantitative analysis. A two-way differential kinetic model, previously determined to have

the highest accuracy and robustness of the models tested, was applied to ROI data from the two patients, as well as to data from the second healthy volunteer brain, averaged over the whole central slice. The k_P values obtained from this analysis were within the range previously reported from the only other human tumour study that has been published, however the results from the volunteer suggest higher levels of normal brain lactate metabolism than in other healthy tissues. The pyruvate T_1 was also calculated, ranging between 18-25 in the brain and 30 s in the breast, where the expected range was 25-30 s. The low brain T_1 observed may be due to conversion of pyruvate into bicarbonate, a process not accounted for by the model.

There is still a long way to go before hyperpolarised imaging with ^{13}C-labelled compounds will be considered a standard imaging modality, or even a clinical rather than a research technique. Nevertheless, the early data produced at Addenbrooke's, as well as at other sites with clinical capability, is encouraging and clearly demonstrates both the feasibility and safety of human imaging. In the immediate future, emphasis must be placed on demonstrating the reliability and repeatability of both data acquisition and quantification. Although the methods presented in this work for the analysis of ^{13}C data are designed specifically to be robust to the known sources of variability, rigorous testing on patient data will be required to assess their suitability for each specific clinical application. It is likely that a different analysis approach will be required for quantifying brain metabolism compared to other tissues, where blood brain barrier transit and background tissue metabolism significantly influence data acquisition.

Test retest studies, whereby patients receive multiple scans within a short time frame, are needed to assess the intrinsic variability of the imaging approach and the reliability of any derived quantification metrics. Furthermore, it remains to be seen whether the data produced from hyperpolarised imaging can be replicated at other sites, a key requirement for multi-centre studies. One crucial element of this, both within and between sites, is the need to understand how the choice of imaging sequence affects the results. Theoretically, the same k_P value should be derived from the imaging data regardless of the exact scanner and pulse sequence that was used to acquire it. In reality, the complicated experimental ^{13}C sequences and their reconstructions, which still need much refinement and optimisation, are likely to have intrinsic biases which skew results. As variable flip angle schemes and clever optimisations for maximising the signal from each metabolite become more widely used, the resulting process of quantifying the data they produce is burdened with

additional sources of error. Understanding and compensating for these errors will be an important part of the process as ^{13}C data analysis methods develop.

Many early studies, both clinical and preclinical, have been focused on the applications of ^{13}C imaging in oncology. The suitability of pyruvate for polarisation, combined with the almost ubiquitous glycolytic metabolism observed in cancers, mean this is a natural first application of the technique in patients. Aside from simply detecting tumours, imaging with ^{13}C-pyruvate has the potential to detect early metabolic changes in neoplastic tissue before a mass is visible with anatomical imaging. By quantifying the conversion rate to lactate, it may be possible to grade cancers based on imaging; early data from Memorial Sloane Kettering suggests this is possible in human prostate cancer. The application of ^{13}C imaging that is most highly anticipated however, is in the early detection of treatment response. Quantifying changes in metabolism before and after treatment is likely to become one of the key uses of the technique should it prove clinically viable. This is certainly looking likely, as a wealth of preclinical studies, in addition to a recent case report on a single prostate cancer patient at UCSF, demonstrate the feasibility of this application.

Abnormal metabolism is by no means limited to cancer. There is significant interest in imaging ischaemia, with early studies concentrating on the heart and the loss of ^{13}C-bicarbonate production observed following an ischaemic event. The potential for imaging the human heart has already been demonstrated and it is hoped that the technique will be valuable for identifying damaged myocardium. The early signs of hypoxic renal damage that occur with diabetes may be detected by imaging the increased conversion of ^{13}C-pyruvate to ^{13}C-lactate in the kidney. It may also be possible to image ischaemic damage to the brain, following stroke or traumatic injury. Although limited preclinical data is available due to the difficulty in producing a preclinical model of stroke, this remains an exciting potential application with studies in patients already planned. The blood brain barrier is known to be compromised following a stroke, which may facilitate perfusion of pyruvate to the region peripheral to the occlusion; areas of lactate production would indicate perfused and metabolically active tissue as opposed to ischaemic tissue, offering the potential to determine the ischaemic penumbra and the extent of tissue damage.

Other neurological applications include imaging the metabolic changes that occur with degenerative diseases and the increased lactate production observed in multiple sclerosis (MS) plaques due to high immune activity; a physiological trial to image MS in patients is already under way in Cambridge. Similar metabolic changes are known to occur at sites of inflammation. Although little has been investigated in this area so

far, there is potential for hyperpolarised ^{13}C-pyruvate imaging as a tool for studying autoimmune diseases, infection and immunometabolism.

Although ^{13}C-pyruvate is the first molecule to gain clinical approval and has been the focus of a majority of studies so far, there are a number of other ^{13}C-labelled biomarkers which are likely to be approved in the near future, each with a wealth of potential applications. Notable forerunners include ^{13}C-fumarate, the conversion of which to ^{13}C-malate is a negative marker of cellular necrosis and may be valuable alongside ^{13}C-pyruvate for determining treatment response in tumours. ^{13}C-urea is being developed as a marker of perfusion and ^{13}C-bicarbonate as a marker of pH. Preclinical research into new ^{13}C tracers continues to identify molecules of biological significance suitable for polarization and as the technique improves, the possibilities continue to expand. The vast number of potential ^{13}C agents which may provide unique insights into *in vivo* tissue metabolism and which could be imaged simultaneously or sequentially, are some of the strengths of hyperpolarised imaging.

One of the major challenges to widespread adoption of any new technique is demonstrating that it fulfils some unmet clinical requirement. This may be by providing valuable information unattainable with current technologies, or by demonstrating a significant improvement to competing modalities on either cost or patient safety. The main competitor in the case of hyperpolarised imaging is clearly PET, with the most commonly used tracer, ^{18}F-FDG, providing comparable clinical information to ^{13}C-pyruvate as a marker of tumour glycolysis. The two modalities are similar in terms of in-plane image resolution, however PET has much higher 3D resolution and has far higher molecular sensitivity; ^{18}F-FDG may be detected in nanomolar quantities compared to ^{13}C-pyruvate in the millimolar or high micromolar range. Whole body imaging is common with PET, however the field of view for hyperpolarised imaging is currently limited to small regions and few slices.

One of the main advantages offered by ^{13}C is the dynamic information it provides. Where ^{18}F-FDG PET shows only a map of glucose uptake, hyperpolarised imaging is capable of dynamically imaging multiple metabolites at once, making it a much more specific marker of glycolysis, but also expanding the use of the tracer to applications such as cardiac metabolism. Although dynamic imaging is possible with PET, it is rarely used in clinical practice. Similarly, the wide range of alternative PET tracers have been confined almost exclusively to research uses due to their high cost and difficult manufacture, often requiring an on-site cyclotron. Introducing new stable ^{13}C tracers should be far more straightforward. ^{18}F-FDG demonstrates high uptake in the brain, heart gut and urinary system which can often obscure disease in these

regions; with much more specific uptake, this problem is avoided with hyperpolarised imaging. Finally, ^{13}C-pyruvate MRI is a radiation-free technology which may be applied repeatedly. Compared to the high radiation dose associated with PET-CT, there are clear benefits for hyperpolarised imaging in terms of patient safety, opening up the potential to repeatedly image patients especially children and pregnant women.

There are currently two major limitations facing clinical hyperpolarised imaging. The first is its high operational cost: a single injection of hyperpolarised [1-^{13}C]pyruvate costs around £3000 and this is coupled with the cost of time on the MRI scanner, plus the high costs of purchasing and maintaining a hyperpolariser system and establishing a pharmacy. Clearly this is a very high barrier for many sites to overcome, however there is no reason why costs will not reduce as demand for sterile fluid paths (SFPs) or pharmacy kits and ^{13}C-labelled pharmaceuticals increases, due to economy of scale. Furthermore, the high cost of the procedure may be offset by its utility; if [1-^{13}C]pyruvate proves to be a valuable tool for assessing treatment response, huge sums could be saved on expensive and ineffective cancer drugs and unnecessary surgical procedures, making the technique financially viable in the long run.

The second limitation is quite simply the technical difficulty involved in producing hyperpolarised data. From SFP assembly, the hyperpolarisation procedure, QC testing, to the injection and acquisition, there are many points in the process that are vulnerable to both human and technical error and variation. The rapid decay of hyperpolarised signal leaves little buffering for errors and images acquired after a delay of even a minute demonstrate unusably low SNR. Furthermore, the current sterile fluid path design is prone to variability of pH and pyruvate concentration, with around 10-50% of samples rejected during QC analysis. Initial polarisation is also prone to high levels of variation, significantly affecting the images produced. Despite these difficulties, early patient data of good quality has been acquired at Cambridge and at other sites. As the number of patients imaged grows, it is hoped that protocols will become optimised, with many sources of error being reduced or eliminated over time. However, the current procedure is in need of simplification if hyperpolarisation is to become more than a research technique.

With these limitations in mind, it is interesting to consider possible solutions for technical developments which could dramatically improve access to hyperpolarised imaging. One suggestion for both reducing cost and hardware requirements is to have a central facility which is capable of polarising and shipping injectable solutions to multiple sites. Retaining the polarisation during transit will be the challenge to

overcome, however in high magnetic field and low temperature it should be possible to reduce the T_1 of molecules significantly to several hours or even days. One of the huge advantages of hyperpolarised imaging is that it uses existing MRI technology already present in most clinical facilities. If the need for an on-site hyperpolariser and pharmacy is removed then the cost of the technique is significantly reduced, with the added benefit of immensely simplifying the clinical procedure required of on-site staff. Although a centralised hyperpolarisation system is currently theoretical, it would provide an excellent way of overcoming many of the obstructions to widespread clinical use.

Hyperpolarised imaging has the potential to dynamically image the *in vivo* metabolism ^{13}C-labelled compounds, providing a unique insight into cellular metabolism and the changes that may occur through disease. This is a remarkable time to be a part of the field; few novel imaging techniques develop into multi-site clinical studies, and the acid test will be the results from early clinical trials published over the coming years. The possibilities of this technique should not be underestimated. The brief summery given above does not cover the full potential of ^{13}C-pyruvate as a metabolic biomarker, let alone the multitude of other possible compounds. Even so, the application of [1-^{13}C]pyruvate and its conversion to [1-^{13}C]lactate as a measure of tumour response to treatment is sufficiently strong to propel the technique forward. It is with this particular application in mind that the work in this thesis has been developed. It is hoped that the mathematical approaches presented here will provide the means to both analyse and interpret hyperpolarised ^{13}C imaging data, aiding the clinical translation of this novel imaging modality.

References

[1] D. Hanahan and R. A. Weinberg, "Hallmarks of Cancer: The Next Generation," *Cell*, vol. 144, pp. 646–674, Mar. 2011.

[2] O. Warburg, "On the Origin of Cancer Cells," *Science*, vol. 123, pp. 309–314, Feb. 1956.

[3] R. A. Gatenby, E. T. Gawlinski, A. F. Gmitro, B. Kaylor, and R. J. Gillies, "Acid-Mediated Tumor Invasion: a Multidisciplinary Study," *Cancer Research*, vol. 66, pp. 5216–5223, May 2006.

[4] N. Draoui and O. Feron, "Lactate shuttles at a glance: from physiological paradigms to anti-cancer treatments," *Disease Models & Mechanisms*, vol. 4, pp. 727–732, Nov. 2011.

[5] F. Boumezbeur, K. F. Petersen, G. W. Cline, G. F. Mason, K. L. Behar, G. I. Shulman, and D. L. Rothman, "The contribution of blood lactate to brain energy metabolism in humans measured by dynamic ^{13}C nuclear magnetic resonance spectroscopy," *The Journal of Neuroscience*, vol. 30, pp. 13983–13991, Oct. 2010.

[6] G. van Hall, M. Strmstad, P. Rasmussen, . Jans, M. Zaar, C. Gam, B. Quistorff, N. H. Secher, and H. B. Nielsen, "Blood lactate is an important energy source for the human brain," *Journal of Cerebral Blood Flow & Metabolism*, vol. 29, pp. 1121–1129, Apr. 2009.

[7] G. van Hall, "Lactate kinetics in human tissues at rest and during exercise," *Acta Physiologica*, vol. 199, pp. 499–508, Aug. 2010.

[8] E. L. Pearce, M. C. Poffenberger, C.-H. Chang, and R. G. Jones, "Fueling Immunity: Insights into Metabolism and Lymphocyte Function," *Science*, vol. 342, p. 1242454, Oct. 2013.

[9] A. Vazquez, J. Liu, Y. Zhou, and Z. N. Oltvai, "Catabolic efficiency of aerobic glycolysis: The Warburg effect revisited," *BMC Systems Biology*, vol. 4, p. 58, 2010.

[10] D. R. Wise and C. B. Thompson, "Glutamine addiction: a new therapeutic target in cancer," *Trends in Biochemical Sciences*, vol. 35, pp. 427–433, Aug. 2010.

[11] J. Son, C. A. Lyssiotis, H. Ying, X. Wang, S. Hua, M. Ligorio, R. M. Perera, C. R. Ferrone, E. Mullarky, N. Shyh-Chang, Y. Kang, J. B. Fleming, N. Bardeesy, J. M. Asara, M. C. Haigis, R. A. DePinho, L. C. Cantley, and A. C. Kimmelman, "Glutamine supports pancreatic cancer growth through a Kras-regulated metabolic pathway," *Nature*, vol. 496, pp. 101–105, Apr. 2013.

[12] C. T. Hensley, A. T. Wasti, and R. J. DeBerardinis, "Glutamine and cancer: cell biology, physiology, and clinical opportunities," *The Journal of Clinical Investigation*, vol. 123, pp. 3678–3684, Sept. 2013.

[13] R. J. DeBerardinis, A. Mancuso, E. Daikhin, I. Nissim, M. Yudkoff, S. Wehrli, and C. B. Thompson, "Beyond aerobic glycolysis: Transformed cells can engage in glutamine metabolism that exceeds the requirement for protein and nucleotide synthesis," *Proceedings of the National Academy of Sciences*, vol. 104, pp. 19345–19350, Dec. 2007.

[14] D. R. Wise, R. J. DeBerardinis, A. Mancuso, N. Sayed, X.-Y. Zhang, H. K. Pfeiffer, I. Nissim, E. Daikhin, M. Yudkoff, S. B. McMahon, and C. B. Thompson, "Myc regulates a transcriptional program that stimulates mitochondrial glutaminolysis and leads to glutamine addiction," *Proceedings of the National Academy of Sciences*, vol. 105, pp. 18782–18787, Dec. 2008.

[15] E. Currie, A. Schulze, R. Zechner, T. C. Walther, and R. V. Farese, "Cellular Fatty Acid Metabolism and Cancer," *Cell Metabolism*, vol. 18, pp. 153–161, Aug. 2013.

[16] J. N. Thupari, M. L. Pinn, and F. P. Kuhajda, "Fatty Acid Synthase Inhibition in Human Breast Cancer Cells Leads to Malonyl-CoA-Induced Inhibition of Fatty Acid Oxidation and Cytotoxicity," *Biochemical and Biophysical Research Communications*, vol. 285, pp. 217–223, July 2001.

[17] Y. Cai, J. Wang, L. Zhang, D. Wu, D. Yu, X. Tian, J. Liu, X. Jiang, Y. Shen, L. Zhang, M. Ren, and P. Huang, "Expressions of fatty acid synthase and HER2 are correlated with poor prognosis of ovarian cancer," *Medical Oncology (Northwood, London, England)*, vol. 32, 2015.

[18] P. L. Alo, M. Amini, F. Piro, L. Pizzuti, V. Sebastiani, C. Botti, R. Murari, G. Zotti, and U. D. Tondo, "Immnunohistochemical Expression and Prognostic Significance of Fatty Acid Synthase in Pancreatic Carcinoma," *Anticancer Research*, vol. 27, pp. 2523–2527, July 2007.

[19] F. Fazio, M. Picchio, and C. Messa, "Is ^{11}C-choline the most appropriate tracer for prostate cancer?," *European Journal of Nuclear Medicine and Molecular Imaging*, vol. 31, pp. 753–756, May 2004.

[20] T. Hara, K. Inagaki, N. Kosaka, and T. Morita, "Sensitive detection of mediastinal lymph node metastasis of lung cancer with ^{11}C-choline PET," *Journal of Nuclear Medicine: Official Publication, Society of Nuclear Medicine*, vol. 41, pp. 1507–1513, Sept. 2000.

[21] A. Becherer, M. Szab, G. Karanikas, P. Wunderbaldinger, P. Angelberger, M. Raderer, A. Kurtaran, R. Dudczak, and K. Kletter, "Imaging of Advanced Neuroendocrine Tumors with ^{18}F-FDOPA PET," *Journal of Nuclear Medicine*, vol. 45, pp. 1161–1167, July 2004.

[22] W. Chen, D. H. S. Silverman, S. Delaloye, J. Czernin, N. Kamdar, W. Pope, N. Satyamurthy, C. Schiepers, and T. Cloughesy, "^{18}F-FDOPA PET imaging of brain tumors: comparison study with ^{18}F-FDG PET and evaluation of diagnostic accuracy," *Journal of Nuclear Medicine*, vol. 47, pp. 904–911, June 2006.

[23] A. M. Groves, T. Win, S. B. Haim, and P. J. Ell, "Non-[^{18}F]FDG PET in clinical oncology," *The Lancet Oncology*, vol. 8, pp. 822–830, Sept. 2007.

[24] P. Jwiak, E. Forma, M. Bry, and A. Krzelak, "O-GlcNAcylation and Metabolic Reprograming in Cancer," *Frontiers in Endocrinology*, vol. 5, 2014.

[25] C. E. Meacham and S. J. Morrison, "Tumor heterogeneity and cancer cell plasticity," *Nature*, vol. 501, pp. 328–337, Sept. 2013.

[26] R. A. Burrell, N. McGranahan, J. Bartek, and C. Swanton, "The causes and consequences of genetic heterogeneity in cancer evolution," *Nature*, vol. 501, pp. 338–345, Sept. 2013.

[27] J. Mattern, R. Koomgi, and M. Volm, "Association of vascular endothelial growth factor expression with intratumoral microvessel density and tumour cell proliferation in human epidermoid lung carcinoma.," *British Journal of Cancer*, vol. 73, pp. 931–934, Apr. 1996.

[28] B. Delahunt, P. Bethwaite, and A. Thornton, "Prognostic significance of microscopic vascularity for clear cell renal cell carcinoma," *British Journal of Urology*, vol. 80, pp. 401–404, Sept. 1997.

[29] I. H. Chaudhry, D. G. O'Donovan, P. E. C. Brenchley, H. Reid, and I. S. D. Roberts, "Vascular endothelial growth factor expression correlates with tumour grade and vascularity in gliomas," *Histopathology*, vol. 39, pp. 409–415, Oct. 2001.

[30] N. Ferrara, K. J. Hillan, H.-P. Gerber, and W. Novotny, "Discovery and development of bevacizumab, an anti-VEGF antibody for treating cancer," *Nature Reviews. Drug Discovery*, vol. 3, pp. 391–400, May 2004.

[31] P. Carmeliet, "Angiogenesis in life, disease and medicine.," *Nature*, vol. 438, pp. 932–936, Dec. 2005.

[32] F. Shojaei, "Anti-angiogenesis therapy in cancer: Current challenges and future perspectives," *Cancer Letters*, vol. 320, pp. 130–137, July 2012.

[33] R. A. Gatenby and R. J. Gillies, "Glycolysis in cancer: A potential target for therapy," *The International Journal of Biochemistry & Cell Biology*, vol. 39, pp. 1358–1366, July 2007.

[34] W. G. Kaelin and P. J. Ratcliffe, "Oxygen sensing by metazoans: the central role of the HIF hydroxylase pathway," *Molecular Cell*, vol. 30, pp. 393–402, May 2008.

[35] G. A. Brooks, "Anaerobic threshold: review of the concept and directions for future research," *Medicine and Science in Sports and Exercise*, vol. 17, pp. 22–34, Feb. 1985.

[36] S. Mangia, I. A. Simpson, S. J. Vannucci, and A. Carruthers, "The in vivo neuron-to-astrocyte lactate shuttle in human brain: evidence from modeling of measured lactate levels during visual stimulation," *Journal of Neurochemistry*, vol. 109, pp. 55–62, May 2009.

[37] I. L. Romero, A. Mukherjee, H. A. Kenny, L. M. Litchfield, and E. Lengyel, "Molecular Pathways: Trafficking of Metabolic Resources in the Tumor Microenvironment," *Clinical Cancer Research*, vol. 21, pp. 680–686, Feb. 2015.

[38] P. Sonveaux, F. Vgran, T. Schroeder, M. C. Wergin, J. Verrax, Z. N. Rabbani, C. J. De Saedeleer, K. M. Kennedy, C. Diepart, B. F. Jordan, M. J. Kelley, B. Gallez, M. L. Wahl, O. Feron, and M. W. Dewhirst, "Targeting lactate-fueled respiration selectively kills hypoxic tumor cells in mice," *The Journal of Clinical Investigation*, vol. 118, pp. 3930–3942, Dec. 2008.

[39] C. J. De Saedeleer, T. Copetti, P. E. Porporato, J. Verrax, O. Feron, and P. Sonveaux, "Lactate activates HIF-1 in oxidative but not in Warburg-phenotype human tumor cells," *PloS One*, vol. 7, no. 10, p. e46571, 2012.

[40] H. Lu, R. A. Forbes, and A. Verma, "Hypoxia-inducible Factor 1 Activation by Aerobic Glycolysis Implicates the Warburg Effect in Carcinogenesis," *Journal of Biological Chemistry*, vol. 277, pp. 23111–23115, June 2002.

[41] M. I. Koukourakis, A. Giatromanolaki, A. L. Harris, and E. Sivridis, "Comparison of Metabolic Pathways between Cancer Cells and Stromal Cells in Colorectal Carcinomas: a Metabolic Survival Role for Tumor-Associated Stroma," *Cancer Research*, vol. 66, pp. 632–637, Jan. 2006.

[42] F. Capuani, D. De Martino, E. Marinari, and A. De Martino, "Quantitative constraint-based computational model of tumor-to-stroma coupling via lactate shuttle," *Scientific Reports*, vol. 5, p. 11880, July 2015.

[43] D. Basanta, J. G. Scott, M. N. Fishman, G. Ayala, S. W. Hayward, and A. R. A. Anderson, "Investigating prostate cancer tumourstroma interactions: clinical and biological insights from an evolutionary game," *British Journal of Cancer*, vol. 106, pp. 174–181, Jan. 2012.

[44] S. Pavlides, D. Whitaker-Menezes, R. Castello-Cros, N. Flomenberg, A. K. Witkiewicz, P. G. Frank, M. C. Casimiro, C. Wang, P. Fortina, S. Addya, and others, "The reverse Warburg effect: aerobic glycolysis in cancer associated

fibroblasts and the tumor stroma," *Cell cycle*, vol. 8, no. 23, pp. 3984–4001, 2009.

[45] T. M. Williams and M. P. Lisanti, "Caveolin-1 in oncogenic transformation, cancer, and metastasis," *American Journal of Physiology - Cell Physiology*, vol. 288, pp. C494–C506, Mar. 2005.

[46] K. Wiechen, L. Diatchenko, A. Agoulnik, K. M. Scharff, H. Schober, K. Arlt, B. Zhumabayeva, P. D. Siebert, M. Dietel, R. Schfer, and C. Sers, "Caveolin-1 Is Down-Regulated in Human Ovarian Carcinoma and Acts as a Candidate Tumor Suppressor Gene," *The American Journal of Pathology*, vol. 159, pp. 1635–1643, Nov. 2001.

[47] A. K. Witkiewicz, A. Dasgupta, F. Sotgia, I. Mercier, R. G. Pestell, M. Sabel, C. G. Kleer, J. R. Brody, and M. P. Lisanti, "An Absence of Stromal Caveolin-1 Expression Predicts Early Tumor Recurrence and Poor Clinical Outcome in Human Breast Cancers," *The American Journal of Pathology*, vol. 174, pp. 2023–2034, June 2009.

[48] S. Sayhan, G. Diniz, T. Karadeniz, D. Ayaz, D. S. Kahraman, M. Gokcu, and H. T. Yildirim, "Expression of caveolin-1 in peritumoral stroma is associated with histological grade in ovarian serous tumors," *Ginekologia Polska*, vol. 86, pp. 424–428, June 2015.

[49] U. E. Martinez-Outschoorn, Z. Lin, C. Trimmer, N. Flomenberg, C. Wang, S. Pavlides, R. G. Pestell, A. Howell, F. Sotgia, and M. P. Lisanti, "Cancer cells metabolically "fertilize" the tumor microenvironment with hydrogen peroxide, driving the Warburg effect: implications for PET imaging of human tumors," *Cell Cycle (Georgetown, Tex.)*, vol. 10, pp. 2504–2520, Aug. 2011.

[50] S. Pavlides, A. Tsirigos, I. Vera, N. Flomenberg, P. G. Frank, M. C. Casimiro, C. Wang, P. Fortina, S. Addya, R. G. Pestell, U. E. Martinez-Outschoorn, F. Sotgia, and M. P. Lisanti, "Loss of stromal caveolin-1 leads to oxidative stress, mimics hypoxia and drives inflammation in the tumor microenvironment, conferring the reverse Warburg effect: A transcriptional informatics analysis with validation," *Cell Cycle*, vol. 9, pp. 2201–2219, June 2010.

[51] P. Boyle and B. Levin, "World Cancer Report 2008.," p. 510 pp., 2008.

[52] A. Jemal, R. Siegel, J. Xu, and E. Ward, "Cancer statistics, 2010," *CA: a cancer journal for clinicians*, vol. 60, no. 5, pp. 277–300, 2010.

[53] R. C. Bast, M. Brewer, C. Zou, M. A. Hernandez, M. Daley, R. Ozols, K. Lu, Z. Lu, D. Badgwell, G. B. Mills, S. Skates, Z. Zhang, D. Chan, A. Lokshin, and Y. Yu, "Prevention and early detection of ovarian cancer: mission impossible?," *Recent Results in Cancer Research. Fortschritte Der Krebsforschung. Progrs Dans Les Recherches Sur Le Cancer*, vol. 174, pp. 91–100, 2007.

[54] J. A. Gubbels, N. Claussen, A. K. Kapur, J. P. Connor, and M. S. Patankar, "The detection, treatment, and biology of epithelial ovarian cancer," *Journal of Ovarian Research*, vol. 3, no. 1, p. 8, 2010.

[55] D. K. Armstrong, "Relapsed Ovarian Cancer: Challenges and Management Strategies for a Chronic Disease," *The Oncologist*, vol. 7, pp. 20–28, Oct. 2002.

[56] Y. Lee, F. Medeiros, D. Kindelberger, M. J. Callahan, M. G. Muto, and C. P. Crum, "Advances in the recognition of tubal intraepithelial carcinoma: applications to cancer screening and the pathogenesis of ovarian cancer," *Advances in Anatomic Pathology*, vol. 13, pp. 1–7, Jan. 2006.

[57] Y. Lee, A. Miron, R. Drapkin, M. R. Nucci, F. Medeiros, A. Saleemuddin, J. Garber, C. Birch, H. Mou, R. W. Gordon, D. W. Cramer, F. D. McKeon, and C. P. Crum, "A candidate precursor to serous carcinoma that originates in the distal fallopian tube," *The Journal of Pathology*, vol. 211, pp. 26–35, Jan. 2007.

[58] L. Dubeau, "The cell of origin of ovarian epithelial tumours," *The Lancet Oncology*, vol. 9, pp. 1191–1197, Dec. 2008.

[59] M. J. Callahan, C. P. Crum, F. Medeiros, D. W. Kindelberger, J. A. Elvin, J. E. Garber, C. M. Feltmate, R. S. Berkowitz, and M. G. Muto, "Primary Fallopian Tube Malignancies in BRCA-Positive Women Undergoing Surgery for Ovarian Cancer Risk Reduction," *Journal of Clinical Oncology*, vol. 25, pp. 3985–3990, Sept. 2007.

[60] I. Boger-Megiddo and N. S. Weiss, "Histologic subtypes and laterality of primary epithelial ovarian tumors," *Gynecologic Oncology*, vol. 97, pp. 80–83, Apr. 2005.

[61] A. W. Kurian, R. R. Balise, V. McGuire, and A. S. Whittemore, "Histologic types of epithelial ovarian cancer: have they different risk factors?," *Gynecologic Oncology*, vol. 96, pp. 520–530, Feb. 2005.

[62] D. S. Tan, R. Agarwal, and S. B. Kaye, "Mechanisms of transcoelomic metastasis in ovarian cancer," *The Lancet Oncology*, vol. 7, pp. 925–934, Nov. 2006.

[63] K. M. Nieman, H. A. Kenny, C. V. Penicka, A. Ladanyi, R. Buell-Gutbrod, M. R. Zillhardt, I. L. Romero, M. S. Carey, G. B. Mills, G. S. Hotamisligil, S. D. Yamada, M. E. Peter, K. Gwin, and E. Lengyel, "Adipocytes promote ovarian cancer metastasis and provide energy for rapid tumor growth," *Nature Medicine*, vol. 17, pp. 1498–1503, Nov. 2011.

[64] P. G. Rose, M. S. Piver, Y. Tsukada, and T. Lau, "Metastatic patterns in histologic variants of ovarian cancer. An autopsy study," *Cancer*, vol. 64, pp. 1508–1513, Oct. 1989.

[65] A. Fishman, E. Shalom-Paz, M. Fejgin, E. Gaber, M. Altaras, and A. Amiel, "Comparing the genetic changes detected in the primary and secondary tumor sites of ovarian cancer using comparative genomic hybridization," *International Journal of Gynecological Cancer*, vol. 15, pp. 261–266, Apr. 2005.

[66] S. L. Sangisetty and T. J. Miner, "Malignant ascites: A review of prognostic factors, pathophysiology and therapeutic measures," *World Journal of Gastrointestinal Surgery*, vol. 4, pp. 87–95, Apr. 2012.

[67] F.-q. Wang, J. So, S. Reierstad, and D. A. Fishman, "Vascular endothelial growth factorregulated ovarian cancer invasion and migration involves expression and activation of matrix metalloproteinases," *International Journal of Cancer*, vol. 118, pp. 879–888, Feb. 2006.

[68] X. Fang, M. Schummer, M. Mao, S. Yu, F. H. Tabassam, R. Swaby, Y. Hasegawa, J. L. Tanyi, R. LaPushin, A. Eder, R. Jaffe, J. Erickson, and G. B. Mills, "Lysophosphatidic acid is a bioactive mediator in ovarian cancer," *Biochimica et Biophysica Acta (BBA) - Molecular and Cell Biology of Lipids*, vol. 1582, pp. 257–264, May 2002.

[69] A. Labiche, N. Heutte, P. Herlin, J. Chasle, P. Gauduchon, and N. Elie, "Stromal Compartment as a Survival Prognostic Factor in Advanced Ovarian Carcinoma:," *International Journal of Gynecological Cancer*, vol. 20, pp. 28–33, Jan. 2010.

[70] H. A. Kenny, T. Krausz, S. D. Yamada, and E. Lengyel, "Use of a novel 3d culture model to elucidate the role of mesothelial cells, fibroblasts and extra-cellular matrices on adhesion and invasion of ovarian cancer cells to the omentum," *International Journal of Cancer. Journal International Du Cancer*, vol. 121, pp. 1463–1472, Oct. 2007.

[71] E. S. Jeon, S. C. Heo, I. H. Lee, Y. J. Choi, J. H. Park, K. U. Choi, D.-S. Suh, M.-S. Yoon, J. H. Kim, and others, "Ovarian cancer-derived lysophosphatidic acid stimulates secretion of VEGF and stromal cell-derived factor-1 from human mesenchymal stem cells," *Experimental & molecular medicine*, vol. 42, no. 4, pp. 280–293, 2010.

[72] Y. Zhang, H. Tang, J. Cai, T. Zhang, J. Guo, D. Feng, and Z. Wang, "Ovarian cancer-associated fibroblasts contribute to epithelial ovarian carcinoma metastasis by promoting angiogenesis, lymphangiogenesis and tumor cell invasion," *Cancer Letters*, vol. 303, pp. 47–55, Apr. 2011.

[73] J. Cai, H. Tang, L. Xu, X. Wang, C. Yang, S. Ruan, J. Guo, S. Hu, and Z. Wang, "Fibroblasts in omentum activated by tumor cells promote ovarian cancer growth, adhesion and invasiveness," *Carcinogenesis*, vol. 33, pp. 20–29, Jan. 2012.

[74] J. A. Parrott, E. Nilsson, R. Mosher, G. Magrane, D. Albertson, D. Pinkel, J. W. Gray, and M. K. Skinner, "Stromal-epithelial interactions in the progression of ovarian cancer: influence and source of tumor stromal cells," *Molecular and Cellular Endocrinology*, vol. 175, pp. 29–39, Apr. 2001.

[75] D. Granot, Y. Addadi, V. Kalchenko, A. Harmelin, L. A. Kunz-Schughart, and M. Neeman, "In vivo Imaging of the Systemic Recruitment of Fibroblasts to the Angiogenic Rim of Ovarian Carcinoma Tumors," *Cancer Research*, vol. 67, pp. 9180–9189, Oct. 2007.

[76] K. M. Nieman, I. L. Romero, B. Van Houten, and E. Lengyel, "Adipose tissue and adipocytes supports tumorigenesis and metastasis," *Biochimica et biophysica acta*, vol. 1831, pp. 1533–1541, Oct. 2013.

[77] L. Zhang, J. R. Conejo-Garcia, D. Katsaros, P. A. Gimotty, M. Massobrio, G. Regnani, A. Makrigiannakis, H. Gray, K. Schlienger, M. N. Liebman, S. C. Rubin, and G. Coukos, "Intratumoral T Cells, Recurrence, and Survival in Epithelial Ovarian Cancer," *New England Journal of Medicine*, vol. 348, pp. 203–213, Jan. 2003.

[78] T. J. Curiel, G. Coukos, L. Zou, X. Alvarez, P. Cheng, P. Mottram, M. Evdemon-Hogan, J. R. Conejo-Garcia, L. Zhang, M. Burow, Y. Zhu, S. Wei, I. Kryczek, B. Daniel, A. Gordon, L. Myers, A. Lackner, M. L. Disis, K. L. Knutson, L. Chen, and W. Zou, "Specific recruitment of regulatory T cells in ovarian carcinoma fosters immune privilege and predicts reduced survival," *Nature Medicine*, vol. 10, pp. 942–949, Sept. 2004.

[79] J. Chien, R. Kuang, C. Landen, and V. Shridhar, "Platinum-Sensitive Recurrence in Ovarian Cancer: The Role of Tumor Microenvironment," *Frontiers in Oncology*, vol. 3, Sept. 2013.

[80] E. R. Jamieson and S. J. Lippard, "Structure, Recognition, and Processing of CisplatinDNA Adducts," *Chemical Reviews*, vol. 99, pp. 2467–2498, Sept. 1999.

[81] L. P. Martin, T. C. Hamilton, and R. J. Schilder, "Platinum Resistance: The Role of DNA Repair Pathways," *Clinical Cancer Research*, vol. 14, pp. 1291–1295, Mar. 2008.

[82] L. Galluzzi, L. Senovilla, I. Vitale, J. Michels, I. Martins, O. Kepp, M. Castedo, and G. Kroemer, "Molecular mechanisms of cisplatin resistance," *Oncogene*, vol. 31, pp. 1869–1883, Apr. 2012.

[83] A. D. Steg, K. S. Bevis, A. A. Katre, A. Ziebarth, Z. C. Dobbin, R. D. Alvarez, K. Zhang, M. Conner, and C. N. Landen, "Stem cell pathways contribute to clinical chemoresistance in ovarian cancer," *Clinical Cancer Research*, vol. 18, no. 3, pp. 869–881, 2012.

[84] A. Kreso, C. A. O'Brien, P. van Galen, O. I. Gan, F. Notta, A. M. Brown, K. Ng, J. Ma, E. Wienholds, C. Dunant, and others, "Variable clonal repopulation dynamics influence chemotherapy response in colorectal cancer," *Science*, vol. 339, no. 6119, pp. 543–548, 2013.

[85] Z. Lu, R. Z. Luo, Y. Lu, X. Zhang, Q. Yu, S. Khare, S. Kondo, Y. Kondo, Y. Yu, G. B. Mills, and others, "The tumor suppressor gene ARHI regulates autophagy and tumor dormancy in human ovarian cancer cells," *The Journal of clinical investigation*, vol. 118, no. 12, p. 3917, 2008.

[86] C. A. Sherman-Baust, A. T. Weeraratna, L. B. A. Rangel, E. S. Pizer, K. R. Cho, D. R. Schwartz, T. Shock, and P. J. Morin, "Remodeling of the extracellular matrix through overexpression of collagen VI contributes to cisplatin resistance in ovarian cancer cells," *Cancer Cell*, vol. 3, pp. 377–386, Apr. 2003.

[87] D. T. Scadden, "The stem-cell niche as an entity of action," *Nature*, vol. 441, pp. 1075–1079, June 2006.

[88] R. A. Gatenby and P. K. Maini, "Mathematical oncology: Cancer summed up," *Nature*, vol. 421, pp. 321–321, Jan. 2003.

[89] A. R. A. Anderson and V. Quaranta, "Integrative mathematical oncology," *Nature Reviews. Cancer*, vol. 8, no. 3, pp. 227–234, 2008.

[90] H. Enderling, A. R. A. Anderson, M. A. J. Chaplain, A. J. Munro, and J. S. Vaidya, "Mathematical modelling of radiotherapy strategies for early breast cancer," *Journal of Theoretical Biology*, vol. 241, pp. 158–171, July 2006.

[91] A. H. Chauviere, H. Hatzikirou, J. S. Lowengrub, H. B. Frieboes, A. M. Thompson, and V. Cristini, "Mathematical Oncology: How Are the Mathematical and Physical Sciences Contributing to the War on Breast Cancer?," *Current Breast Cancer Reports*, vol. 2, pp. 121–129, Sept. 2010.

[92] H. Enderling, M. A. J. Chaplain, A. R. A. Anderson, and J. S. Vaidya, "A mathematical model of breast cancer development, local treatment and recurrence," *Journal of Theoretical Biology*, vol. 246, pp. 245–259, May 2007.

[93] S. Turner and J. A. Sherratt, "Intercellular Adhesion and Cancer Invasion: A Discrete Simulation Using the Extended Potts Model," *Journal of Theoretical Biology*, vol. 216, pp. 85–100, May 2002.

[94] M. a. J. Chaplain and G. Lolas, "Mathematical modelling of cancer cell invasion of tissue: the role of the urokinase plasminogen activation system," *Mathematical Models and Methods in Applied Sciences*, vol. 15, pp. 1685–1734, Nov. 2005.

[95] A. Gerisch and M. A. J. Chaplain, "Mathematical modelling of cancer cell invasion of tissue: Local and non-local models and the effect of adhesion," *Journal of Theoretical Biology*, vol. 250, pp. 684–704, Feb. 2008.

[96] A. R. A. Anderson, M. a. J. Chaplain, E. L. Newman, R. J. C. Steele, and A. M. Thompson, "Mathematical Modelling of Tumour Invasion and Metastasis," 2000. DOI: 10.1080/10273660008833042.

[97] J. Gallaher, L. M. Cook, S. Gupta, A. Araujo, J. Dhillon, J. Y. Park, J. G. Scott, J. Pow-Sang, D. Basanta, and C. C. Lynch, "Improving treatment strategies for patients with metastatic castrate resistant prostate cancer through personalized computational modeling," *Clinical & Experimental Metastasis*, vol. 31, pp. 991–999, Dec. 2014.

[98] A. Araujo, L. M. Cook, C. C. Lynch, and D. Basanta, "An Integrated Computational Model of the Bone Microenvironment in Bone-Metastatic Prostate Cancer," *Cancer Research*, vol. 74, pp. 2391–2401, May 2014.

[99] T. Roose, S. Chapman, and P. Maini, "Mathematical Models of Avascular Tumor Growth," *SIAM Review*, vol. 49, pp. 179–208, Jan. 2007.

[100] J. F. Speer, V. E. Petrosky, M. W. Retsky, and R. H. Wardwell, "A Stochastic Numerical Model of Breast Cancer Growth That Simulates Clinical Data," *Cancer Research*, vol. 44, pp. 4124–4130, Sept. 1984.

[101] L. Norton, "A Gompertzian Model of Human Breast Cancer Growth," *Cancer Research*, vol. 48, pp. 7067–7071, Dec. 1988.

[102] J. P. Ward and J. R. King, "Mathematical modelling of avascular-tumour growth," *Mathematical Medicine and Biology: A Journal of the IMA*, vol. 14, pp. 39–69, Mar. 1997.

[103] M. J. Tindall, C. P. Please, and M. J. Peddie, "Modelling the formation of necrotic regions in avascular tumours," *Mathematical Biosciences*, vol. 211, pp. 34–55, Jan. 2008.

[104] P. P. Delsanto, C. A. Condat, N. Pugno, A. S. Gliozzi, and M. Griffa, "A multilevel approach to cancer growth modeling," *Journal of Theoretical Biology*, vol. 250, pp. 16–24, Jan. 2008.

[105] A. R. A. Anderson and M. a. J. Chaplain, "Continuous and discrete mathematical models of tumor-induced angiogenesis," *Bulletin of Mathematical Biology*, vol. 60, pp. 857–899, Sept. 1998.

[106] J. Xu, G. Vilanova, and H. Gomez, "A Mathematical Model Coupling Tumor Growth and Angiogenesis," *PLOS ONE*, vol. 11, p. e0149422, Feb. 2016.

[107] K. R. Swanson, R. C. Rockne, J. Claridge, M. A. Chaplain, E. C. Alvord, and A. R. A. Anderson, "Quantifying the Role of Angiogenesis in Malignant Progression of Gliomas: In Silico Modeling Integrates Imaging and Histology," *Cancer Research*, vol. 71, pp. 7366–7375, Dec. 2011.

[108] J. Gallaher, A. Babu, S. Plevritis, and A. R. A. Anderson, "Bridging population and tissue scale tumor dynamics: A new paradigm for understanding differences in tumor growth and metastatic disease," *Cancer research*, vol. 74, pp. 426–435, Jan. 2014.

[109] J. Moreira and A. Deutsch, "Cellular automaton models of tumor development: a critical review," *Advances in Complex Systems*, vol. 05, pp. 247–267, June 2002.

[110] S. Sanga, H. B. Frieboes, X. Zheng, R. Gatenby, E. L. Bearer, and V. Cristini, "Predictive oncology: a review of multidisciplinary, multiscale in silico modeling linking phenotype, morphology and growth," *NeuroImage*, vol. 37 Suppl 1, pp. S120–134, 2007.

[111] Z. Wang, J. D. Butner, R. Kerketta, V. Cristini, and T. S. Deisboeck, "Simulating cancer growth with multiscale agent-based modeling," *Seminars in Cancer Biology*, vol. 30, pp. 70–78, Feb. 2015.

[112] A. R. Kansal, S. Torquato, G. R. Harsh, E. A. Chiocca, and T. S. Deisboeck, "Simulated Brain Tumor Growth Dynamics Using a Three-Dimensional Cellular Automaton," *Journal of Theoretical Biology*, vol. 203, pp. 367–382, Apr. 2000.

[113] . Monteagudo and J. Santos, "Studying the capability of different cancer hallmarks to initiate tumor growth using a cellular automaton simulation. Application in a cancer stem cell context," *Biosystems*, vol. 115, pp. 46–58, Jan. 2014.

[114] S. Dormann and A. Deutsch, "Modeling of Self-Organized Avascular Tumor Growth with a Hybrid Cellular Automaton," *In Silico Biology*, vol. 2, pp. 393–406, Jan. 2002.

[115] Z. Wang, L. Zhang, J. Sagotsky, and T. S. Deisboeck, "Simulating non-small cell lung cancer with a multiscale agent-based model," *Theoretical Biology & Medical Modelling*, vol. 4, p. 50, Dec. 2007.

[116] J. Chapa, R. J. Bourgo, G. L. Greene, S. Kulkarni, and G. An, "Examining the pathogenesis of breast cancer using a novel agent-based model of mammary ductal epithelium dynamics," *PloS One*, vol. 8, no. 5, p. e64091, 2013.

[117] E. K. Markert and A. Vazquez, "Mathematical models of cancer metabolism," *Cancer & Metabolism*, vol. 3, Dec. 2015.

[118] R. Venkatasubramanian, M. A. Henson, and N. S. Forbes, "Incorporating energy metabolism into a growth model of multicellular tumor spheroids," *Journal of Theoretical Biology*, vol. 242, pp. 440–453, Sept. 2006.

[119] J. J. Casciari, S. V. Sotirchos, and R. M. Sutherland, "Mathematical modelling of microenvironment and growth in EMT6/Ro multicellular tumour spheroids," *Cell Proliferation*, vol. 25, pp. 1–22, Jan. 1992.

[120] R. A. Gatenby and E. T. Gawlinski, "The Glycolytic Phenotype in Carcinogenesis and Tumor Invasion Insights through Mathematical Models," *Cancer Research*, vol. 63, pp. 3847–3854, July 2003.

[121] R. A. Gatenby and E. T. Gawlinski, "A Reaction-Diffusion Model of Cancer Invasion," *Cancer Research*, vol. 56, pp. 5745–5753, Dec. 1996.

[122] S. D. Webb, J. A. Sherratt, and R. G. Fish, "Mathematical Modelling of Tumor Acidity: Regulation of Intracellular pH," *Journal of Theoretical Biology*, vol. 196, pp. 237–250, Jan. 1999.

[123] T. Alarcn, H. M. Byrne, and P. K. Maini, "A cellular automaton model for tumour growth in inhomogeneous environment," *Journal of Theoretical Biology*, vol. 225, pp. 257–274, Nov. 2003.

[124] A. R. A. Anderson, "A hybrid mathematical model of solid tumour invasion: the importance of cell adhesion," *Mathematical Medicine and Biology: A Journal of the IMA*, vol. 22, pp. 163–186, June 2005.

[125] A. A. Patel, E. T. Gawlinski, S. K. Lemieux, and R. A. Gatenby, "A Cellular Automaton Model of Early Tumor Growth and Invasion: The Effects of Native Tissue Vascularity and Increased Anaerobic Tumor Metabolism," *Journal of Theoretical Biology*, vol. 213, pp. 315–331, Dec. 2001.

[126] P. Gerlee and A. R. A. Anderson, "An evolutionary hybrid cellular automaton model of solid tumour growth," *Journal of Theoretical Biology*, vol. 246, pp. 583–603, June 2007.

[127] P. Gerlee and A. R. A. Anderson, "A hybrid cellular automaton model of clonal evolution in cancer: The emergence of the glycolytic phenotype," *Journal of Theoretical Biology*, vol. 250, pp. 705–722, Feb. 2008.

[128] M. Robertson-Tessi, R. J. Gillies, R. A. Gatenby, and A. R. A. Anderson, "Impact of Metabolic Heterogeneity on Tumor Growth, Invasion, and Treatment Outcomes," *Cancer Research*, vol. 75, pp. 1567–1579, Apr. 2015.

[129] A. Kianercy, R. Veltri, and K. J. Pienta, "Critical transitions in a game theoretic model of tumour metabolism," *Interface Focus*, vol. 4, p. 20140014, Aug. 2014.

[130] H. Mayer, K. S. Zaenker, and U. an der Heiden, "A basic mathematical model of the immune response," *Chaos: An Interdisciplinary Journal of Nonlinear Science*, vol. 5, pp. 155–161, Mar. 1995.

[131] L. G. d. Pillis, A. E. Radunskaya, and C. L. Wiseman, "A Validated Mathematical Model of Cell-Mediated Immune Response to Tumor Growth," *Cancer Research*, vol. 65, pp. 7950–7958, Sept. 2005.

[132] M. Robertson-Tessi, A. El-Kareh, and A. Goriely, "A mathematical model of tumorimmune interactions," *Journal of Theoretical Biology*, vol. 294, pp. 56–73, Feb. 2012.

[133] A. Matzavinos, M. A. J. Chaplain, and V. A. Kuznetsov, "Mathematical modelling of the spatio-temporal response of cytotoxic T-lymphocytes to a solid tumour," *Mathematical medicine and biology: a journal of the IMA*, vol. 21, pp. 1–34, Mar. 2004.

[134] K. S. Kim, G. Cho, and I. H. Jung, "Optimal treatment strategy for a tumor model under immune suppression," *Computational and Mathematical Methods in Medicine*, vol. 2014, p. 206287, 2014.

[135] V. S. Rozova and A. S. Bratus, "Therapy strategy in tumour cells and immune system interaction mathematical model," *Applicable Analysis*, vol. 95, pp. 1548–1559, July 2016.

[136] F. Castiglione and B. Piccoli, "Optimal control in a model of dendritic cell transfection cancer immunotherapy," *Bulletin of Mathematical Biology*, vol. 68, pp. 255–274, Feb. 2006.

[137] A. Cappuccio, F. Castiglione, and B. Piccoli, "Determination of the optimal therapeutic protocols in cancer immunotherapy," *Mathematical Biosciences*, vol. 209, pp. 1–13, Sept. 2007.

[138] F. Castiglione and B. Piccoli, "Cancer immunotherapy, mathematical modeling and optimal control," *Journal of Theoretical Biology*, vol. 247, pp. 723–732, Aug. 2007.

[139] F. A. Rihan, D. H. Abdelrahman, F. Al-Maskari, F. Ibrahim, and M. A. Abdeen, "Delay differential model for tumour-immune response with chemoimmunotherapy and optimal control," *Computational and Mathematical Methods in Medicine*, vol. 2014, p. 982978, 2014.

[140] M. Robertson-Tessi, A. El-Kareh, and A. Goriely, "A model for effects of adaptive immunity on tumor response to chemotherapy and chemoimmunotherapy," *Journal of Theoretical Biology*, vol. 380, pp. 569–584, Sept. 2015.

[141] A. Overhauser, "Polarization of Nuclei in Metals," *Physical Review*, vol. 92, no. 2, pp. 411–415, 1953. 01076.

[142] T. Carver, "Polarization of Nuclear Spins in Metals," *Physical Review*, vol. 92, no. 1, pp. 212–213, 1953. 00296.

[143] A. Abragam, "Overhauser Effect in Nonmetals," *Physical Review*, vol. 98, no. 6, pp. 1729–1735, 1955. 00207.

[144] C. D. Jeffries, "Polarization of Nuclei by Resonance Saturation in Paramagnetic Crystals," *Physical Review*, vol. 106, pp. 164–165, Apr. 1957. 00112.

[145] W. De Boer, M. Borghini, K. Morimoto, T. O. Niinikosko, and F. Udo, "Sizeable pure tensor polarization of deuterons in a solid," *Physics Letters A*, vol. 46, pp. 143–144, Dec. 1973. 00019.

[146] W. d. Boer, M. Borghini, K. Morimoto, T. O. Niinikoski, and F. Udo, "Dynamic polarization of protons, deuterons, and carbon-13 nuclei: Thermal contact between nuclear spins and an electron spin-spin interaction reservoir," *Journal of Low Temperature Physics*, vol. 15, pp. 249–267, May 1974. 00089.

[147] A. Abragam and M. Goldman, "Principles of dynamic nuclear polarisation," *Reports on Progress in Physics*, vol. 41, pp. 395–467, Mar. 1978. 00474.

[148] A. Abragam, *Nuclear magnetism : order and disorder*. Oxford: Clarendon Press, 1982. 00941.

[149] Y. Hovav, A. Feintuch, and S. Vega, "Theoretical aspects of dynamic nuclear polarization in the solid state The solid effect," *Journal of Magnetic Resonance*, vol. 207, pp. 176–189, Dec. 2010. 00046.

[150] S. Jannin, A. Comment, and J. J. v. d. Klink, "Dynamic Nuclear Polarization by Thermal Mixing Under Partial Saturation," *Applied Magnetic Resonance*, vol. 43, pp. 59–68, July 2012. 00015.

[151] R. A. Wind, M. J. Duijvestijn, C. van der Lugt, A. Manenschijn, and J. Vriend, "Applications of dynamic nuclear polarization in ^{13}C NMR in solids," *Progress in Nuclear Magnetic Resonance Spectroscopy*, vol. 17, pp. 33–67, 1985. 00000.

[152] J. H. Ardenkjr-Larsen, B. Fridlund, A. Gram, G. Hansson, L. Hansson, M. H. Lerche, R. Servin, M. Thaning, and K. Golman, "Increase in signal-to-noise ratio of >10,000 times in liquid-state NMR," *Proceedings of the National Academy of Sciences*, vol. 100, pp. 10158–10163, Feb. 2003. 00000 PMID: 12930897.

[153] J. Wolber, F. Ellner, B. Fridlund, A. Gram, H. Jhannesson, G. Hansson, L. H. Hansson, M. H. Lerche, S. Mnsson, R. Servin, M. Thaning, K. Golman, and J. H. Ardenkjr-Larsen, "Generating highly polarized nuclear spins in solution using dynamic nuclear polarization," *Nuclear Instruments and Methods in Physics Research Section A: Accelerators, Spectrometers, Detectors and Associated Equipment*, vol. 526, pp. 173–181, June 2004. 00102.

[154] K. Golman, L. E. Olsson, O. Axelsson, S. Mnsson, M. Karlsson, and J. S. Petersson, "Molecular imaging using hyperpolarized ^{13}C," *The British Journal of Radiology*, vol. 76 Spec No 2, pp. S118–127, 2003.

[155] J. H. Ardenkjaer-Larsen, A. M. Leach, N. Clarke, J. Urbahn, D. Anderson, and T. W. Skloss, "Dynamic nuclear polarization polarizer for sterile use intent," *NMR in Biomedicine*, vol. 24, pp. 927–932, Oct. 2011. 00045.

[156] S. J. Nelson, J. Kurhanewicz, D. B. Vigneron, P. E. Z. Larson, A. L. Harzstark, M. Ferrone, M. v. Criekinge, J. W. Chang, R. Bok, I. Park, G. Reed, L. Carvajal, E. J. Small, P. Munster, V. K. Weinberg, J. H. Ardenkjaer-Larsen, A. P. Chen, R. E. Hurd, L.-I. Odegardstuen, F. J. Robb, J. Tropp, and J. A. Murray, "Metabolic Imaging of Patients with Prostate Cancer Using Hyperpolarized [1-^{13}C]Pyruvate," *Science Translational Medicine*, vol. 5, p. 198ra108, Aug. 2013.

[157] "*http://dnpnmr.weebly.com/research.html*, the Lumata Group: Hyperpolarized Magnetic Resonance Lab."

[158] J. H. Ardenkjaer-Larsen, S. Macholl, and H. Jhannesson, "Dynamic Nuclear Polarization with Trityls at 1.2 K," *Applied Magnetic Resonance*, vol. 34, pp. 509–522, Aug. 2008. 00051.

[159] T. Maly, G. T. Debelouchina, V. S. Bajaj, K.-N. Hu, C.-G. Joo, M. L. MakJurkauskas, J. R. Sirigiri, P. C. A. v. d. Wel, J. Herzfeld, R. J. Temkin, and R. G. Griffin, "Dynamic nuclear polarization at high magnetic fields," *The Journal of Chemical Physics*, vol. 128, p. 052211, Feb. 2008. 00280.

[160] J. Heckmann, W. Meyer, E. Radtke, G. Reicherz, and S. Goertz, "Electron spin resonance and its implication on the maximum nuclear polarization of deuterated solid target materials," *Physical Review B*, vol. 74, p. 134418, Oct. 2006. 00041.

[161] B. P. Soule, F. Hyodo, K.-i. Matsumoto, N. L. Simone, J. A. Cook, M. C. Krishna, and J. B. Mitchell, "The chemistry and biology of nitroxide compounds," *Free Radical Biology and Medicine*, vol. 42, pp. 1632–1650, June 2007. 00202.

[162] T. J. Reddy, T. Iwama, H. J. Halpern, and V. H. Rawal, "General Synthesis of Persistent Trityl Radicals for EPR Imaging of Biological Systems," *The Journal of Organic Chemistry*, vol. 67, pp. 4635–4639, July 2002. 00092.

[163] R. E. Hurd, Y.-F. Yen, A. Chen, and J. H. Ardenkjaer-Larsen, "Hyperpolarized 13 C metabolic imaging using dissolution dynamic nuclear polarization,"

Journal of Magnetic Resonance Imaging, vol. 36, pp. 1314–1328, Dec. 2012. 00000.

[164] H. Jhannesson, S. Macholl, and J. H. Ardenkjaer-Larsen, "Dynamic Nuclear Polarization of [1-^{13}C]pyruvic acid at 4.6 tesla," *Journal of Magnetic Resonance*, vol. 197, pp. 167–175, Apr. 2009. 00000.

[165] F. A. Gallagher, M. I. Kettunen, S. E. Day, D.-E. Hu, J. H. Ardenkjr-Larsen, R. i. . Zandt, P. R. Jensen, M. Karlsson, K. Golman, M. H. Lerche, and K. M. Brindle, "Magnetic resonance imaging of pH in vivo using hyperpolarized ^{13}C-labelled bicarbonate," *Nature*, vol. 453, pp. 940–943, June 2008. 00287.

[166] L. Lumata, M. E. Merritt, C. R. Malloy, A. D. Sherry, and Z. Kovacs, "Impact of Gd^{3+} on DNP of [1-^{13}c]Pyruvate Doped with Trityl OX063, BDPA, or 4-Oxo-TEMPO," *The Journal of Physical Chemistry A*, vol. 116, pp. 5129–5138, May 2012.

[167] H. Niebuhr, "Behavior of NMR Structures under Dynamic Nuclear Polarization in Polycrystalline and Amorphous Solids," *Physical Review B*, vol. 5, no. 11, pp. 4226–4231, 1972. 00000.

[168] F. A. Gallagher, M. I. Kettunen, D.-E. Hu, P. R. Jensen, R. i. . Zandt, M. Karlsson, A. Gisselsson, S. K. Nelson, T. H. Witney, S. E. Bohndiek, G. Hansson, T. Peitersen, M. H. Lerche, and K. M. Brindle, "Production of hyperpolarized [1,4-$^{13}C_2$]malate from [1,4-$^{13}C_2$]fumarate is a marker of cell necrosis and treatment response in tumors," *Proceedings of the National Academy of Sciences*, vol. 106, pp. 19801–19806, Nov. 2009. 00102 PMID: 19903889.

[169] S. E. Day, M. I. Kettunen, F. A. Gallagher, D.-E. Hu, M. Lerche, J. Wolber, K. Golman, J. H. Ardenkjaer-Larsen, and K. M. Brindle, "Detecting tumor response to treatment using hyperpolarized ^{13}C magnetic resonance imaging and spectroscopy," *Nature Medicine*, vol. 13, pp. 1382–1387, Nov. 2007. 00337.

[170] M. L. Zierhut, Y.-F. Yen, A. P. Chen, R. Bok, M. J. Albers, V. Zhang, J. Tropp, I. Park, D. B. Vigneron, J. Kurhanewicz, R. E. Hurd, and S. J. Nelson, "Kinetic modeling of hyperpolarized $^{13}C_1$-pyruvate metabolism in normal rats and TRAMP mice," *Journal of Magnetic Resonance*, vol. 202, pp. 85–92, Jan. 2010.

[171] N. Chattergoon, F. Martnez-Santiesteban, W. B. Handler, J. H. Ardenkjr-Larsen, and T. J. Scholl, "Field dependence of T1 for hyperpolarized [1-^{13}C]pyruvate," *Contrast Media & Molecular Imaging*, vol. 8, no. 1, pp. 57–62, 2013.

[172] D. J. Kushner, A. Baker, and T. G. Dunstall, "Pharmacological uses and perspectives of heavy water and deuterated compounds," *Canadian Journal of Physiology and Pharmacology*, vol. 77, pp. 79–88, Feb. 1999.

[173] F. A. Gallagher, M. I. Kettunen, and K. M. Brindle, "Biomedical applications of hyperpolarized ^{13}C magnetic resonance imaging," *Progress in Nuclear Magnetic Resonance Spectroscopy*, vol. 55, pp. 285–295, Nov. 2009. 00000.

[174] H. Han and B. J. Balcom, "Magnetic resonance imaging inside metallic vessels," *Measurement Science and Technology*, vol. 21, p. 103001, Oct. 2010.

[175] E. Johansson, L. E. Olsson, S. Månsson, J. S. Petersson, K. Golman, F. Ståhlberg, and R. Wirestam, "Perfusion assessment with bolus differentiation: a technique applicable to hyperpolarized tracers," *Magnetic Resonance in Medicine*, vol. 52, pp. 1043–1051, Nov. 2004.

[176] R. F. Schulte, J. I. Sperl, E. Weidl, M. I. Menzel, M. A. Janich, O. Khegai, M. Durst, J. H. Ardenkjaer-Larsen, S. J. Glaser, A. Haase, M. Schwaiger, and F. Wiesinger, "Saturation-recovery metabolic-exchange rate imaging with hyperpolarized [1- ^{13}C] pyruvate using spectral-spatial excitation," *Magnetic Resonance in Medicine*, vol. 69, pp. 1209–1216, May 2013.

[177] S. E. Day, M. I. Kettunen, M. K. Cherukuri, J. B. Mitchell, M. J. Lizak, H. D. Morris, S. Matsumoto, A. P. Koretsky, and K. M. Brindle, "Detecting response of rat C6 glioma tumors to radiotherapy using hyperpolarized [1-^{13}C]pyruvate and ^{13}C magnetic resonance spectroscopic imaging," *Magnetic Resonance in Medicine*, vol. 65, pp. 557–563, Feb. 2011.

[178] M. A. Schroeder, L. E. Cochlin, L. C. Heather, K. Clarke, G. K. Radda, and D. J. Tyler, "In vivo assessment of pyruvate dehydrogenase flux in the heart using hyperpolarized carbon-13 magnetic resonance," *Proceedings of the National Academy of Sciences of the United States of America*, vol. 105, pp. 12051–12056, Aug. 2008.

[179] K. Golman, J. S. Petersson, P. Magnusson, E. Johansson, P. keson, C.-M. Chai, G. Hansson, and S. Mnsson, "Cardiac metabolism measured noninvasively by hyperpolarized ^{13}C MRI," *Magnetic Resonance in Medicine*, vol. 59, pp. 1005–1013, May 2008.

[180] P. E. Z. Larson, S. Hu, M. Lustig, A. B. Kerr, S. J. Nelson, J. Kurhanewicz, J. M. Pauly, and D. B. Vigneron, "Fast dynamic 3d MR spectroscopic imaging with compressed sensing and multiband excitation pulses for hyperpolarized ^{13}C studies," *Magnetic Resonance in Medicine*, vol. 65, pp. 610–619, Mar. 2011.

[181] D. Mayer, Y.-F. Yen, J. Tropp, A. Pfefferbaum, R. E. Hurd, and D. M. Spielman, "Application of subsecond spiral chemical shift imaging to real-time multislice metabolic imaging of the rat in vivo after injection of hyperpolarized $^{13}C_1$-pyruvate," *Magnetic Resonance in Medicine*, vol. 62, pp. 557–564, Sept. 2009.

[182] F. Wiesinger, E. Weidl, M. I. Menzel, M. A. Janich, O. Khegai, S. J. Glaser, A. Haase, M. Schwaiger, and R. F. Schulte, "IDEAL spiral CSI for dynamic metabolic MR imaging of hyperpolarized [1-^{13}C]pyruvate," *Magnetic Resonance in Medicine*, vol. 68, pp. 8–16, July 2012.

[183] D. Mayer, Y.-F. Yen, Y. S. Levin, J. Tropp, A. Pfefferbaum, R. E. Hurd, and D. M. Spielman, "In vivo application of sub-second spiral chemical shift imaging (CSI) to hyperpolarized ^{13}C metabolic imaging: Comparison with phase-encoded CSI," *Journal of Magnetic Resonance*, vol. 204, pp. 340–345, June 2010.

[184] R. Schmidt, C. Laustsen, J.-N. Dumez, M. I. Kettunen, E. M. Serrao, I. Marco-Rius, K. M. Brindle, J. H. Ardenkjaer-Larsen, and L. Frydman, "In vivo single-shot ^{13}C spectroscopic imaging of hyperpolarized metabolites by spatiotemporal encoding," *Journal of Magnetic Resonance*, vol. 240, pp. 8–15, Mar. 2014.

[185] K. Golman, J.-H. Ardenkjaer-Larsen, J. Svensson, O. Axelsson, G. Hansson, L. Hansson, H. Jhannesson, I. Leunbach, S. Mnsson, J. S. Petersson, G. Pettersson, R. Servin, and L.-G. Wistrand, "^{13}c-Angiography," *Academic Radiology*, vol. 9, pp. S507–S510, Feb. 2002.

[186] K. Golman, J. H. Ardenkjaer-Larsen, J. S. Petersson, S. Mansson, and I. Leunbach, "Molecular imaging with endogenous substances," *Proceedings of the National Academy of Sciences of the United States of America*, vol. 100, pp. 10435–10439, Sept. 2003. 00283 PMCID: PMC193579 00283 PMID: 12930896.

[187] K. Golman, R. i. . Zandt, and M. Thaning, "Real-time metabolic imaging," *Proceedings of the National Academy of Sciences*, vol. 103, pp. 11270–11275, July 2006.

[188] S. J. Kohler, Y. Yen, J. Wolber, A. P. Chen, M. J. Albers, R. Bok, V. Zhang, J. Tropp, S. Nelson, D. B. Vigneron, J. Kurhanewicz, and R. E. Hurd, "In vivo 13 carbon metabolic imaging at 3t with hyperpolarized ^{13}C-1-pyruvate," *Magnetic Resonance in Medicine: Official Journal of the Society of Magnetic Resonance in Medicine / Society of Magnetic Resonance in Medicine*, vol. 58, pp. 65–69, July 2007. 00000 PMID: 17659629.

[189] M. I. Kettunen, D.-e. Hu, T. H. Witney, R. McLaughlin, F. A. Gallagher, S. E. Bohndiek, S. E. Day, and K. M. Brindle, "Magnetization transfer measurements of exchange between hyperpolarized [1-^{13}C]pyruvate and [1-^{13}C]lactate in a murine lymphoma," *Magnetic Resonance in Medicine*, vol. 63, pp. 872–880, Apr. 2010.

[190] K. Golman and J. S. Petersson, "Metabolic Imaging and Other Applications of Hyperpolarized $^{13}C_1$," *Academic Radiology*, vol. 13, pp. 932–942, Aug. 2006.

[191] A. P. Chen, M. J. Albers, C. H. Cunningham, S. J. Kohler, Y.-F. Yen, R. E. Hurd, J. Tropp, R. Bok, J. M. Pauly, S. J. Nelson, J. Kurhanewicz, and D. B. Vigneron, "Hyperpolarized C-13 spectroscopic imaging of the TRAMP mouse at 3t-initial experience," *Magnetic Resonance in Medicine*, vol. 58, pp. 1099–1106, Dec. 2007. 00130 PMID: 17969006.

[192] K. R. Keshari, R. Sriram, B. L. Koelsch, M. V. Criekinge, D. M. Wilson, J. Kurhanewicz, and Z. J. Wang, "Hyperpolarized ^{13}c-Pyruvate Magnetic Resonance Reveals Rapid Lactate Export in Metastatic Renal Cell Carcinomas," *Cancer Research*, vol. 73, pp. 529–538, Jan. 2013.

[193] M. J. Albers, R. Bok, A. P. Chen, C. H. Cunningham, M. L. Zierhut, V. Y. Zhang, S. J. Kohler, J. Tropp, R. E. Hurd, Y.-F. Yen, S. J. Nelson, D. B. Vigneron, and J. Kurhanewicz, "Hyperpolarized ^{13}C Lactate, Pyruvate, and

Alanine: Noninvasive Biomarkers for Prostate Cancer Detection and Grading," *Cancer Research*, vol. 68, pp. 8607–8615, Oct. 2008. 00215 PMID: 18922937.

[194] P. Seth, A. Grant, J. Tang, E. Vinogradov, X. Wang, R. Lenkinski, and V. P. Sukhatme, "On-target Inhibition of Tumor Fermentative Glycolysis as Visualized by Hyperpolarized Pyruvate," *Neoplasia (New York, N.Y.)*, vol. 13, pp. 60–71, Jan. 2011.

[195] A. Lodi, S. M. Woods, and S. M. Ronen, "Treatment with the MEK inhibitor U0126 induces decreased hyperpolarized pyruvate to lactate conversion in breast, but not prostate, cancer cells," *NMR in Biomedicine*, vol. 26, pp. 299–306, Mar. 2013.

[196] D. J. Tyler, "Cardiovascular Applications of Hyperpolarized MRI," *Current Cardiovascular Imaging Reports*, vol. 4, pp. 108–115, Apr. 2011.

[197] M. A. Schroeder, K. Clarke, S. Neubauer, and D. J. Tyler, "Hyperpolarized Magnetic Resonance A Novel Technique for the In Vivo Assessment of Cardiovascular Disease," *Circulation*, vol. 124, pp. 1580–1594, Apr. 2011.

[198] C. Laustsen, J. A. stergaard, M. H. Lauritzen, R. Nrregaard, S. Bowen, L. V. Sgaard, A. Flyvbjerg, M. Pedersen, and J. H. Ardenkjr-Larsen, "Assessment of early diabetic renal changes with hyperpolarized [1-^{13}C]pyruvate," *Diabetes/Metabolism Research and Reviews*, vol. 29, pp. 125–129, Feb. 2013.

[199] H. Shaghaghi, S. Kadlecek, C. Deshpande, S. Siddiqui, D. Martinez, M. Pourfathi, H. Hamedani, M. Ishii, H. Profka, and R. Rizi, "Metabolic spectroscopy of inflammation in a bleomycin-induced lung injury model using hyperpolarized 1-^{13}c pyruvate," *NMR in Biomedicine*, vol. 27, pp. 939–947, Aug. 2014.

[200] B. Pullinger, H. Profka, J. H. Ardenkjaer-Larsen, N. N. Kuzma, S. Kadlecek, and R. R. Rizi, "Metabolism of hyperpolarized [1-^{13}C]pyruvate in the isolated perfused rat lung an ischemia study," *NMR in Biomedicine*, vol. 25, pp. 1113–1118, Oct. 2012.

[201] M. R. Clatworthy, M. I. Kettunen, D.-E. Hu, R. J. Mathews, T. H. Witney, B. W. C. Kennedy, S. E. Bohndiek, F. A. Gallagher, L. B. Jarvis, K. G. C. Smith, and K. M. Brindle, "Magnetic resonance imaging with hyperpolarized

[1,4-$^{13}C_2$]fumarate allows detection of early renal acute tubular necrosis," *Proceedings of the National Academy of Sciences of the United States of America*, vol. 109, pp. 13374–13379, Aug. 2012.

[202] F. A. Gallagher, M. I. Kettunen, and K. M. Brindle, "Imaging pH with hyperpolarized ^{13}C," *NMR in Biomedicine*, vol. 24, pp. 1006–1015, Oct. 2011. 00028.

[203] C. Cabella, M. Karlsson, C. Canap, G. Catanzaro, S. Colombo Serra, L. Miragoli, L. Poggi, F. Uggeri, L. Venturi, P. Jensen, M. Lerche, and F. Tedoldi, "In vivo and in vitro liver cancer metabolism observed with hyperpolarized [5-^{13}C]glutamine," *Journal of Magnetic Resonance*, vol. 232, pp. 45–52, July 2013.

[204] F. A. Gallagher, M. I. Kettunen, S. E. Day, D.-e. Hu, M. Karlsson, A. Gisselsson, M. H. Lerche, and K. M. Brindle, "Detection of tumor glutamate metabolism in vivo using ^{13}C magnetic resonance spectroscopy and hyperpolarized [1-^{13}C]glutamate," *Magnetic Resonance in Medicine*, vol. 66, pp. 18–23, July 2011.

[205] J. A. Bastiaansen, T. Cheng, M. Mishkovsky, J. M. Duarte, A. Comment, and R. Gruetter, "In vivo enzymatic activity of acetylCoA synthetase in skeletal muscle revealed by ^{13}C turnover from hyperpolarized [1-^{13}C]acetate to [1-^{13}C]acetylcarnitine," *Biochimica et Biophysica Acta (BBA) - General Subjects*, vol. 1830, pp. 4171–4178, Aug. 2013.

[206] M. M. Chaumeil, P. E. Z. Larson, S. M. Woods, L. Cai, P. Eriksson, A. E. Robinson, J. M. Lupo, D. B. Vigneron, S. J. Nelson, R. O. Pieper, J. J. Phillips, and S. M. Ronen, "Hyperpolarized [1-^{13}C] Glutamate: A Metabolic Imaging Biomarker of IDH1 Mutational Status in Glioma," *Cancer Research*, vol. 74, pp. 4247–4257, Aug. 2014.

[207] T. B. Rodrigues, E. M. Serrao, B. W. C. Kennedy, D.-E. Hu, M. I. Kettunen, and K. M. Brindle, "Magnetic resonance imaging of tumor glycolysis using hyperpolarized ^{13}C-labeled glucose," *Nature Medicine*, vol. 20, pp. 93–97, Dec. 2013.

[208] P. Bhattacharya, E. Y. Chekmenev, W. H. Perman, K. C. Harris, A. P. Lin, V. A. Norton, C. T. Tan, B. D. Ross, and D. P. Weitekamp, "Towards hyperpolarized ^{13}c-succinate imaging of brain cancer," *Journal of Magnetic Resonance*, vol. 186, pp. 150–155, May 2007.

[209] R. E. Hurd, Y.-F. Yen, J. Tropp, A. Pfefferbaum, D. M. Spielman, and D. Mayer, "Cerebral dynamics and metabolism of hyperpolarized [1-^{13}C]pyruvate using time-resolved MR spectroscopic imaging," *Journal of Cerebral Blood Flow & Metabolism*, vol. 30, pp. 1734–1741, Oct. 2010.

[210] I. Park, P. E. Z. Larson, J. L. Tropp, L. Carvajal, G. Reed, R. Bok, F. Robb, J. Bringas, A. Kells, P. Pivirotto, K. Bankiewicz, D. B. Vigneron, and S. J. Nelson, "Dynamic hyperpolarized carbon-13 MR metabolic imaging of nonhuman primate brain," *Magnetic Resonance in Medicine*, vol. 71, pp. 19–25, Jan. 2014.

[211] K. Granlund, E. Morris, H. Vargas, S. Lyashchenko, P. DeNoble, V. Sacchini, R. Sosa, M. Kennedy, D. Nicholson, Y. Guo, A. P. Chen, J. Tropp, H. Hricak, and K. R. Keshari, "First-in-woman study of in vivo breast cancer metabolism using hyperpolarized [1-^{13}C] pyruvate," in *In Proceedings of the 24th Annual Meeting of the International Society for Magnetic Resonance in Medicine (ISMRM)*, (Singapore), May 2016.

[212] I. Park, P. E. Z. Larson, L. Carvajal, H.-Y. Chen, M. VanCriekinge, R. Bok, J. Crane, J. Kurhanewicz, D. B. Vigneron, S. Chang, and S. J. Nelson, "Dynamic Hyperpolarized ^{13}C Metabolic Imaging of Patients with Brain Tumors," in *In Proceedings of the 25th Annual Meeting of the International Society for Magnetic Resonance in Medicine (ISMRM)*, (Honolulu, Hawaii, USA), Apr. 2017.

[213] K. Granlund, H. Vargas, S. Lyashchenko, P. DeNoble, V. Laudone, A. Chen, J. Tropp, H. Hricak, and K. R. Keshari, "Utilizing hyperpolarized MRI in prostate cancer to assess metabolic dynamics and histopathologic grade," in *In Proceedings of the 25th Annual Meeting of the International Society for Magnetic Resonance in Medicine (ISMRM)*, (Honolulu, Hawaii, USA), Apr. 2017.

[214] C. H. Cunningham, J. Y. Lau, A. P. Chen, B. J. Geraghty, W. J. Perks, I. Roifman, G. A. Wright, and K. A. Connelly, "Hyperpolarized ^{13}C Metabolic MRI

of the Human Heart: Initial Experience," *Circulation Research*, p. CIRCRESAHA.116.309769, Sept. 2016.

[215] R. Aggarwal, D. B. Vigneron, and J. Kurhanewicz, "Hyperpolarized [1-^{13}C]-Pyruvate Magnetic Resonance Imaging Detects an Early Metabolic Response to Androgen Ablation Therapy in Prostate Cancer," *European Urology*, July 2017.

[216] K. M. Brindle, I. D. Campbell, and R. J. Simpson, "A 1h-NMR study of the activity expressed by lactate dehydrogenase in the human erythrocyte," *European Journal of Biochemistry*, vol. 158, pp. 299–305, July 1986. 00022.

[217] K. M. Brindle, "NMR methods for measuring enzyme kinetics in vivo," *Progress in Nuclear Magnetic Resonance Spectroscopy*, vol. 20, no. 3, pp. 257–293, 1988. 00083.

[218] H. M. McConnell, "Reaction Rates by Nuclear Magnetic Resonance," *The Journal of Chemical Physics*, vol. 28, pp. 430–431, Mar. 1958.

[219] T. Harris, G. Eliyahu, L. Frydman, and H. Degani, "Kinetics of hyperpolarized ^{13}c-pyruvate transport and metabolism in living human breast cancer cells," *Proceedings of the National Academy of Sciences*, vol. 106, pp. 18131–18136, Oct. 2009. 00075 PMID: 19826085.

[220] T. H. Witney, M. I. Kettunen, and K. M. Brindle, "Kinetic Modeling of Hyperpolarized ^{13}C Label Exchange between Pyruvate and Lactate in Tumor Cells," *The Journal of Biological Chemistry*, vol. 286, pp. 24572–24580, July 2011.

[221] T. Xu, D. Mayer, M. Gu, Y.-F. Yen, S. Josan, J. Tropp, A. Pfefferbaum, R. Hurd, and D. Spielman, "Quantification of in vivo metabolic kinetics of hyperpolarized pyruvate in rat kidneys using dynamic ^{13}C MRSI," *NMR in Biomedicine*, vol. 24, pp. 997–1005, Oct. 2011.

[222] J. M. Park, S. Josan, T. Jang, M. Merchant, Y.-F. Yen, R. E. Hurd, L. Recht, D. M. Spielman, and D. Mayer, "Metabolite kinetics in C6 rat glioma model using magnetic resonance spectroscopic imaging of hyperpolarized [1-^{13}C]pyruvate," *Magnetic Resonance in Medicine*, vol. 68, pp. 1886–1893, Dec. 2012.

[223] C. Harrison, C. Yang, A. Jindal, R. J. DeBerardinis, M. A. Hooshyar, M. Merritt, A. Dean Sherry, and C. R. Malloy, "Comparison of kinetic models for analysis of pyruvate-to-lactate exchange by hyperpolarized ^{13}C NMR," *NMR in Biomedicine*, vol. 25, pp. 1286–1294, Nov. 2012.

[224] F. Schilling, S. Dwel, U. Kllisch, M. Durst, R. F. Schulte, S. J. Glaser, A. Haase, A. M. Otto, and M. I. Menzel, "Diffusion of hyperpolarized ^{13}C-metabolites in tumor cell spheroids using real-time NMR spectroscopy," *NMR in Biomedicine*, vol. 26, pp. 557–568, May 2013.

[225] S. M. Kazan, S. Reynolds, A. Kennerley, E. Wholey, J. E. Bluff, J. Berwick, V. J. Cunningham, M. N. Paley, and G. M. Tozer, "Kinetic modeling of hyperpolarized [1-^{13}C]pyruvate metabolism in tumors using a measured arterial input function," *Magnetic Resonance in Medicine*, vol. 70, pp. 943–953, Oct. 2013.

[226] D. K. Hill, M. R. Orton, E. Mariotti, J. K. R. Boult, R. Panek, M. Jafar, H. G. Parkes, Y. Jamin, M. F. Miniotis, N. M. S. Al-Saffar, M. Beloueche-Babari, S. P. Robinson, M. O. Leach, Y.-L. Chung, and T. R. Eykyn, "Model Free Approach to Kinetic Analysis of Real-Time Hyperpolarized ^{13}C Magnetic Resonance Spectroscopy Data," *PLoS ONE*, vol. 8, Sept. 2013.

[227] G. Pages and P. W. Kuchel, "Mathematical Modeling and Data Analysis of NMR Experiments using Hyperpolarized ^{13}C Metabolites," *Magnetic Resonance Insights*, vol. 6, pp. 13–21, Feb. 2013.

[228] F. M. Jeffrey, I. Marin-Valencia, L. B. Good, A. A. Shestov, P.-G. Henry, J. M. Pascual, and C. R. Malloy, "Modeling of brain metabolism and pyruvate compartmentation using ^{13}C NMR in vivo: caution required," *Journal of Cerebral Blood Flow & Metabolism*, vol. 33, pp. 1160–1167, Aug. 2013.

[229] G. Pags and P. W. Kuchel, "FmR analysis: Rapid and direct estimation of relaxation and kinetic parameters from dynamic nuclear polarization time courses," *Magnetic Resonance in Medicine*, vol. 73, pp. 2075–2080, June 2015.

[230] F. A. Gallagher, S. E. Bohndiek, M. I. Kettunen, D. Y. Lewis, D. Soloviev, and K. M. Brindle, "Hyperpolarized ^{13}C MRI and PET: In Vivo Tumor Biochemistry," *Journal of Nuclear Medicine*, vol. 52, pp. 1333–1336, Sept. 2011.

[231] H. Gutte, A. E. Hansen, M. M. E. Larsen, S. Rahbek, S. T. Henriksen, H. H. Johannesen, J. Ardenkjaer-Larsen, A. T. Kristensen, L. Højgaard, and A. Kjær, "Simultaneous Hyperpolarized ^{13}c-Pyruvate MRI and ^{18}f-FDG PET (Hyper-PET) in 10 Dogs with Cancer," *Journal of Nuclear Medicine*, vol. 56, pp. 1786–1792, Nov. 2015.

[232] F. Castell and G. J. R. Cook, "Quantitative techniques in ^{18}F-FDG PET scanning in oncology," *British Journal of Cancer*, vol. 98, pp. 1597–1601, May 2008.

[233] A. Almuhaideb, N. Papathanasiou, and J. Bomanji, "^{18}F-FDG PET/CT Imaging In Oncology," *Annals of Saudi Medicine*, vol. 31, no. 1, pp. 3–13, 2011.

[234] D. Delbeke, D. M. Rose, W. C. Chapman, C. W. Pinson, and e. al, "Optimal interpretation of FDG PET in the diagnosis, staging and management of pancreatic carcinoma," *The Journal of Nuclear Medicine; New York*, vol. 40, pp. 1784–91, Nov. 1999.

[235] G. Moulin-Romsee, E. Hindi, X. Cuenca, P. Brice, D. Decaudin, M. Bnamor, J. Brire, M. Anitei, J.-E. Filmont, D. Sibon, E. d. Kerviler, and J.-L. Moretti, "^{18}F-FDG PET/CT bone/bone marrow findings in Hodgkins lymphoma may circumvent the use of bone marrow trephine biopsy at diagnosis staging," *European Journal of Nuclear Medicine and Molecular Imaging*, vol. 37, pp. 1095–1105, June 2010.

[236] C. Schiepers, J.-E. Filmont, and J. Czernin, "PET for staging of Hodgkin's disease and non-Hodgkin's lymphoma," *European Journal of Nuclear Medicine and Molecular Imaging*, vol. 30, pp. S82–S88, June 2003.

[237] G. Antoch, J. Stattaus, A. T. Nemat, S. Marnitz, T. Beyer, H. Kuehl, A. Bockisch, J. F. Debatin, and L. S. Freudenberg, "NonSmall Cell Lung Cancer: Dual-Modality PET/CT in Preoperative Staging," *Radiology*, vol. 229, pp. 526–533, Nov. 2003.

[238] C. Schiepers, F. Penninckx, N. De Vadder, E. Merckx, L. Mortelmans, G. Bormans, G. Marchal, L. Filez, and R. Aerts, "Contribution of PET in the diagnosis of recurrent colorectal cancer: comparison with conventional imaging," *European Journal of Surgical Oncology (EJSO)*, vol. 21, pp. 517–522, Oct. 1995.

[239] S. Adams, R. P. Baum, T. Stuckensen, K. Bitter, and G. Hr, "Prospective comparison of ^{18}F-FDG PET with conventional imaging modalities (CT, MRI, US) in lymph node staging of head and neck cancer," *European Journal of Nuclear Medicine*, vol. 25, pp. 1255–1260, Sept. 1998.

[240] Y. Nakamoto, T. Saga, and S. Fujii, "Positron emission tomography application for gynecologic tumors," *International Journal of Gynecological Cancer*, vol. 15, pp. 701–709, Sept. 2005.

[241] W. Römer, N. Avril, J. Dose, S. Ziegler, W. Kuhn, M. Herz, F. Jänicke, and M. Schwaiger, "[Metabolic characterization of ovarian tumors with positron-emission tomography and F-18 fluorodeoxyglucose]," *RoFo : Fortschritte auf dem Gebiete der Rontgenstrahlen und der Nuklearmedizin*, vol. 166, pp. 62–68, Jan. 1997.

[242] M. M. Thrall, J. A. DeLoia, H. Gallion, and N. Avril, "Clinical use of combined positron emission tomography and computed tomography (FDG-PET/CT) in recurrent ovarian cancer," *Gynecologic Oncology*, vol. 105, pp. 17–22, Apr. 2007.

[243] N. Avril, S. Sassen, B. Schmalfeldt, J. Naehrig, S. Rutke, W. A. Weber, M. Werner, H. Graeff, M. Schwaiger, and W. Kuhn, "Prediction of Response to Neoadjuvant Chemotherapy by Sequential F-18-Fluorodeoxyglucose Positron Emission Tomography in Patients With Advanced-Stage Ovarian Cancer," *Journal of Clinical Oncology*, vol. 23, pp. 7445–7453, Oct. 2005.

[244] M. Hutchings, A. Loft, M. Hansen, L. M. Pedersen, T. Buhl, J. Jurlander, S. Buus, S. Keiding, F. D'Amore, A.-M. Boesen, A. K. Berthelsen, and L. Specht, "FDG-PET after two cycles of chemotherapy predicts treatment failure and progression-free survival in Hodgkin lymphoma," *Blood*, vol. 107, pp. 52–59, Jan. 2006.

[245] M. P. Mac Manus, R. J. Hicks, J. P. Matthews, A. McKenzie, D. Rischin, E. K. Salminen, and D. L. Ball, "Positron Emission Tomography Is Superior to Computed Tomography Scanning for Response-Assessment After Radical Radiotherapy or Chemoradiotherapy in Patients With NonSmall-Cell Lung Cancer," *Journal of Clinical Oncology*, vol. 21, pp. 1285–1292, Apr. 2003.

[246] H. A. Wieder, B. L. Brcher, F. Zimmermann, K. Becker, F. Lordick, A. Beer, M. Schwaiger, U. Fink, J. R. Siewert, H. J. Stein, and W. A. Weber, "Time

Course of Tumor Metabolic Activity During Chemoradiotherapy of Esophageal Squamous Cell Carcinoma and Response to Treatment," *Journal of Clinical Oncology*, vol. 22, pp. 900–908, Mar. 2004.

[247] C. Beckers, C. Ribbens, B. Andr, S. Marcelis, O. Kaye, L. Mathy, M.-J. Kaiser, R. Hustinx, J. Foidart, and M. G. Malaise, "Assessment of Disease Activity in Rheumatoid Arthritis with ^{18}F-FDG PET," *Journal of Nuclear Medicine*, vol. 45, pp. 956–964, June 2004.

[248] D. Sobic-Saranovic, V. Artiko, and V. Obradovic, "FDG PET imaging in sarcoidosis," *Seminars in Nuclear Medicine*, vol. 43, pp. 404–411, Nov. 2013.

[249] M. Sathekge, A. Maes, and C. V. d. Wiele, "FDG-PET Imaging in HIV Infection and Tuberculosis," *Seminars in Nuclear Medicine*, vol. 43, pp. 349–366, Sept. 2013.

[250] A. E. Heald, J. M. Hoffman, J. A. Bartlett, and H. A. Waskin, "Differentiation of central nervous system lesions in AIDS patients using positron emission tomography (PET)," *International Journal of STD & AIDS*, vol. 7, pp. 337–346, Aug. 1996.

[251] J. Meller, C.-O. Sahlmann, and A. K. Scheel, "^{18}F-FDG PET and PET/CT in Fever of Unknown Origin," *Journal of Nuclear Medicine*, vol. 48, pp. 35–45, Jan. 2007.

[252] R. Wang and D. R. Green, "Metabolic reprogramming and metabolic dependency in T cells," *Immunological reviews*, vol. 249, pp. 14–26, Sept. 2012.

[253] R. Wang and D. R. Green, "The immune diet: meeting the metabolic demands of lymphocyte activation," *F1000 Biology Reports*, vol. 4, May 2012.

[254] U. Nestle, S. Kremp, A. Schaefer-Schuler, C. Sebastian-Welsch, D. Hellwig, C. Rbe, and C.-M. Kirsch, "Comparison of Different Methods for Delineation of ^{18}F-FDG PET-Positive Tissue for Target Volume Definition in Radiotherapy of Patients with Non-Small Cell Lung Cancer," *Journal of Nuclear Medicine*, vol. 46, pp. 1342–1348, Aug. 2005.

[255] M. Hatt, C. C. L. Rest, N. Albarghach, O. Pradier, and D. Visvikis, "PET functional volume delineation: a robustness and repeatability study," *European Journal of Nuclear Medicine and Molecular Imaging*, vol. 38, pp. 663–672, Apr. 2011.

[256] D. A. Rottenberg, J. R. Moeller, S. C. Strother, V. Dhawan, and M. L. Sergi, "Effects of Percent Thresholding on the Extraction of [18F]Fluorodeoxyglucose Positron Emission Tomographic Region-of-Interest Data," *Journal of Cerebral Blood Flow & Metabolism*, vol. 11, pp. A83–A88, Mar. 1991.

[257] W. Jentzen, L. Freudenberg, E. G. Eising, M. Heinze, W. Brandau, and A. Bockisch, "Segmentation of PET Volumes by Iterative Image Thresholding," *Journal of Nuclear Medicine*, vol. 48, pp. 108–114, Jan. 2007.

[258] F. Hofheinz, C. Ptzsch, L. Oehme, B. Beuthien-Baumann, J. Steinbach, J. Kotzerke, and J. v. d. Hoff, "Automatic volume delineation in oncological PET," *Nuklearmedizin*, vol. 51, no. 1, pp. 9–16, 2012.

[259] H. Zaidi and I. E. Naqa, "PET-guided delineation of radiation therapy treatment volumes: a survey of image segmentation techniques," *European Journal of Nuclear Medicine and Molecular Imaging*, vol. 37, pp. 2165–2187, Mar. 2010.

[260] N. Sharma and L. M. Aggarwal, "Automated medical image segmentation techniques," *Journal of Medical Physics / Association of Medical Physicists of India*, vol. 35, no. 1, pp. 3–14, 2010.

[261] L. Drever, W. Roa, A. McEwan, and D. Robinson, "Comparison of three image segmentation techniques for target volume delineation in positron emission tomography," *Journal of Applied Clinical Medical Physics*, vol. 8, pp. 93–109, Mar. 2007.

[262] X. Geets, J. A. Lee, A. Bol, M. Lonneux, and V. Grgoire, "A gradient-based method for segmenting FDG-PET images: methodology and validation," *European Journal of Nuclear Medicine and Molecular Imaging*, vol. 34, pp. 1427–1438, Sept. 2007.

[263] C.-Y. Hsu, C.-Y. Liu, and C.-M. Chen, "Automatic segmentation of liver PET images," *Computerized Medical Imaging and Graphics*, vol. 32, pp. 601–610, Oct. 2008.

[264] H. Li, W. L. Thorstad, K. J. Biehl, R. Laforest, Y. Su, K. I. Shoghi, E. D. Donnelly, D. A. Low, and W. Lu, "A novel PET tumor delineation method based on adaptive region-growing and dual-front active contours," *Medical Physics*, vol. 35, pp. 3711–3721, Aug. 2008.

[265] S. Osher and J. A. Sethian, "Fronts propagating with curvature-dependent speed: Algorithms based on Hamilton-Jacobi formulations," *Journal of Computational Physics*, vol. 79, pp. 12–49, Nov. 1988.

[266] K. J. Friston, A. Holmes, J.-B. Poline, C. J. Price, and C. D. Frith, "Detecting Activations in PET and fMRI: Levels of Inference and Power," *NeuroImage*, vol. 4, pp. 223–235, Dec. 1996.

[267] J. Cheng-Liao and J. Qi, "Segmentation of mouse dynamic PET images using a multiphase level set method," *Physics in Medicine & Biology*, vol. 55, no. 21, p. 6549, 2010.

[268] Y. Dong, E. Frey, I. Madar, and Y. Du, "Automatic segmentation of left ventricle myocardium volume-of-interest from cardiac PET images," *Journal of Nuclear Medicine*, vol. 55, pp. 2039–2039, May 2014.

[269] Q. Xie, X. Pan, and H. Zhu, "A multiphase level set clustering approach using MRF-based Student's-t mixture model," in *2016 8th International Conference on Wireless Communications Signal Processing (WCSP)*, pp. 1–5, Oct. 2016.

[270] M. X. H. Yan and J. S. Karp, "Segmentation of 3d brain MR using an adaptive K-means clustering algorithm," in *Nuclear Science Symposium and Medical Imaging Conference, 1994., 1994 IEEE Conference Record*, vol. 4, pp. 1529–1533 vol.4, Oct. 1994.

[271] L.-H. Juang and M.-N. Wu, "MRI brain lesion image detection based on color-converted K-means clustering segmentation," *Measurement*, vol. 43, pp. 941–949, Aug. 2010.

[272] D.-Q. Zhang and S.-C. Chen, "A novel kernelized fuzzy C-means algorithm with application in medical image segmentation," *Artificial Intelligence in Medicine*, vol. 32, pp. 37–50, Sept. 2004.

[273] H. Zaidi, M. Diaz-Gomez, A. Boudraa, and D. O. Slosman, "Fuzzy clustering-based segmented attenuation correction in whole-body PET imaging," *Physics in Medicine and Biology*, vol. 47, no. 7, p. 1143, 2002.

[274] A.-E.-O. Boudraa, J. Champier, L. Cinotti, J.-C. Bordet, F. Lavenne, and J.-J. Mallet, "Delineation and quantitation of brain lesions by fuzzy clustering in Positron Emission Tomography," *Computerized Medical Imaging and Graphics*, vol. 20, pp. 31–41, Jan. 1996.

[275] S. Belhassen and H. Zaidi, "A novel fuzzy C-means algorithm for unsupervised heterogeneous tumor quantification in PET," *Medical Physics*, vol. 37, pp. 1309–1324, Mar. 2010.

[276] L. Szilagyi, Z. Benyo, S. M. Szilagyi, and H. S. Adam, "MR brain image segmentation using an enhanced fuzzy C-means algorithm," in *Proceedings of the 25th Annual International Conference of the IEEE Engineering in Medicine and Biology Society, 2003*, vol. 1, pp. 724–726 Vol.1, Sept. 2003.

[277] M. Aristophanous, B. C. Penney, M. K. Martel, and C. A. Pelizzari, "A Gaussian mixture model for definition of lung tumor volumes in positron emission tomography," *Medical Physics*, vol. 34, pp. 4223–4235, Nov. 2007.

[278] M. Hatt, C. C. l. Rest, A. Turzo, C. Roux, and D. Visvikis, "A Fuzzy Locally Adaptive Bayesian Segmentation Approach for Volume Determination in PET," *IEEE Transactions on Medical Imaging*, vol. 28, pp. 881–893, June 2009.

[279] S. Bricq, C. Collet, and J. P. Armspach, "Unifying framework for multimodal brain MRI segmentation based on Hidden Markov Chains," *Medical Image Analysis*, vol. 12, pp. 639–652, Dec. 2008.

[280] M. Ibrahim, N. John, M. Kabuka, and A. Younis, "Hidden Markov models-based 3d MRI brain segmentation," *Image and Vision Computing*, vol. 24, pp. 1065–1079, Oct. 2006.

[281] M. Martn-Fernndez, C.-F. Westin, and C. Alberola-Lpez, "3d Bayesian Regularization of Diffusion Tensor MRI Using Multivariate Gaussian Markov Random Fields," in *Medical Image Computing and Computer-Assisted Intervention MICCAI 2004* (C. Barillot, D. R. Haynor, and P. Hellier, eds.), no. 3216 in Lecture Notes in Computer Science, pp. 351–359, Springer Berlin Heidelberg, Sept. 2004. DOI: 10.1007/978-3-540-30135-6_43.

[282] Y. Zhang, M. Brady, and S. Smith, "Segmentation of brain MR images through a hidden Markov random field model and the expectation-maximization algorithm," *IEEE Transactions on Medical Imaging*, vol. 20, pp. 45–57, Jan. 2001.

[283] R. S. Alomari, S. Kompalli, and V. Chaudhary, "Segmentation of the Liver from Abdominal CT Using Markov Random Field Model and GVF Snakes," in *International Conference on Complex, Intelligent and Software Intensive Systems, 2008. CISIS 2008*, pp. 293–298, Mar. 2008.

[284] S. Kadoury, H. Labelle, and N. Paragios, "Automatic inference of articulated spine models in CT images using high-order Markov Random Fields," *Medical Image Analysis*, vol. 15, pp. 426–437, Aug. 2011.

[285] J. L. Chen, S. R. Gunn, M. S. Nixon, and R. N. Gunn, "Markov Random Field Models for Segmentation of PET Images," in *Information Processing in Medical Imaging* (M. F. Insana and R. M. Leahy, eds.), no. 2082 in Lecture Notes in Computer Science, pp. 468–474, Springer Berlin Heidelberg, June 2001. DOI: 10.1007/3-540-45729-1_50.

[286] M. Hatt, F. Lamare, N. Boussion, A. Turzo, C. Collet, F. Salzenstein, C. Roux, P. Jarritt, K. Carson, C. C.-L. Rest, and D. Visvikis, "Fuzzy hidden Markov chains segmentation for volume determination and quantitation in PET," *Physics in Medicine and Biology*, vol. 52, no. 12, p. 3467, 2007.

[287] Y. Guo, Y. Feng, J. Sun, N. Zhang, W. Lin, Y. Sa, and P. Wang, "Automatic Lung Tumor Segmentation on PET/CT Images Using Fuzzy Markov Random Field Model," *Computational and Mathematical Methods in Medicine*, vol. 2014, p. e401201, May 2014.

[288] J. Solomon, J. A. Butman, and A. Sood, "Segmentation of brain tumors in 4d MR images using the hidden Markov model," *Computer Methods and Programs in Biomedicine*, vol. 84, pp. 76–85, Dec. 2006.

[289] L. Cordero-Grande, G. Vegas-Snchez-Ferrero, P. Casaseca-de-la Higuera, J. Alberto San-Romn-Calvar, A. Revilla-Orodea, M. Martn-Fernndez, and C. Alberola-Lpez, "Unsupervised 4d myocardium segmentation with a Markov Random Field based deformable model," *Medical Image Analysis*, vol. 15, pp. 283–301, June 2011.

[290] X. Descombes, F. Kruggel, and D. Y. V. Cramon, "Spatio-temporal fMRI analysis using Markov random fields," *IEEE Transactions on Medical Imaging*, vol. 17, pp. 1028–1039, Dec. 1998.

[291] K. Golman, R. i. Zandt, M. Lerche, R. Pehrson, and J. H. Ardenkjaer-Larsen, "Metabolic Imaging by Hyperpolarized ^{13}C Magnetic Resonance Imaging for In vivo Tumor Diagnosis," *Cancer Research*, vol. 66, pp. 10855–10860, Nov. 2006. 00290 PMID: 17108122.

[292] P. E. Kinahan and J. W. Fletcher, "PET/CT Standardized Uptake Values (SUVs) in Clinical Practice and Assessing Response to Therapy," *Seminars in ultrasound, CT, and MR*, vol. 31, pp. 496–505, Dec. 2010.

[293] O. Khegai, R. F. Schulte, M. A. Janich, M. I. Menzel, E. Farrell, A. M. Otto, J. H. Ardenkjaer-Larsen, S. J. Glaser, A. Haase, M. Schwaiger, and F. Wiesinger, "Apparent rate constant mapping using hyperpolarized [1^{13}C]pyruvate," *NMR in Biomedicine*, vol. 27, pp. 1256–1265, Oct. 2014.

[294] A. J. Miller and P. M. Joseph, "The use of power images to perform quantitative analysis on low SNR MR images," *Magnetic Resonance Imaging*, vol. 11, no. 7, pp. 1051–1056, 1993.

[295] L. Z. Li, S. Kadlececk, H. N. Xu, D. Daye, B. Pullinger, H. Profka, L. Chodosh, and R. Rizi, "Ratiometric analysis in hyperpolarized NMR (I): Test of the two-site exchange model and the quantification of reaction rate constants," *NMR in biomedicine*, vol. 26, pp. 1308–1320, Oct. 2013.

[296] D. M. Spielman, D. Mayer, Y.-F. Yen, J. Tropp, R. E. Hurd, and A. Pfefferbaum, "In vivo measurement of ethanol metabolism in the rat liver using magnetic resonance spectroscopy of hyperpolarized [1-^{13}C]pyruvate," *Magnetic Resonance in Medicine*, vol. 62, pp. 307–313, Aug. 2009.

[297] P. A. Gmez Damin, J. I. Sperl, M. A. Janich, O. Khegai, F. Wiesinger, S. J. Glaser, A. Haase, M. Schwaiger, R. F. Schulte, and M. I. Menzel, "Multisite Kinetic Modeling of ^{13}C Metabolic MR Using [1-^{13}C]Pyruvate," *Radiology Research and Practice*, vol. 2014, 2014.

[298] J. H. Steiger, "Tests for comparing elements of a correlation matrix," *Psychological Bulletin*, vol. 87, pp. 245–251, Mar. 1980.

[299] J. E. Cavanaugh, "Unifying the derivations for the Akaike and corrected Akaike information criteria," *Statistics & Probability Letters*, vol. 33, pp. 201–208, Apr. 1997.

[300] K. A. Johnson and R. S. Goody, "The Original Michaelis Constant: Translation of the 1913 Michaelis-Menten Paper," *Biochemistry*, vol. 50, pp. 8264–8269, Oct. 2011.

[301] M. J. Beresford, A. R. Padhani, N. J. Taylor, M.-L. Ah-See, J. J. Stirling, A. Makris, J. A. d'Arcy, and D. J. Collins, "Inter- and intraobserver variability in the evaluation of dynamic breast cancer MRI," *Journal of Magnetic Resonance Imaging*, vol. 24, pp. 1316–1325, Dec. 2006.

[302] J. Van de Steene, N. Linthout, J. de Mey, V. Vinh-Hung, C. Claassens, M. Noppen, A. Bel, and G. Storme, "Definition of gross tumor volume in lung cancer: inter-observer variability," *Radiotherapy and Oncology*, vol. 62, pp. 37–49, Jan. 2002.

[303] D. F. Emerich, R. L. Dean, P. Snodgrass, D. Lafreniere, M. Agostino, T. Wiens, H. Xiong, B. Hasler, J. Marsh, M. Pink, B. S. Kim, B. Perdomo, and R. T. Bartus, "Bradykinin Modulation of Tumor Vasculature: II. Activation of Nitric Oxide and Phospholipase A2/Prostaglandin Signaling Pathways Synergistically Modifies Vascular Physiology and Morphology to Enhance Delivery of Chemotherapeutic Agents to Tumors," *Journal of Pharmacology and Experimental Therapeutics*, vol. 296, pp. 632–641, Feb. 2001.

[304] M. F. Santarelli, V. Positano, G. Giovannetti, F. Frijia, L. Menichetti, J.-H. Ardenkjaer-Larsen, D. De Marchi, V. Lionetti, G. Aquaro, M. Lombardi, and L. Landini, "How the signal-to-noise ratio influences hyperpolarized ^{13}C dynamic MRS data fitting and parameter estimation," *NMR in Biomedicine*, vol. 25, pp. 925–934, July 2012.

[305] Y. F. Yen, S. J. Kohler, A. P. Chen, J. Tropp, R. Bok, J. Wolber, M. J. Albers, K. A. Gram, M. L. Zierhut, I. Park, V. Zhang, S. Hu, S. J. Nelson, D. B. Vigneron, J. Kurhanewicz, H. a. a. M. Dirven, and R. E. Hurd, "Imaging considerations for in vivo ^{13}C metabolic mapping using hyperpolarized ^{13}C-pyruvate," *Magnetic Resonance in Medicine*, vol. 62, pp. 1–10, July 2009. 00051 PMCID: PMC2782538 00051 PMID: 19319902.

[306] M. Durst, U. Koellisch, A. Frank, G. Rancan, C. V. Gringeri, V. Karas, F. Wiesinger, M. I. Menzel, M. Schwaiger, A. Haase, and R. F. Schulte, "Comparison of acquisition schemes for hyperpolarised ^{13}C imaging," *NMR in Biomedicine*, vol. 28, pp. 715–725, June 2015.

[307] C. J. Daniels, M. A. McLean, R. F. Schulte, F. J. Robb, A. B. Gill, N. McGlashan, M. J. Graves, M. Schwaiger, D. J. Lomas, K. M. Brindle, and F. A. Gallagher, "A comparison of quantitative methods for clinical imaging with

hyperpolarized ^{13} C-pyruvate: Comparison of Hyperpolarized ^{13} C-pyruvate Quantitative Methods," *NMR in Biomedicine*, vol. 29, pp. 387–399, Apr. 2016.

[308] S. Ruan, B. Moretti, J. Fadili, and D. Bloyet, "Fuzzy Markovian Segmentation in Application of Magnetic Resonance Images," *Computer Vision and Image Understanding*, vol. 85, pp. 54–69, Jan. 2002.

[309] S. P. Chatzis and T. A. Varvarigou, "A Fuzzy Clustering Approach Toward Hidden Markov Random Field Models for Enhanced Spatially Constrained Image Segmentation," *IEEE Transactions on Fuzzy Systems*, vol. 16, pp. 1351–1361, Oct. 2008.

[310] J. Zhang, "The mean field theory in EM procedures for Markov random fields," *IEEE Transactions on Signal Processing*, vol. 40, pp. 2570–2583, Oct. 1992.

[311] H. Ichihashi, K. Miyagishi, and K. Honda, "Fuzzy c-means clustering with regularization by K-L information," in *The 10th IEEE International Conference on Fuzzy Systems, 2001*, vol. 2, pp. 924–927 vol.3, Dec. 2001.

[312] S. M. Larson, Y. Erdi, T. Akhurst, M. Mazumdar, H. A. Macapinlac, R. D. Finn, C. Casilla, M. Fazzari, N. Srivastava, H. W. D. Yeung, J. L. Humm, J. Guillem, R. Downey, M. Karpeh, A. E. Cohen, and R. Ginsberg, "Tumor Treatment Response Based on Visual and Quantitative Changes in Global Tumor Glycolysis Using PET-FDG Imaging: The Visual Response Score and the Change in Total Lesion Glycolysis," *Clinical Positron Imaging*, vol. 2, pp. 159–171, May 1999.

[313] S. Ben-Haim and P. Ell, "^{18}F-FDG PET and PET/CT in the Evaluation of Cancer Treatment Response," *Journal of Nuclear Medicine*, vol. 50, pp. 88–99, Jan. 2009.

[314] K. Pietras and A. Östman, "Hallmarks of cancer: Interactions with the tumor stroma," *Experimental Cell Research*, vol. 316, pp. 1324–1331, May 2010.

[315] M. P. Lisanti, U. E. Martinez-Outschoorn, B. Chiavarina, S. Pavlides, D. Whitaker-Menezes, A. Tsirigos, A. K. Witkiewicz, Z. Lin, R. M. Balliet, A. Howell, and others, "Understanding the" lethal" drivers of tumor-stroma co-evolution: emerging role (s) for hypoxia, oxidative stress and autophagy/mitophagy in the tumor microenvironment," *Cancer biology & therapy*, vol. 10, no. 6, pp. 537–542, 2010.

[316] G. Bonuccelli, D. Whitaker-Menezes, R. Castello-Cros, S. Pavlides, R. G. Pestell, A. Fatatis, A. K. Witkiewicz, M. G. Vander Heiden, G. Migneco, B. Chiavarina, and others, "The reverse Warburg effect: glycolysis inhibitors prevent the tumor promoting effects of caveolin-1 deficient cancer associated fibroblasts," *Cell cycle*, vol. 9, no. 10, pp. 1960–1971, 2010.

[317] U. Martinez-Outschoorn, F. Sotgia, and M. P. Lisanti, "Tumor Microenvironment and Metabolic Synergy in Breast Cancers: Critical Importance of Mitochondrial Fuels and Function," *Seminars in Oncology*, vol. 41, pp. 195–216, Apr. 2014.

[318] A. G. Rockall, N. Avril, R. Lam, R. Iannone, P. D. Mozley, C. Parkinson, D. Bergstrom, E. Sala, S.-J. Sarker, I. A. McNeish, and J. D. Brenton, "Repeatability of Quantitative FDG-PET/CT and Contrast-Enhanced CT in Recurrent Ovarian Carcinoma: TestRetest Measurements for Tumor FDG Uptake, Diameter, and Volume," *American Association for Cancer Research*, vol. 20, pp. 2751–2760, May 2014.

[319] I. G. Schauer, A. K. Sood, S. Mok, and J. Liu, "Cancer-Associated Fibroblasts and Their Putative Role in Potentiating the Initiation and Development of Epithelial Ovarian Cancer," *Neoplasia*, vol. 13, pp. 393–405, May 2011.

[320] A. K. Mitra, M. Zillhardt, Y. Hua, P. Tiwari, A. E. Murmann, M. E. Peter, and E. Lengyel, "MicroRNAs Reprogram Normal Fibroblasts into Cancer-Associated Fibroblasts in Ovarian Cancer," *Cancer Discovery*, vol. 2, pp. 1100–1108, Dec. 2012.

[321] J. Ferlay, I. Soerjomataram, R. Dikshit, S. Eser, C. Mathers, M. Rebelo, D. M. Parkin, D. Forman, and F. Bray, "Cancer incidence and mortality worldwide: Sources, methods and major patterns in GLOBOCAN 2012," *International Journal of Cancer*, vol. 136, pp. E359–E386, Mar. 2015.

[322] A. Calon, D. V. F. Tauriello, and E. Batlle, "TGF-beta in CAF-mediated tumor growth and metastasis," *Seminars in Cancer Biology*, vol. 25, pp. 15–22, Apr. 2014.

[323] Y. Kim, J. Wallace, F. Li, M. Ostrowski, and A. Friedman, "Transformed epithelial cells and fibroblasts/myofibroblasts interaction in breast tumor: a mathematical model and experiments," *Journal of Mathematical Biology*, vol. 61, pp. 401–421, Nov. 2009.

[324] P. Hinow, P. Gerlee, L. J. McCawley, V. Quaranta, M. Ciobanu, S. Wang, J. M. Graham, B. P. Ayati, J. Claridge, K. R. Swanson, M. Loveless, and A. R. A. Anderson, "A spatial model of tumor-host interaction: application of chemotherapy," *Mathematical biosciences and engineering : MBE*, vol. 6, pp. 521–546, July 2009.

[325] P. C. Hinkle, "P/O ratios of mitochondrial oxidative phosphorylation," *Biochimica et Biophysica Acta (BBA) - Bioenergetics*, vol. 1706, pp. 1–11, Jan. 2005.

[326] E. A. Swabb, J. Wei, and P. M. Gullino, "Diffusion and Convection in Normal and Neoplastic Tissues," *Cancer Research*, vol. 34, pp. 2814–2822, Oct. 1974.

[327] D. Bray, *Cell Movements: From Molecules to Motility*. Garland Science, Jan. 2001.

[328] J. Shi, K. R. Badri, R. Choudhury, and L. Schuger, "P311-induced myofibroblasts exhibit ameboid-like migration through RalA activation," *Experimental Cell Research*, vol. 312, pp. 3432–3442, Oct. 2006.

[329] E. D. H. Bard, J. B.L., "The behavior of fibroblasts from the developing avian cornea. Morphology and movement in situ and in vitro. J. Cell Biol. 67, 400-418," *The Journal of cell biology*, vol. 67, no. 2PT.1, pp. 400–18, 1975.

[330] L. M. Misell, E. S. Hwang, A. Au, L. Esserman, and M. K. Hellerstein, "Development of a novel method for measuring in vivo breast epithelial cell proliferation in humans," *Breast Cancer Research and Treatment*, vol. 89, pp. 257–264, Feb. 2005.

[331] R. S. J. Frackowiak, G.-l. Lenzi, T. Jones, and J. D. Heather, "Quantitative Measurement of Regional Cerebral Blood Flow and Oxygen Metabolism in Man Using : Theory, Procedure, and Normal Values15: Theory, Procedure, and Normal Valueso and Positron Emission Tomography: Theory, Procedure, and Normal Values," *Journal of Computer Assisted Tomography*, vol. 4, pp. 727–736, Dec. 1980.

[332] J. J. Casciari, S. V. Sotirchos, and R. M. Sutherland, "Variations in tumor cell growth rates and metabolism with oxygen concentration, glucose concentration, and extracellular pH," *Journal of Cellular Physiology*, vol. 151, pp. 386–394, May 1992.

[333] C. T. Su, M. J. Im, and J. E. Hoopes, "Tissue glucose and lactate following vascular occlusion in island skin flaps.," *Plastic and reconstructive surgery*, vol. 70, pp. 202–205, Aug. 1982.

[334] S. Friberg and S. Mattson, "On the growth rates of human malignant tumors: implications for medical decision making," *Journal of Surgical Oncology*, vol. 65, pp. 284–297, Aug. 1997.

[335] R. C. Bast, B. Hennessy, and G. B. Mills, "The biology of ovarian cancer: new opportunities for translation," *Nature reviews. Cancer*, vol. 9, p. 415, June 2009.

[336] B. Hobson and J. Denekamp, "Endothelial proliferation in tumours and normal tissues: continuous labelling studies.," *British Journal of Cancer*, vol. 49, pp. 405–413, Apr. 1984.

[337] L. A. Kunz-Schughart, S. Wenninger, T. Neumeier, P. Seidl, and R. Knuechel, "Three-dimensional tissue structure affects sensitivity of fibroblasts to TGF-beta 1," *American Journal of Physiology. Cell Physiology*, vol. 284, pp. C209–219, Jan. 2003.

[338] D. H. Kohn, M. Sarmadi, J. I. Helman, and P. H. Krebsbach, "Effects of pH on human bone marrow stromal cells in vitro: Implications for tissue engineering of bone," *Journal of Biomedical Materials Research*, vol. 60, pp. 292–299, May 2002.

[339] P. Vaupel, F. Kallinowski, and P. Okunieff, "Blood Flow, Oxygen and Nutrient Supply, and Metabolic Microenvironment of Human Tumors: A Review," *Cancer Research*, vol. 49, pp. 6449–6465, Dec. 1989.

[340] K. Zierler, "Whole body glucose metabolism," *American Journal of Physiology - Endocrinology and Metabolism*, vol. 276, pp. E409–E426, Mar. 1999.

[341] J. P. Kirkpatrick, D. M. Brizel, and M. W. Dewhirst, "A Mathematical Model of Tumor Oxygen and Glucose Mass Transport and Metabolism with Complex Reaction Kinetics," *Radiation Research*, vol. 159, pp. 336–344, Mar. 2003.

[342] H. J. Park, J. C. Lyons, T. Ohtsubo, and C. W. Song, "Acidic environment causes apoptosis by increasing caspase activity," *British Journal of Cancer*, vol. 80, pp. 1892–1897, Aug. 1999.

[343] D. F. Rolfe and G. C. Brown, "Cellular energy utilization and molecular origin of standard metabolic rate in mammals," *Physiological Reviews*, vol. 77, pp. 731–758, July 1997.

[344] A. Andersson, J. Fagerberg, R. Lewensohn, and H. Ehrsson, "Pharmacokinetics of cisplatin and its monohydrated complex in humans," *Journal of Pharmaceutical Sciences*, vol. 85, pp. 824–827, Aug. 1996.

[345] P. J. O'Dwyer, J. P. Stevenson, and S. W. Johnson, "Clinical Pharmacokinetics and Administration of Established Platinum Drugs," *Drugs*, vol. 59, pp. 19–27, June 2000.

[346] Q. Nie, Y.-T. Zhang, and R. Zhao, "Efficient semi-implicit schemes for stiff systems," *Journal of Computational Physics*, vol. 214, pp. 521–537, May 2006.

[347] C. Chou, Y. Zhang, R. Zhao, and Q. Nie, "Numerical methods for stiff reaction-diffusion systems," *Discrete and Continuous Dynamical Systems Series B*, vol. 7, no. 3, p. 515, 2007.

[348] *expv.m* documentation, "https://www.maths.uq.edu.au/expokit/matlab/expv.m," July 2017.

[349] M. L. Goodwin, L. B. Gladden, M. W. N. Nijsten, and K. B. Jones, "Lactate and cancer: revisiting the Warburg effect in an era of lactate shuttling," *Neuroenergetics, Nutrition and Brain Health*, vol. 1, p. 27, 2015.

[350] G. A. Brooks, "Cellcell and intracellular lactate shuttles," *The Journal of Physiology*, vol. 587, pp. 5591–5600, Dec. 2009.

[351] J. Crane, I. Park, M. Olsen, D. B. Vigneron, and S. J. Nelson, "Automated Kinetic Modeling of Hyperpolarized ^{13}C Metabolism in Human Brain Tumors," in *In Proceedings of the 25th Annual Meeting of the International Society for Magnetic Resonance in Medicine (ISMRM)*, (Honolulu, Hawaii, USA), Apr. 2017.

[352] J. Gordon, H.-Y. Chen, P. E. Z. Larson, I. Park, M. V. Criekinge, E. Milshteyn, R. Bok, R. Aggarwal, M. Ferrone, J. Slater, J. Kurhanewicz, and D. B. Vigneron, "Human Hyperpolarized C-13 MRI Using a Novel Echo-Planar Imaging (EPI) Approach," in *In Proceedings of the 25th Annual Meeting of the International Society for Magnetic Resonance in Medicine (ISMRM)*, (Honolulu, Hawaii, USA), Apr. 2017.

[353] Z. Zhu, I. Marco-Rius, M. Ohliger, L. Carvajal, J. Gordon, H.-Y. Chen, I. Park, P. Cao, P. Shin, J. Kurhanewicz, P. Munster, and D. B. Vigneron, "Hyperpolarized ^{13}C Dynamic Breath-held Molecular Imaging to Detect Targeted Therapy Response in Patients with Liver Metastases," in *In Proceedings of the 25th Annual Meeting of the International Society for Magnetic Resonance in Medicine (ISMRM)*, (Honolulu, Hawaii, USA), Apr. 2017.